LASER-BASED FIBRE-OPTIC SENSOR FOR MEASUREMENT OF SURFACE PROPERTIES

BY

Brian Cahill, BE

This thesis is submitted as the fulfilment of the requirement for the award of degree of-

Master of Engineering (MEng)

by research from

Dublin City University

Faculty of Engineering and Design

School of Mechanical & Manufacturing Engineering

May 1998

Dr M A. El Baradie

Project Supervisor

Abstract

Laser-Based Fibre-Optic Sensors for Measurement of Surface Properties

by

Brian Cahill

This project deals with the design and development of an optoelectronic sensor system and its possible use in online applications There are two different configurations of this sensor a sensor for surface roughness and another for defect detection In each configuration the mechanical and optical design are almost identical - optical fibres convey light to and from a surface Light source driving circuits and photodetection circuits were developed for each sensor Data acquisition and analysis algorithms were developed for each sensor

The defect sensor detects through holes and blind holes in sample plates of the following materials brass, copper, stainless steel, and polycarbonate Edge detection is achieved through the development of a photoelectric sensor system that senses the proximity of a surface within a certain displacement range using a multimode laser diode light source emitting at 1300 nm This sensor uses a voltage cut-off system to avoid the effects of light source intensity variation, vibration, surface roughness and other causes of variable reflectivity in online measurement of engineering surfaces The through holes had 2 mm diameter and the blind holes had 3 mm diameter and a depth of 0 6 mm A spatial resolution of approximately 100 μm was achieved – the diameter of the collecting fibre's core

Surface roughness is estimated between 0 025 μm and 0 8 μm, average surface roughness, through a light scattering technique Specular reflectivity was measured at incident angles of 45° and 60° The causes of error, noise and drift are investigated for this system and recommendations are made to account for these problems A carrier frequency system using an electronically modulated LED light source was implemented to improve the noise rejection of the system Digital signal processing system was implemented to digitally filter the acquired signal

DECLARATION

I hereby certify that this material, which I now submit for assessment on the programme of study leading to the award of Master of Engineering is entirely my own work and has not been taken from the work of others save to the extent that such work has been cited and acknowledged within the text of my work

Signed _____ Date _____

Candidate

Table of Contents

CHAPTER FOUR

CHAPTER FIVE

CHAPTER SIX

CHAPTER SEVEN

CHAPTER EIGHT

CHAPTER NINE

ACKNOWLEDGEMENTS

I would like to thank all of the many people who contributed to the success of this project, in particular the following

Dr M A El Baradie, my academic supervisor, for his supervision and guidance

Dr Lisa Looney for her advice and encouragement

All of my fellow postgraduate students for their friendship and good humour - Gareth O'Donnell, J C Tan, Khalid Bakkar, Mohammed Iqbal, Shaestagir, Helen, Joe and Dave

Liam Domican, Martin Johnson, Michelle Considine and all of the staff of the School who have my utmost respect for the massive contribution they made to the project and for the good nature they always showed me

Alan Hughes of the School of Physical Sciences, DCU, and Liam Meany of the School of Electronic Engineering, DCU, for their help with electronic circuits

My family, especially my mother, who have always provided tremendous support throughout my life

CHAPTER ONE

1 Introduction

Over the last twenty years optical technology has become commonplace and successful applications have included the optical disk player, photocopier, laser printer, bar-code reader, and fibre-optic telecommunications The advantages of optical applications may include high speed, high resolution, improved quality, low cost and non-contact operation The research presented in this thesis details the design and development of two sensors a defect sensor and a surface roughness sensor These sensors are outlined in figure 1 1

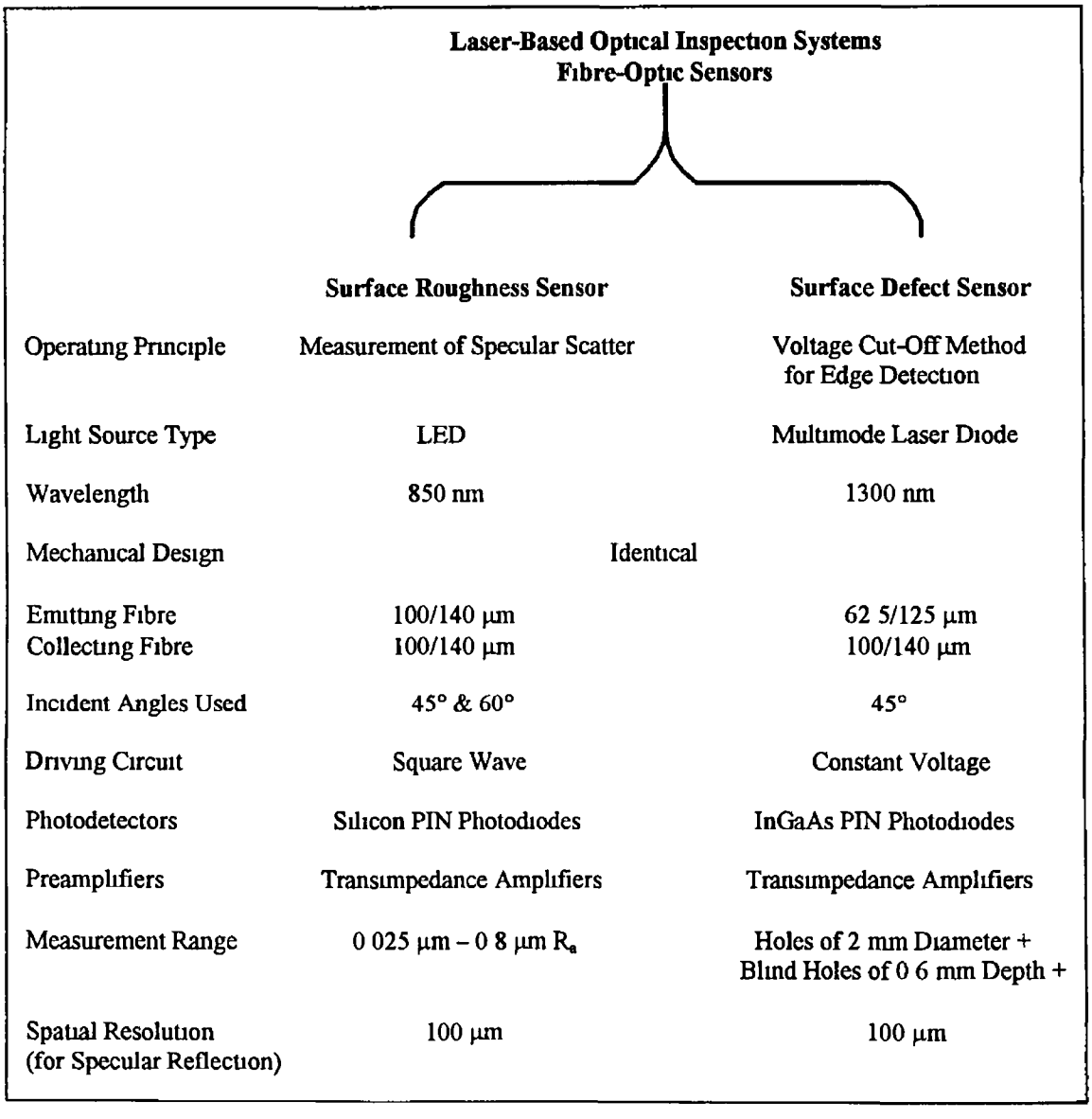

Figure 1 1 Laser-Based Optical Inspection Systems

In manufacturing, optical scanning systems have been used for automatic inspection in several industrial processes The limiting factor of such systems is the scanning element, which is usually mechanical – a rotating mirror or polygon These systems are expensive and are limited in terms of scanning speed - speed is most important in high volume manufacturing This project assesses the possibility of using fibre-optic sensing technology to develop low cost solutions for defect sensing and surface roughness measurement in manufacturing engineering applications It is envisaged that an array of the unit sensors developed for this project will be constructed to perform line scanning at high speed online

A design for a fibre-optic sensor achieving two-dimensional representation of a surface is presented The simple operating principle is similar to that of a barcode reader or photoelectric sensor Receiving and transmitting fibres are oriented in the same plane at equal incident angles to a surface Collected optical radiation is conveyed to a PIN photodiode and preamplifier If the sensed voltage exceeds a predetermined cut-off level, the sensor concludes the presence of a surface, thus, enabling the detection of through holes in a plate or the edge of a plate The sensed signal is dependent on the displacement of the fibres from a surface This dependence allows the sensor to detect blind holes The small core size of fibres, 100 μm, allows 2-mm diameter holes to be adequately sensed, it is likely that holes of under 1-mm diameter could be sensed Blind holes of 0 6-mm depth were sensed successfully

The optical disk player has comprehensively replaced use of the mechanical stylus in the music industry In the field of surface roughness measurement, numerous optical methods have been used in the place of the mechanical stylus Surface roughness can be measured through the effect of light scattering from rough surfaces In the transition from a smooth surface, which transmits light specularly, to a rough surface a higher proportion of incident light is scattered diffusely This transition can be related to the surface roughness of the surface in question Surface roughness can be described as a point quantity using light scattering methods, averaging roughness over the incident spot of the beam The fibre-optic surface roughness sensor presented here investigates the phenomenon of light scattering from surfaces of different surface roughness The factors affecting this transition are discussed

The sensor is designed to replace the use of stylus instruments in the control of surface roughness The sensor can be applied to surface roughness of rolled sheet, semiconductor wafers, hard disk substrates and precision-machined parts In the manufacture of sheet metal, surface smoothness is an important quantity The manufacturing process consists of reducing an input sheet or billet using rollers to perform the deformation, often at high temperatures and pressure In performing this work, the roller becomes worn and needs to be reground A fibre-optic surface roughness sensor can perform higher speed, online, non-contact measurements of surface roughness Production of sub standard produce can be reduced in comparison to offline stylus inspection This fibre-optic sensor need only give an indication of the surface roughness of the ground sheet, not necessarily a very accurate measurement

Chapter 2 reviews contains a literature review of the basics of optical fibres and optical fibre sensors Chapter 3 reviews surface roughness, and surface roughness measurement by the light scattering Applications of fibre-optic and optical sensors using the light scattering method are detailed

Chapter 4 describes the method of operation of each of the surface defect sensor and the surface roughness sensor Chapter 5 outlines the practical knowledge and equipment necessary to construct this sensor The basics of optoelectronic devices, such as lasers, LEDs, and PIN photodiodes, are presented along with associated electronic circuitry The choices made with regard to fibre-optics and mechanical design are outlined Chapter 6 consists of information regarding data acquisition and data processing algorithms These algorithms were implemented using Labview programming

Chapter 7 contains the presentation of the results of both sensor systems Chapter 8 discusses these results and the performance of the sensors Chapter 9 contains conclusions and the recommendations for further work

CHAPTER TWO

2 Literature Survey – Fibre-Optic Technology

This chapter deals with the development of optical fibre technology It reviews intensity-based fibre-optic sensors and their applications

2 1 Optical Fibres – Introductory Theory [1-8]

Optical fibres are layered cylinders of dielectric material, such as glass or plastic, that convey electromagnetic radiation (principally light or near infrared radiation) from one end to the other They have found widespread use in communications technology, medical endoscopy and in fibre-optic sensing The characteristics of optical fibres will now be discussed

2 1 1 Numerical Aperture

Fibre optics work through the principle of total internal reflection as illustrated in figure 2 1 (b) – when a light ray passes from a denser medium to a less dense medium it refracts closer to the interface - thus for a range of angles the ray will be confined in the denser medium The density of a medium is indicated by the refractive index, n, of that medium The refractive index of a medium is determined by the ratio of the speed of light in a vacuum, c, to the speed of light in that medium, v, according to equation 2 1

$$n = \frac{c}{v} \qquad 2\ 1$$

Light is refracted in accordance with Snell's law

$$n_1 \sin i = n_2 \sin r \qquad 2\ 2$$

n_1 and n_2 are the refractive indices of each medium, i is the angle of incidence and r is the angle of refraction, these are illustrated in figure 2 1 (a) Refraction is caused by the wave nature of light As the angle of incidence increases, a point is reached where

r = 90° Angles greater than the critical angle are completely reflected – total internal reflection The angle of incidence at this point is called the critical angle, i_c From Snell's Law

$$i_c = \sin^{-1}(n_2/n_1) \qquad 2\,3$$

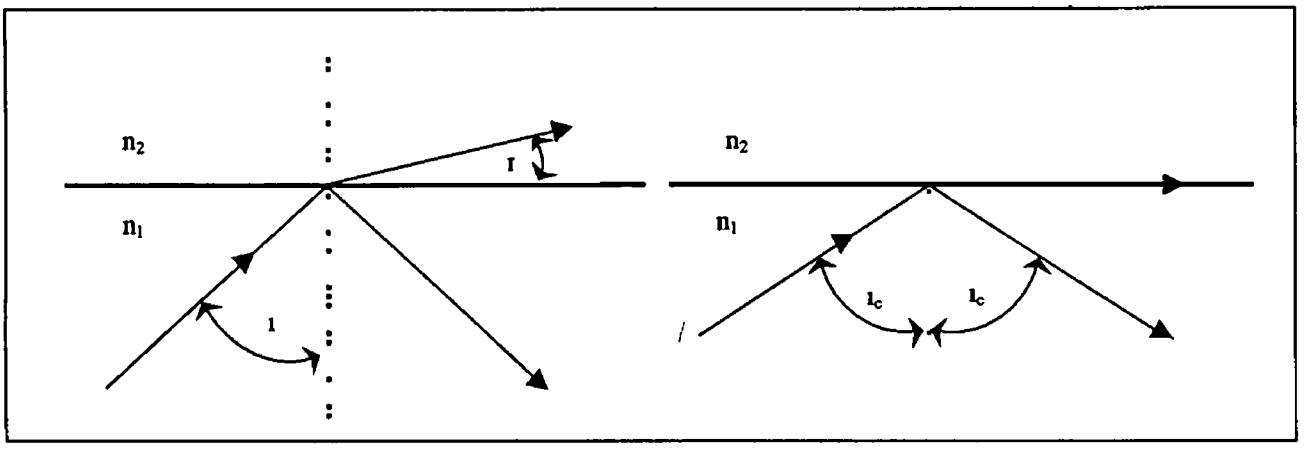

Figure 2 1 (a) Refraction at an interface (b) Total Internal Reflection

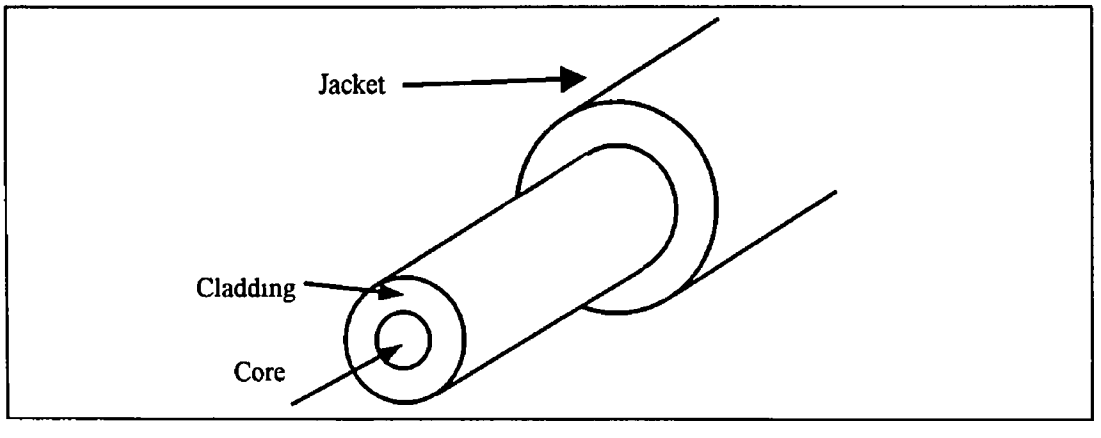

Figure 2 2 Illustration of core and cladding of an optical fibre

Figure 2 2 illustrates the basic structure of optical fibres, at the interface between core and cladding there is a change in refractive index This interface keeps light rays travelling through the core by the principle of total internal reflection Figure 2 3 (a) shows how this angle of acceptance is defined by the critical angle described above If this figure is rotated around the axis of the fibre, the acceptance angle becomes an acceptance cone Figure 2 3 (b) shows how light rays at angles greater than θ light will be refracted out of the core after travelling for a few centimetres of fibre and that rays at angles less than θ will be confined to the core for long distances

Numerical aperture (NA) is the quantity that is used to measure the acceptance angle for an optical fibre Numerical aperture is defined by equation 2 4

$$NA = n_0 \sin \theta \qquad 2\,4$$

n_0 is the refractive index of the medium the ray is travelling from, n_0 is considered equal to 1 for air - n_0 is defined as 1 for a vacuum From Snell's Law

$$n_0 \sin \theta = n_1 \sin (90° - i_c) = n_1 \cos i_c \qquad 2\,5$$

It follows from the above equations that the numerical aperture is given by

$$NA = n_1 (1 - \sin^2 i_c)^{½} \qquad 2\,6$$

Substituting from equation 2 3

$$NA = (n_1^2 - n_2^2)^{½} \qquad 2\,7$$

Equation 2 7 shows that the numerical aperture of an optical fibre depends on n_1 and n_2 alone and is independent of any variation in n_0

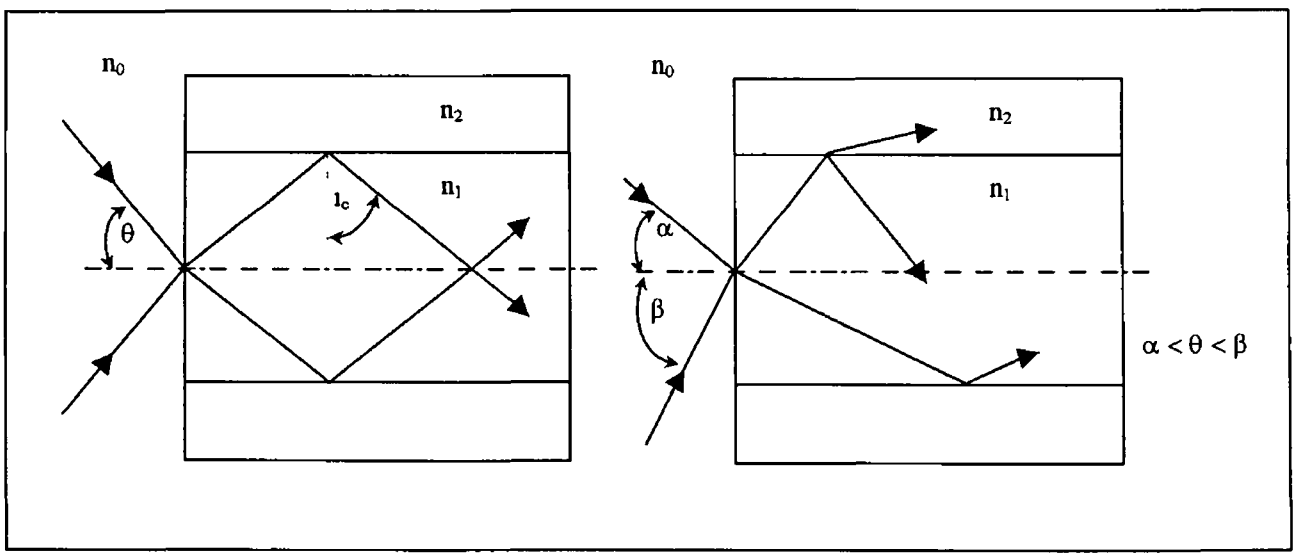

Figure 2 3 (a) Acceptance cone for optical fibre (b) Transmitted and attenuated rays

2 1 2 Dispersion

Dispersion is a quantity that affects the signal carrying properties of optical fibres, i e the bandwidth of a fibre It is the degradation of the input signal as it travels through the fibre This is illustrated in figure 2 4 – the pulse becomes longer in duration and generally loses shape Dispersion can be divided into material dispersion and modal dispersion

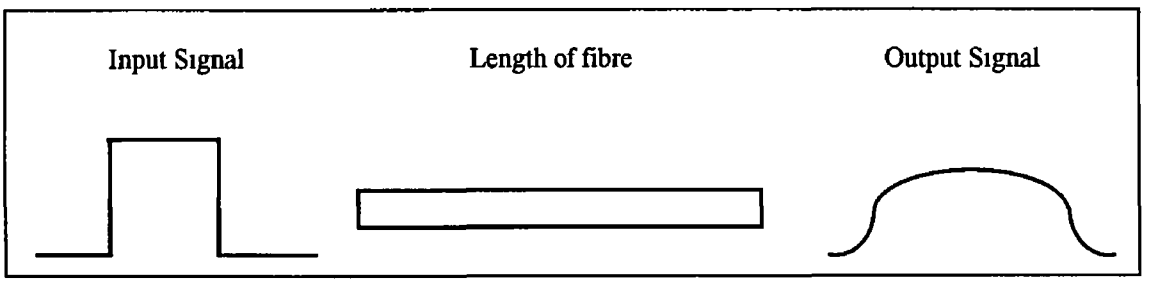

Figure 2 4 Dispersion of a square wave in an optical fibre

Electromagnetic waves travel at different speeds in dielectric media depending on optical wavelength, i e the refractive index of the materials that optical fibres are made of is not constant with wavelength This causes material dispersion when the light source emits over a broad spectrum, e g a Light Emitting Diode (LED), and less so for a coherent laser source

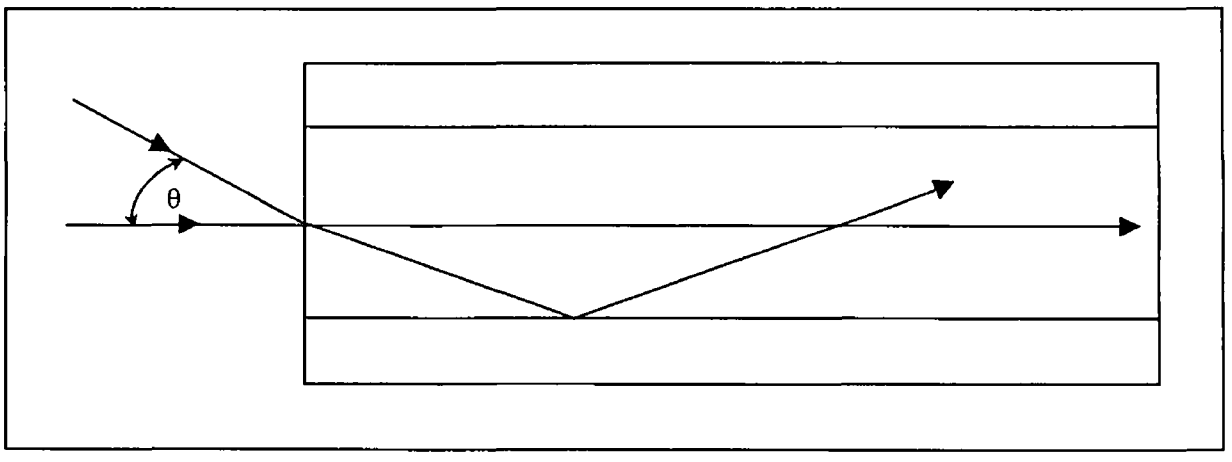

Figure 2 5 Modal Dispersion through a multimode step-index fibre

The differing velocities of modes in a multimode optical fibre cause modal dispersion Prior to this we have assumed light to travel as rays, because of the wave nature of light this is not completely true For a fibre a certain number of modes are supported

The number of modes a fibre supports changes with variation in the core diameter, optical wavelength and the refractive indices of core and cladding To simplify, as core diameter increases many modes are supported in a fibre and the ray optics analysis proves adequate, unless mode coupling in multimode fibre is of interest An analysis of modes in optical fibres is considered beyond the scope of this thesis and can be found in the literature [1,7] Figure 2 5 shows how a beam travelling along the centreline of a step index multimode fibre reaches the end of the fibre more quickly – thus dispersing the input signal

Singlemode fibre does not suffer from modal dispersion – having only one mode In the section 2 1 5 it will be shown how graded index multimode fibre reduces modal dispersion

2 1 3 Attenuation

Attenuation is the property of optical fibres that measures power loss as a signal travels through an optical fibre Optical power, I, is measured in Watts Attenuation, A, is described in equation 2 8 below, relates input optical power, I_0, to optical power at a distance z, I_z Attenuation is commonly expressed in units of decibels per kilometre (dB/km) for optical fibres Attenuation is important in intensity based fibre-optic sensors as it is a cause of error particularly if the loss is variable

$$A = -\frac{10}{z}\log_{10}\frac{I_z}{I_o} \qquad 2\ 8$$

There are four separate causes of attenuation in optical fibres (i) material absorption, (ii) scattering losses, (iii) manufacturing induced losses and (iv) bending losses

Material absorption is due to absorption of optical energy into the electronic energy levels of transition metal impurities, such as iron, copper, chromium, and nickel, and into the vibrational levels of hydroxyl ions (OH^-) in the core and innermost sections of the cladding In these cases, energy is absorbed from the optical beam and is reradiated into the molecular lattice in the form of heat Strong electronic absorption occurs at

ultra-violet wavelengths while at infrared wavelengths vibrational absorption becomes dominant.

Scattering losses are caused by three scattering mechanisms - Rayleigh, Brillouin and Raman scattering. Of these Brillouin and Raman scattering can be neglected apart from at high optical intensities. Rayleigh scattering is caused by microscopic density fluctuations that are frozen into the random molecular structure of the fibre core when it cools to its relatively high solidification temperature. These density fluctuations may be resolved into spatial frequencies that have wavelengths much shorter than the optical wavelength. Rayleigh scattering varies inversely with the optical wavelength, λ, $\sim 1/\lambda^4$.

The sum of the intrinsic losses (material losses and scattering losses) gives the "estimated total loss curve" when plotted against optical wavelength. Figure 2.6 below shows this intrinsic loss curve for graded index silica fibre. Note that for the most part Rayleigh scattering predominates apart from the OH^- peak at 1.38 μm. Infrared absorption predominates at higher wavelengths. Research in electronic light sources for optical fibres telecommunications has focussed on the troughs of this curve. For plastic fibres and for other glasses the intrinsic loss curve is different from silica.

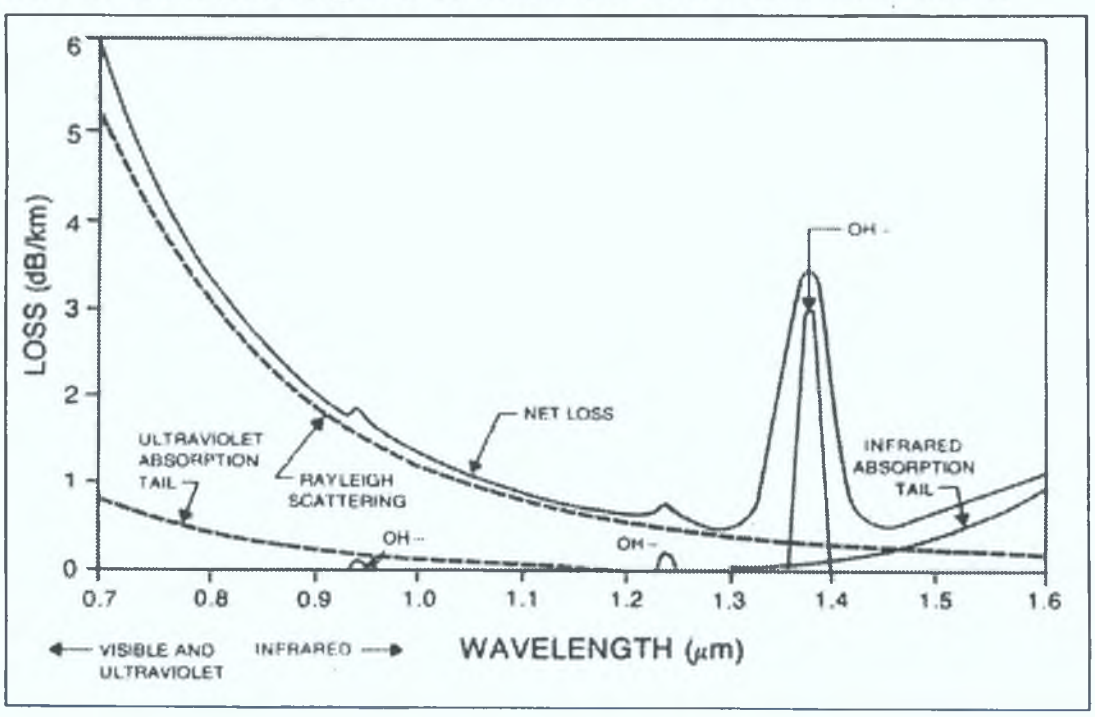

Figure 2.6 Attenuation characteristics of graded-index fibre [6]

The manufacturing process may cause losses. These include inclusions in the fibre, irregularities in fibre size and micro-bends caused by coating and cabling. The manufacturing process is usually under sufficient control to keep losses caused by fibre drawing and coating negligible. Losses caused by micro-bends are discussed below.

There are two causes of bending losses: sharp bend, and micro-bends. Figure 2.7 below shows through ray optics how a constant radius bend will cause optical power to leak out of a fibre. At each reflection at the outer arc of the bend, power will refract into the cladding.

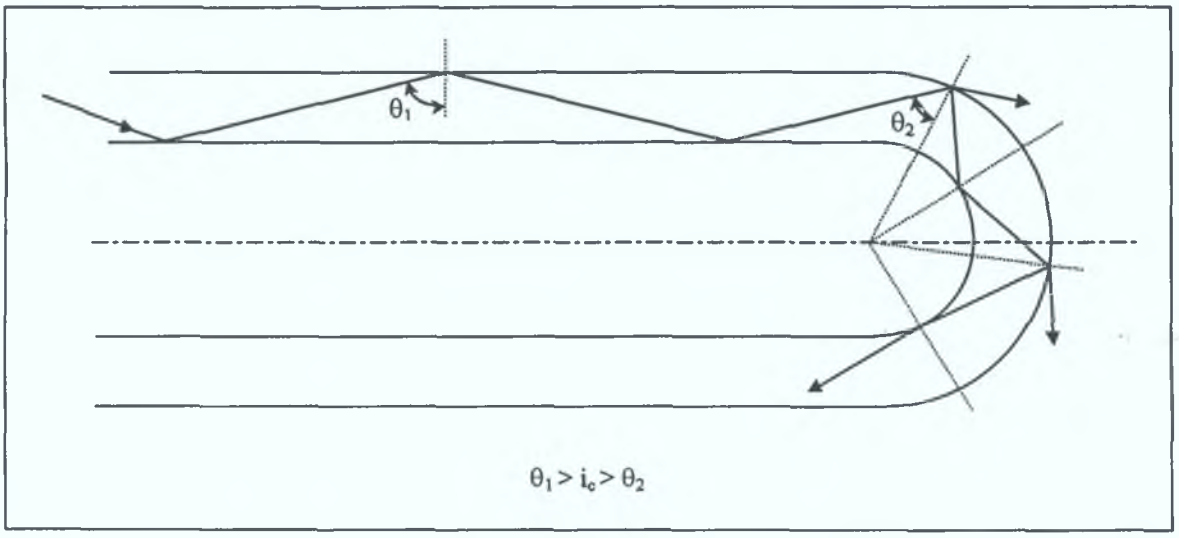

Figure 2.7 Loss of optical power from an optical fibre due to a constant radius bend

It is possible to compute the expected losses due to a constant radius bend [8]. Figure 2.8 shows how attenuation varies with bend radius for constant numerical aperture. Thus for bend radii of the order of centimetres for fibre with numerical apertures of over 0.20 attenuation is negligible.

A micro-bend is a microscopic, short period, random bend typically impressed on the fibre during the process of jacketing and cabling. Micro-bends become a serious problem when the radius of curvature becomes small but large in comparison with the core size of the fibre. Figure 2.9 illustrates leakage of power from an optical fibre due to micro-bending losses.

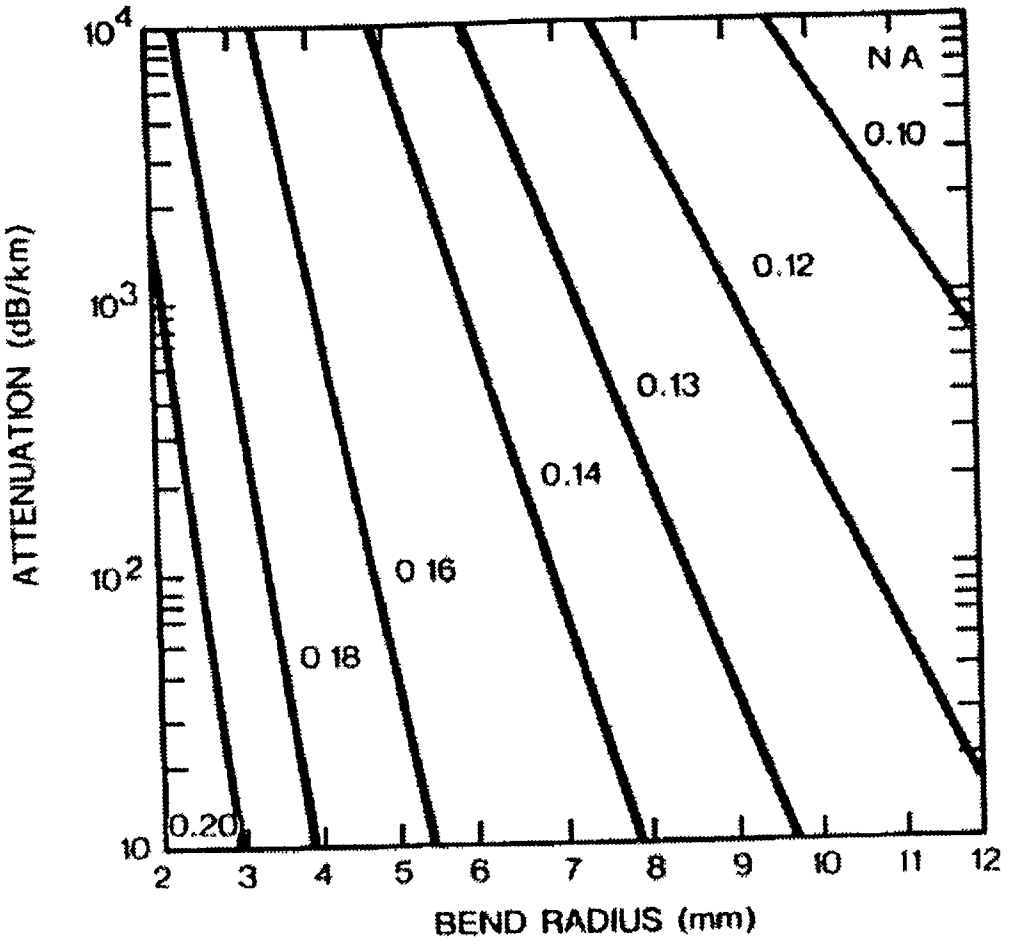

Figure 2 8 The variation of optical power attenuation rate as a function of bend radius for constant radius bends in typical optical fibres for various values of numerical aperture using a 0 83 μm optical source

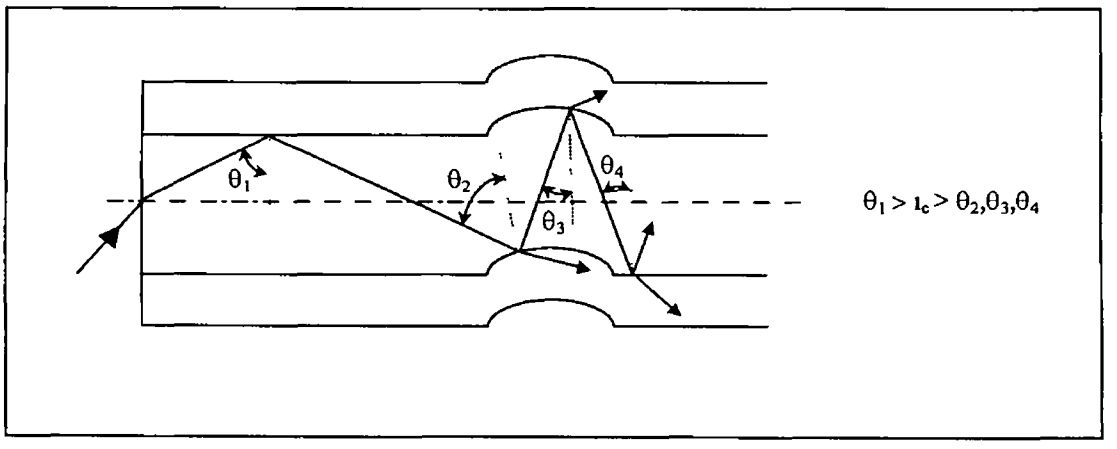

Figure 2 9 Attenuation due to micro bending

In short lengths of fibre coupling between modes contributes to attenuation Different modes in a fibre are attenuated at different rates Depending on the launch conditions

of the fibre, some modes may receive light preferentially over others Over long lengths of fibre this preferential distribution of optical power gradually reaches an equilibrium distribution or steady state, through mode coupling Mode coupling is the transfer of optical power between modes - because of the effect of slight fibre imperfections and bends When this steady state is reached, loss is independent of the launch conditions Mode coupling is highly sensitive to the external condition of the fibre, e g a jacketed fibre will have different loss values than an unjacketed fibre In Chapter 3 the fabrication of a mode coupler is described – this allows small lengths of fibre to be used in optical sensing

2 1 4 Classification of optical fibres

Optical fibre can be divided into two main types - singlemode and multimode - multimode can be further divided into stepped index and graded index Figure 2 10 describes the refractive index profile and the path of radiation in each type of fibre Table 2 1 describes the ranges of fibre properties for several different types of fibre The most obvious difference between single and multimode fibre is the difference in core size, singlemode fibre has a core size which approaches that of the wavelength of light

	Multimode Fibre – Step Index	Multimode Fibre – Step Index	Multimode Fibre – Graded Index	Singlemode Fibre
Core/cladding Material	Glass/Glass	Glass/Plastic	Glass/Glass	Glass/Glass
Dispersion at 850 nm	10-100 ns km^{-1}	10-180 ns km^{1}	1-10 ns km^{1}	50 – 100 ps nm^{-1} km^{1}
Attenuation at 850 nm (dB km^{-1})	2-60	3-2000	2-10	2-6
Core Diameter (μm)	80-200	200-1000	50-100	2-8
Cladding Diameter (μm)	100-250	230-1250	125-150	80-125
Numerical Aperture	0 1-0 3	0 18-0 50	0 18-0 50	0 10-0 15

Table 2 1 Summary characteristics of common types of optical fibre [3]

As the core size of a fibre approaches the optical wavelength used the fibre supports only a single mode Singlemode fire has highly significant properties – low attenuation and low dispersion As the core size of singlemode optical fibre is quite small (2 – 12 μm) a focussed laser source is usually used This coherent source further reduces material dispersion Coherent interferometric sensors use singlemode fibres exclusively, as they preserve the coherence of the light source

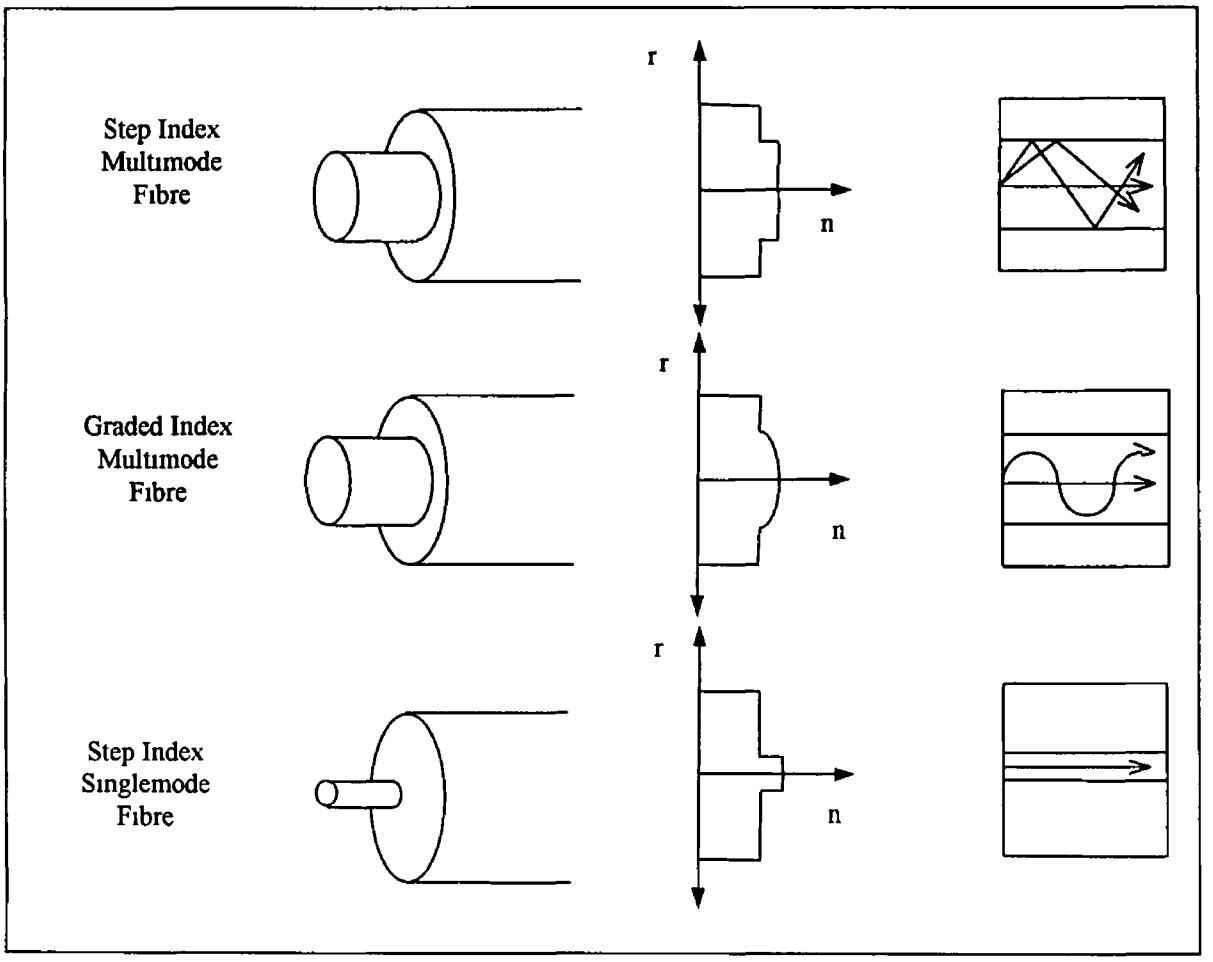

Figure 2 10 Types of fibre – Core/Cladding Size, Refractive Index Profile, and Ray Path

The refractive index profile of multimode fibre distinguishes between graded index fibre and step index fibre All the analysis of fibre until this point has assumed step index multimode fibre with a single value of refractive index for the fibre core Graded index fibre has a refractive index profile across the fibre, as defined by equation 2 9 n_1 is the refractive index at the axis and n_2 is the refractive index of the cladding The profile parameter, α, is optimised for $\alpha=2$, resulting in a parabolic index profile This

profile results in rays travelling faster at higher radii from the centre. Some of the rays travelling in graded index fibre do not travel in straight lines. Depending on launch conditions, rays travel as sine waves or helixes or in the primary mode - straight along the axis of the fibre (figure 2.11). As rays travel faster at higher radii those rays travelling further distances travel at a faster rate – this reduces dispersion in a graded index fibre in comparison with a multimode step index fibre.

$$n(r) = n_1\left[1 - 2\Delta\left(\frac{r}{a}\right)^{\alpha}\right]^{1/2} \qquad 2.9$$

where $$\Delta = \frac{n_1^{\,2} - n_2^{\,2}}{2n_1^{\,2}}$$

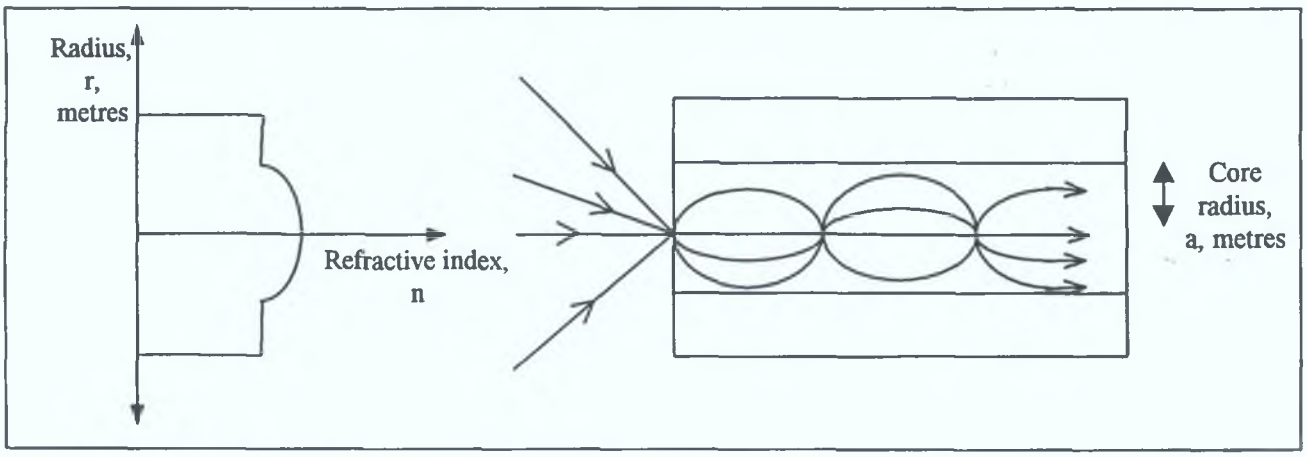

Figure 2.11 Ray paths in a graded index fibre

Multimode fibres have disadvantages and advantages in comparison to single mode fibres. Their larger core sizes facilitate the launching of light and splicing of similar fibres. Laser sources are almost exclusively used with singlemode fibres, LEDs or other white light sources can also be used with multimode sources. Light Emitting Diodes are simpler to manufacture and cost less than laser sources; in addition they are more stable and have longer lifetimes.

As detailed above singlemode fibres have superior dispersion and attenuation characteristics. Singlemode fibres are necessary for use in coherent interferometry using fibre-optics as they preserve the coherency of the input signal. In addition to the fibres mentioned previously there are polarisation-controlled fibres - in a typical singlemode fibre there is one tranverse mode with two orthogonal polarisations. These

polarisations will travel at slightly different speeds In some sensing applications these fibres must be used [3]

Fibres are generally manufactured from glass or plastic or a combination of both Different materials transmit at different optical wavelengths, thus silica fibres will transmit light best at the wavelengths indicated by the troughs of the curve of figure 2 6 Plastic transmits well over the visible spectrum alone Chalcogenide and silver halide glasses are being used to manufacture fibre that transmits over longer infrared wavelengths

2 2 Fibre-Optic Sensors

In this section, the application of fibre-optics sensors sensing extrinsically from the fibre itself is discussed This section limits itself to intensity-based fibre-optic and photoelectric sensors

Fibre-optic sensors have the advantage that they are relatively immune from electromagnetic interference, have low power consumption, small size and weight, high sensitivity in some measurements and compatibility with electronic control and modulation Measurement can be made in hostile environments and the fibre can transmit the signal to a remote distance

Fibre-optic sensors are designated as either extrinsic or intrinsic sensors Intrinsic sensors use the fibre itself as a sensing transducer The fibre itself is affected by the measurand without optical power leaving the fibre, for example using the effect of micro-bends [8] In extrinsic sensing, optical power is emitted from the fibre and is recollected for measurement, the optical fibre is only used to convey optical power – any effect the fibre has on the signal contributes to error This project is concerned with extrinsic sensors where the reflection from a surface modifies the output of the sensor Figure 2 12 distinguishes between intrinsic and extrinsic sensors

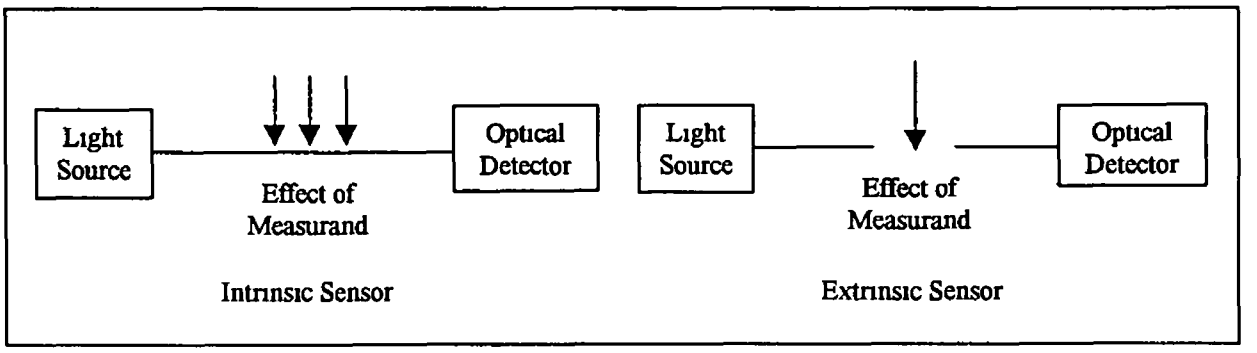

Figure 2 12 Intrinsic sensor, signal is affected while inside the fibre, and extrinsic sensor, signal is affected while it is outside the fibre

Fibre-optic sensors have the capacity to use the high-performance light sources, detectors, and fibres developed for the telecommunications industry [9] and the technology used in optical discs [10,11] There are applications in fibre-optic sensing using most devices developed for these industries The ingenuity of the optoelectronics engineer in using the available tools determines the advance of optical sensing Currently there is the emergence of LEDs that emit white light [12] and laser diodes that emit blue light [13] to fuel further optical sensor technology

This project is concerned with the use of intensity-based fibre-optic sensors Fibre-optic interferometers have also been the focus of much research in the optical engineering area Coherent interferometry is capable of achieving high sensitivity in the measurement of displacement [14] Fibre-optic versions of all the classical interferometer arrangements using bulk optics have been developed and these reduce complexity and cost In addition, the emergence of fibre-optics has allowed practical interferometers to be used in situations outside of the laboratory In recent years, there has been much research into the use of the interference patterns of white light to measure displacement with fibre-optic sensors [3,15,16] This method has many advantages in measuring displacement – large range, high resolution, high accuracy, absolute measurement of displacement and no over-stringent requirements in relation to light sources other than that they are incoherent [17] Most importantly low coherence interferometry can be implemented at lower cost than coherent interferometry Low coherence interferometry can use either multimode or singlemode fibres [18] and has found many interesting applications [19-21]

2 2 1 Intensity Based Fibre-Optic Sensors

Intensity-based fibre-optic displacement sensors were among the first implementations of fibre-optic sensing They have also been used to measure other parameters such as pressure, strain and vibration In intensity-based sensors, the parameter of interest affects the intensity of the signal collected by the photodetector The intensity-based sensor is simpler and cheaper to implement than coherent interferometry or low coherence interferometry, but it is limited to highly reflective surfaces Although the other two methods work best with reflective surfaces, their principle of operation is not reliant on the reflectivity of the surface in question, being based on the wave nature of light In addition, the intensity-based sensor is sensitive to other disturbances that affect intensity, and a referencing scheme may be necessary to reduce error

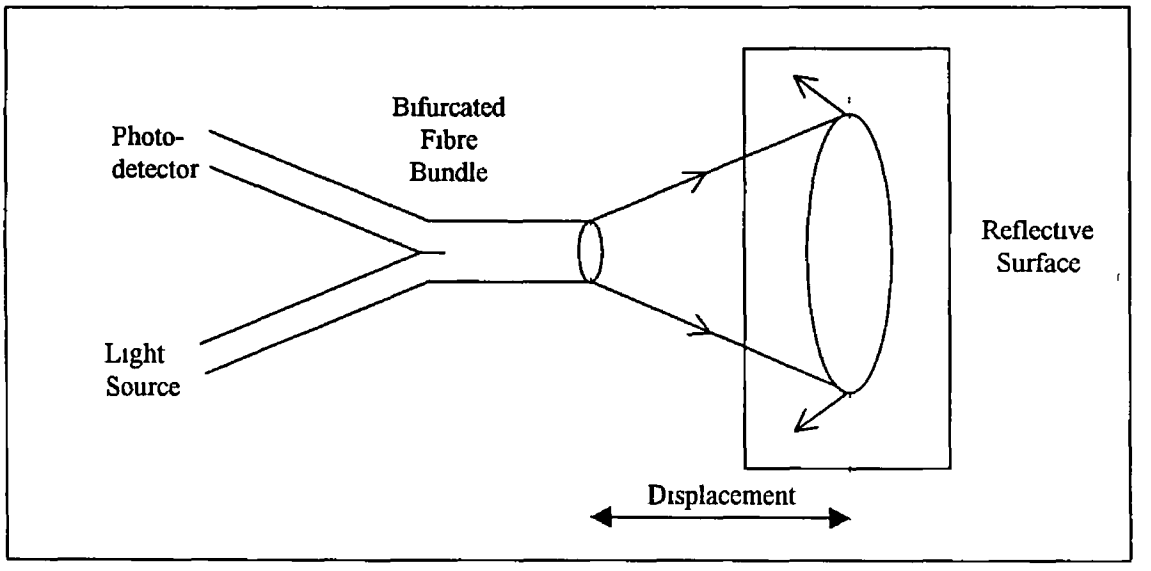

Figure 2 13 Operating principle of fibre-optic bundle type sensor [24]

There are two basic set-ups for displacement measurement using intensity-based fibre-optic sensors one uses a bifurcated fibre-optic bundle and the other uses arrangements of single fibres A bifurcated bundle fibre-optic sensor identical to photoelectric switch sensors [22] can measure displacement from a reflective surface if it has an analogue output Shimamoto et al [23,24] and Hoogenboom et al [25] modelled the operation of these bundle type displacement sensors for different distribution of sensing and emitting fibres in the sensing head of the bundle and compared with experiment Figure 2 14 shows three examples of fibre distributions of sensing heads and figure 2 15 shows the response curves for each of the distributions

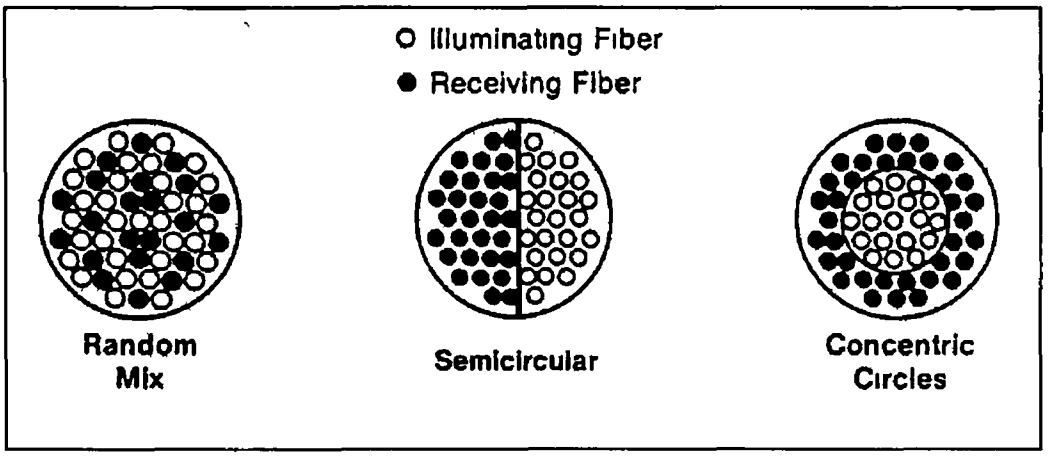

Figure 2 14 Typical fibre distribution configurations of bundle type sensors [25]

This type of sensors uses incoherent fibre bundles, i e the bundle does not convey an image – the orientation of fibres at one end of the bundle is different to that at the other Image carrying bundles such as those used in medical endoscopy are quite expensive Incoherent bundles are used to convey optical power alone

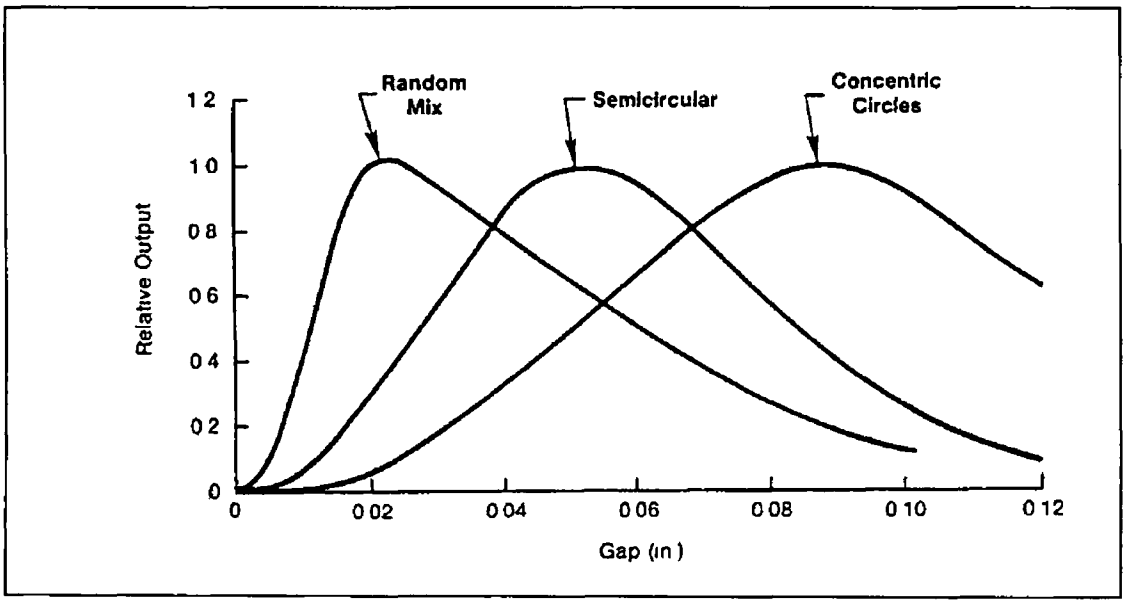

Figure 2 15 Typical response curves for fibre distributions in figure 2 22 [25]

Using single fibres to deliver and collect light in a fibre-optic sensor uses the internal reflection properties of optical fibres These sensors have very high sensitivity to displacement with the disadvantage of close stand-off distance to the surface and short ranges Some different arrangements of single-fibre displacement sensors are shown in figure 2 16 As can be seen it is possible to measure longitudinal, lateral or angular

displacement In this figure the same fibre emits and receives light Figure 2 17 shows an arrangement with separate fibres for emitting and receiving light This removes the need for a fibre coupler to separate the signal travelling from the light source and to the photodetector

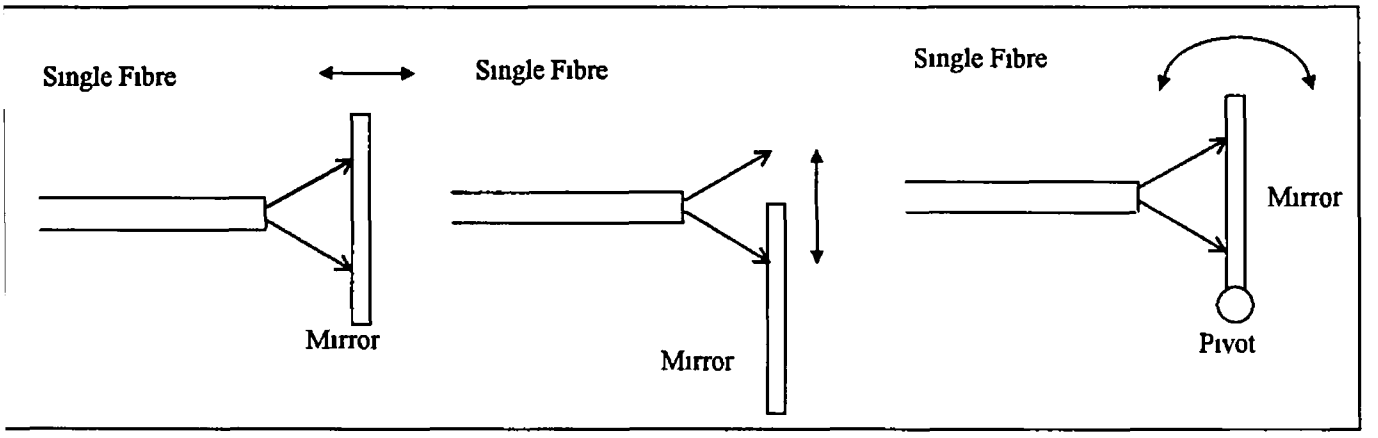

Figure 2 16 (a) Longitudinal Displacement (b) Lateral Displacement (c) Angular Displacement [26]

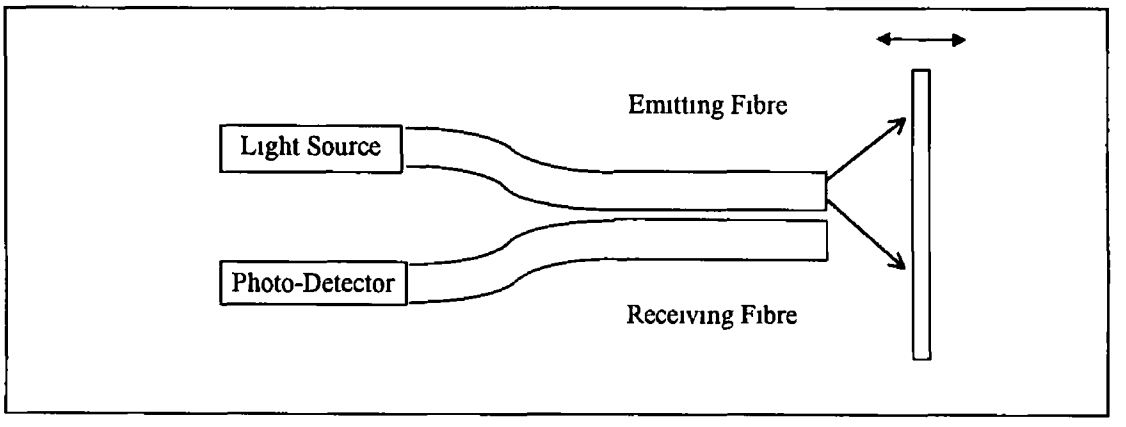

Figure 2 17 Schematic diagram of basic fibre-optic displacement sensor

Figure 2 18 shows the displacement characteristics of a single fibre sensor As can be seen from the shape of the curve, areas I and III, either side of the peak, are useful in measuring displacement The side nearer the surface has a steeper slope and thus has more sensitivity to displacement measurement The other side is less sensitive to displacement but has a greater stand-off distance from the surface The response curve is at its most linear at maximum sensitivity Area II is the peak of the curve and exhibits the least sensitivity to displacement

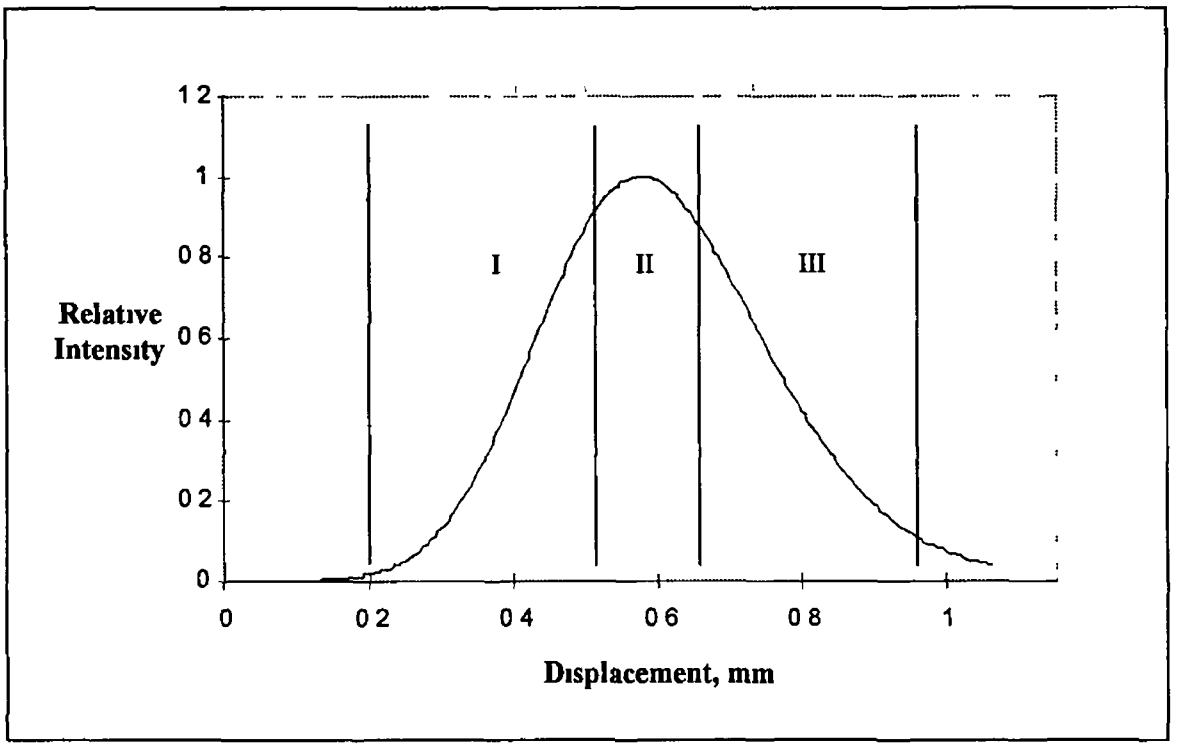

Figure 2 18 Displacement characteristic of a single fibre displacement sensor

Powell [27] implemented a sensor that used plastic fibres with a diameter of 1mm oriented at various incident angles to the surface as shown in figure 2 19 He claimed that this sensor increased the sensitivity to displacement in comparison to then available commercial sensors that used incoherent bundles such as those modelled by Hoogenboom [25]

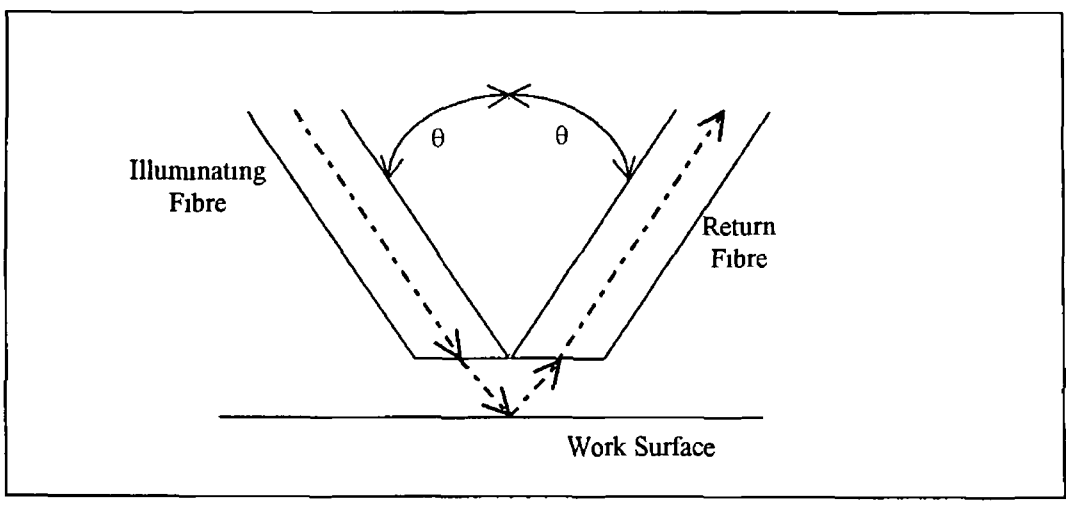

Figure 2 19 Cross-sectional diagram of angled sensor developed by Powell [27]

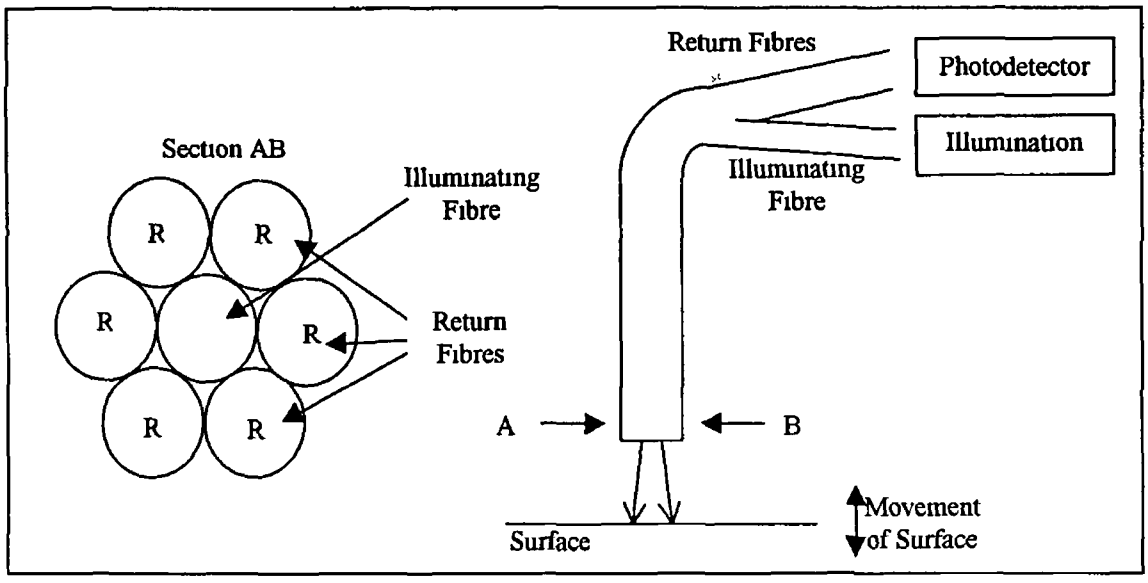

Figure 2 20 Schematic of a basic seven-fibre bundle [28]

Cook and Hamm [28] described the performance limits of an optical fibre displacement sensor with regard to displacement sensitivity, frequency response, displacement detection limit, linear range, dynamic range and working distance They investigated the limits introduced by light sources, detectors, electronic noise and fibres This displacement sensor consisted of a seven-fibre bundle, shown in figure 2 20, with one fibre carrying the input signal from the light source and the six surrounding fibres summing the reflected light

2 2 2 Referencing Intensity Based Fibre-Optic Sensors

The main disadvantage of intensity modulated sensors in this application is that factors other than displacement affect the measurement Fluctuations in the light source will introduce error, although intensity levels of LEDs are more stable than those of laser diodes or incandescent light sources they are still be affected to an extent by thermal drift The effect of temperature on the performance of LEDs, laser diodes and photodiodes and other electronic components is discussed in a later chapter Variations in losses due to fibre bending and losses due to couplers and connectors can also affect readings Variations in the reflectivity of a reflective surface affect the readings as will a change in the angle of the surface These disadvantages introduce a certain level of error, the set-up and calibration procedure need to account for this error There are

many techniques used for referencing intensity based sensors and Murtaza and Senior [29] provide a detailed overview of many of these methods. They conclude that the effectiveness of the referencing can usually be related to the cost and design complexity of the system – there is usually an increase in the number of components of the sensor and the total cost of these components.

Implementing a reference channel to take additional measurements can help to account for these errors. Initial light source intensity may be measured as a reference against light source fluctuations. Measuring the light source intensity alone ignores all the other factors mentioned above. Also measuring light source intensity may reduce the light intensity of the sensing signal. Another cheap and simple referencing scheme is to add a spatial reference such as that outlined by Cockshott and Pacaud [30] and shown in figure 2.21. This form of referencing takes account of fibre losses in the emitting fibre, varying surface reflectivity and light source variations. Libo et al. [31] have shown how this type of sensor can compensate for fibre bending and light source fluctuations, using He-Ne laser and white light lamp light sources. Difference over sum processing [32] of these signals can be used for the final output; this ratio is shown in figure 2.21. Difference over sum processing can also result in an irregular displacement curve that is less suitable for use.

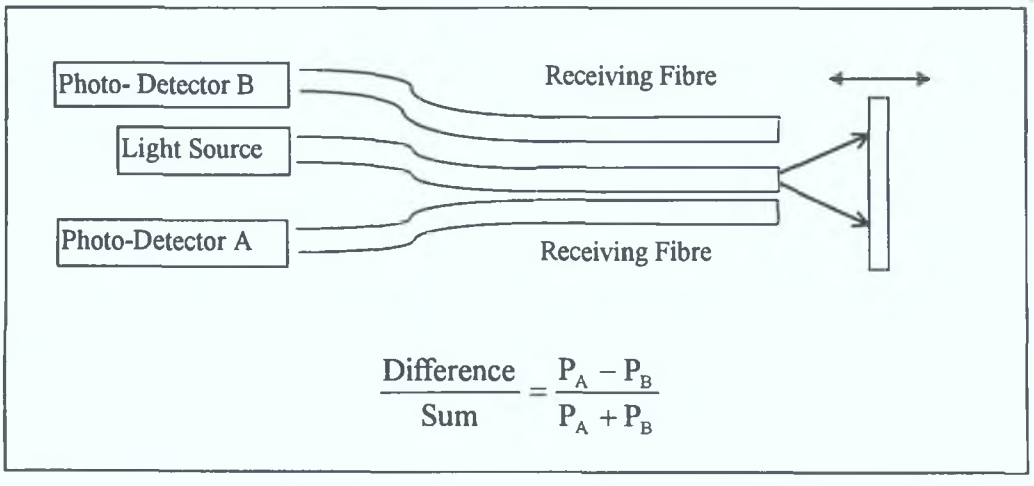

Figure 2.21 Spatially referenced fibre-optic sensor using difference over sum processing

Distinguishing between two different signals can reference against fibre losses. This can be achieved through separating the signals through wavelength or temporal

referencing schemes Temporal referencing is accomplished through using two light sources which can be distinguished through temporal differences, i e amplitude modulation at different frequencies as in figure 2 22b or if each light source is pulsed sequentially as in figure 2 22a In these cases, the signals are sensed by the same photodetector keeping the same number of system components

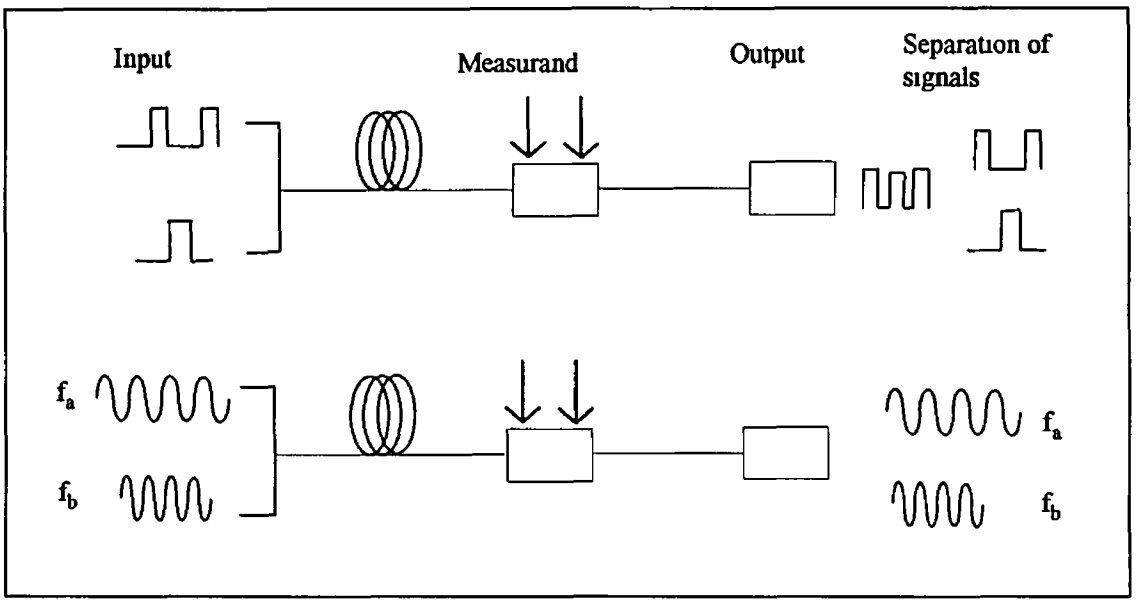

Figure 2 22 Temporal referencing (a) Time Division Multiplexing (b) Frequency Division Multiplexing [29]

Referencing can also make use of the wavelength of light by using either two light sources emitting at different wavelengths or one source whose signal is split into two signals of different wavelength at some stage of the sensor [33,34,35] Wavelength division multiplexing (WDM) is illustrated in figure 2 23 Much research has been carried out in this area for use in telecommunications and some in the area of fibre optic sensors This system requires light sources of differing wavelengths and also a multiplexer and demultiplexer, these conditions increase the cost of the sensor system substantially Senior and Cusworth [33] also discuss simpler dual wavelength sensor system and spectrally modulated systems systems which cause a shift in the central wavelength of the output signal Senior et al [34] and Wang et al [35] developed similar systems which use a reflective coating at the output end of the sensor which selectively transmits and reflects different wavelengths Figure 2 24 illustrates Wang's sensor Through using the signal reflected by the filter to reference the sensor against

variations in light source fluctuation and fibre losses a resolution of 0 13 μm over a range of 250 μm was attained

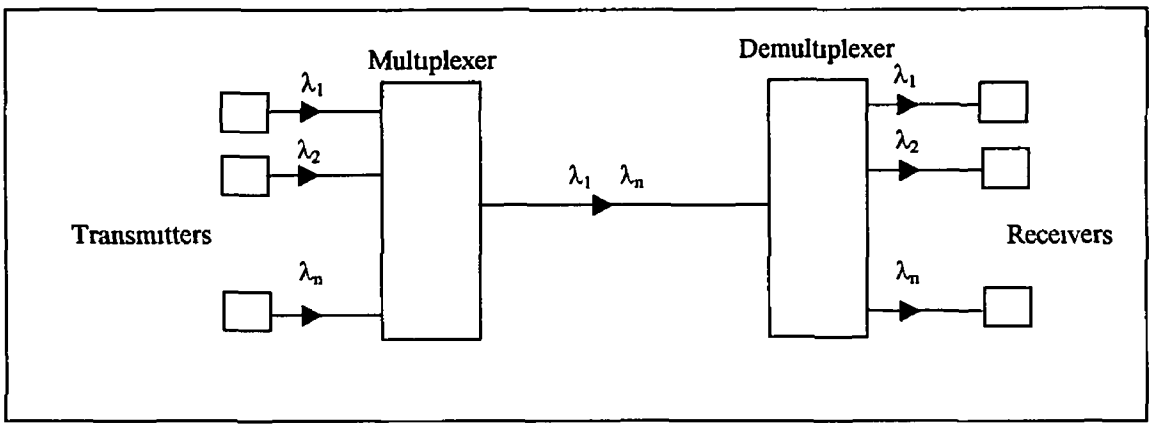

Figure 2 23 Wavelength Division Multiplexing system [33]

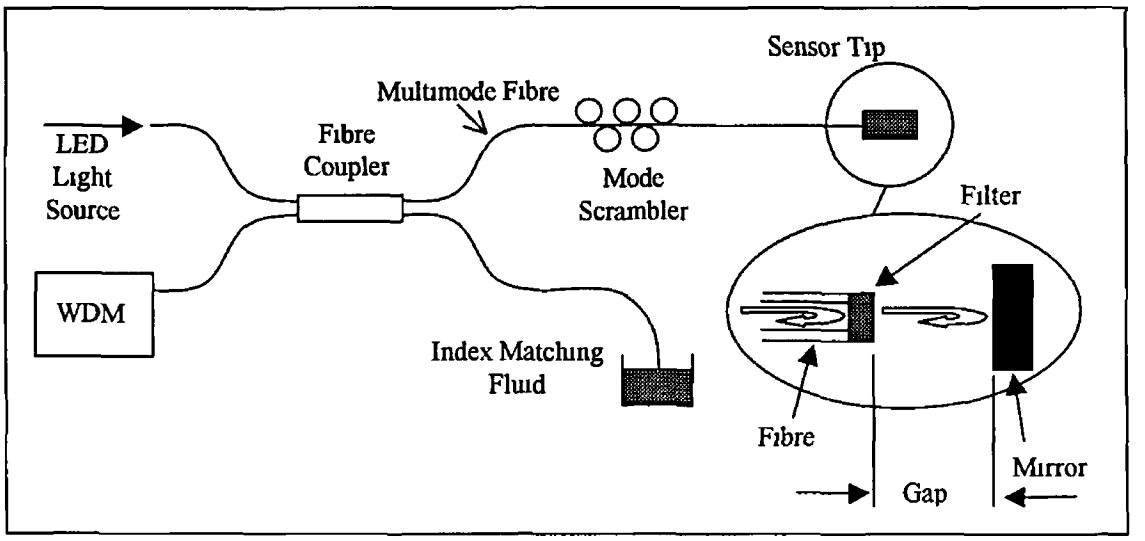

Figure 2 24 Schematic of a loss-compensated sensor for displacement measurement using split spectrum technique [35]

Measuring light source intensity directly effectively monitors the major cause of error in optical fibre sensor systems This may require optical signal tapping using fibre-optic couplers increasing cost and optical power loss Measuring light source intensity allows laser diodes to be used in the place of more stable LEDs Some laser diodes are packaged with integral photodiodes to measure light source intensity

2 2 3 Applications of Intensity Based Fibre-Optic Sensors

Many properties, such as vibration, stress, pressure can be inferred from the precision measurement of displacement and have been measured using fibre–optic sensors

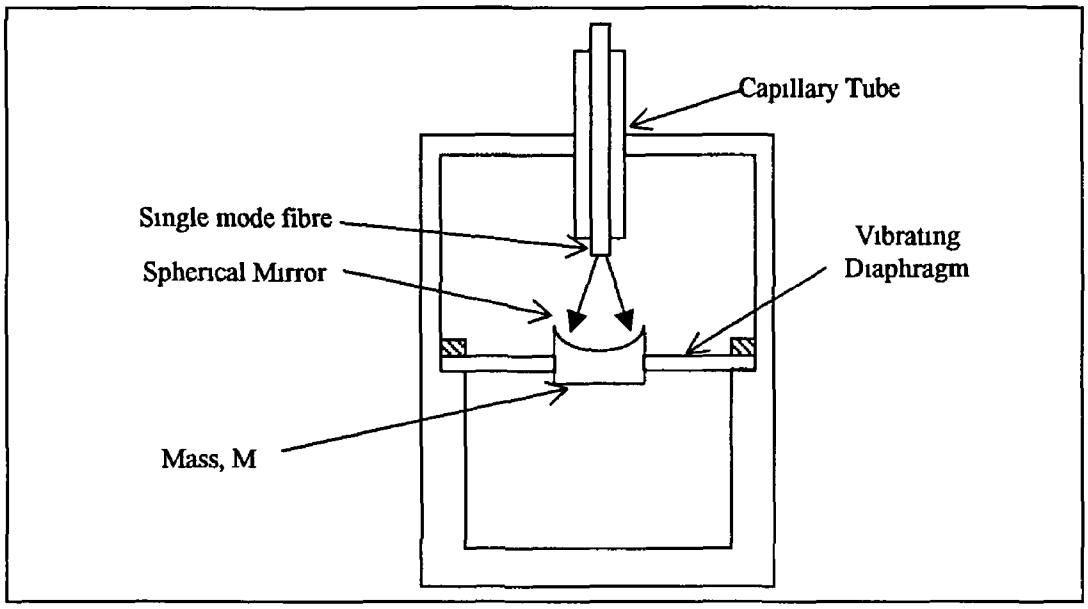

Figure 2 25 Construction of an optical accelerometer [37]

Remo [36] measured vibration using a fibre-optic sensor system similar to figure 2 17 The high sensitivity to displacement allows accurate measurement of small amplitudes, also, the high speed of response allows a wide frequency range Remo constructed two sensor systems with differing light sources, one made use of a laser diode the other an LED Remo concluded that although the laser diode allows greater sensitivity with a longer range that the LED version cost less and was more rugged – the LED version is more suited to in the field and in situ applications Gerges et al [37] described an accelerometer based on measuring the displacement of a weighted diaphragm as shown in figure 2 25 This sensor was based on coherent interferometry but could be implemented as an intensity-based sensor Marty et al [38] developed a fibre-optic accelerometer using the movement of micromachined silicon cantilevers

Wang and Valdivia-Hernandez [39] developed a sensor for inspecting shaft runout, off-round error and eccentricity, for use in mechanical power transmission This sensor used a spatial referencing scheme as shown in figure 2 17 to reference against surface reflectivity and light source variations A laser diode source allowed the sensor to have

an adequate stand-off distance from the surface and also to receive an adequate intensity of light back from the surface They concluded that the sensor gave acceptable results, was cost-effective and could be used for dynamic and automatic quality control

Fibre-optic sensors have been used with nanotechnological instruments [23-24,28] such as optical force microscopes, friction force microscopes, and nanoindentation These applications require non-contact measurement of probe displacement at nanometer order precision Shimamoto and Tanaka [24] present an analysis of drift in optical fibre bundle sensors and demonstrate a carrier amplifier system that significantly reduces drift, in particular thermal drift They also present a geometrical analysis of fibre bundle sensors [23]

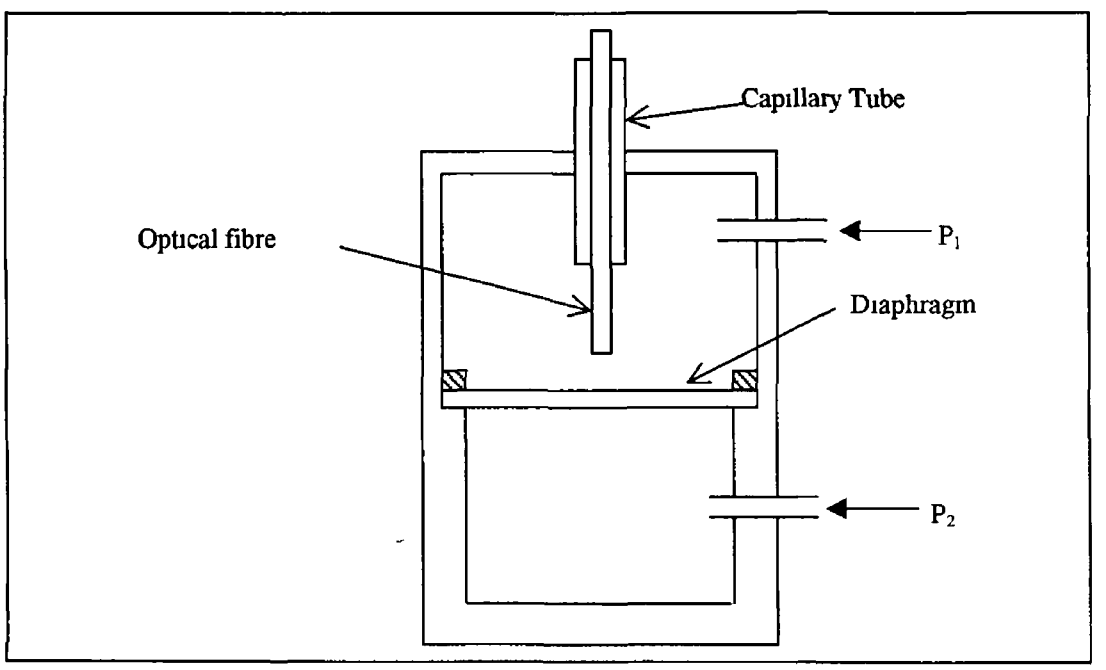

Figure 2 26 Construction of a pressure sensor head to measure differential pressure [35]

It is well known that pressure can be converted into displacement using a Bourdon gauge and diaphragm methods [40] Many fibre-optic sensors have been proposed to measure pressure at high resolution using these principles [35,41-45] Figure 2 26 shows the schematic diagram of a differential pressure sensor utilising the displacement of a diaphragm Wang et al [35] claimed a resolution of 450 Pa over a range from 0-0 8 MPa

Libo et al [42] describe a differential pressure sensor based on corrugated pipes and a rotating reflector as shown in figure 2 27 A linear relationship between differential pressure and the logarithm of the ratio of the output intensities is claimed The sensor also compensates for intensity variations, fibre bending losses and thermal expansion in the corrugated pipes

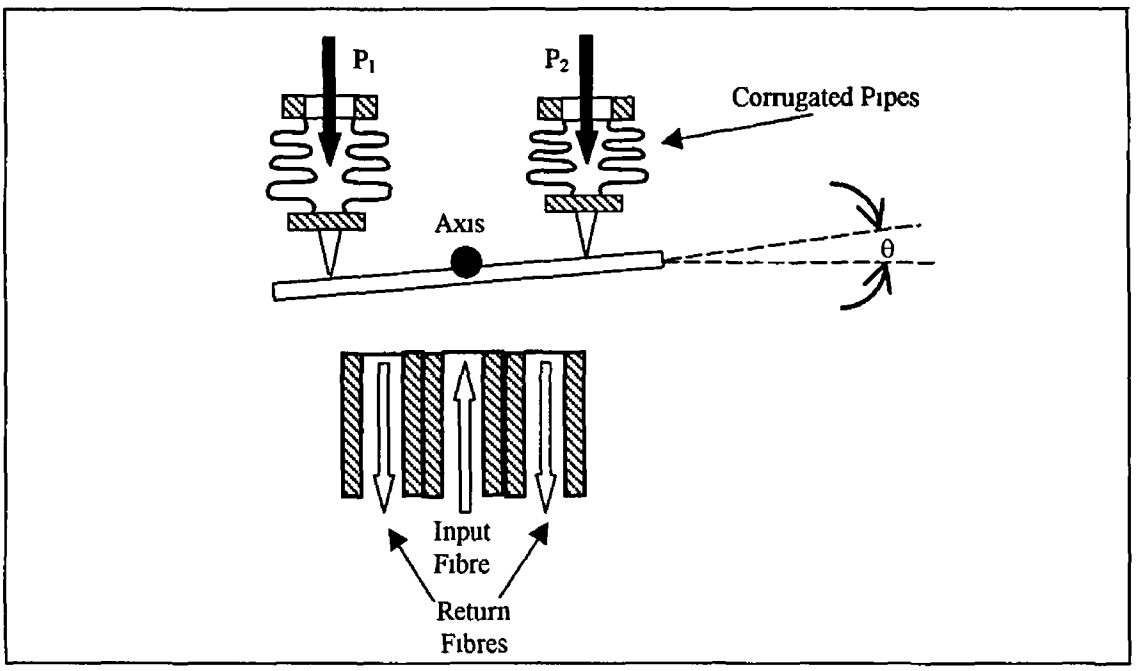

Figure 2 27 Diagram of automatically compensated differential pressure sensor [42]

Fibre-optic sensors can be integrated with silicon micro-machining [26] to provide mechanical assemblies for sensors based on these principles among others This interesting area has lead to low cost sensors for many instrumentation applications especially in the area of biomedical sensors This is especially true where small size is required in combination with high performance Silicon micromachining exploits the optical and mechanical and even the semiconductor properties of silicon Silicon micromachining is based on the techniques for manufacturing integrated circuits The major difference is that while in microelectronics the critical dimensions of a device may be below 0 25 μm – for sensors the critical dimensions may range from 10–1000 μm [46] Also there is no need for expensive clean rooms – consequently micro-mechanical and micro-optical sensors are relatively inexpensive Dorey and Bradley [47] provide an overview of the development of these "mechatronic" systems

Tohyama et al [44] and Strandman et al [45] have developed pressure sensors for biomedical purposes that are based on micromachining These sensors measure the pressure in the catheter balloon used to dilate the coronary artery for treatment of heart disease As these sensors are based on silicon micromachining they are suitable for mass production, in the case of Strandman et al 10,000 units per year are produced For this application, the small size of the sensor head is critical - Tohyama et al developed a sensor head with dimensions of 350 μm × 350 μm × 350 μm as against dimensions of 55 μm × 76 μm × 1240 μm for Strandman's sensor The price of micromechanical pressure sensors has decreased sufficiently to allow these devices to be used disposably [48]

2 2 4 Fibre-Optic Photoelectric Sensing [22, 49-54]

Industrially photoelectric sensing is the most common application of fibre-optic sensing [49] Photoelectric sensors are electrical devices that respond to a change in the light intensity falling on the photodetector They detect the presence of an object or of the edge of an object Photoelectric sensing can be used with light source/detector, control electronics and lens encapsulated in the one package [52] but the use of fibre-optics can have advantages The use of fibre-optics allows a photoelectric sensor's electronic controls to be remotely positioned from a hostile sensing environment Where space is limited, a bulky sensing head may not fit into the space that fibre-optics can

There are three basic sensing modes for these sensors opposed, retroreflective and diffuse [52] These are shown in figure 2 28 All of these modes can be implemented without lenses but the addition of a lens extends the range of the sensor Typically, a photoelectric sensor uses a fibre bundle rather than telecommunications type optical fibre This is because a single optical fibre collects a relatively small percentage of the light emitted from a single Light Emitting Diode (LED) In addition, if a single fibre fails for any reason, e g the end-face isn't polished properly or is covered in dirt the sensor fails Telecommunications type fibres are less robust than the fibres used in incoherent fibre bundles A bundle can tolerate the failure of a substantial number of fibres before the sensor stops working It is easier to position a bundle to collect light than it is to position a single fibre Bundles come in two types coherent and

incoherent Coherent bundles consist of fibres that are arranged carefully and transmit an image This type of bundle is mainly used in medical instruments such as the endoscope Coherent bundles are quite expensive Most applications in industry use incoherent bundles, as illustrated in figure 2 14 Fibres are arranged randomly in incoherent bundles resulting in a much lower cost

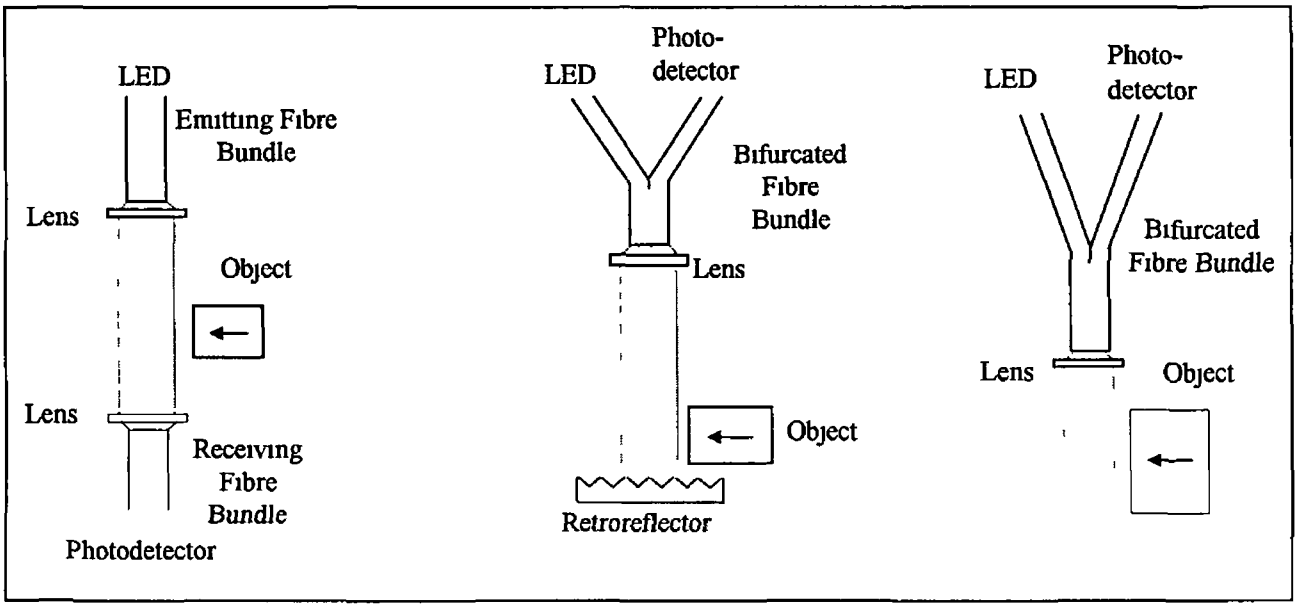

Figure 2 28 (a) Opposed mode sensing (b) Retroreflective mode sensing (c) Diffuse mode sensing

In opposed mode sensing the emitter and the receiver are positioned opposite each other and the signal varies as an object breaks the beam In retroreflective mode sensing the sensing head contains a bifurcated fibre bundle, a bundle that contains both emitting fibres and receiving fibres as shown in figure 2 28b Light reflects off a target, such as a mirror but in most cases a retroreflector, a target made up of many angled cubes A retroreflector is less susceptible than a mirror to positioning problems In common with opposed mode sensing the sensor recognises whether an object breaks the beam In diffuse sensing, the presence of an object is detected by reflection off the object itself This type of sensing works best for reflective objects such as the pins of an integrated circuit Diffuse mode sensing is unreliable for detecting objects of variable reflectivity

In the figure above, it appears that the emitted light travels in a straight line, in fact, the light diverges and these lines represent the effective beam width In diffuse sensing

there can be an advantage in focusing the light to a spot. This will increase the scanning length, objects outside the depth of field affect the sensor less and smaller objects may be sensed. The depth of field is the distance either side of focus at which an object can be detected. Thus the depth of field varies with the size of an object (in the limit where an object is smaller than the spot size at the focus) and the object's reflectivity. Photoelectric sensing is concerned with the detection of an object or the location of the edge of that object. Convergent sensors, as illustrated in figure 2.29, can detect curved objects such as bottles better than other types. Convergent sensors are often used for edge detection as they offer higher resolution in the detection of edges. Focusing light to a spot increases problems with positioning and vibration. If the object vibrates it may move in and out of the depth of field and the object will be counted twice. Positioning is more highly critical in convergent sensors and thus more expertise is required in installation.

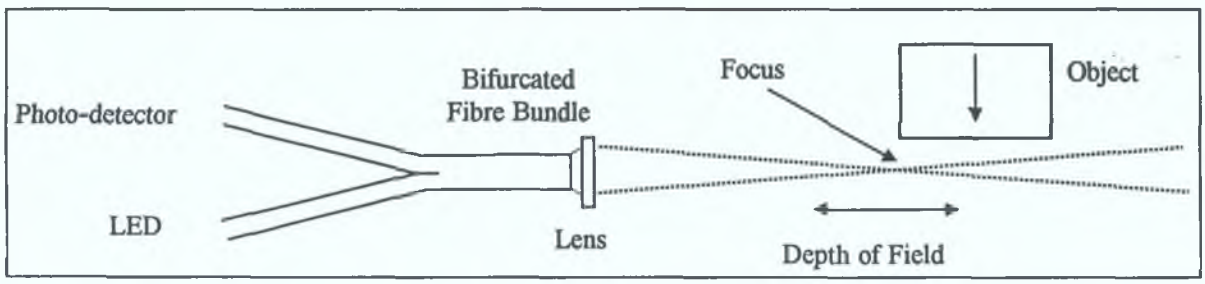

Figure 2.29 Convergent Mode Sensing

In photoelectric sensing the transition between the sensor receiving light and not receiving light causes the output to switch on or off. All photoelectric sensors work best when there is a contrast between the light and dark condition. The light condition is the position where the photodetector is receiving light i.e. for opposed and retroreflective sensing the absence of an object, for diffuse sensing the presence of an object. The dark condition is the position where the photo detector is receiving a lower intensity of light than the light condition. The transition between dark and light condition determines whether the output of the sensor is either on or off at a given time. The speed of response is time taken for the sensor to switch from one condition to another. To make sure that the sensor isn't triggered falsely it is wise for delay logic to be employed between the light and dark condition or vice versa [54].

CHAPTER THREE

3 Surface Roughness Measurement

With the increased importance of quality control and micromachining of precision parts in the engineering industry, there is a need for on-line measurement of surface roughness Measuring surface roughness between 0 01 and 1 μm is of particular importance for online inspection of optical surfaces, rolled aluminium film, precision-machined parts and substrates for hard disks The traditional method for measuring surface roughness in this range is the contact stylus method but optical methods can have many advantages over this method including the high speed needed in quality control Optical methods due to their non-contact nature can perform measurements of surface roughness very quickly, often while the sample is in motion

The standard method of measuring surface roughness is through stylus techniques Statistical techniques are applied to a displacement profile to calculate the surface roughness, surface slope or surface spatial frequency Surface roughness is treated as a point quantity by using light scattering techniques, while stylus techniques, both optical and mechanical, take a profile and apply statistics to calculate surface roughness Fibre-optics offer many advantages in the measurement of surface roughness The most important of these is the prospect of high-speed on-line measurement

3 1 Surface Roughness Parameters

This section defines the various parameters that are of importance in the measurement of surface texture and surface roughness Bennett and Mattson [55] give the following description of surface roughness – "Roughness is a measure of the topographic relief of a surface Examples of surface relief include polishing marks on optical surfaces, machining marks on machined surfaces, grains of magnetic material on memory disks, undulations on silicon wafers, or marks left by rollers on sheet stock " It is important to note that surface metrology is as much concerned with the nature of a surface and its use as it is with the practical aspects of measurement In application, R_q tends to be used by optical engineers and physicists, R_a tends to be used by mechanical engineers

for use with turned or rolled surfaces, and R_z tends to be used by mechanical engineers for use with precision ground surfaces where elimination of scratches is important

Traditionally surface roughness has been calculated from a statistical analysis of a surface profile such as that shown in figure 3 1 below The profile is measured along a line of length, l, with n discrete, equally spaced, points lying along the surface profile Height variations are shown in the z plane The mean surface level is a line defined by the following equation such that equal amounts of the surface lie above and below the line

$$\sum_{1}^{n} |z_i| = 0 \qquad 3\ 1$$

Average roughness, Ra, is defined as the arithmetical mean deviation of the profile or as the following

$$Ra = \frac{1}{l}\int_0^l |z(x)|dx \qquad 3\ 2$$

or approximately,

$$Ra = \frac{1}{n}\sum_{i=1}^{n} |z_i| \qquad 3\ 3$$

Average roughness is generally used to describe the roughness of machined surfaces while root-mean-square (RMS) roughness, Rq, is used to describe the roughness of optical surfaces RMS roughness is defined as the square root of the mean values of the squares of the distances z_i of the points from the mean surface level Expressed in equation form this is

$$Rq = \sqrt{\frac{1}{n}\sum_{i=1}^{n} z_i^{\,2}} \qquad 3\ 4$$

Figure 3 1 shows the surface roughness of a diamond turned aluminium surface with 3 47 nm RMS surface roughness [55] As will be explained later because of the machining process this surface profile shows a definite pattern There are two obvious periodicties in this pattern the first is caused by the grooves cut by the diamond tool and the second caused by the periodic error of the machine

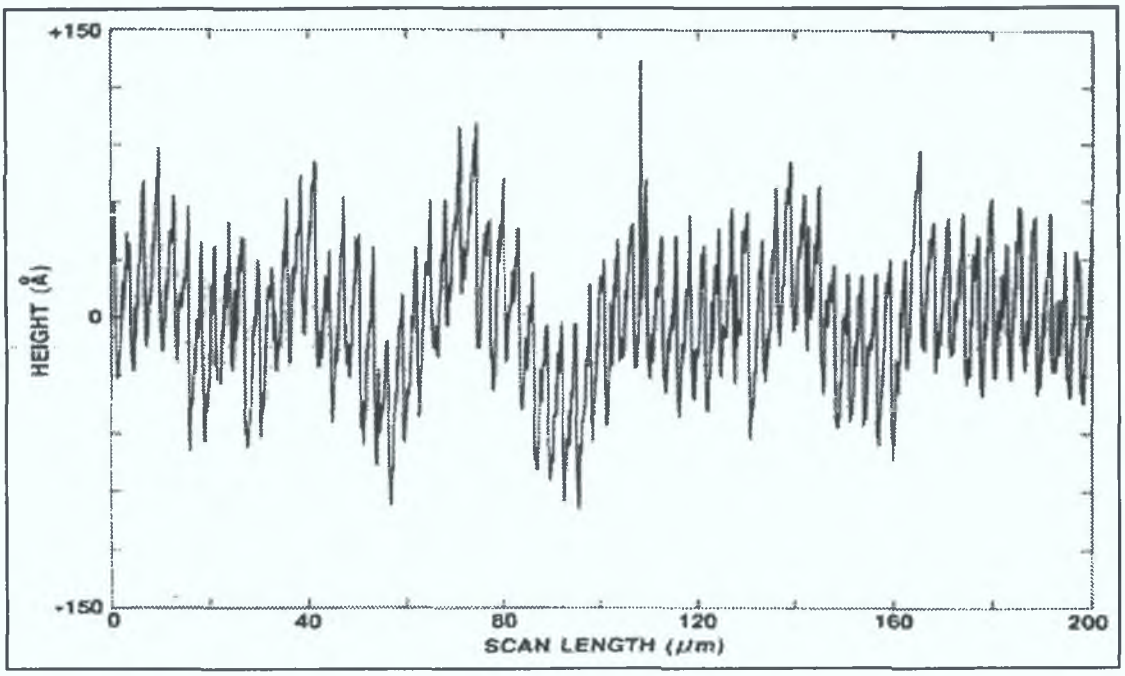

Figure 3.1 A surface roughness profile [55].

RMS and average roughness work best for near sinusoidal surfaces but work poorly for surfaces composed of long flat sections interrupted by sudden jumps. The roughness profile of ground surfaces normally consists of many jagged peaks and deep pits. Thus it is useful to use the ten-point height; Rz. Rz is defined as the average height difference between the five highest peaks and the five lowest valleys within the sampling length. Figure 3.2 describes these peaks and valleys and the following equation describes Rz mathematically:

$$Rz = \frac{\left(z_{p1} + z_{p2} + z_{p3} + z_{p4} + z_{p5}\right) - \left(z_{v1} + z_{v2} + z_{v3} + z_{v4} + z_{v5}\right)}{5} \qquad 3.5$$

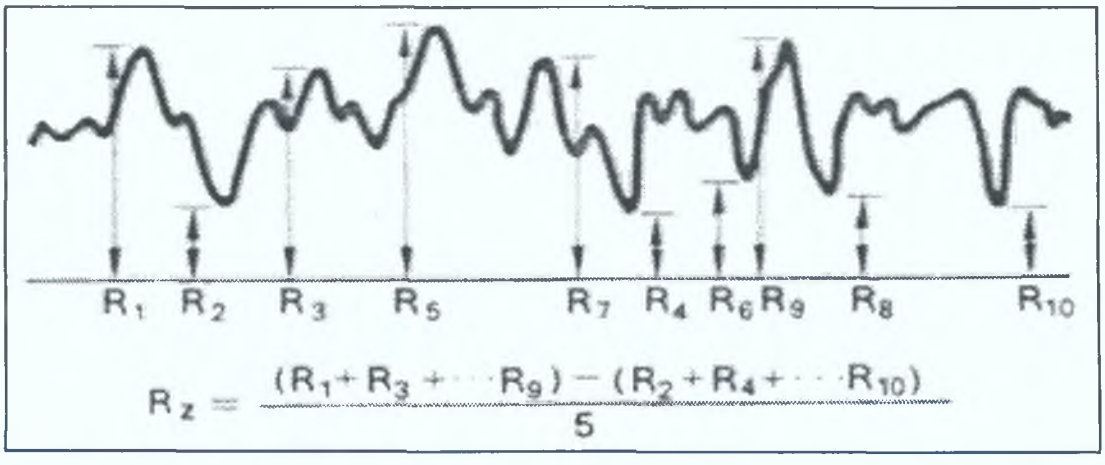

Figure 3.2 Five highest peaks and deepest valleys in a surface determine Rz [56].

R_a and R_q are dependent on height alone and as shown in figure 3 3 two quite different surfaces may have the same statistical value for roughness Also R_z is highly dependent on the length of the profile - a longer profile will have a larger value for R_z Thus measurement of a roughness level alone is not adequate to describe a surface RMS slope, m, can be defined as the square root of the mean of the squares of the slopes Each slope, m_i, is the height difference between adjacent points divided by the data sampling interval, τ_0 Expressed in mathematical form this is

$$m = \sqrt{\frac{1}{n}\sum_{i=1}^{n} m_i^2} \qquad \text{for RMS slope} \qquad 3\,6$$

also

$$m = \frac{1}{n}\sum_{i=1}^{n} |m_i| \qquad \text{for average slope} \qquad 3\,7$$

where

$$m_i = \frac{(z_{i+1} - z_i)}{\tau_0} \qquad 3\,8$$

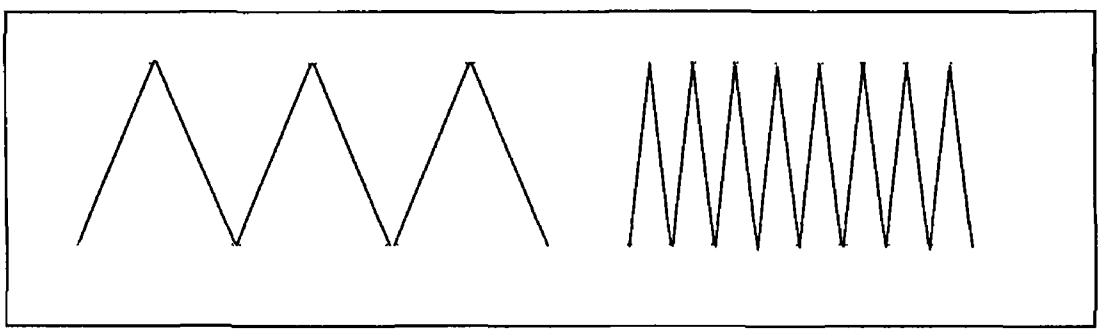

Figure 3 3 Surfaces of the same average roughness that are quite different [57]

Although surface slope values should be dimensionless, they are sometimes quoted in units of angstroms per micrometre or nanometres per micrometre Alternatively RMS slope can also be expressed as an angle using tan(slope angle, α)=m There are a number of difficulties with measurement of surface slope Firstly it is highly dependent on instrumental noise because the height difference can be small Secondly it is highly dependent on the separation of data points used Thirdly the amount of averaging of surface area for each data point affects the measurement, i e the area of the stylus tip, or spot size of an optical profiler Thus the measurement of surface slope is highly

dependent on the particular instrument used and different instruments can give widely differing values for surface slope

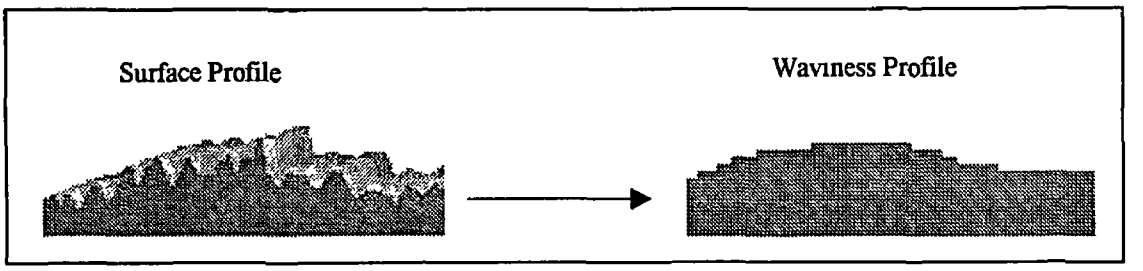

Figure 3 4 Illustration of waviness

Waviness is the general shape of the surface profile at a lower spatial resolution than the original profile measured– it shows the overall trend of the surface profile Figure 3 4 above shows how the waviness profile relates to the original surface profile

Machined surfaces are inherently different than random wear surfaces in that the surface defects tend to be formed in a regular or periodic manner A simple example of this is a metal disc produced by a lathe-turning process The predominant pattern direction on a surface is known as the "Lay"

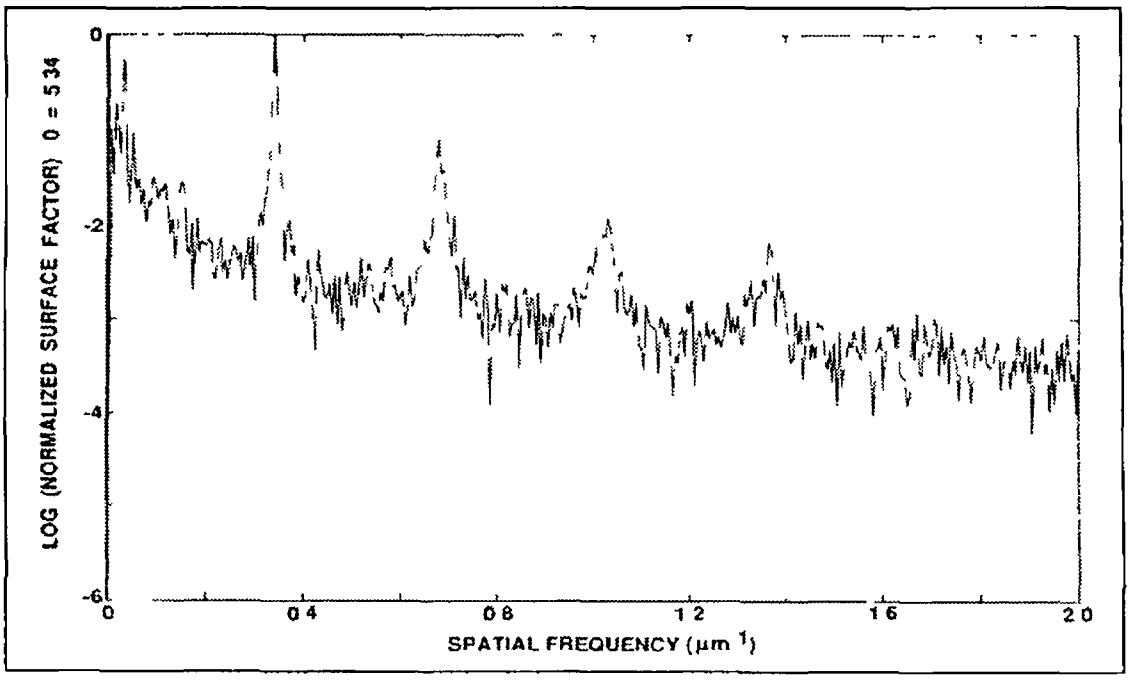

Figure 3 5 The Power Spectral Density function reveals surface spatial frequency [54]

Surface spatial frequency is a measure of the periodicity of a surface profile A perfectly sinusoidal surface of a period, T, has a unique spatial frequency, f, that is equal to the inverse of T Surfaces are generally not pure sinusoids and because of this the power spectral density function is used to extract spatial frequency information from a surface profile The power spectral density function has been used for many years in different engineering applications It can transform a surface profile from the displacement domain to the spatial frequency domain [55] This is accomplished by Fourier analysis and random signal theory [57] – details of which are beyond the scope of this dissertation Figure 3 5 shows the Power Spectral Density Function (PSDF) of the roughness profile shown in figure 3 1 The curve shows definite peaks at a few spatial frequencies indicating the periodic nature of the surface m question that were caused for the reasons noted previously

3 2 Contact and Non-Contact Profilometers

Traditionally the diamond stylus profilometer has been the most widely accepted instrument for measurement of surface roughness in engineering The stylus touches the surface and either the surface or the stylus is translated relative to each other The vertical movement of the stylus is converted into an electrical signal that is then amplified to give a DC output The profile is generally plotted by a chart recorder and the various different surface parameters including roughness can be calculated The vertical resolution of the stylus depends mainly on the level of ambient vibration and electrical noise in the amplifier [58]

Interferometry has been used to generate a surface profile for measurement of surface parameters [60-64] These generally use focussed laser illumination that allows a lateral resolution of the order of magnitude of the wavelength of light Coherent interferometry can have a vertical resolution of the order of nanometres [60] but the range may be limited Optical profilometers have been developed as fibre-optic sensors [63-65]

Optical disk technology has also been used to profile surfaces Brodmann [66] developed an instrument that tracked the autofocus mechanism of a CD player A spot

diameter of 1-2 μm with a vertical precision of 1 nm over a range of ±10 μm was achieved The development of the blue laser would allow the spot diameter to be reduced [13]

Whitehouse [58] states that optical techniques were developed to help the biologist or metallurgist rather than engineers for whom the stylus was developed There are advantages and disadvantages in considering either the stylus technique or an optical technique [66-68] For example a stylus needs to touch the surface and in so doing may damage the surface or be damaged itself by the surface Conversely, in making contact with the surface the stylus may scrape away dirt that would invalidate the readings of an optical stylus In addition, it is possible to measure nano-hardness and friction by using a contact stylus [58] For our considerations, the main disadvantage of the stylus is that it is an offline measurement and that optical methods are capable of quicker measurement online

Stout [69] states that stylus instruments are prone to error because they sample along a plane and that a technique that yields area analysis is likely to be more significant The three dimensional measurement of surface features has been identified as an area of interest [70] as this method recognises the directionality of the surface This study [70] was developed through using the contact stylus The use of optical techniques for three-dimensional surface mapping has also been an area of activity [71] and is much quicker than the stylus method

3 3 Light Scattering Surface Roughness Measurement

Light scattering surface roughness measurement is concerned with the transition in roughness between highly smooth surfaces that scatter no light diffusely and less smooth surfaces that scatter some light diffusely Figure 3 6 shows the difference between a surface that reflects specularly such as a mirror and diffusely such as a white page Perfect diffuse reflection reflects light equally in all directions

Light scattering techniques for surface roughness measurement measure scatter from the area of incidence of the incident beam in this way, they differ from profilometers

that sample along a line Surface roughness is treated as a point quantity over the incident area

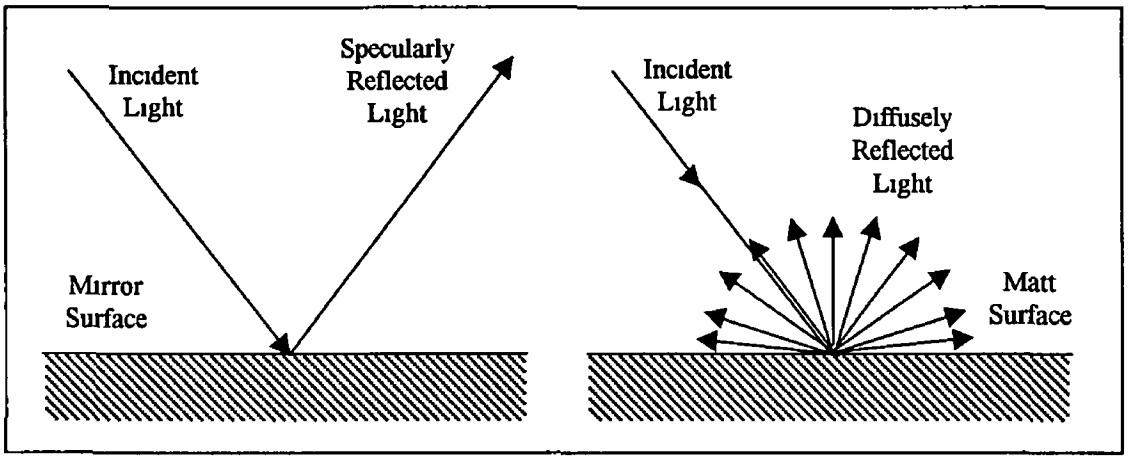

Figure 3 6 Specularly and diffusely reflecting surfaces

3 3 1 Light Scattering

The smoothness of a surface is determined through whether the surface reflects specularly, in this way a surface can be considered smooth or rough for different wavelengths of electromagnetic radiation as will be seen Reflection from a surface depends on the wavelength and incident angle of the incident beam and the properties of the surface

surface features

- surface roughness
- shape parameters
- lay
- directionality
- surface slope
- surface spatial frequency

electrical properties

- permittivity
- permeability
- conductivity

The electrical properties of the surface can be considered material constants. It is possible to infer some of these surface features from the light scattering characteristics of the surface. Equation 3.9, Beckmann & Spizzichino [72], describes the scattering of electromagnetic radiation from a random rough surface:

$$\frac{I_s}{I_o} \propto \exp\left[-\left(\frac{4\pi R_q \cos\theta}{\lambda}\right)^2\right] \quad \text{for} \quad \frac{I_S}{I_O} > 0.6 \qquad 3.9$$

where I_S is the specular reflectance, I_0 is the total reflectance, θ is the incident angle, R_q is the RMS surface roughness and λ is the optical wavelength. This equation assumes a Gaussian distribution of roughness. To estimate roughness from this equation the scattering ratio I_S/I_0 must be above 0.6. This equation describes how in the transition from a mirror like surface to a rougher surface the fraction of light intensity that is transmitted specularly and how incident angle, surface roughness and wavelength affect this reflectivity

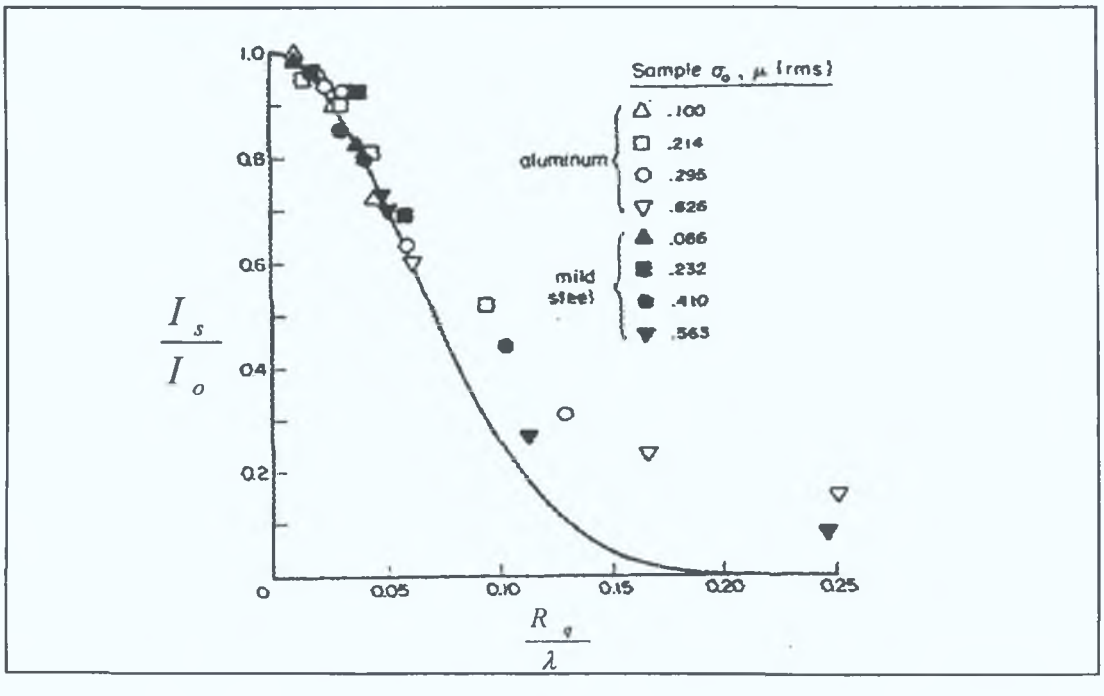

Figure 3.7 Scattering ratio against Rq/λ for incident angle of 20° [74].

Equation 3.9 was investigated experimentally by Hensler [73] and Depew et al. [74] for reflection of light off rough surfaces. Figure 3.7 illustrates equation 3.9 for an

incident angle of 20° and experimental results obtained by Depew For I_S/I_0 less than 0 6 it is clear that the scattering characteristics do not agree with equation 3 9 This is because at these roughness levels specular reflection is affected by surface spatial frequency and diffraction effects [70] In this region, the angular distribution of reflected light is most important

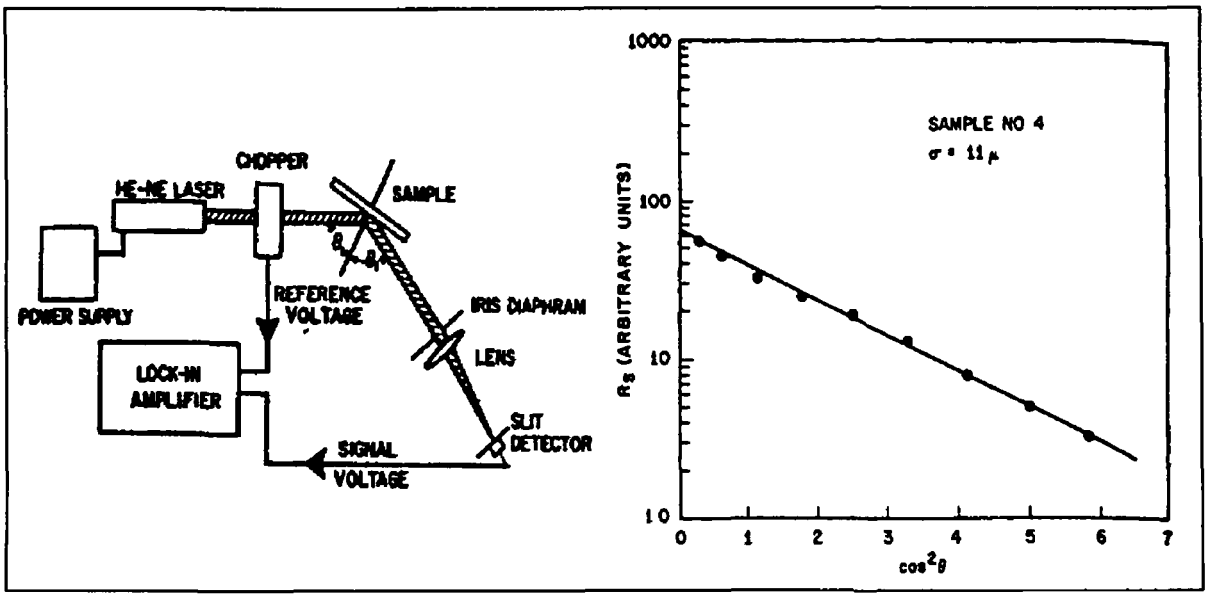

Figure 3 8 (a) Schematic diagram of experimental apparatus Hensler [73] used to measure angular dependence of specular reflectivity and (b) resulting graph

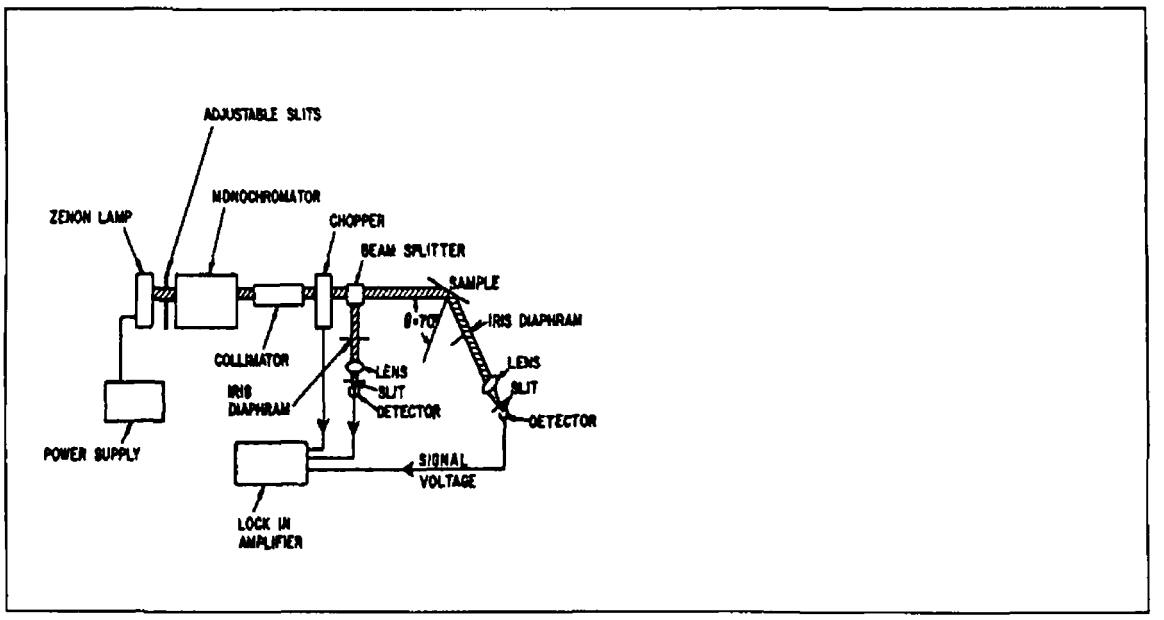

Figure 3 9 (a) Schematic diagram of experimental apparatus Hensler [73] used to measure wavelength dependence of specular reflectivity and (b) resulting graph

Hensler investigated the angular dependence of reflectivity using the apparatus shown in figure 3 8a The incident angle was varied for a sample and the variation of the scattering ratio was observed to change as in figure 3 8b He also investigated the wavelength dependence of scatter by varying the wavelength of light emitted from the monochromator as shown in figure 3 9a Figure 3 9b shows the dependence of the scattering ratio on wavelength

3 3 2 Total Integrated Scattering and Angle Resolved Scattering Methods

Total integrated scattering (TIS) is illustrated in figure 3 10 A beam is incident on a surface and two components of the reflection are measured Firstly the specular component, I_0, is measured and secondly the scattered portion, I_s, is measured The light scatters off the sample and is then directed towards a detector by the integrating sphere TIS is defined by the ratio of the scattered light collected to the specular reflection

$$TIS = \frac{I_s}{I_o} \qquad 3\ 10$$

thus from equation 3 9 [75]

$$TIS \approx (4\pi R_q \cos\theta / \lambda) \qquad 3\ 11$$

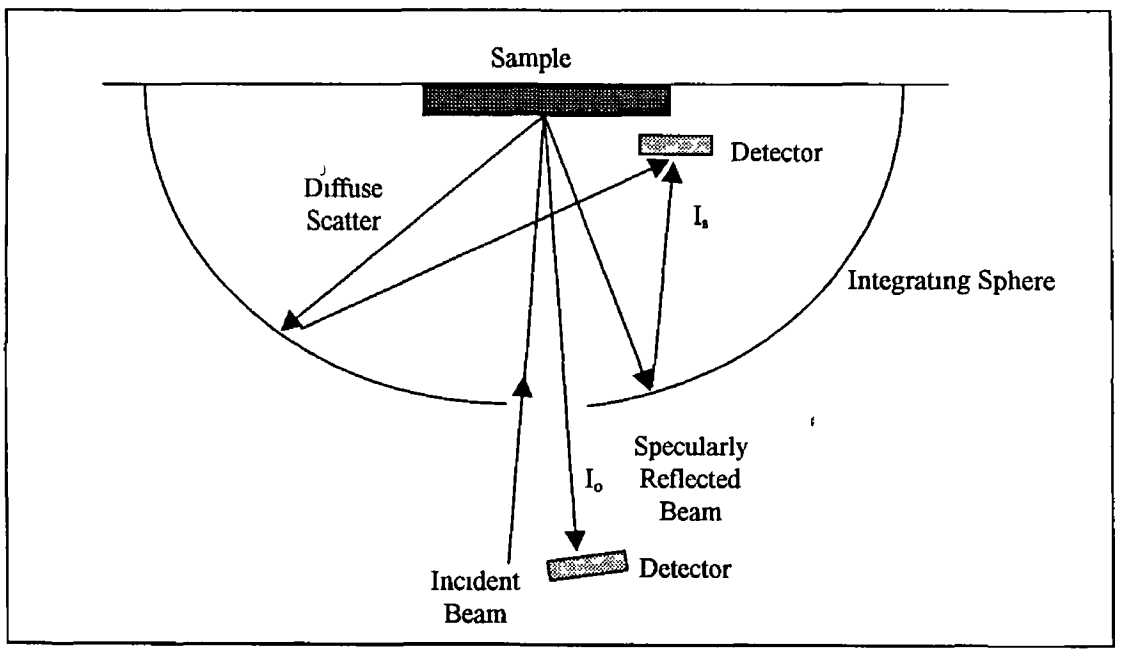

Figure 3 10 Schematic diagram of TIS Scatterometer

TIS measures total scatter and specular reflection rather than just specular reflection in isolation. In figure 3.10 an integrating sphere is used to direct the scattered light onto a detector. The other detector measures the intensity of the specularly reflected beam. TIS allows fast and repeatable measurements of light scattering; only two measurements are made which with simple electronic circuitry can be used to give Rq. TIS gives repeatable readings as fluctuation of the laser source affects both the scattered and specular reflected components of the ratio. The use of a high power laser source in conjunction with a highly sensitive detector such as a photomultiplier or an avalanche photodiode allows extremely small amounts of scattered light to be measured accurately.

Scatter from the smooth surface specimens tends to be close to the specular direction. This means to collect scatter an accurate set-up is necessary to prevent the specular beam from reaching the scattered light detector. This stipulation prevents TIS from being used outside the laboratory. Also when used with a HeNe laser operating at a wavelength of 633 nm the range of TIS only extends to around 100 nm. This limits TIS to measurement of very smooth surfaces.

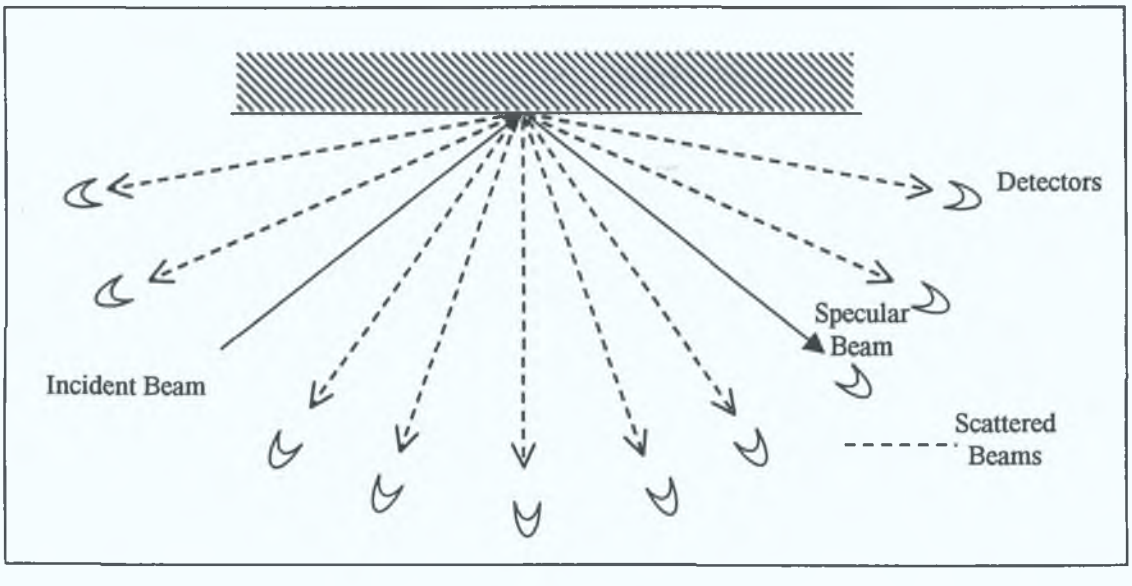

Figure 3.11 Schematic diagram of ARS scatterometer.

In angle resolved scattering (ARS) measurement many detectors are used to collect scatter at multiple angles, because of this more spatial information is gained about the

surface than in TIS As the roughness of a surface rises to the order of the wavelength of light the spatial frequencies of the surface can give rise to diffraction effects As ARS measures in many directions, it can be used to measure surface spatial frequency Alignment is no longer a problem as the direction of the specular beam can be measured in turn giving information about the form of the specimen Marx and Vorburger [76] describe an ARS system and conclude that surface roughness can be estimated where the surface is smooth enough to provide a discernible specular peak They also concluded that ARS might be a better indicator of surface slope than RMS surface roughness

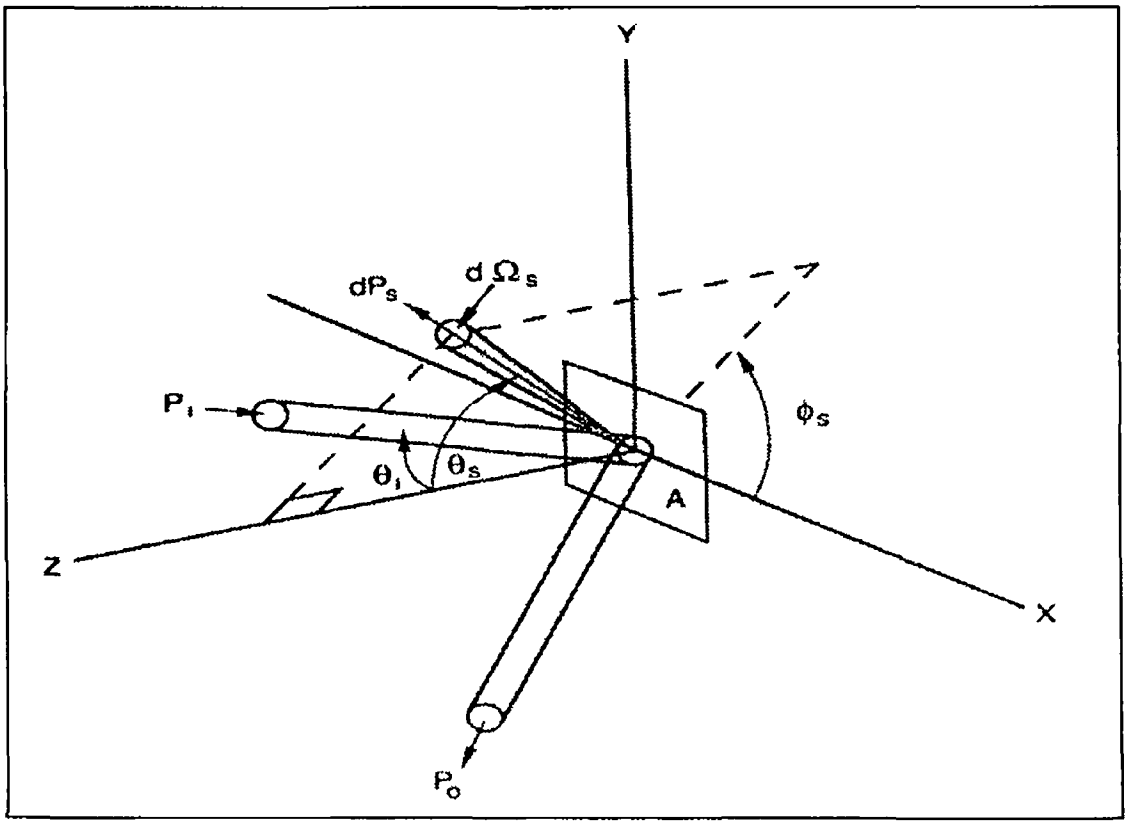

Figure 3 12 Geometry defining the parameters used in BRDF

ARS also has many more components and is more expensive than TIS It collects more information that can be analysed to give more information about the specimen in question This information can be extracted using the Bidirectional Reflectance Distribution Function (BRDF) [57], which is derived from vector scattering theory BRDF is the scattered surface radiance divided by the surface irradiance Surface irradiance is the light flux (Watts) incident on the surface, P_0, per unit illuminated

surface area Scattered surface radiance is the light scattered, P_s, through solid angle Ω_s per unit illuminated surface area per unit projected solid angle Thus, BRDF becomes

$$BRDF \equiv \frac{\text{differential radiance}}{\text{differential irradiance}} \cong \frac{1}{P_0 \cos\theta_s} \frac{dP_s}{d\Omega_s} \cong \frac{1}{P_0 \cos\theta_s} \frac{P_s}{\Omega_s} \qquad 3\ 12$$

BDRF is measured at many scattering angles, θ_s, for each detector and a graph plotted that shows the angular distribution of scatter Analysis of this graph can give an indication of surface texture parameters [57]

ARS and TIS have been used to detect surface defects on silicon wafers in the semiconductor industry [77-80] and for inspecting computer disks [81] In conjunction with high-speed laser scanning, they provide a quick non-contact form of inspection for contamination and other defects at an early stage of semiconductor manufacture, thus improving fabrication yield TIS is generally used for bare silicon wafers and ARS for patterned wafers Defects in these applications consist of contamination, scratches, pits and polishing defects Hard disk substrates require a certain amount of roughness as controlled texturing promotes adhesion of the magnetic layer that stores data In these applications light scattered due to the surface roughness of the sample is considered background noise Work in this area has focused on reducing the minimum size for defect detection

3 3 3 On-line and Fibre-Optic Methods of Surface Roughness Measurement

Much work has been done in the field of measuring surface roughness through measurement of light scattering Most of this applies to measuring the roughness of highly smooth surfaces such as optical parts using ARS and TIS, and has been in the field of bulk optics The bulk optic configurations of ARS and TIS are mainly unsuitable for on-line use using fibre-optics

Any on-line commercial sensor needs to be simpler than these methods figure 3 13 shows the three methods that suit on-line use specular reflectance, specular and diffuse reflectance and angular reflectance Specular reflectance was the first method

to be implemented using fibre optics, a single fibre emits and another detects light, but it has drawbacks - a single measurement is unsuited to measure a property as complex as surface finish, also sensitivity to displacement can affect measurement Measuring diffuse scatter as well as specular reflectance references the sensor against light source fluctuations as noted above for displacement sensors It is possible to estimate displacement, in addition, the scattering ratio is measured more accurately The intensity profile can be measured using a photodiode array or an array of fibres This method is an adaptation of ARS that has been implemented for online sensing Many of the latter group of sensors attempt to extend the surface roughness range beyond that dictated by equation 3 9

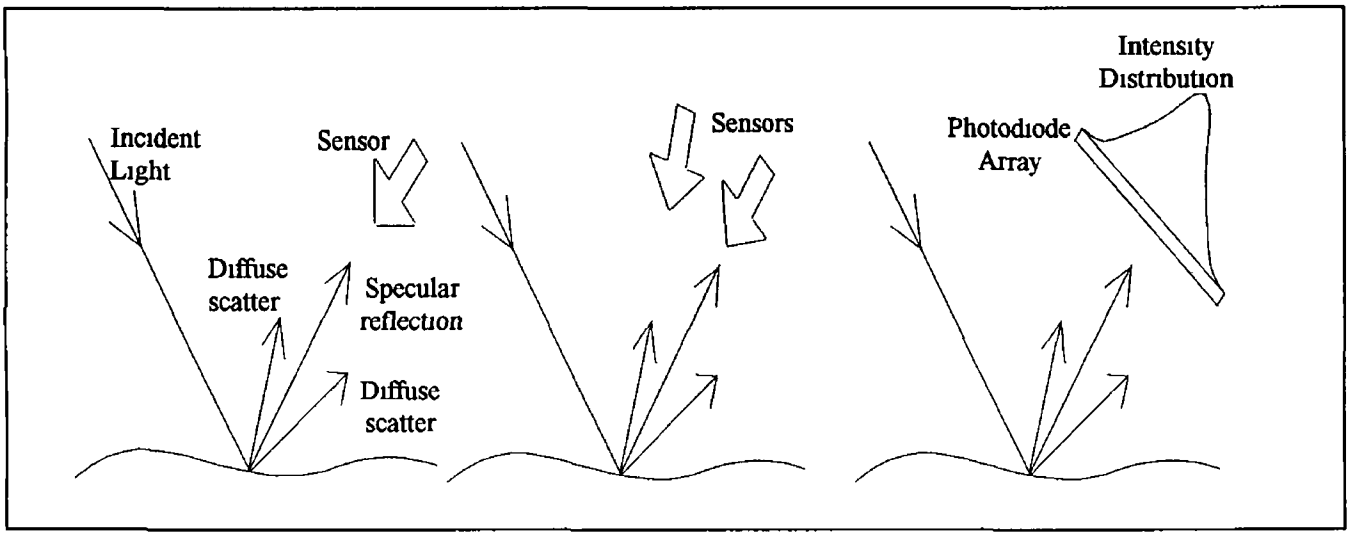

Figure 3 13 (a) Specular reflectance (b) Specular and diffuse reflectance (c) Angular reflectance

Cielo [82] includes light scattering measurement of surface roughness in his study of optical inspection techniques Griffiths et al [83] review light scattering methods with regard to engineering surfaces and the possibility of their use in on-line applications Mitsui [84] includes a fibre-optic sensor using the light scattering technique in a review of in-process sensors for surface roughness

The Institute of Physics at the Technical University of Warsaw under Domanski [85-89] has developed many different types of fibre-optic surface roughness sensors Domanski et al [85] developed a fibre-optic sensor which is illustrated in figure 3 14 Two 50 μm core multimode fibres are positioned at a 45° angle to the surface The

measuring head is placed on or above the sample at a vertical distance of 1 mm The results of these experiments were not directly related to surface roughness, but were compared to RMS surface slope, m, and length correlation, λ_q Length correlation is defined by the following equation

$$\lambda_q = 2\pi R_q / m \qquad 3\ 13$$

This expression relates RMS surface roughness to RMS slope The results of this experiment showed a strong correlation between both surface slope and length correlation This dependency on surface slope is caused by the restricted aperture leading from the fact a smaller surface area reflects light, as against lensed or bundled fibre-optic sensors These sensors average reflection over a larger surface area Reflection from a smaller surface area is more sensitive to variation due to high spatial frequencies, edge effects and shadows This sensor had the advantage of simple construction and operation Near identical orientation for any sample could be attained by placing the housing on the sample

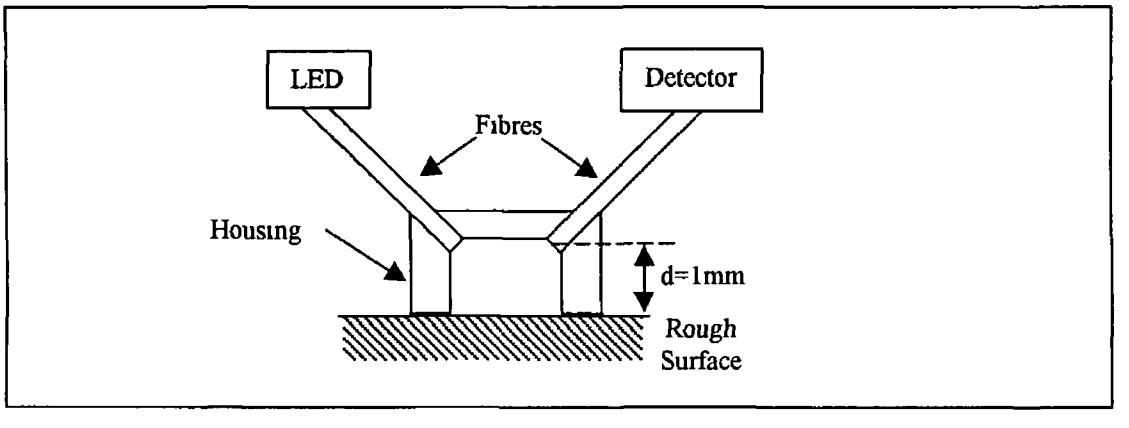

Figure 3 14 Schematic diagram of Domanski et al 's [85] fibre-optic surface roughness sensor

Domanski et al [86] developed a lensed fibre-optic sensor as illustrated in figure 3 15 A fibre emits a cone of light that reflects from a surface and is focused by a lens into a receiving fibre This paper [86] noted the construction of the sensor without presenting any results Dowden et al [90] describe the construction of an optoelectronic sensor for measuring the reflectivity of optical surfaces This sensor consists of an LED whose output beam is collimated and collection optics that focus reflected light onto a

large-area photodiode. This sensor did not measure surface roughness but is of interest as an optoelectronic surface measurement instrument.

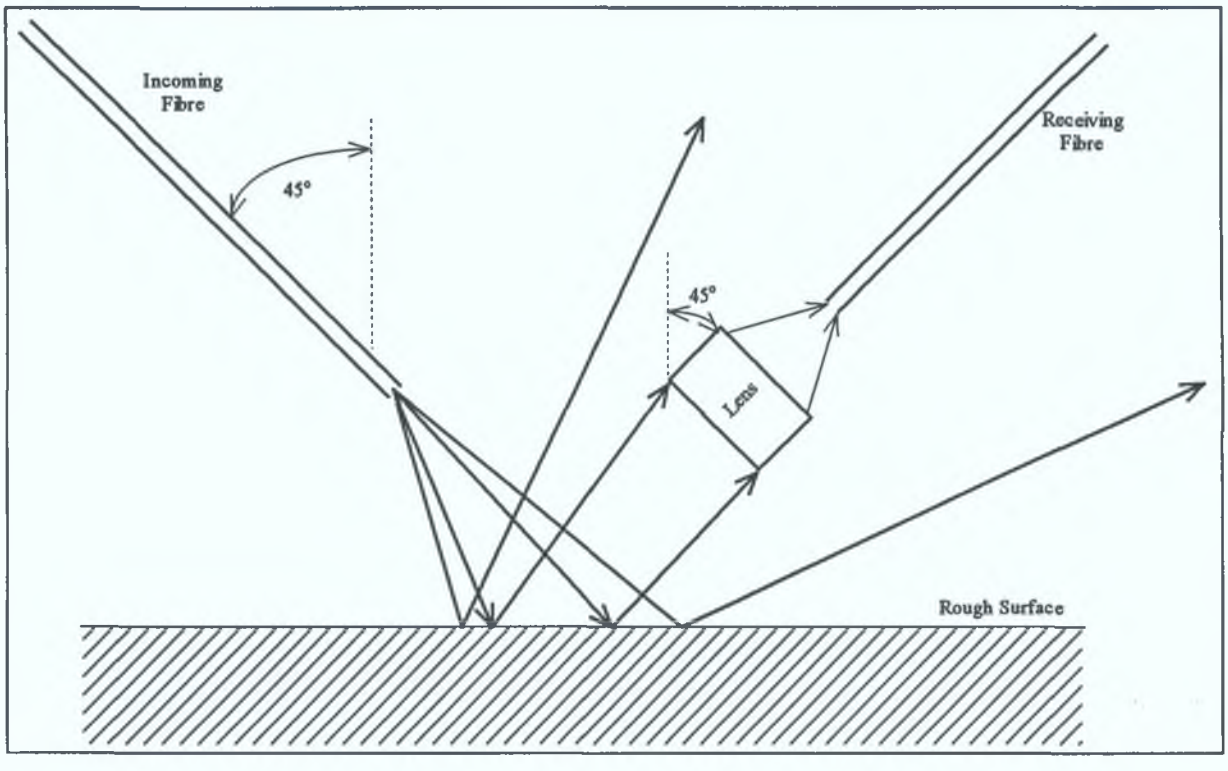

Figure 3.15 Schematic diagram of Domanski et al.'s [86] fibre-optic surface roughness sensor.

Domanski et al. [87] used a fibre-optic bundle type sensor to measure surface roughness. This sensor was similar in construction to those used in photoelectric [48-53] and displacement sensing [23-25]. A trifurcated bundle delivers light from two LEDs of differing wavelengths, 0.66 μm and 0.93 μm. Backscattered light is collected by the bundle and its intensity measured by a large-area photodiode. This bundle is oriented at normal incidence to the surface. This bundle type sensor is more robust than single fibre version; thus it is more suited to online use. Also the comparison of two different signals helps reference the sensor against errors - in this case displacement, in the form of vibration, is one of those errors. This sensor claimed to measure RMS surface roughness in a range from 0.5 μm to 30 μm at a displacement from the sample of around 3 cm, thus it is highly suitable for online use. Perhaps reflection from a larger surface area provides a more reliable measure of surface roughness.

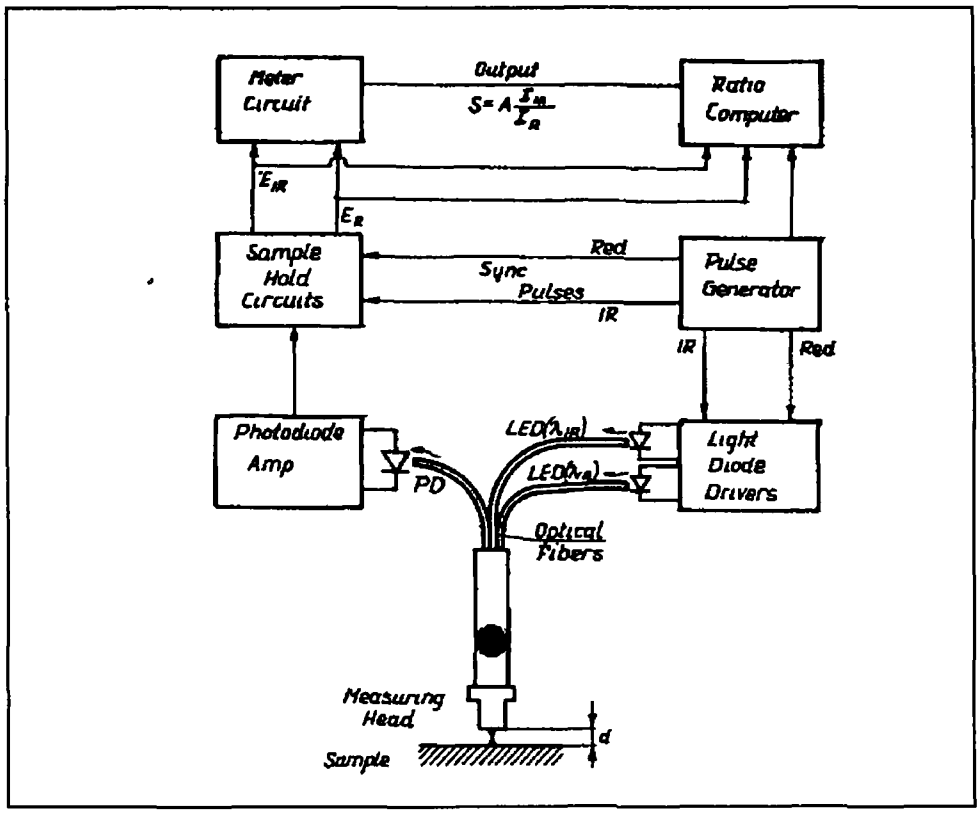

Figure 3 16 Block Diagram of Domanski et al 's [87] bundle-type surface roughness sensor

Domanski et al [88-89] developed a further polarisation-based fibre-optic sensor This sensor used the depolarisation of reflected light from a rough surface as the basis of the sensor A smooth surface will preserve the polarisation of incident light while a rough surface changes the state of polarisation Collins [91] describes a commercial sensor that operated on a similar principle This sensor used the change of polarisation of reflected light to teach subtle differences in reflectivity using fuzzy logic This sensor was designed to operate as a photoelectric sensor detecting the transition from two different surfaces, e g for an envelope – the transition from paper to glue

Moslehi describes two interesting fibre-optic sensors [92-93] for online use in semiconductor manufacture that involve measuring surface roughness The first [92] measured surface roughness, in addition to film thickness and spectral emissivity As illustrated in figure 3 17 optical power from a 1 3 μm laser is collimated and is incident on the surface of the semiconductor wafer at normal incidence The original laser power, scattered reflected power, specularly reflected power, scattered transmitted

power and specularly transmitted power are used to calculate the parameters of interest Silicon is partially transparent to 1 3 μm wavelengths and it is a requirement of the sensor that both sides of the silicon wafer are polished Moslehi used the ratio of scattered reflected power to total reflected power, i e TIS, to indicate surface roughness

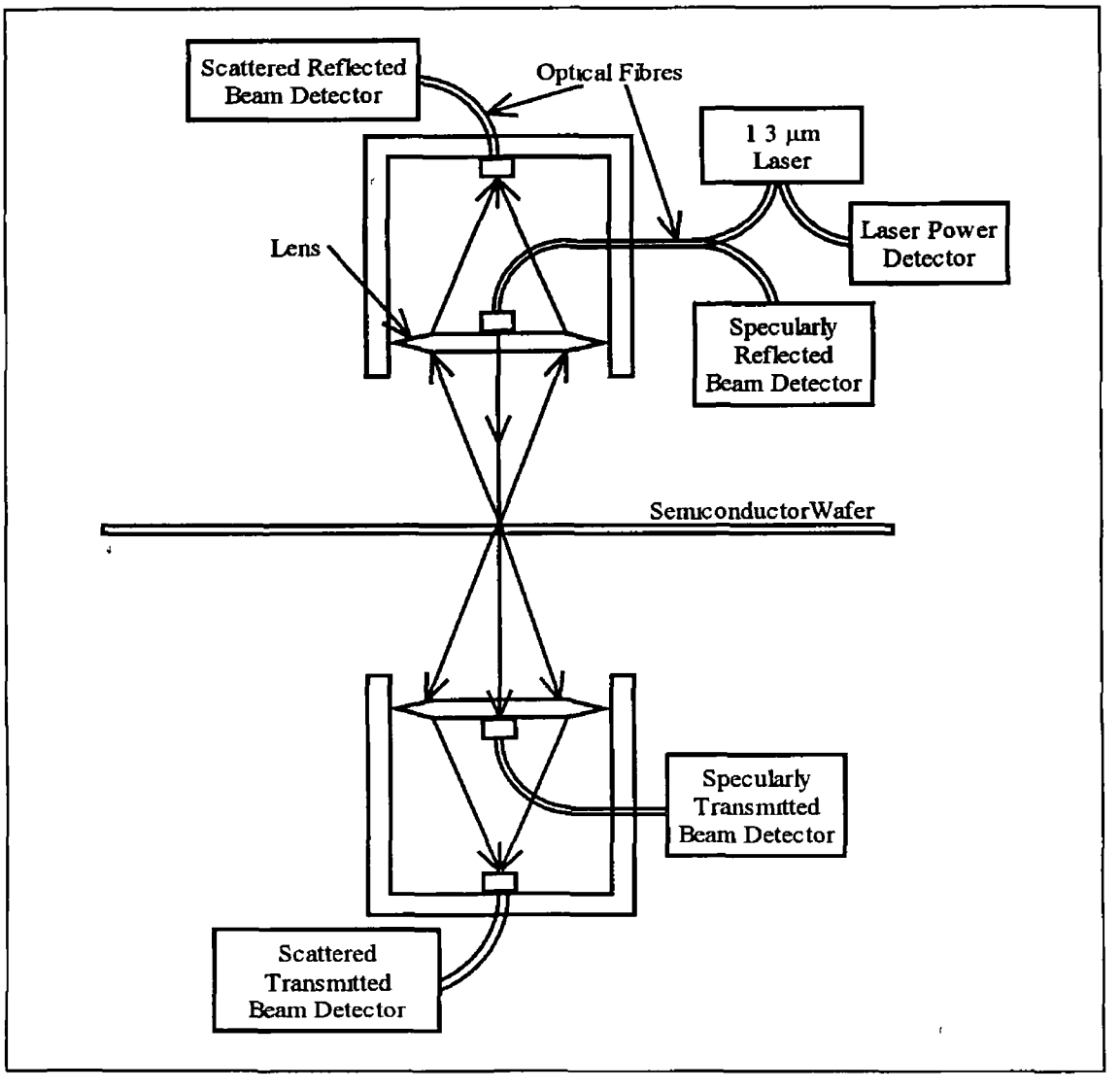

Figure 3 17 Schematic diagram of Moslehi's [92] surface roughness sensor

Thermal expansion causes a corresponding change in surface roughness - Moslehi describes a sensor that uses this variation to measure temperature online in semiconductor manufacturing [93] Figure 3 18 shows the components of this temperature sensor, two lasers of differing wavelengths are coupled into the same fibre This fibre leads to a termination where the output light is collimated at normal

incidence to the wafer surface The collimator lens collects any light that reflects specularly A wavelength demultiplexer separates the two wavelength components of the reflected signal and their output powers are measured The surface roughness is measured through ratio of specular reflectance of the sample, R_s, to the specular reflectance of a polished surface, R_o Moslehi calculated RMS surface roughness by substituting R_s as I_s and R_o as I_o into equation 3 9

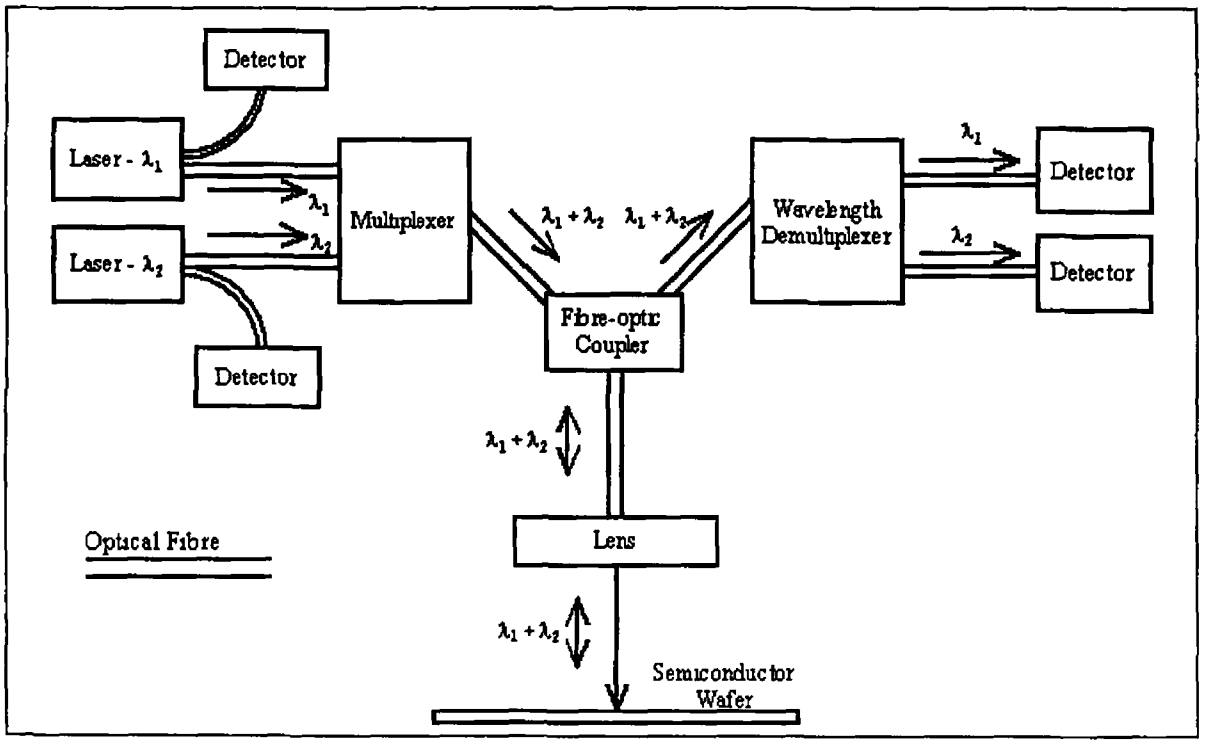

Figure 3 18 Schematic diagram of Moslehi's [93] temperature sensor

Moslehi used the following equation to represent the change in surface roughness due to thermal expansion

$$R_q = R_{qo}[1+\alpha(T-T_o)] \qquad 3\ 14$$

where α is the coefficient of thermal expansion, T is the wafer temperature, T_o is room temperature and R_{qo} is RMS surface roughness at room temperature This equation is fulfilled for each of the light sources resulting in two simultaneous equations in R_q and T Moslehi chose lasers emitting at 820 nm and 850 nm, wavelengths at which silicon wafer is opaque

Fawcett and Keltie [94] investigated the use of Cook and Hamm's [27] fibre-optic displacement sensor as a surface finish sensor Figure 2 20 shows the construction of

this sensor, an emitting fibre is surrounded by six receiving fibres and is oriented at normal incidence to the surface The displacement characteristic curve was evaluated for a number of nickel-plated samples of differing surface roughness and differing surface finish, grinding, milling, lapping, etc Peak voltages and sensitivities (to displacement) were evaluated This study made no attempt to measure surface roughness, but was intended for use in monitoring tool wear and its effect on surface reflectivity

Gardner and Streight [95] presented an optoelectronic surface roughness sensor that used measurements of both specular and diffuse reflection for online use Figure 3 19 shows an LED that emits a beam of light such that light reflects specularly to one of four photodiodes The other four photodiodes are arranged to collect diffuse reflection, with one photodiode arranged to collect light outside the plane of reflection The ratio of the sum of the intensities of the diffuse signals to the specular signal is used as the basis of an estimation of the surface roughness It was noted that the gauge is sensitive to the orientation of the lay Dapeng et al [96] developed a fibre-optic sensor that operated in a similar manner

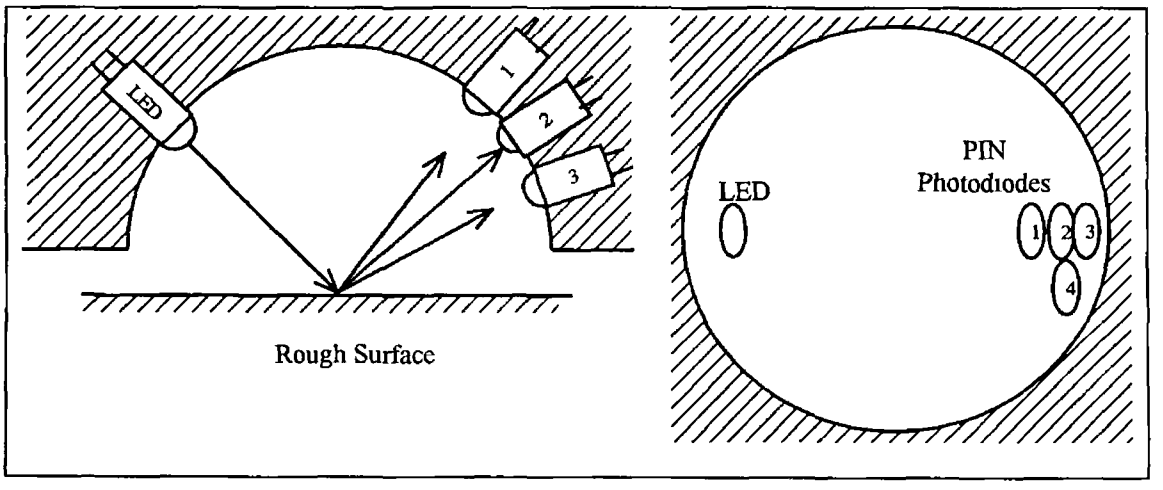

Figure 3 19 Illustration of an embodiment of Gardner et al 's [95] sensor head (a) Section View (b) Bottom View

Measurement of the angular profile of reflection from a surface using a linear CCD array or a photodiode array has been used as the basis of a number of sensors [97-105] Measurement of angular profile has the advantage of variability of the orientation

of the sample, it is even possible to use samples with curved surfaces Measurement of the profile allows rougher surfaces that scatter more diffusely to be considered

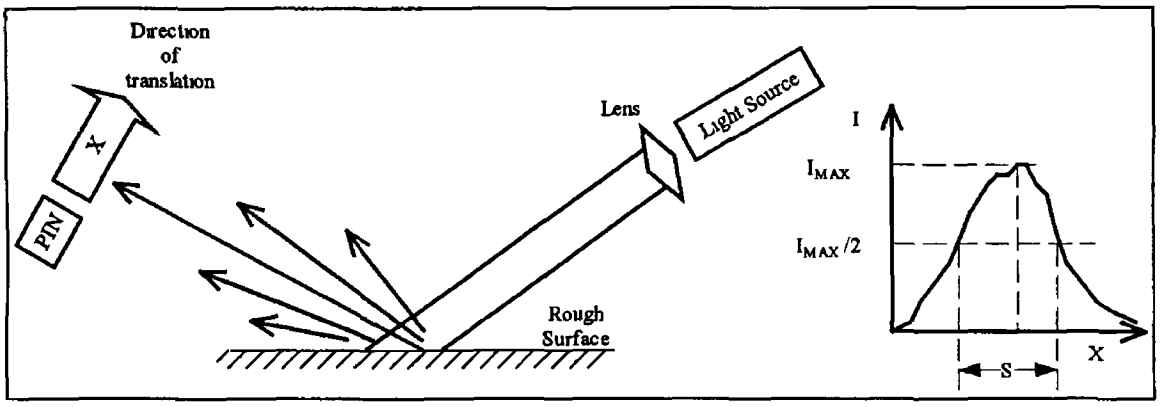

Figure 3 20 Schematic diagram of an embodiment of Dandliker et al 's [97] surface roughness sensor

Dandliker et al [97] patented a surface roughness sensor that used the intensity profile of scattering from a rough surface as the measurement principle A collimated light source is incident on a surface and the reflected profile could be measured in a number of ways For example, figure 3 20 illustrates the translation of a single photodiode through the profile, the use of an array of photodiodes or a television camera was also suggested Roughness was estimated using the half-width of the scattering profile, S, as illustrated above The half width is the distance along the profile for which the intensity is above a certain fraction, i e half, of the peak intensity, I_{MAX} This sensor was designed for use in the measurement of paper glossiness, as a measure of how diffusely paper reflects

Thurn and Gast [98] patented an optoelectronic sensor that used the angular distribution of scatter to evaluate surface roughness In figure 3 21 a collimated infrared LED is incident at normal incidence to a sample The collection optics convey scattered light to a photodiode array, preserving the angular profile, resulting in an intensity graph

The operation and performance of this sensor was analysed a number of times [99-101] The intensity graph was interpreted differently than by Dandliker et al , a new

parameter, S_N, was proposed as a measure of surface roughness S_N is defined by the following equation

$$S_N = K\sum_{i=1}^{n}(i-\bar{i})^2 p_i \qquad 3\ 15$$

where, K is a constant, i is the diode number, $\bar{i}$ is the mean diode number ascertained using the intensity values and p_i is the normalised intensity at the *ith* diode This parameter is affected by both the angular distribution of scatter and its intensity, it gives higher values of S_N at higher roughness

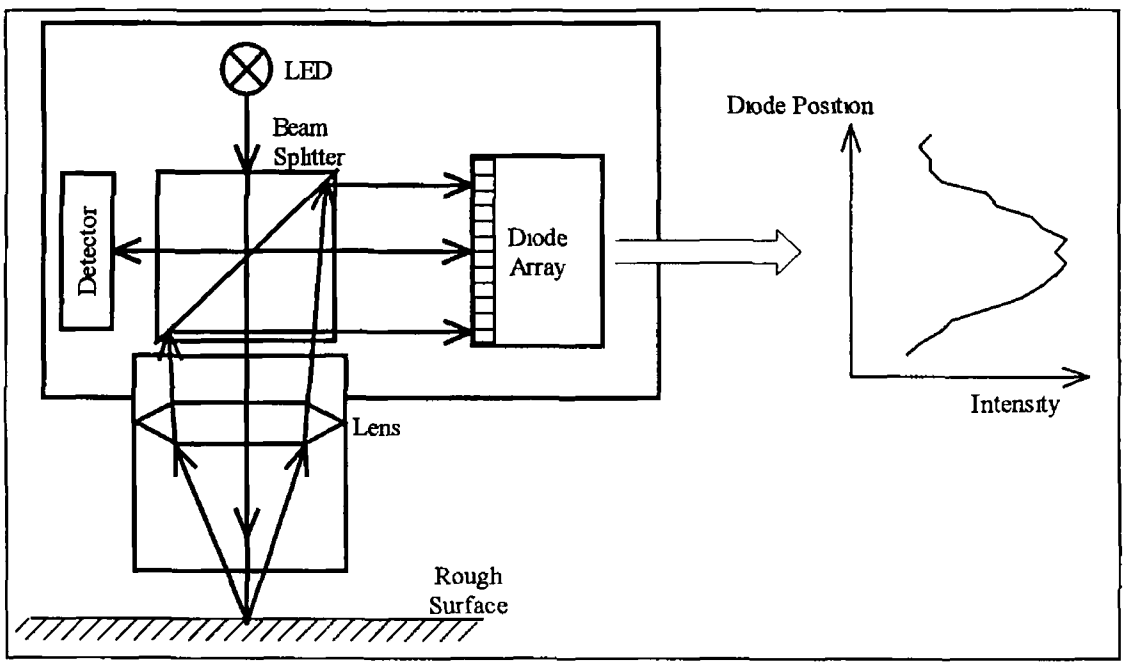

Figure 3 21 Set-up of Thurn and Gast's scattered light sensor

The sensor measured roughness in the range 0 005 μm to 2 μm R_a with highest sensitivity and linearity in the range 0 02 μm to 0 5 μm R_a A configuration using a 20-element photodiode array and 20-bit data acquisition achieved a measurement time of around 40 ms Brodmann et al [99], through experiment with roughness comparison standards from different companies, noted the sensitivity of this sensor to both surface roughness and surface spatial frequency

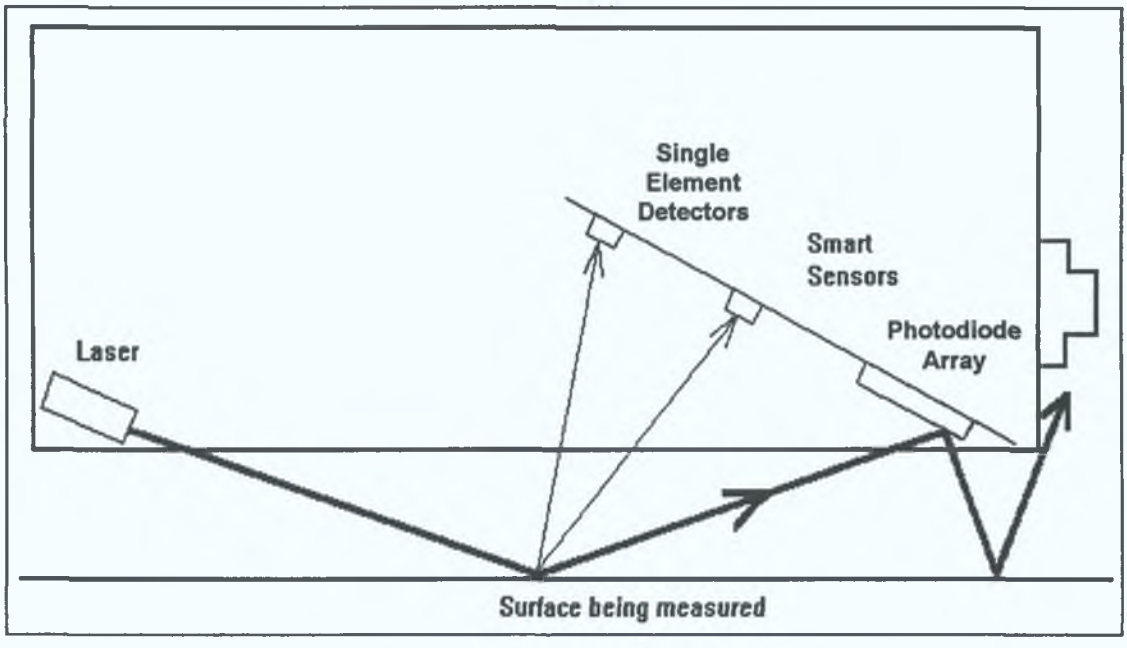

Figure 3.22 Schematic diagram of Valliant et al.'s [102] commercial surface roughness sensor.

Valliant and Goebel [102] patented the sensor illustrated in figure 3.22 that used a 35-element photodiode array, for measurement of scatter around the specular peak, and two single element photodiodes, for measurement of diffuse scatter. A visible laser diode (670 nm) emits a laser beam from the bottom of the gage illuminating the surface beneath it. This laser was selected to achieve a less stringent laser safety rating. An algorithm for evaluating R_a is detailed that normalises all scatter values with regard to the angle and intensity of the specular reflection, then summarising normalised scatter values and taking the square root. Thereafter the application of a calibration equation gives the R_a value. This sensor is available as a commercial sensor that performs 10 measurements per second, and claims a range of 0.0005 to 1 μm R_a roughness with accuracy of ±2%.

CCD cameras were used by Luk et al. [103] and by Yanagi et al. [104] to measure surface scattering. Similarly to Valliant et al. Yanagi viewed the scattering profile of the light scattering. Yanagi used a CCD camera with a polarisation filter to enhance the contrast of the measurement to scattering. Luk used a collimated light source but did not orient the camera to measure specular reflection – he oriented the light source at a grazing angle to the sample and the CCD camera at a normal incidence to the surface. In this way he measured diffuse scattering alone. He used a histogram of the

intensity values of each pixel of the array to indicate roughness For smooth surfaces he noted most pixels were at lower light intensities, for rougher surfaces higher intensities were noted with a less pixels at these intensities as shown in figure 3 23 below

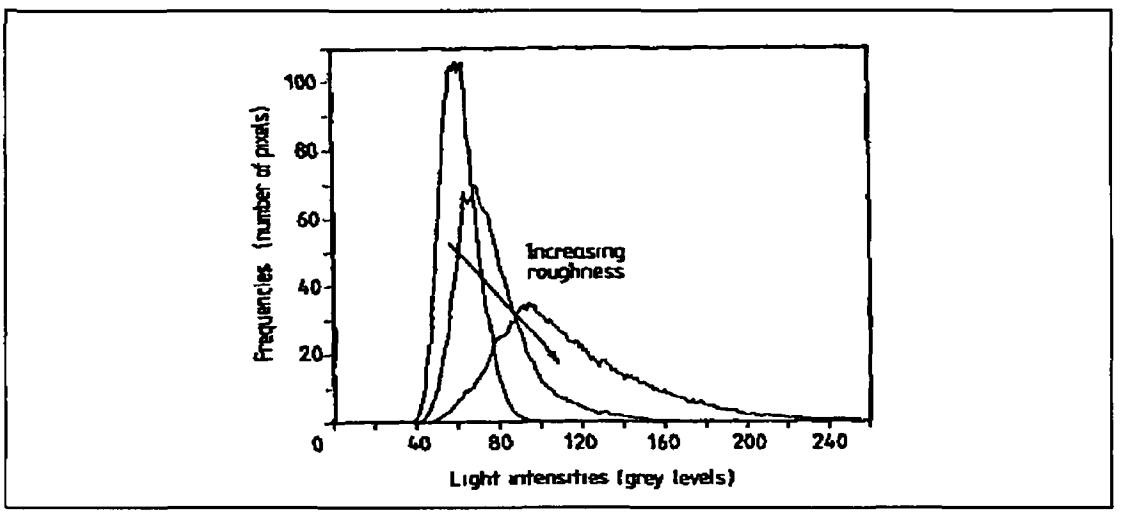

Figure 3 23 Grey-level histograms of the image pattern of reflected light from tool steel specimens, [103]

Luk then used the ratio of the standard deviation to the root mean square height of the histogram as an indicator of surface roughness The effect of grazing angles and illumination distance was evaluated and the system was optimised to achieve a range of between 0 1 to 1 μm Different sample materials were examined and tool steel was seen to behave quite differently to brass and copper samples

Geary et al [105] developed a fibre-optic scatterometer that was a direct application of ARS This included information on arranging a linear array of fibres to a linear array detector The BDRF was evaluated and roughness measured accordingly

CHAPTER FOUR

4 Design of Sensor for the Measurement of Surface Roughness and Defects

This project is concerned with developing a fibre optic sensor for measurement of surface properties. This chapter serves to illustrate the principle of operation of this sensor and to optimise the sensor's design with regard to measurement of surface roughness and defects.

Both sensor systems use the same equipment but various components and the data acquisition and analysis may differ as will be detailed in chapter four. The basic block diagram of the system is shown below in figure 4.1. Fixturing attached to the translation stage position bare optical fibres above a sample. The fibres are positioned at equal but opposite angles above a sample surface. One set of fibres emits light while the other receives light. The light sources and detectors used are discussed in chapter five, while specific componenets are detailed in chapter seven. Light detection is followed by a stage of preamplification before data acquisition by the analog to digital converter. The personal computer performs data retrieval, analysis and presentation using LabView software.

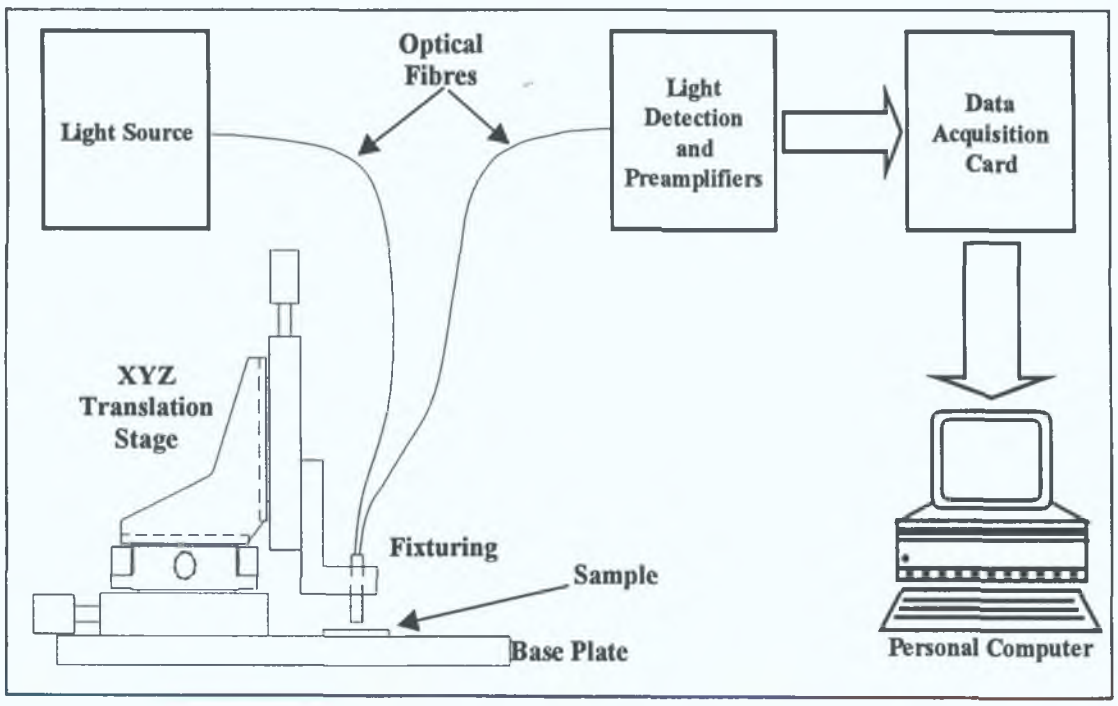

Figure 4.1 Block diagram of fibre optic sensor system.

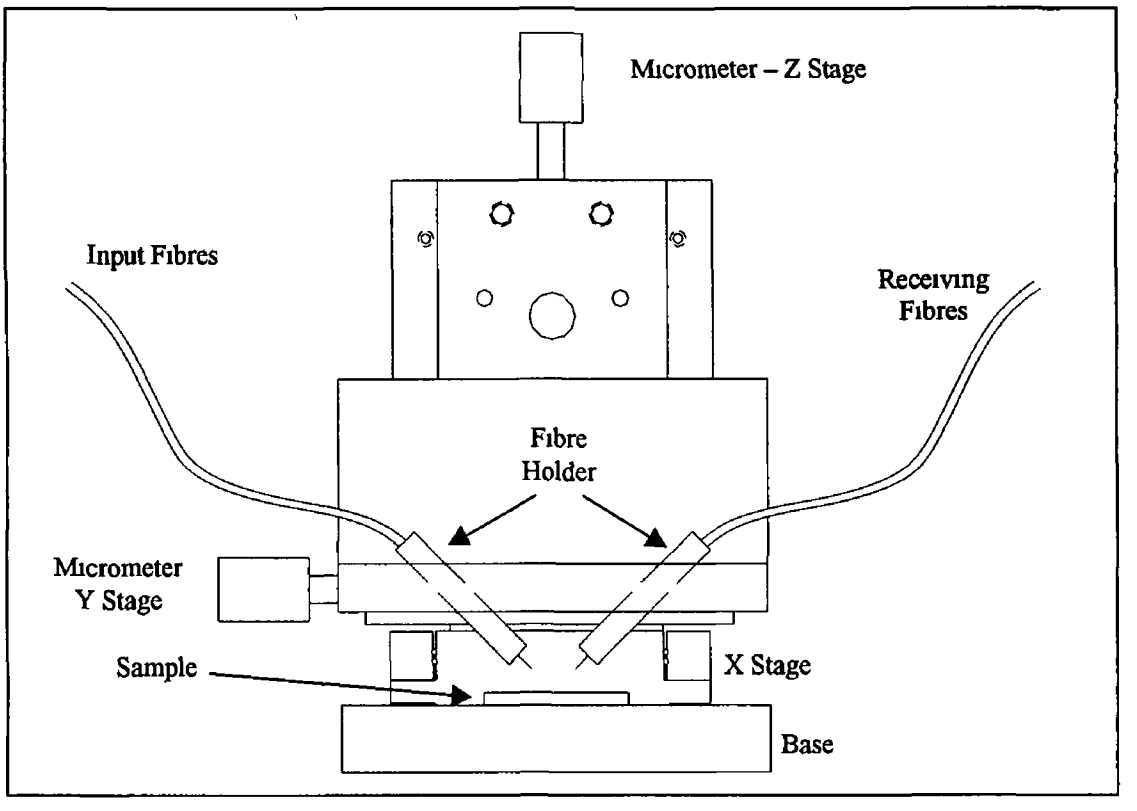

Figure 4 2 System for positioning input and receiving fibres

Figure 4 2 shows the side view of the XYZ translation stage and fixturing for fibres shown in figure 4 1 Drawings of the various components of this rig can be found in the appendix Fibres can be held at incident angles of 45° and 60° to normal incidence Bare fibres can be seen protruding from the ends of the fibre holders – for this reason the position of the fibres is uncertain

This project is concerned with a fibre-optic sensor for measurement of surface properties and these are divided into surface defects and surface roughness For the purposes of this project, a surface defect is defined as a hole in a sheet of metal Surface roughness is to be measured through the measurement of specular scatter

4 1 Model of System – Surface Defects

The principle of operation of this surface defect sensor is similar to that of photoelectric sensing, the sensor ascertains the presence or absence of a surface within a certain range This sensor could be used to sense the edge of an object

Consider the displacement characteristic shown in figure 2 18, this sensor is quite close to the surface of the sample 0 5 – 1 mm A laser diode light source gives the advantage of greater stand-off distance than an LED This would also introduce additional light source noise and modal noise In addition, most engineering surfaces reflect light diffusely and irregularly Any displacement curve will be less smooth than figure 2 18 and multiple displacement curves may be quite different in relation to peak intensity For these reasons, if a certain cut-off voltage is exceeded the sensor considers a surface present and absent otherwise

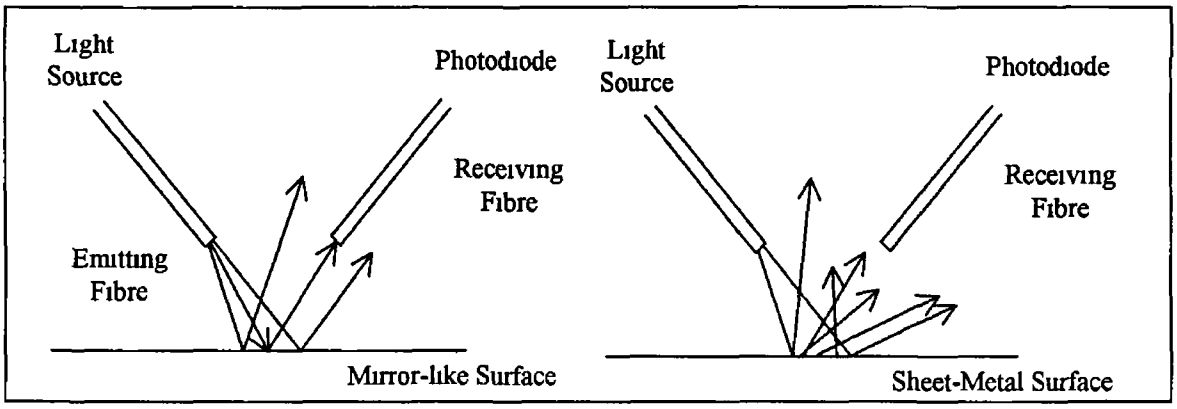

Figure 4 3 Reflection profile from a mirror-like surface and from a rough surface

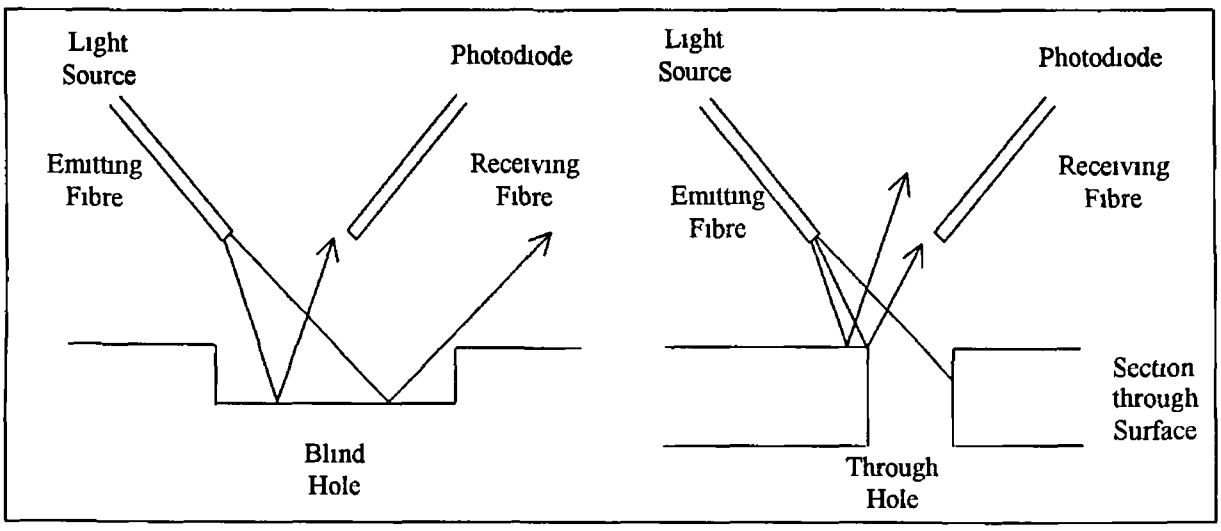

Figure 4 4 Affect of a blind and a through hole on reflection

Figure 4 3 shows a ray diagram of the reflection from a mirror-like surface and from a rough surface such as sheet metal Obviously light reflection from a rough surface is not specular and can be quite irregular - this restricts the use of a intensity-based fibre-optic sensor for displacement sensing with sheet metal Figure 4 4 illustrates the

principle of operation of this fibre-optic sensor using the example of a through hole and a blind hole A blind hole is the equivalent of a displacement change in figure 2 18 A through hole will scatter no optical power towards the return fibre while a blind hole may do so The choice of cut-off voltage determines the shallowest blind hole that can be distinguished The sensor acts as a crude displacement sensor as a blind hole will be sensed if the hole is deep enough The use of fibres at an incident angle to the surface means that shallower blind holes can be sensed than if the fibres were oriented at normal incidence to the surface

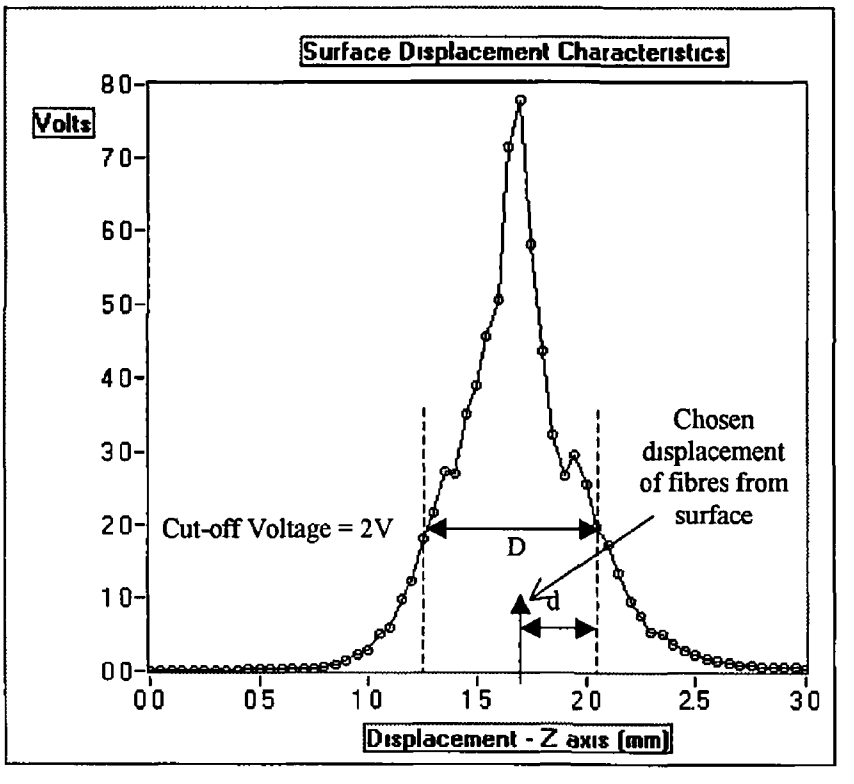

Figure 4 5 Displacement characteristics for a polycarbonate surface

Figure 4 5 shows the displacement curve for a polycarbonate surface This configuration used a laser-diode light source in conjunction with multimode fibres Note that the displacement curve is noisier than that shown in figure 2 18, but it is at a greater displacement from the surface and it is wider The affect of surface roughness and light source variation can be seen in the irregularity of the curve The sensor uses a cut-off voltage system, such as photoelectric sensors use [52], to detect holes in the surface Choosing a cut-off voltage determines the vertical range, D, for which the sensor considers a surface present Choosing the initial displacement of the fibres

from the surface determines the depth, d, of the shallowest blind hole that can be sensed

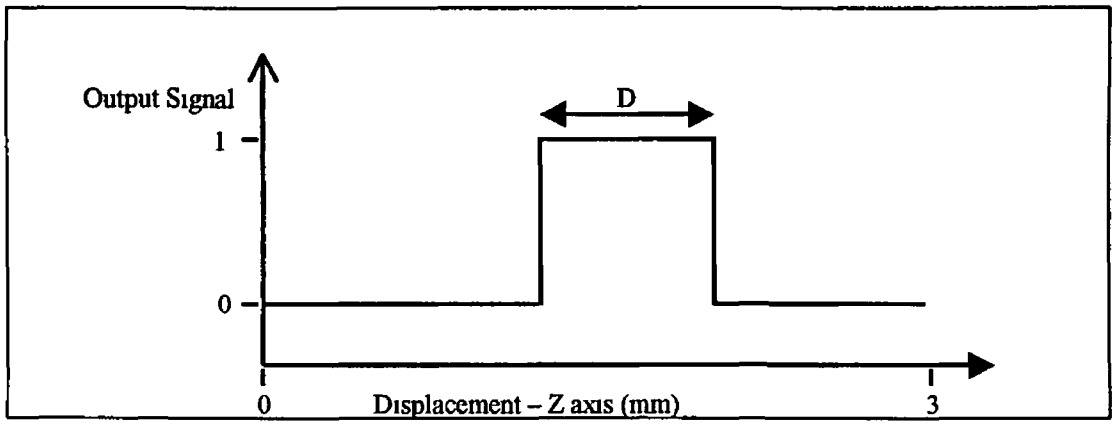

Figure 4 6 Output signal of sensor for displacement characteristics shown in figure 4 5 and a cut-off voltage of 2 Volts

Figure 4 6 shows the output signal of the sensor for this displacement curve if a cut-off voltage of 2 Volts is chosen An output signal of 1 indicates the presence of the surface within the vertical range, D, and 0 otherwise The choice of D and d is determined by the properties of the surface, the tolerable variation in the output voltage, due to noise, surface roughness, etc , may be such that a low cut-off voltage is necessary The effect of incident angle on displacement characteristics is shown by figure 4 7, for higher incident angles, there is narrower peak closer to the surface As this peak is narrower it has higher peak intensity

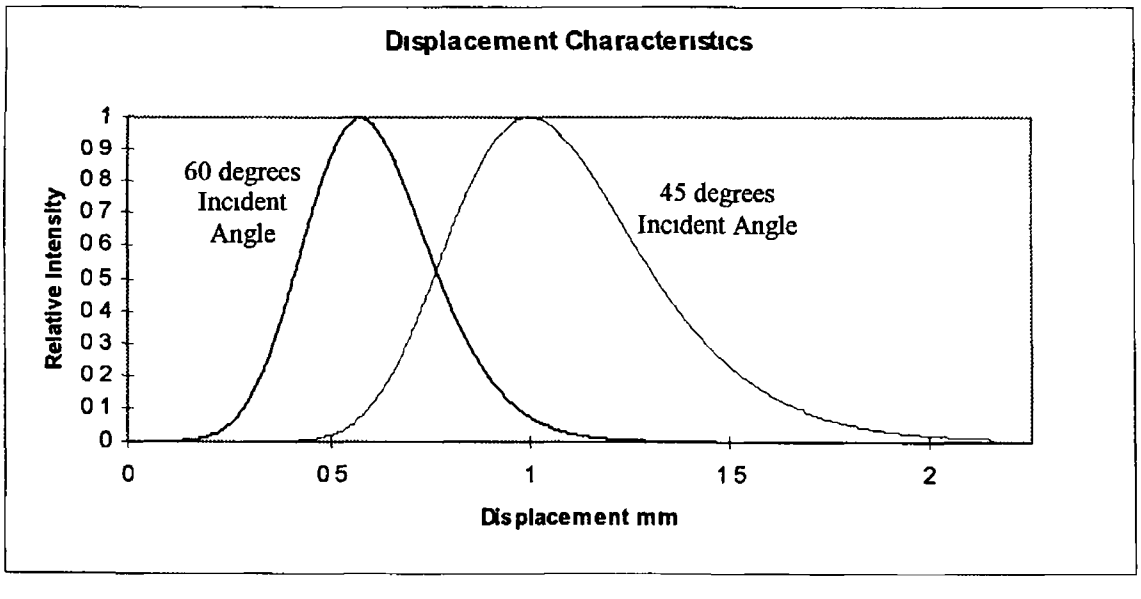

Figure 4 7 Displacement characteristics at various incident angles

4 2 Model of System – Surface Roughness

This system measures surface roughness through measuring the displacement characteristic curve for surface roughness samples at different incident angles, namely 45° and 60° Experiment will determine whether the shape of the displacement characteristic is affected by the roughness of the surface involved The main reference for this section is equation 3 9, which defines scattering from a relatively smooth surface having a Gaussian distribution of roughness The scattering ratio, I_s/I_o, will be determined using the peak voltage alone or the sum of all voltages above a certain fraction of peak intensity for I_s and a reference value for I_o All graphs presented in this section are determined using some form of equation 3 9

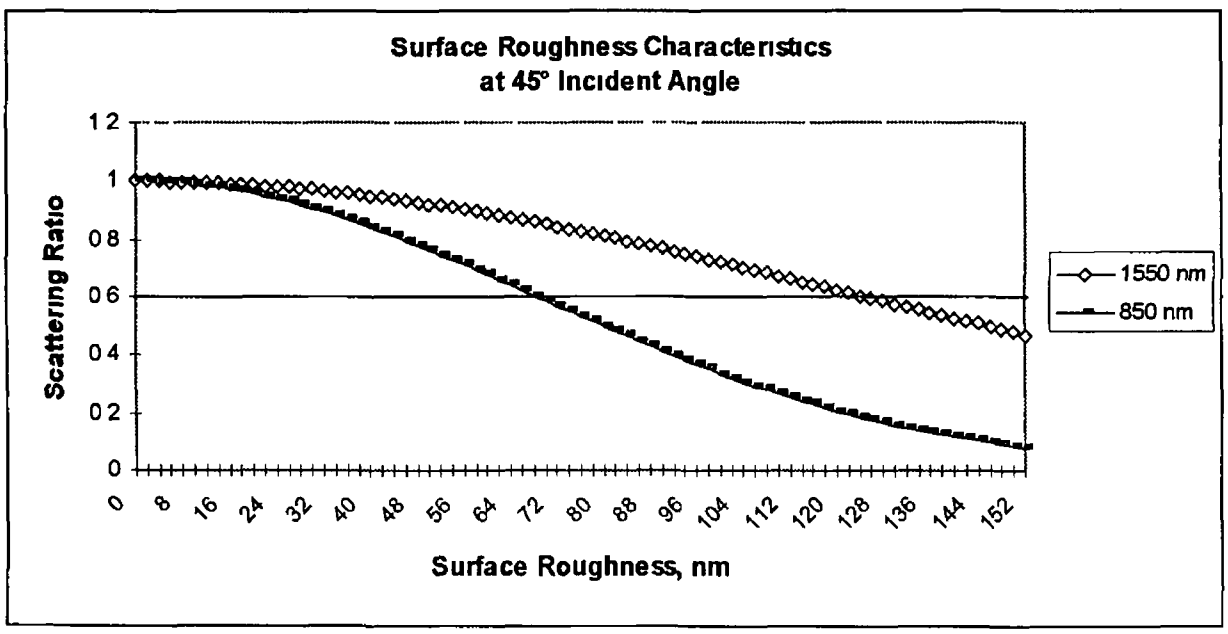

Figure 4 8 Surface Roughness Characteristics at 45° Incident Angle - the influence of light source wavelength

Figures 4 8 and 4 9 show the surface roughness characteristics at incident angles of 45° and 60° respectively The two curves show the effect of using light sources at infrared wavelengths of 850 nm and 1550 nm These wavelength light sources are, along with 1300 nm and 1550 nm sources, the most common light sources used in fibre-optic telecommunications It is clear from these graphs that longer wavelength and higher incident angles extend the range of these sensors when relying on equation

3.9 to measure surface roughness. This limits the range of measurement to beneath 0.2 μm R_q using a 1550 nm light source and an incident angle of 60°, but perhaps greater using the angular profile of scattering.

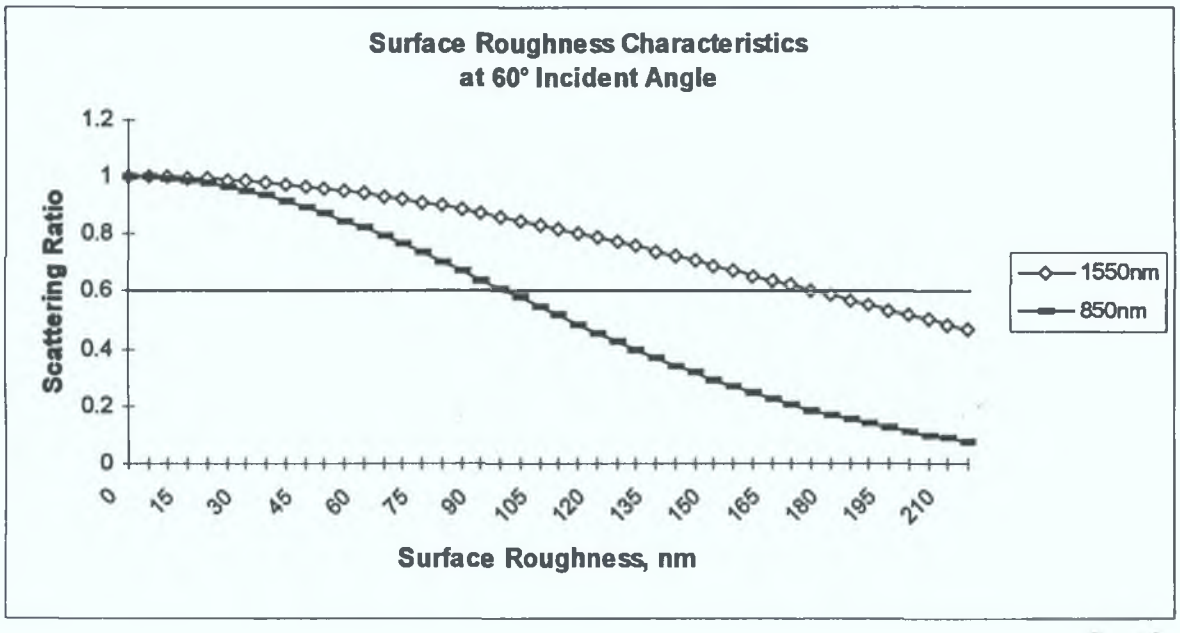

Figure 4.9 Surface Roughness Characteristics at 60° Incident Angle - the influence of light source wavelength

Evaluating the displacement characteristics of a particular set-up against surface roughness standards is the basis of measurement with this sensor. The peak voltage of the displacement characteristic or the sum of the voltage levels of each increment above a certain percentage of the peak voltage level was correlated against the surface roughness characteristics of a particular sample.

4.3 Components of each Sensor

Figure 1.1 describes the components of each sensor highlighting the differences between each set-up. Physically each sensor requires the same configuration with regard to mechanical design and optical fibres. As sensors, the defect sensor and surface roughness sensor have different requirements. The surface roughness sensor is sensitive to noise and the design of the sensor system with regard to light source, light detection and data analysis should consider this. The defect sensor is designed to

withstand a large level of noise and the design, of these system components, disregards noise in preference to speed of operation, stand-off distance, and simplicity. The surface roughness sensor uses a modulated driving circuit to drive an LED. The defect sensor uses a laser light source driven at a constant current. Identical low noise preamplification was used for both sensors for practical reasons. All light sources and photodetectors are coupled to optical fibres using telecommunications type housings, ST and FC. With regard to data processing; the surface roughness sensor uses digital filtering and windowing to reduce noise, while the defect sensor uses a similar arrangement; a simpler method would suffice. In this way, the surface roughness sensor can be categorised with regard to noise levels, while the defect sensor either senses correctly or fails.

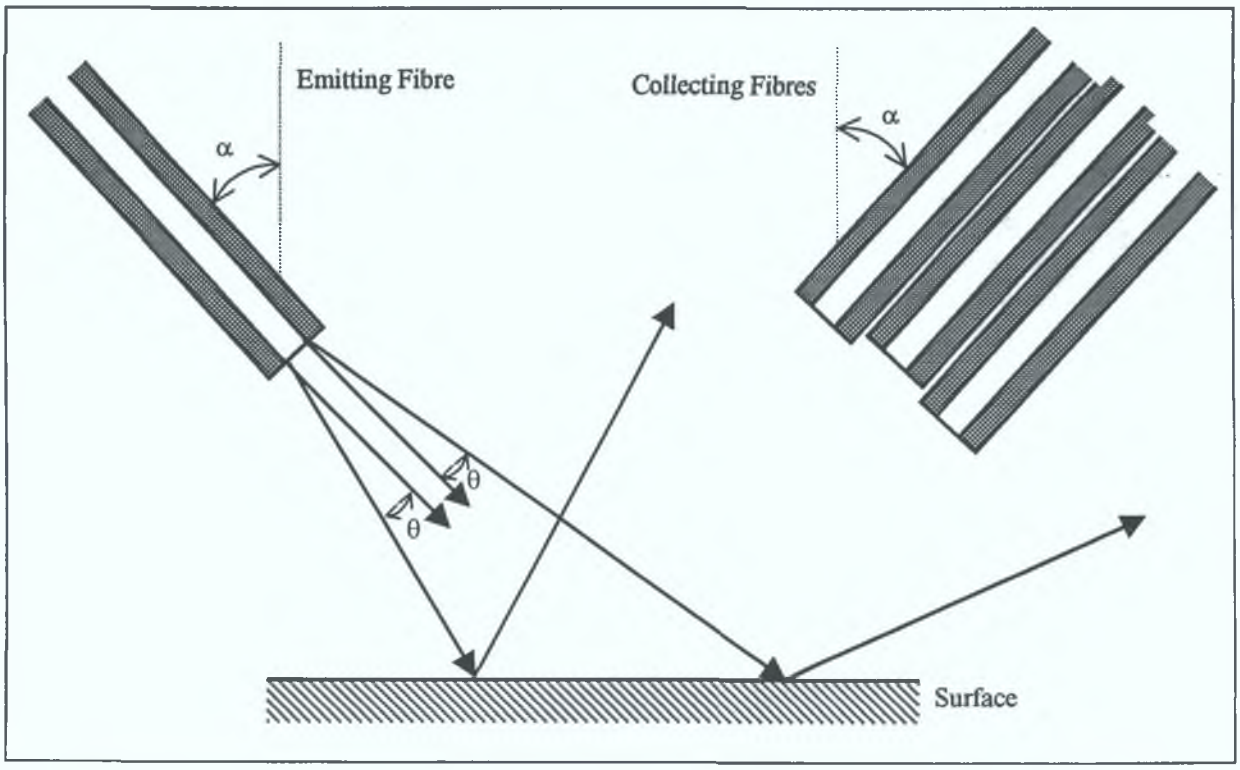

Figure 4.10 Multiple receiving fibres, not to scale

The sensor can be configured with multiple receiving fibres as illustrated in figure 4.10. This arrangement allows the spatial distribution of optical power to be measured. The angle α denotes the angle of incidence of the emitting and collecting fibres relative to normal to the surface. The angle θ can be determined from the numerical aperture of the fibre using equation 2.4.

CHAPTER FIVE

5 Design and Development of Optical Inspection System

This chapter details the practical design of the system outlined in figure 5 1 and 5 2 This includes optoelectronic design, i e light sources and photodetectors, associated electronic circuitry, the influence of noise and error on design, choice of fibres, and mechanical design

5 1 Light Sources

The light source is the primary choice in designing an optical sensor For this project the criteria for selecting light sources are the following

- coupling to optical fibres
- optical power
- optical safety
- wavelength
- stability of light source
- cost
- lifetime of device
- power consumption
- modulation
- coherence

The two commonest light sources used in fibre-optics technology are the light-emitting diode (LED) and laser diode [1-4], these will be described in the next two sections Other possible light sources are incandescent light bulbs (e g tungsten filament bulb), discharge lamps and non-diode lasers [4] This section will deal with the practical aspects of choosing and using electronic light sources for each of the two optical sensing applications being considered

5.1.1 Light-Emitting Diodes

The LED is a solid-state semiconductor device that emits optical radiation. Light-emitting diodes (LED) emit optical radiation in proportion to the forward current through the diode. The LED is a low voltage device that has long lifetime and low cost. It responds quickly to changes in current (10 MHz), as part of an electronic circuit. It produces a narrow spectrum of coherent red or infrared light that can be well collimated.

The optical radiation emitted from an LED is generated by spontaneous emission. The LED is in effect identical in construction to a basic semiconductor diode. As an electron in the conduction band recombines with a hole in the valence band, the electron makes a transition to lower energy state and releases energy in an amount equal to the band-gap energy. In an LED, this energy is emitted as infrared radiation or visible light, whereas in other semiconductor diodes the energy heats the material.

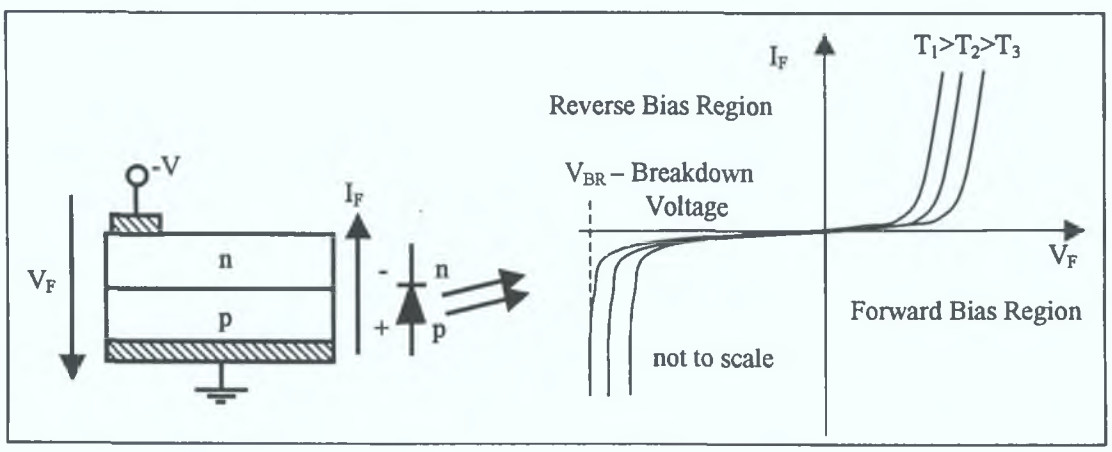

Figure 5.1 Schematic diagram, electronic symbol, and operating curve of a typical LED [106].

Figure 5.1 shows a schematic diagram of a pn diode. V_F is the forward voltage, the voltage drop between the p and n terminal of the diode. I_F, the forward current, is the current flowing from the p terminal, anode, to the n terminal, cathode, of the diode. The operating curve shows the voltage and current that must be applied across to switch the LED on. The same electronic symbol is used for LEDs and laser diodes.

Figure 5 2 shows the operating curves of a typical LED for a constant voltage and a constant current driving circuit Note the temperature dependence of these curves – for a constant voltage driving circuit, any increase in temperature draws a higher current An increase in current causes the temperature of the LED to increase, this in turn causes an increase in current This effect in electronic diodes is called thermal runaway and is inherently unstable On the other hand, a constant current driving circuit is inherently stable An increase in temperature causes less power to be generated, because the voltage across the diode decreases A constant current driving circuit is still dependent on temperature

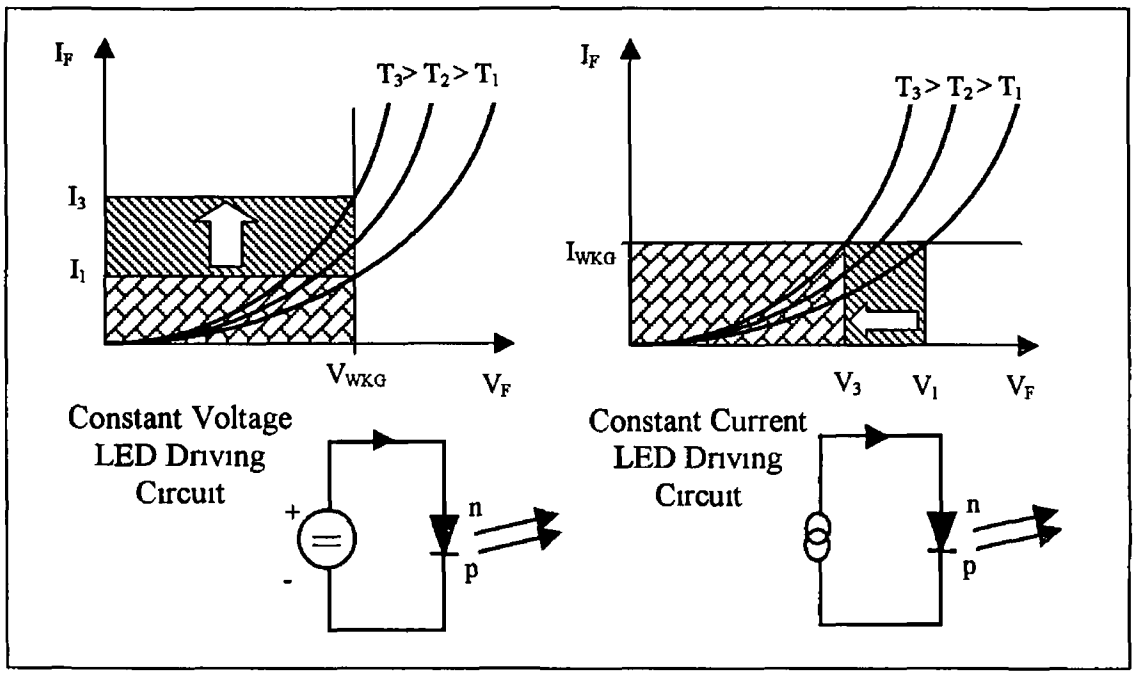

Figure 5 2 I_F versus V_F curves for constant voltage and constant current driving circuits and the effect of temperature variation [2]

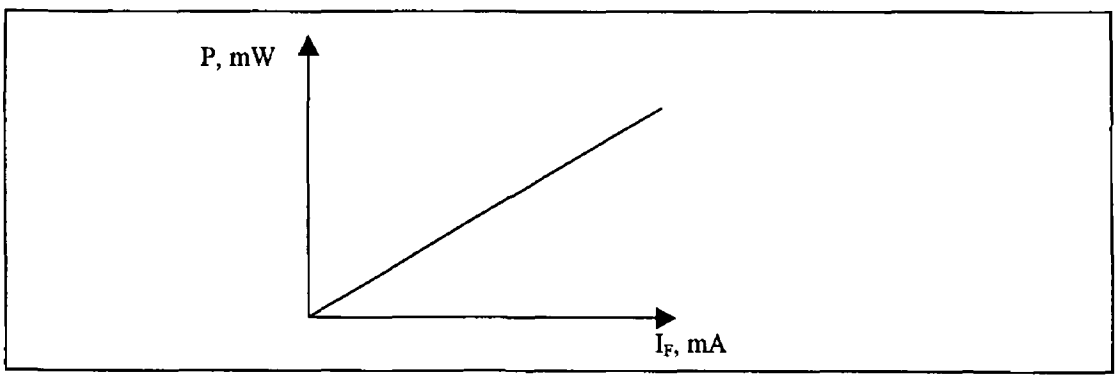

Figure 5 3 Optical power output, P, versus forward current, I_F, for a typical LED

Ultimately, the LED transforms electric current into optical radiation, figure 5 3 shows the variation of optical power output, P, with forward current, I_F Note that the output intensity is proportional to forward current, this is another advantage of choosing a constant current driving circuit

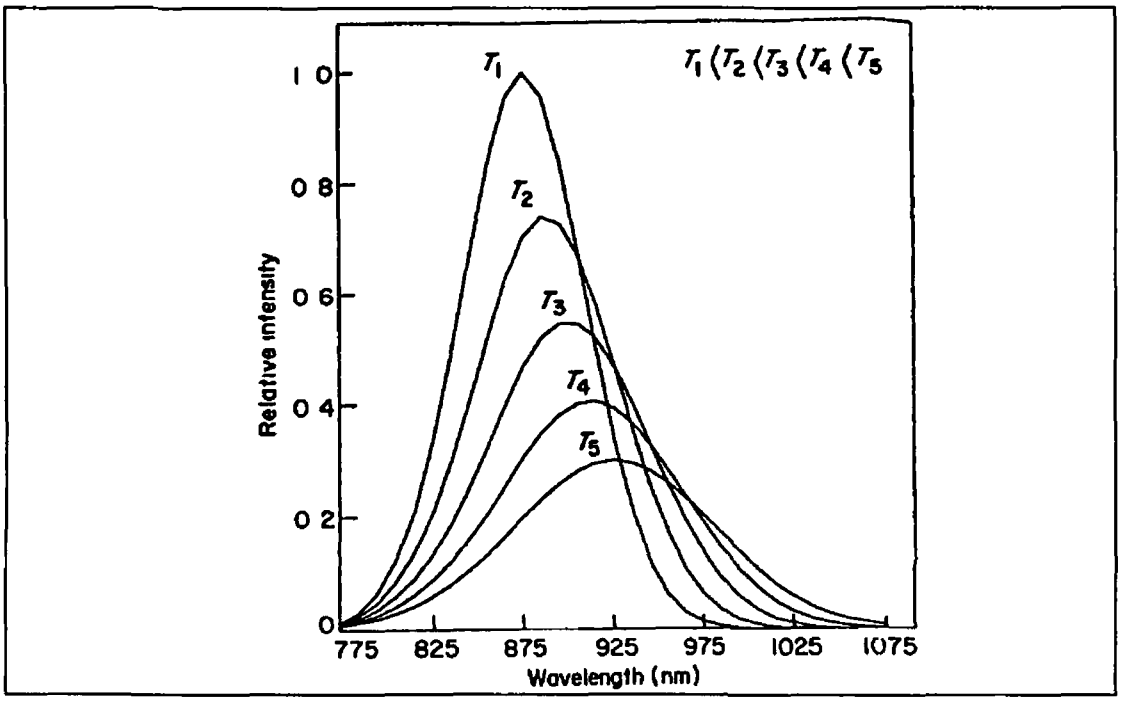

Figure 5 4 Typical thermal and spectral behaviour of an LED source [33]

As noted before the output intensity fluctuates with temperature Figure 5 4 there is a spectral shift with an increase from in temperature from T_1, minimum temperature, to T_5, maximum temperature At lower temperature, an LED may emit at a higher intensity, lower wavelength, and with a wider spectral bandwidth The temperature characteristics depend on the particular LED As will be seen later the response of photodiodes is dependent on wavelength

There are two major designs of the semiconductor structure of LEDs surface-emitting and edge-emitting [1] These are illustrated in figure 5 5 A transparent region, window, is embedded in the device to enable radiation to escape Surface-emitting LEDs are most common, they emit through a window that is in a plane parallel to the surface of the device The emitted light is not directional, with a beam width at half intensity of about 120° Spherical lenses are routinely used to efficiently couple the beam from a surface-emitting LED into a fibre, as in Honeywell's range of "Sweet Spot" devices

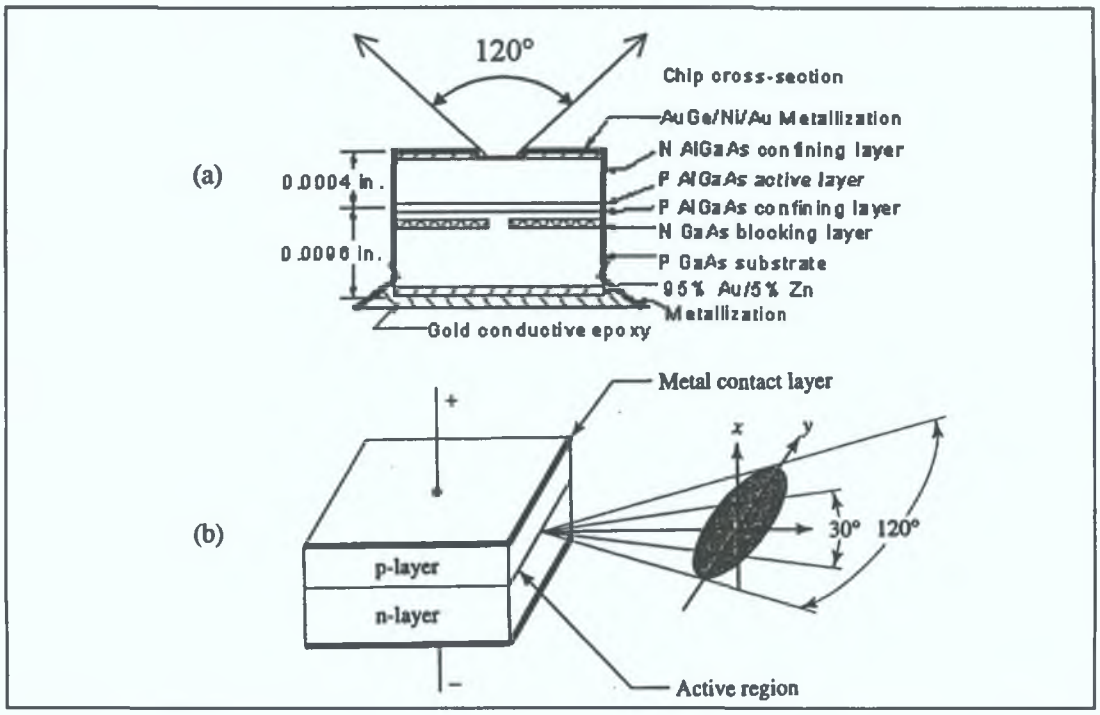

Figure 5.5 (a) Surface-emitting LED [107] (b) Edge-emitting LED [4].

In edge-emitting LEDs the window is embedded between two layers. Radiation is emitted in an elliptical cone pattern and from a very small area, 3 μm x 10 μm. Light output is lower than surface-emitting but output but can be coupled into optical fibres more efficiently.

5.1.2 Lasers

The laser is a light source that produces a high intensity beam of coherent light. LASER is an acronym standing for Light Amplification by Stimulated Emission of Radiation [1]. Stimulated emission contrasts with spontaneous emission where each photon of light is emitted independently. Stimulated emission occurs when through feedback an individual photon stimulates the emission of another photon with identical direction and wavelength. Feedback is achieved through forming a laser cavity as shown in figure 5.6. Light is confined to the lasing cavity by two mirrors, one of which partially transmits to form the output beam. The process of laser amplification provides higher intensity, lower spectral bandwidth, and narrower beamwidth. A laser diode emits an elliptical beam with typical beam divergence angles of 35° and 10° for the x and y axes respectively [4].

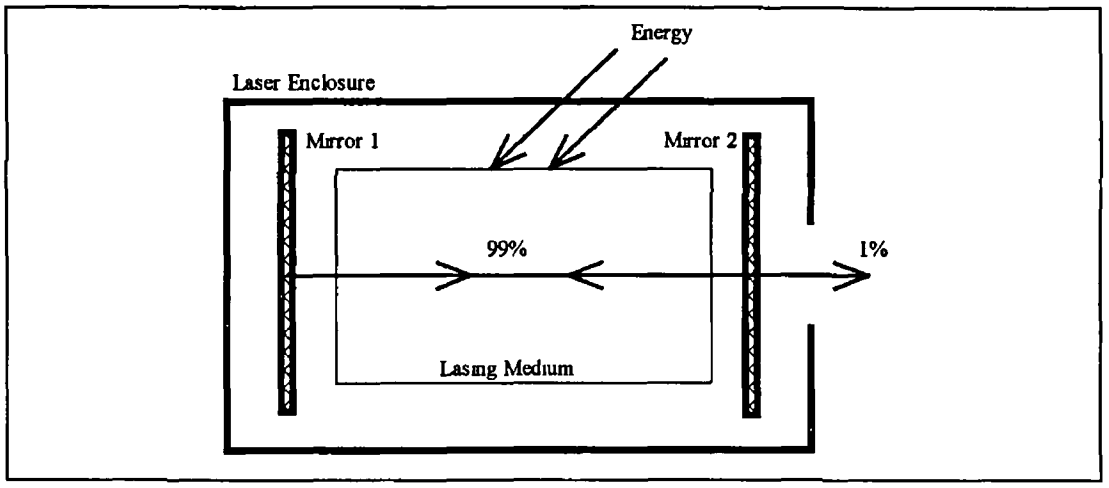

Figure 5 6 Light amplification in a laser cavity

In principle, the laser diode is an edge-emitting LED with an added optical cavity that provides feedback and generates stimulated emission Figure 5 7 shows the layer structure of an AlGaAs laser The shaded layer indicates the laser cavity A mirror is formed at either end of the chip by polishing the sides, the difference in refractive index due to the AlGaAs-air interface reflects radiation back into the cavity As this occurs at both ends of the cavity, it is common to include a monitor photodiode at the inactive side

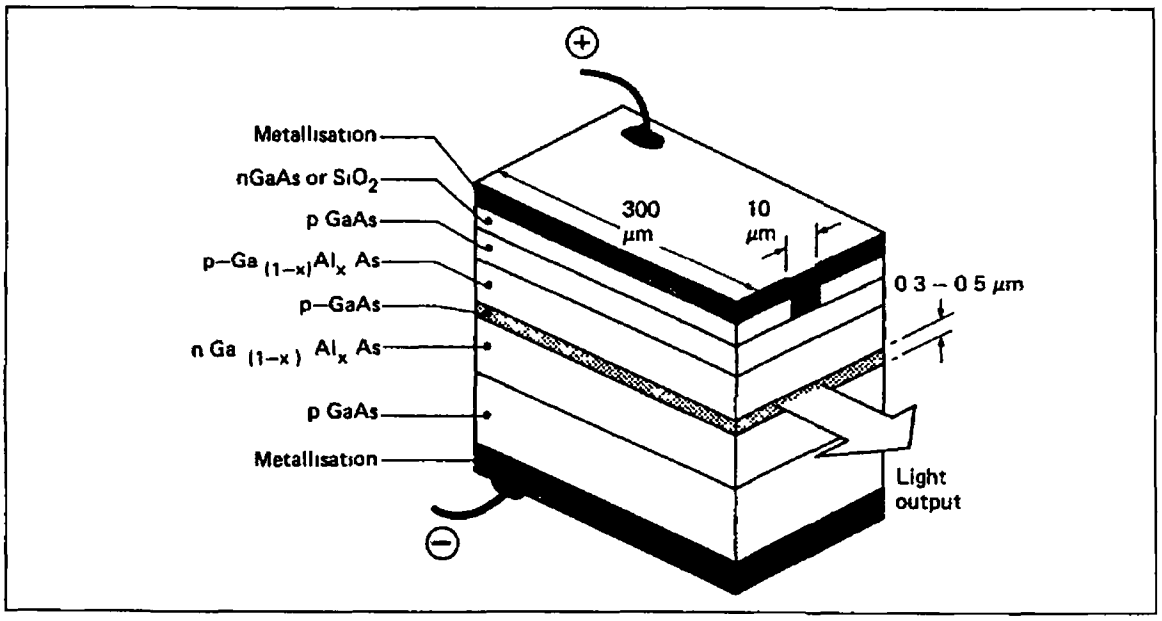

Figure 5 7 Structure of an AlGaAs laser diode [2]

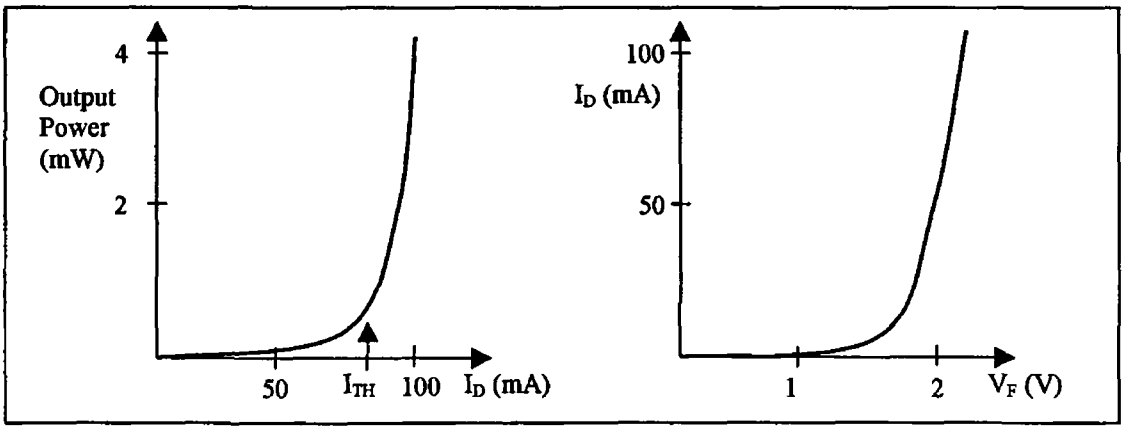

Figure 5 8 (a) Output power versus current and (b) forward current versus voltage [4]

The forward current versus forward voltage characteristic, figure 5 8(b), is similar to those for an LED or for any diode The output power versus forward current curve is quite different, initially the laser diode behaves identically to an LED but when the forward current reaches the threshold current voltage, I_{TH}, the device starts operating as a laser Figure 5 9 shows the sensitivity of threshold current to temperature, for this reason the output power of a laser is highly sensitive to temperature changes

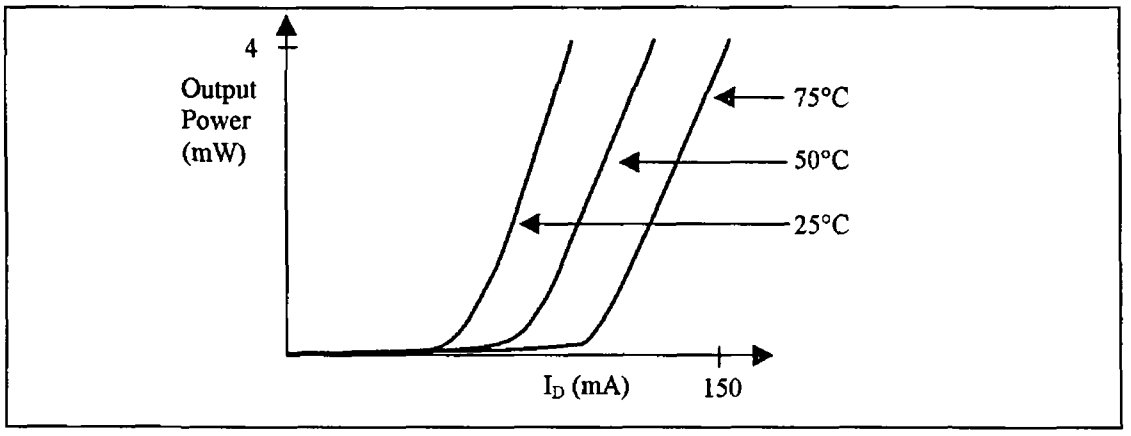

Figure 5 9 Effect of temperature on threshold current and output power [4]

Laser diodes are available as single mode and multimode devices Figure 5 10 shows the spectral pattern of a multimode laser there are multiple peaks at a range of wavelengths These multiple peaks occur because the laser cavity will support oscillation at a number of wavelengths At higher currents, the number of peaks decreases A single mode laser operates with a single wavelength peak and it is possible to make a single mode laser diode, but it is more expensive to do so

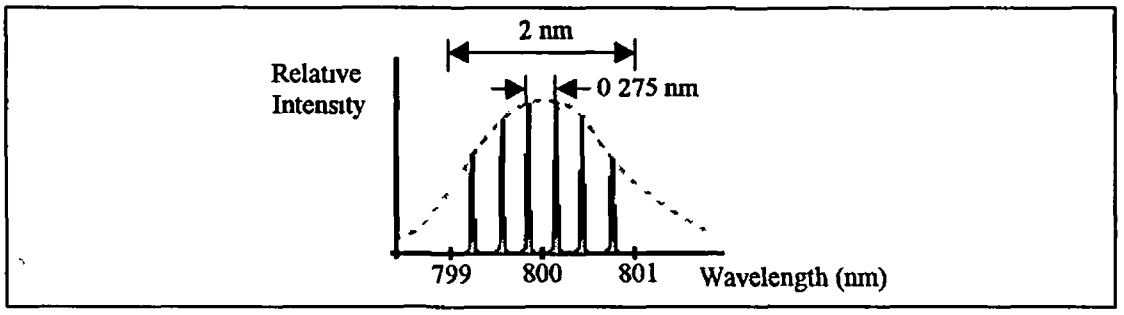

Figure 5 10 Spectral pattern of an 800nm multimode laser diode with 2nm spectral bandwidth [4]

Property	LED	Multimode Laser Diode	Single-mode Laser Diode
Spectral Bandwidth (nm)	20-100	1-5	<0 2
Rise time (ns)	2-250	0 1-1	0 1-1
Mod Bandwidth (GHz)	< 3	<2	2
Temperature Sensitivity	Low	High	High
Lifetime (h)	100,000	10,000-100,000	10,000-100,000
Cost	Low	High	Highest
Fibre-coupled Power (mW) 50 μm core fibre	0 07	1-3 (Low-Power Laser Diode)	1-3

Table 5 1 Comparison of LED and laser diode [4]

The table above compares the properties of laser diodes and LEDs Laser diodes have faster rise times, narrower spectral bandwidth, and higher modulation bandwidth – high performance laser diodes have been designed for optical communications where these quantities are critical For multimode fibre-optic sensing applications, the performance of LEDs with regard to these quantities is adequate The stability and low temperature sensitivity of LEDs are highly important for sensing applications, as is their low cost For these reasons, an LED was chosen as the light source for the surface roughness sensing application

The higher fibre-coupled power of laser diodes is an advantage in sensing applications For an online fibre-optic sensor adequate stand-off distance is required A multimode laser diode was chosen for the fibre-optic defect sensing application

5 1 3 Diode laser safety

Despite their small size and low input power, diode lasers may still represent a significant hazard to vision This is especially true where the output is collimated and/or invisible (near IR), and/or for higher powers than the typical 3 to 5 mW One should never look into the beam of any laser - especially if it is collimated An indirect means of determining proper operation such as projecting the beam onto a white card, using an IR detector card or tester, or laser power meter should be used to test laser operation Note that light at 635 nm appears more than 5 times as intense to the eye as light at 670 nm Therefore, the apparent brightness of a source is not a reliable indication of its actual optical power output – this point is even more important at 850 nm and longer wavelengths

Much higher power visible and IR diode lasers are available (though not common or affordable) and represent even greater danger to vision and potentially even risk of heat damage or fire from a focused beam The divergent beam from bare high power laser diodes is a definite hazard These are extremely dangerous even if not that well collimated Furthermore, they also use near-IR wavelengths so that there is essentially no warning that a beam is present

Common visible laser diodes, diode laser modules, and laser pointers produce 1 to 5 mW at various wavelengths between 670 and 635 nm When collimated (as in the case of a module with internal optics or a laser pointer) the entire beam can enter the eye and burn holes in the retina The beam from a bare laser diode or an optical fibre is highly divergent and therefore less of a hazard since the lens of the eye cannot focus it to a small spot However, there is still no reason to look into the beam

Laser safety signs should be displayed on the laser itself or in close vicinity to the laser if this is impossible due to the small size of laser diodes

5 2 Photodetectors

In an optical sensing system, it is ultimately necessary to transform optical power into an electrical signal, by using a photodetector The basic photodetector generally produces only a low-level electrical signal, which must be amplified before it can undergo further processing The combination of photodetector and its immediate amplification is called a receiver Many different photodetectors are commercially available but PIN (p-i-n) photodiode are most commonly used with optical fibres [1-4, 108,109] The criteria for selecting a photodetector are the following

- responsivity
  - wavelength
  - intensity
- cost
- signal to noise ratio
- speed of response

5 2 1 PIN Photodiodes

A photodiode operates in an opposite fashion to an LED, in this case incident light on a diode causes the generation of electrical energy The diode consists of the semiconductor structure shown in figure 5 11 A PIN diode differs from a pn diode as between the positively doped, p region and negatively doped n region there is an intrinsic, undoped, i region [1] Photons incident through the anti-reflection coating and the p layer are absorbed by the intrinsic layer causing a current, I_D, to flow through the diode as shown

Typical photodiode characteristics are shown in figure 5 12 The two curves differ in that one represents a photodiode that is exposed to optical radiation and the other a photodiode that is unexposed to optical radiation Of the four quadrants shown, quadrant III and IV are suitable for photodiode operation, quadrant III is generally used for optical sensing and quadrant IV, is used for solar cells – electrical generation Use in quadrant III is accomplished using reverse bias (junction voltage, V_D, is

negative). Photodiodes can be classified into two groups: the solar cell and low power photodiodes. Low power photodiodes or signal photodiodes find application in signal detection for communication, control, and metrology. They come in many implementations: planar, PIN, avalanche and Schottky being the most common types. The PIN photodiode is discussed here.

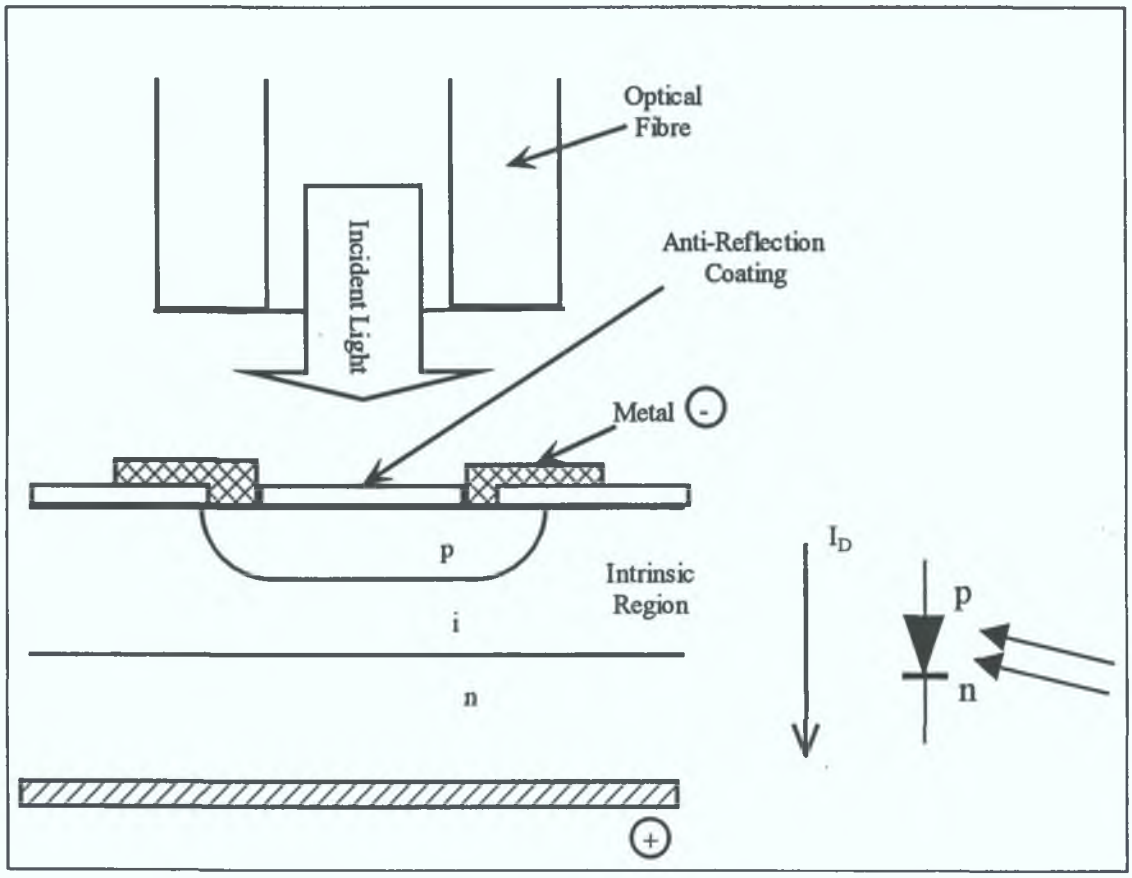

Figure 5.11 A PIN diode structure (reverse biased) and electronic symbol for a photodiode [1].

I_o indicates the dark current; the current generated in reverse biased mode without any radiation being incident on the diode. The dark current depends on the semiconductor material, doping, junction geometry and ambient temperature. The dark current increases by a factor of ten for a 25°C increase in temperature. Dark current noise affects the signal to noise ratio of the sensor system. The effect of dark current noise can be minimised by choosing a photodiode with low dark current and maximising the intensity of the optical signal.

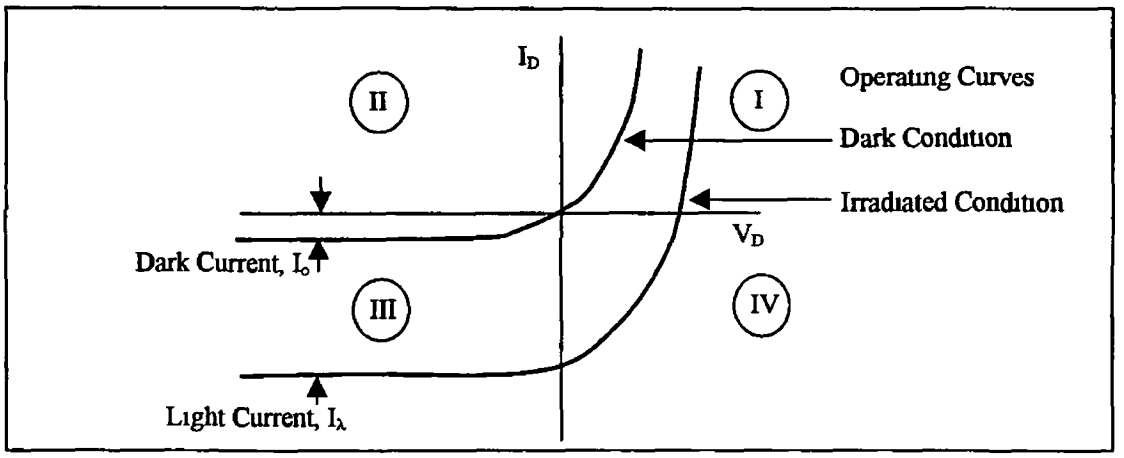

Figure 5 12 The current-voltage relationship of a photodiode [4]

The photocurrent, I_λ, is a linear function of irradiance, this makes the photodiode a valuable measurement device in the reverse biased mode At constant temperature, the open circuit voltage of the photodiode is a logarithmic function of irradiance with a range of several decades, this makes the photodiode a valuable measurement device where logarithmic response is desired [4]

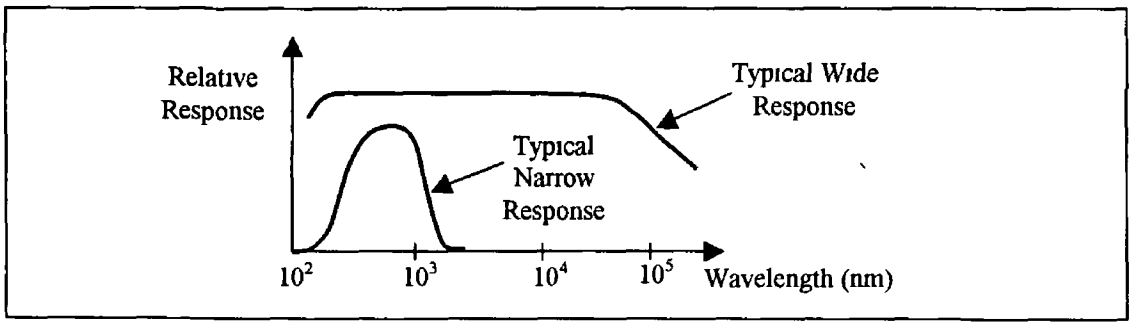

Figure 5 13 Typical response of photodetectors [4]

Responsivity, $\mathcal{R}$, quantifies the photoelectric gain of the detector It is the ratio of the output quantity of the detector to the input quantity at a given wavelength, e g for a current output it is the ratio of the photocurrent generated to the input optical power in units of Amps per Watt Responsivity is often quoted relative to peak detector response in dimensionless units Responsivity is a quantity that is inherently dependent on wavelength, the energy of an input photon is dependent on wavelength – $E=h\nu$ – where h is Planck's constant, E is energy and ν is photon frequency (photon

frequency is inversely proportional to photon wavelength). The dependency on wavelength is shown in figure 5.13, where two different response curves are shown. Of these two curves, the narrow response curve is typical of photodiodes while the wider response curve is typical of thermal detectors, which convert optical radiation into heat. Photodiode responsivity is usually quoted at a single wavelength.

Different semiconductor device designs and semiconductor materials are responsive at the various wavelengths used with fibre-optic light sources. Silicon is commonly used to sense at visible to near infrared wavelengths and InGaAs devices to sense at wavelengths from 900 and 1650 nm.

The speed of response of a photodiode is important when a modulated signal is to be detected. This is important in telecommunications applications and in sensing applications that use a carrier frequency to reduce noise or separate signals. The speed of response determines the bandwidth of the detector; the range of frequencies that can distinguished. In simple photodiode receivers, high bandwidth is not required and the junction capacitance has the dominant effect on response time. This can be reduced by increasing the reverse bias. Junction capacitance is proportional to the diode area; thus, larger area photodiodes are slower [1].

5.3 Electronic Design

Electronic design encompasses the electronic circuitry that drive the light sources, and detect optical signals prior to data acquisition and analysis. The noise sources relating to these circuits are analysed in section 5.4.

5.3.1 Signal Generation Circuits

The simplest LED or laser diode driving circuit is shown in figure 5.14; an LED and resistor are connected in series across the terminals of battery or voltage supply. Two curves are shown; the first is the current voltage characteristic of the LED or laser diode, the second shows the variation of current for different values of the voltage across the LED. The intersection of these lines establishes the operating point of the circuit and the current that flows through the device. The disadvantage of this circuit

is that, due to the tolerances in LED characteristics, resistance value, and variation in the supply voltage, the resulting intensity may exhibit considerable variation This circuit is sufficient where light intensity variation is unimportant

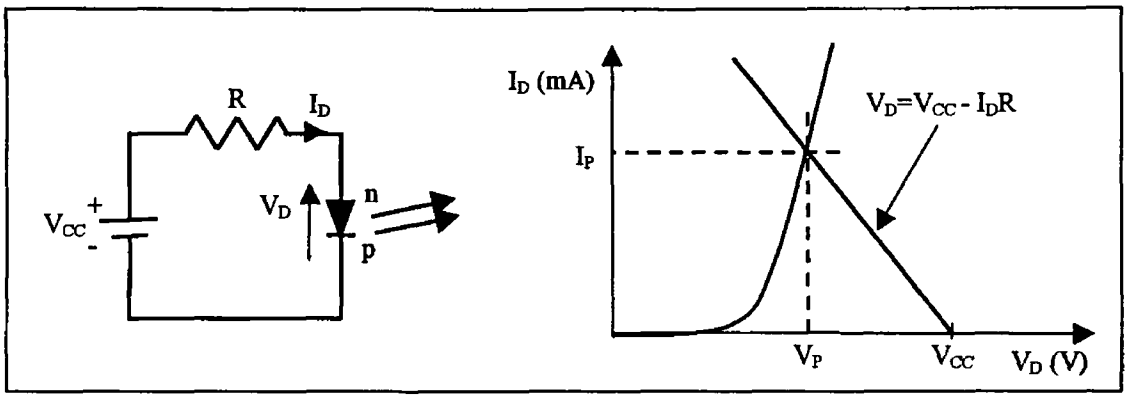

Figure 5 14 Resistor driving circuit [4]

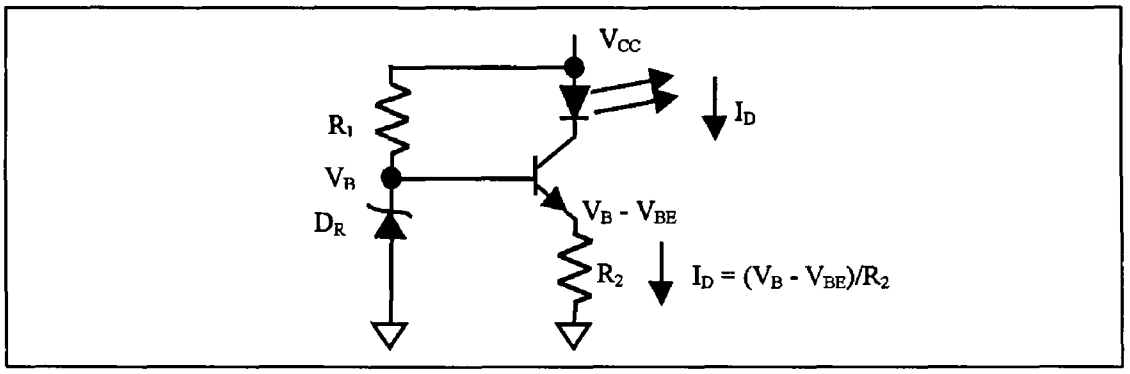

Figure 5 15 Constant current driving circuit [4]

A constant current driving circuit can be constructed using a slightly more complicated circuit as shown in figure 5 15 This circuit uses a transistor and a zener diode to provide a predictable and stable current that is immune to LED characteristic and power supply variations The diode current, I_D is set using the following equation

$$I_D = (V_B - V_{BE})/R_2 \qquad 5\ 1$$

V_B is set by the zener diode, D_R, V_{BE} is the base-emitter drop voltage, a constant 0 7V normally, thus the only variations are due to the thermal variation of the resistor R_2 This circuit uses a bipolar junction transistor but a similar circuit could be constructed using a field-effect transistor

It may be necessary to modulate the signal to the LED and this can be achieved using the circuit in appendix B1 Digital filtering can be implemented to reduce noise when

the signal is modulated and flicker noise is reduced In addition, the LED can be driven instantaneously at a current that is higher than the maximum permitted current, while average current is still lower Figure 5 16 shows a block diagram of this circuit

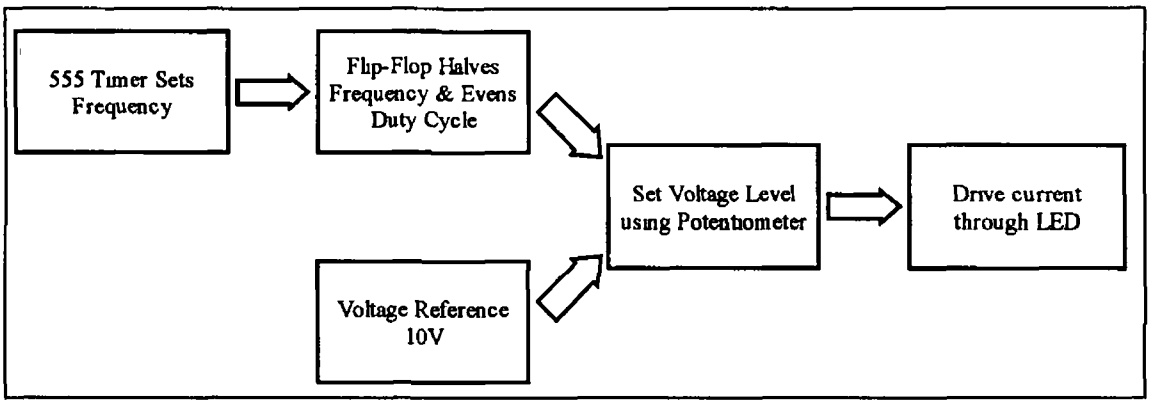

Figure 5 16 Block diagram of square-wave driving circuit

The 555 timer is an inexpensive integrated circuit that can operate as a free-running oscillator producing a continuous square wave of variable frequency and duty cycle Figure 5 17 (a) shows the necessary external connections and components and the equations for determining the frequency and duty cycle of the signal The waveform produced by the timer is shown in figure 5 17 (b) – the frequency and duty cycle are determined from this waveform

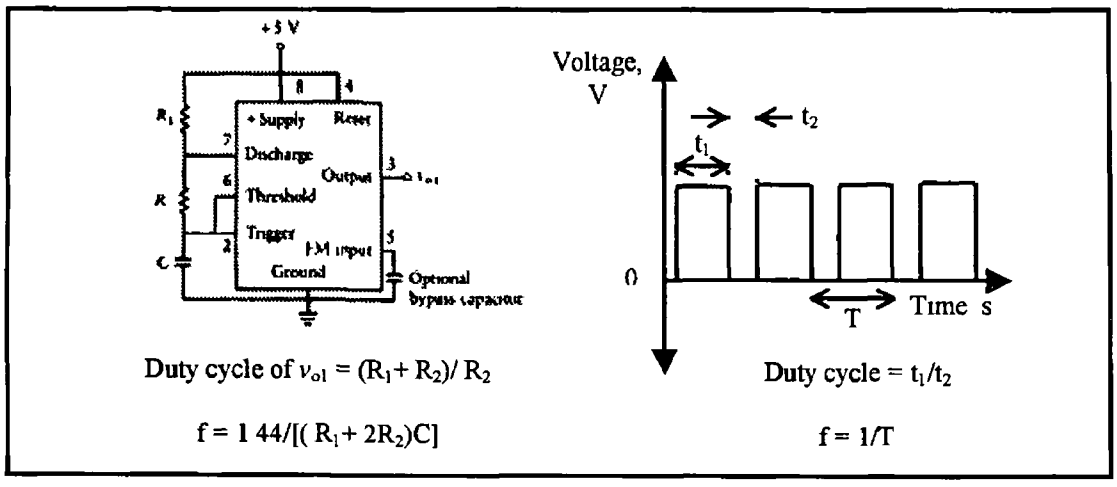

Figure 5 17 (a) 555 timer as a pulse generator [106] (b) output waveform

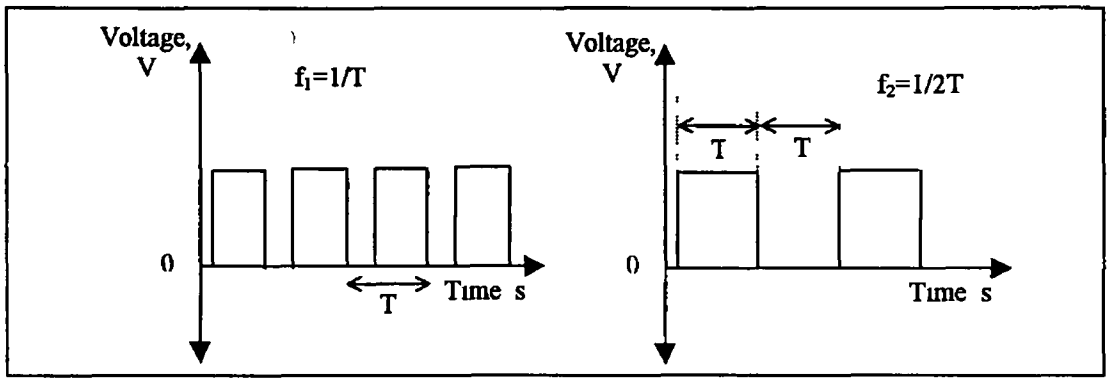

Figure 5 18 (a) Signal from 555 timer, (b) signal from flip-flop

The flip-flop, CD4013, in the configuration shown in Appendix B1 serves to convert the signal from the 555 timer to a signal with an even duty cycle and a halved frequency, as shown in figure 5 18

Op-amp U3A converts the signal from the flip-flop to a square wave between voltage levels of ±12V, while preserving frequency and duty cycle The REF10 integrated circuit provides a precision 10 V reference The potentiometer, P2, is used to set the voltage level of the signal using this precision 10V reference A FET controlled constant current generator drives the LED in a fashion not dissimilar to the transistor-controlled circuit in figure 5 15 Resistor R11 sets the maximum current that can be driven through the LED If 2V is the maximum voltage across the resistor of 20 Ω, the diode current is 100 mA using Ohm's Law The potentiometer can adjust this downwards In practice, the power dissipated by a current of 100 mA in one 20 Ω resistor is 2mW ($P=I^2R$) Thus, a series of resistors in parallel or in series with a resultant value of 20 Ω should be used The resistor R10 is a safety feature preventing damage to the LED in the case of a short circuit

Laser diodes should not be modulated by this circuit problems due to thermal variations in threshold current necessitate circuits where feedback photodiode controls the drive current Sell [110] details a circuit where feedback controls a prebias current - prebias current follows laser threshold current Total laser drive current is set by this prebias current and a modulation current In the surface defect sensor system, a simple single resistor driving circuit was used to drive a laser diode, figure 5 14 The system accommodated any thermal variations in power output

5 3 2 Signal Sensing Circuits

Signal sensing involves preamplification of the signal from the photodetector This section details the design of the photodiode preamplifiers Photodiode response can be estimated through measuring voltage across the photodiode, a photovoltaic detector, or through measuring current through the photodiode, photoconductive detector As stated above photoconductive measurement responds linearly as is required

Photoconductive detection needs a preamplifier that converts the photocurrent to a voltage The simplest configuration, shown in figure 5 19 (a), is a circuit consisting of a resistor and a photodiode Photocurrent is related to voltage output by the relation

$$V_{OUT}=I_{PH}R \qquad 5\ 2$$

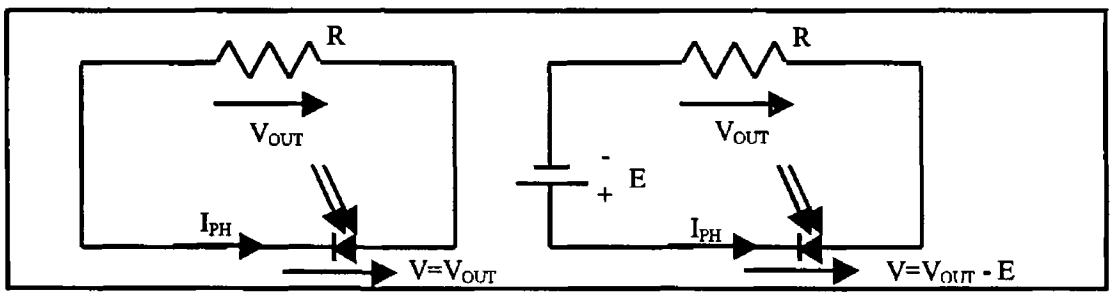

Figure 5 19 Voltage across a resistive load – (a) unbiased and (b) reverse biased circuit [2]

The resistive load line, shown in figure 5 20, is the line along which photodiode characteristics vary for each circuit described An unbiased resistive load results in an amplifier whose range is limited by the inherent diode effect that limits amplification to around 0 6 V for a silicon photodiode The value of the load resistor is limited by the internal shunt resistance of the photodiode [111] further limiting amplification This circuit also has the disadvantage of limited speed and linearity Applying a reverse bias, figure 5 19 (b), improves the range of the circuit, and also linearity and speed but at the expense of increasing noise due to the effect of dark current

An unbiased transimpedance amplifier, figure 5 19 (a), uses a high-gain operational amplifier to effectively short circuit the photodiode, the high gain and feedback of the

amplifier force both positive and negative terminals to the same voltage Thus, the voltage across the photodiode is clamped to 0 V, as shown in figure 5 20 All of the photocurrent flows through the load resistor giving the following output voltage

$$V_{OUT}=-I_{PH}R \qquad 5\ 3$$

The value of the load resistor, R, is unlimited by the diode characteristics increasing output voltage Clamping diode voltage to 0 V improves the range and linearity of the amplifier This circuit has no dark current noise

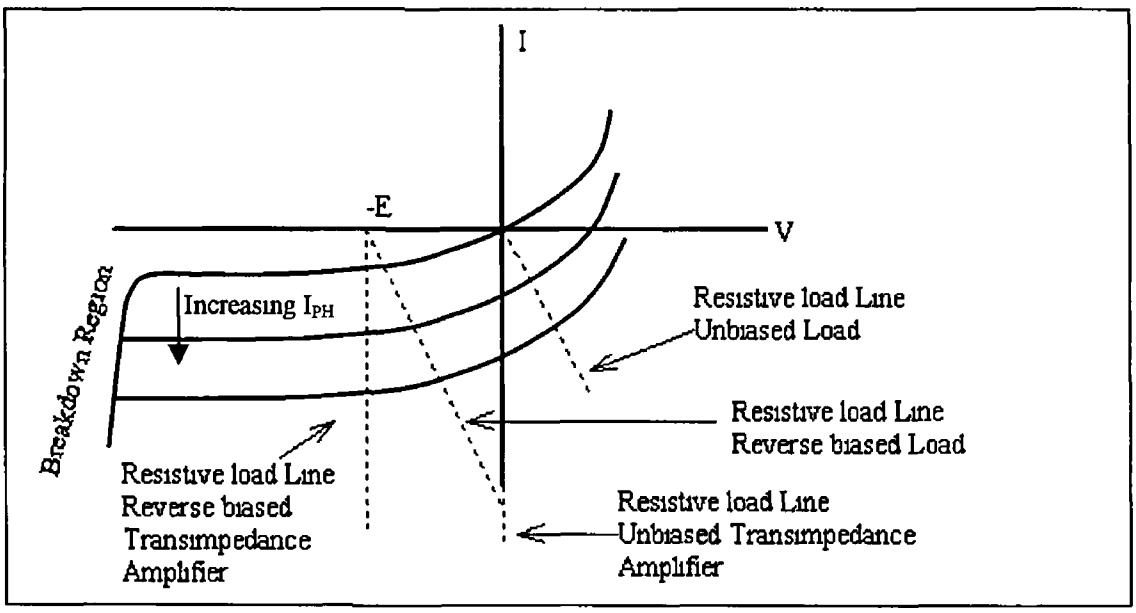

Figure 5 20 Photodiode characteristics showing the resistive load line for various preamplifier circuits [111]

A slight improvement in terms of speed, linearity and voltage output is gained through using a reverse biased transimpedance amplifier Voltage output is also defined by equation 5 2 For our application the advantages of this amplifier are outweighed by the effect of dark current noise

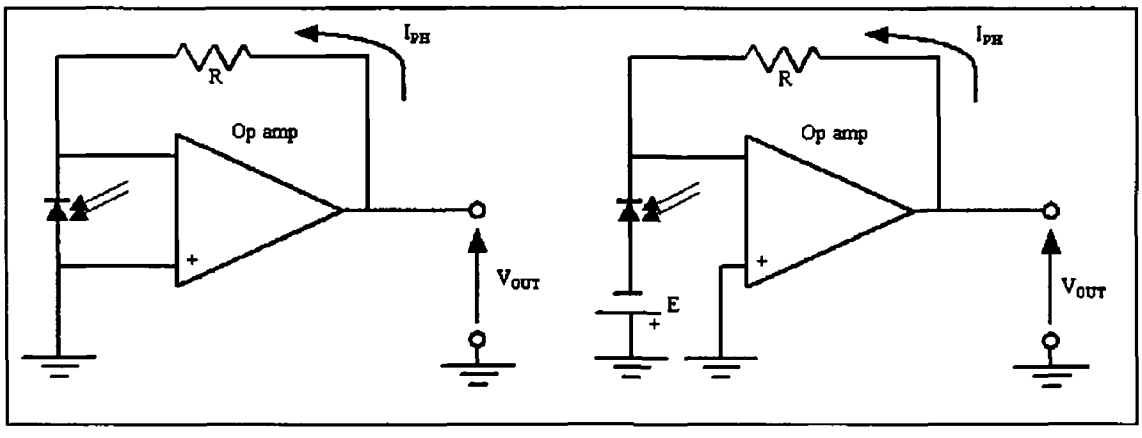

Figure 5 21 Transimpedance amplifier – (a) unbiased and (b) reverse biased circuit [111]

The noise characteristics of the electronics are outlined in the next section The defect sensor system could use a phototransistor or photothyristor as the optical detector and preamplifier like many other photoelectric sensor systems [51,108] For practical reasons, a single detection circuit was constructed for both systems, with only the photodiodes differing between the two systems, appendix B4

5 4 Noise and Error Sources

Noise in the system caused by the following factors

- Light source noise
- Detection circuit noise
- Data Quantisation of DAQ card
- Extraneous noise and error sources

The light source driving circuit, appendix B1, was designed to modulate a light source for subsequent demodulation of the sensed signal using digital signal processing The circuit uses a 10 V precision reference with a temperature sensitivity of 65 ppm/°C The thermal sensitivity of the resistor that determines the diode current, R10, and the potentiometer, P2, have the greatest effect on the light intensity These had

temperature sensitivity of −150 to 800 ppm/°C and ±100 ppm/°C respectively This results in a temperature sensitivity of around 1000 ppm/°C or 0 1%/°C

In addition, the LED light source is sensitive to thermal variations as seen in figure 5 4 A HFE4050 high-power fibre-optic LED, appendix C1, claims a temperature sensitivity of 0 01dB/°C or 0 23%/°C Thus resulting in a total of 0 33%/°C

Detection noise sources result from photodiode noise and amplifier noise Photodiode noise is due to shot noise, Johnson noise and flicker noise [109,110] The input bias current of the op amp [112] and Johnson noise in the load resistor cause amplifier noise, for an unbiased transimpedance amplifier

Shot noise is proportional to the photodiode current, including the dark current Shot noise can be minimised by minimising the dark current, i e using an unbiased transimpedance amplifier

Johnson noise occurs in resistors and is proportional to the square root of absolute temperature divided by the resistance Thus, Johnson noise increases with temperature and decreases with increasing photodiode shunt resistance

Flicker noise is not particularly well understood It is the phenomenon where signals sensed at low frequencies intrinsically have higher noise levels than similar signals sensed at higher frequencies, it varies in inverse proportion to modulation frequency This is significant for a DC signal but insignificant at frequencies above 100 Hz Using digital signal processing to low pass filter a modulated signal removes the effect of low frequency flicker noise

The op-amp used in the transimpedance amplifier, OP37GP, was chosen for its low input bias current and consequent low input bias current noise and its high speed, high slew rate, high gain and low drift The load resistor was made as high as possible, 10 MΩ to minimise Johnson noise and to give a large stand-off distance, due to high gain (equation 5 3) The data acquisition card records voltage levels to 12-bit precision, this quantises data with a precision of 2 44 mV over a range of 10 V Gain is available to reduce this precision further but at the expense of lower range

Extraneous noise and error are contributed by the following

- Electromagnetic Interference (50 Hz Noise)
- Translation Stage Error
- Ambient Vibration
- Thermal Expansion
- Ambient Light

Electromagnetic interference is caused because the photodiode and preamplifier are not encased in a shielded box prior to data acquisition The effects of this interference predominate at 50 Hz, mains frequency Thus, digital signal processing can filter out most of the effect of electromagnetic interference

Translation stage error, ambient vibration, and thermal expansion cause error when the sensor is oriented such that it is sensitive to displacement This will occur while measuring the displacement characteristic curve

Translation stage error can be divided into manual micrometer error, backlash, and run-out error [113] Micrometer resolution is 10 μm, the error in attaining this displacement is dependent on the micrometer operator Backlash is defined as non-responsiveness on reversal of input, when the direction of rotation of the micrometer screw is changed, the stage does not start moving immediately Run-out is off-axis motion of the stage, it is dependent on the loading of the stage Operator micrometer error is presumed to be the dominant error Ambient vibration and thermal expansion cause error when there is high sensitivity to displacement, at these points it is also assumed that operator micrometer error is the dominant displacement error

Ambient light is a possible contributor to error, but is not coupled into a single fibre very efficiently Furthermore, digital signal processing further reduces any possible error

5 5 Optical Fibres, Fibre Connectors, and Fibre Tools

Fibre properties were outlined in chapter 2 The practical aspects of choosing fibres are outlined here Multimode graded-index fibre-optic pigtails, designed for telecommunications technology, are available commercially at following core to cladding ratios 50/125 μm, 65/125 μm, and, 100/140 μm They are designed to interface with fibre-optic devices using standard fibre-optic connectors, ST and FC connectors are shown in appendix A9 and A10 ST connectors use a quick release bayonet coupling, which requires a quarter turn to engage or disengage Built-in keying provides repeatable performance since the connector will always mate with a coupling bushing in the same way FC connectors connect to the module and are tightened in place by a thread Appendices A10 and A11 show ST and FC connectors

In choosing the size of fibre the important criteria are the following

- coupling intensity from light source
- collecting reflected intensity
- stand-off distance from the surface

Core/Cladding Ratio (μm/μm)	Fibre type	Numerical Aperture	Coupled Power (μW)
8/125	Step Index	----	0 8
50/125	Graded Index	0 20	33
62 5/125	Graded Index	0 28	72
100/140	Graded Index	0 29	191

Table 5 2 Typical coupled power (μw) from a Honeywell HFE4050-014 LED, Appendix C1, into a variety of optical fibres, for a drive current of 100 mA

Coupling light intensity to a fibre from a laser diode is relatively simple as the laser emits a narrow beam from a small area Coupling from an LED is more troublesome as an LED emits a wider beam from a larger area Connectors provide mechanical security and optical alignment for the fibres Honeywell fibre-optic LED modules have a ball lens, which focuses light from an LED more efficiently into a fibre pigtail

Nevertheless a fibre with a larger core collects optical power more efficiently, table 5 2 shows typical coupled power from a Honeywell HFE4050-014 LED into a variety of optical fibres, for a drive current of 100 mA The advantage with regard to coupled power of a larger core fibre is obvious When coupling reflected radiation from a surface it is also clear that a larger core fibre will couple more power Appendices C1 and C2 include the design of ST and FC modules respectively

Telecommunications fibre is normally surrounded by a buffer of 0 9 mm diameter, with a thin layer of gel between the fibre and buffer A fibre optic pigtail consists of a buffered fibre with an end connector A patchcord is a pigtail that has a further PVC cable jacket, 2 9 mm diameter, for protection Typically, Kevlar® fibres are inserted between the patchcord jacket and buffer for added strength and protection The structure of a fibre-optic patchcord is shown in figure 5 24

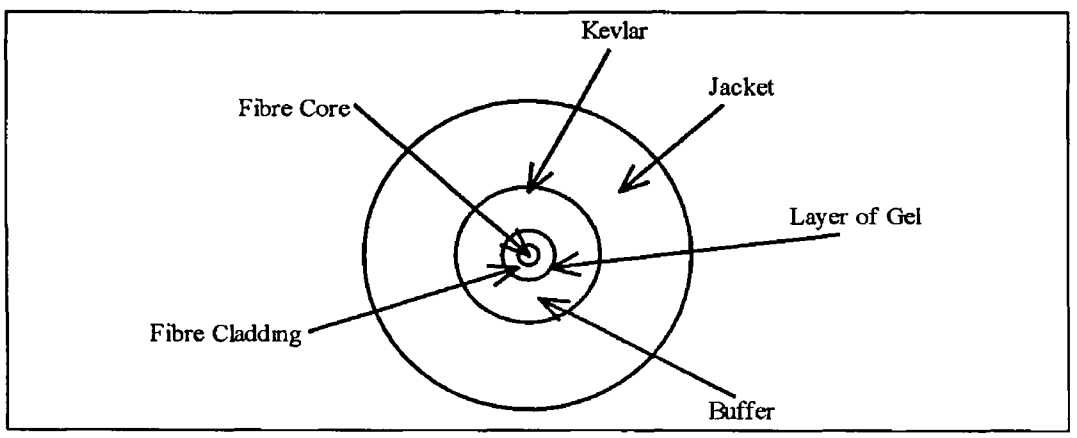

Figure 5 22 The structure of a typical fibre-optic patchcord

Fibre-optic strippers are used to strip the outer jacket and the buffer An optical fibre will not couple or emit light efficiently without fibre endface preparation This is achieved through using a fibre-optic cleaver The manual fibre-optic cleaver used throughout this project is shown in figure 5 23 The buffer is stripped to an appropriate length The fibre is positioned in its guide and the buffer is butted against a stopper The uncleaved end of the fibre is clamped, and then the fibre is scratched by the cleaving edge As little force as possible is used in scratching the fibre and releasing the cleaving edge Meantime, the fibre is still clamped The leaf spring is bent down, causing the scratch on the fibre surface to propagate resulting in cleaved fibre endface

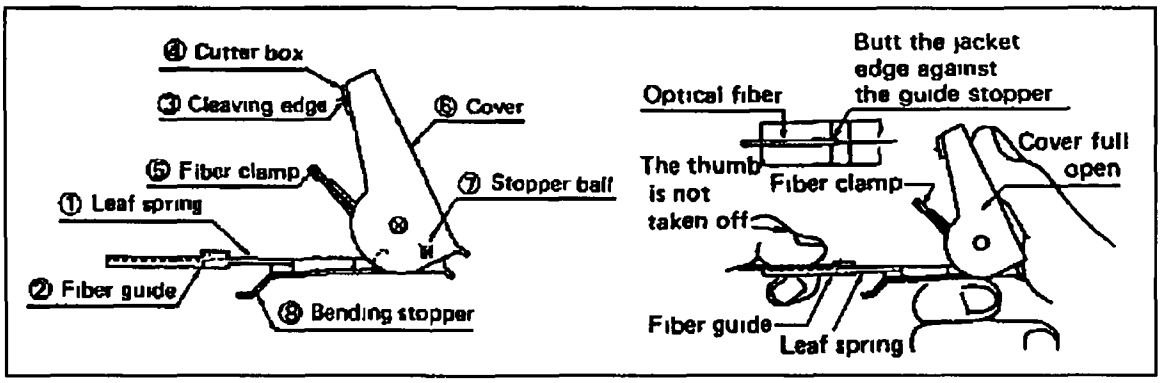

Figure 5 23 (a) Part names of a Fujikura Multimode Fibre-Optic Cleaver, (b) operating method of cleaver [114]

5 6 Mechanical Design

The mechanical design consists of a translation stage, base plate, means for holding optical fibres, boxes for electronic circuitry, and a mode scrambler The designs for these are shown in the appendix A1-9

5 6 1 Translation Stage

The translation stage consists of three micrometer driven stages The stages are Newport precision steel stages – UMR8 25 [113] They have 25 mm/1" travel length and use Newport micrometers - BM11 25 [113] These micrometers have sensitivity of 1 μm and the vernier divisions are of the order of 10 μm The X and Y stages are mounted one on top of the other, oriented perpendicularly, and the Z stage is mounted vertically by means of a 90° The bottom stage is mounted on an aluminium base plate

5 6 2 Fixturing

Fixturing is required to position the fibres, appendix A2 and A3 The fibres are held using Newport fibre holder, FPH-S, designed to hold bare fibres of outside diameter between 80-200 μm The fixturing is designed to hold the fibre holders at incident angles of 60° or 45° to normal Each fibre holder fits tightly to the fixturing plates and is held in place by a plastic screw The fibre holder is designed to hold a single fibre,

but was used in practice to accommodate up to three fibres. To achieve this a fibre clamp was designed to hold the plastic buffer of three fibres and relieve strain in the same manner as the Newport FPH-SR strain relief [113]. Disadvantage of this system was that the fibres were manually adjusted to be at the same displacement and the fibres were not in a straight line, they approximated the configuration shown in figure 5.24. Figure 5.25 shows a photograph of the optical fibres protruding from the end of the fibre holder. The fixturing plates were manufactured from aluminium sheet. One plate is attached to the Z-stage and the other is attached to this first plate.

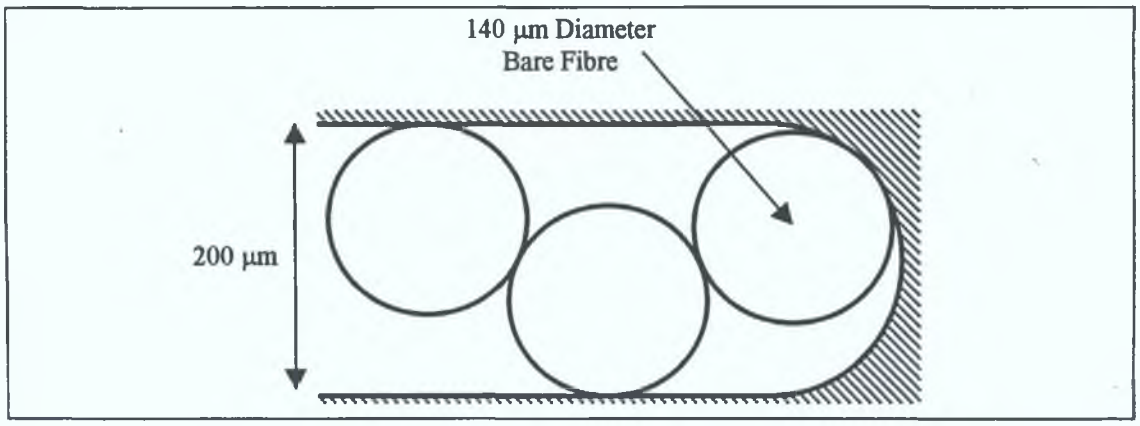

Figure 5.24 Orientation of multiple fibres in fibre holder.

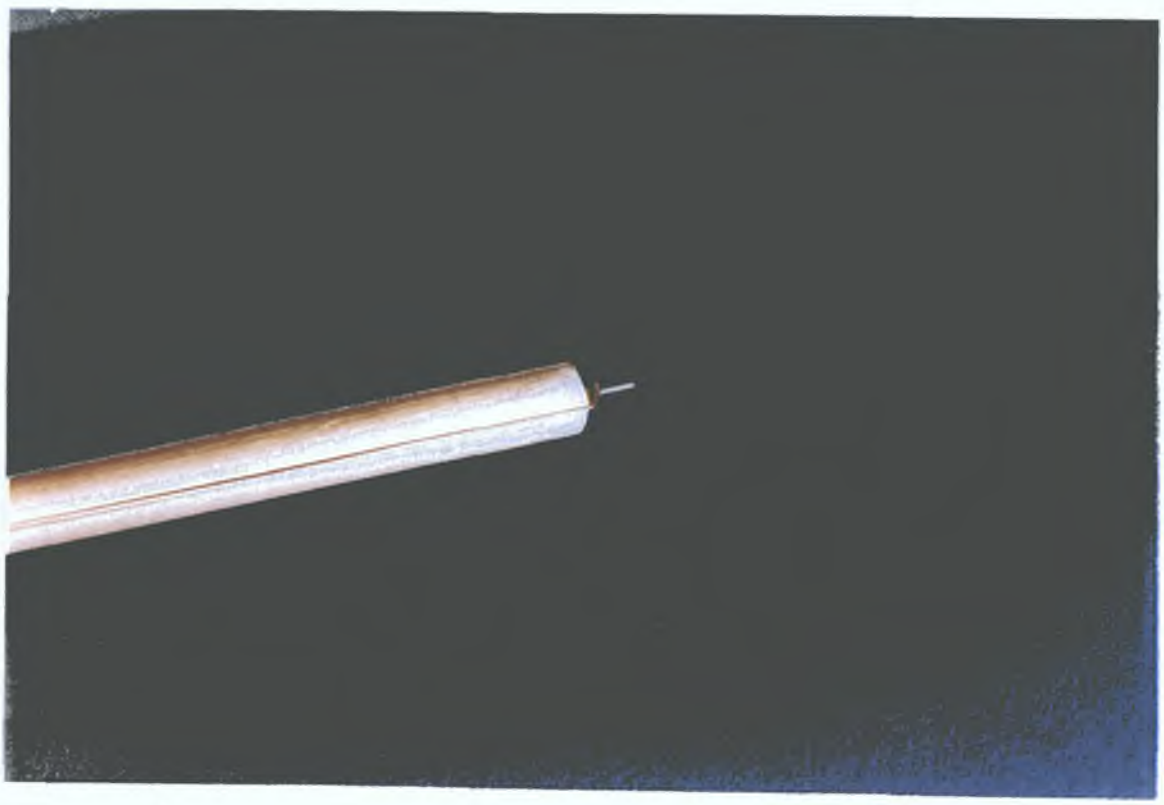

Figure 5.25 Photograph of fibres protruding from end of fibre holder

5 6 3 Mode Scrambler

A mode scrambler is used to achieve an equilibrium mode distribution in an optical fibre When light is launched into a fibre, certain modes are filled more fully than others, e g when a laser fills a fibre the higher order modes are overfilled Uneven mode distribution results in modal attenuation and an uneven distribution in the light intensity profile of emitted light

Mode scramblers have a number of configurations, the optimum configuration is a significant length (kilometres) of fibre [5] Mode scramblers can be constructed by causing the fibre to undergo bending in order to distribute power more evenly among the modes [115-118] Tokuda et al [118] describe a mode scrambler that formed the basis of the mode scrambler shown in appendix A9 Appendix A9 shows the holes that were drilled into which 9 mm dowels were glued Fibres were wound around these dowels in serpentine bends causing mode scrambling

The designed mode scrambler consists of 5 pins of 6 mm diameter assembled at a pitch of 12 mm on top of the lid of the signal generation box In this way, the mode scrambler operates just after the optical radiation is coupled into the fibre This mode scrambler was used with surface roughness sensor alone to distribute power among the modes more evenly

5 6 4 Circuit boxes

Appendices A4 and A5 show boxes for holding the signal generation circuit and holding the signal detection circuit The signal generation circuit box includes means for positioning a PCB circuit The box's lid includes a mode scrambler, appendix A9

A breadboard circuit was attached to the bottom of the signal detection circuit box by means of adhesive pads The lid of this box, appendix A6, includes mounting holes, which allow attachment to the translation stage Attaching to the stage means that fibres are unaffected while the stage moves, problems with this remain for the fibre conveying the input signal Both boxes include means for holding the relevant fibre-optic modules and connectors for power supply inputs

CHAPTER SIX

6 Data Acquisition and Data Analysis Algorithms

This chapter details the procedure and algorithms that were implemented for data acquisition and data analysis It also the use of LabView software for these purposes

A National Instruments AT-MIO-16E-10 data acquisition card [119] was used for analog to digital conversion It has 12-bit resolution and a maximum sampling speed of 100,000 samples/second Data analysis was performed using Labview software [120] This software interfaces with the data acquisition card and provides a graphical user interface to control data acquisition and to perform data analysis All data analysis and presentation was performed using Labview Labview provides a graphical programming language called, G, to create programs in block diagram form Labview has extensive libraries of functions for data acquisition and analysis A Labview program is called a 'virtual instrument' and it controls data acquisition and can present results A virtual instrument consists of user interface that displays the outputs of the data analysis and provides control objects, such as switches and variables, which interface with the underlying program In this way the user can interact with the virtual instrument while data is being acquired

6 1 Surface Roughness Sensor

Data analysis for the surface roughness sensor is based on a carrier frequency system, the light source is modulated at a particular frequency Analog lock-in amplifiers use a square wave as a lock-in signal [121] to achieve noise rejection, some of the optical systems reviewed use lock-in amplifiers [24,73,93] Analog lock-in amplifiers can be quite expensive, though there are inexpensive designs [122,123] Use of a carrier frequency system to reject ambient light improves the performance of a photoelectric sensor [52] This system uses digital signal processing to achieve noise rejection

The power spectral density function [58] computes the temporal frequencies of an input signal in the same fashion as spatial frequencies are computed from a surface profile Windowing is used in digital signal processing applications to reduce the

effect of sampling conditions on the signal, the finite sampling record results in a truncated waveform that has different spectral characteristics from the original continuous time signal Windowing minimises the transition edges of the waveform, were leakage of information regarding the spectral characteristics takes place Windowing is used when spectral analysis and finite impulse response filters are to be used and the beginning and end of the recorded waveform may cause digital processing error In effect, windowing allows shorter sampling lengths to be used in DSP

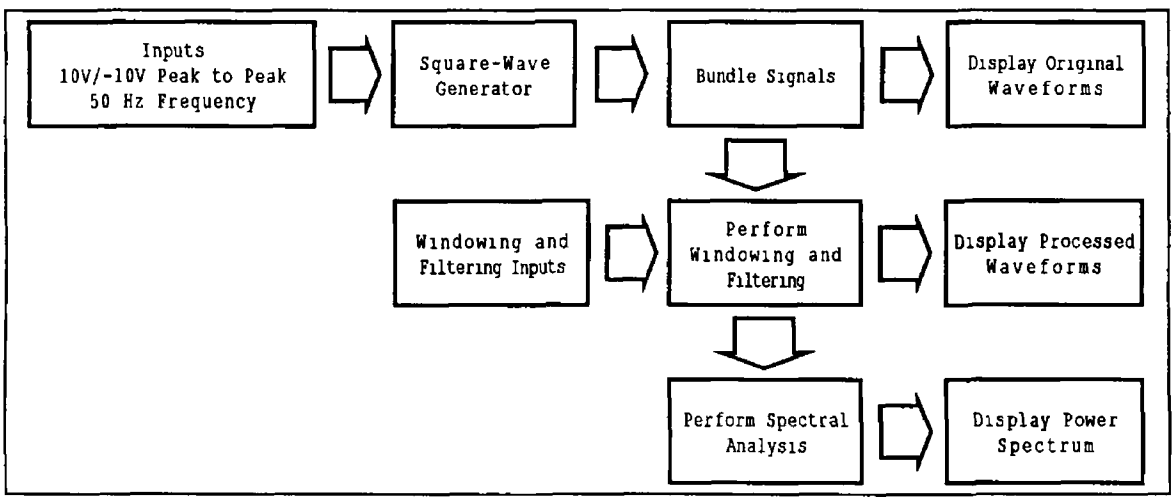

Figure 6 1 Block diagram of program generating graphs illustrating the power spectrum of a square wave and the effect of windowing and filtering

Figure 6 1 shows the block diagram of a program that illustrates a carrier frequency system by spectrally analysing a noise-free square wave signal Figure 6 2 shows the Labview virtual instrument front panel of this program The data analysis libraries that are part of Labview include digital filtering, the power spectral density function and windowing among others [124] The acquired wave, shown in figure 6 2, is the generated noise-free square wave The processed waveform shows said square wave signal after processing using a Hanning window and a Chebshev low pass filter at the filter cut-off indicated in the Power Spectrum Diagram The Power Spectrum of this processed waveform is shown, to consist of a peak frequency at the frequency of the generated square wave and a sequence of harmonics The peak frequency represents a sine wave at 50 Hz and the harmonics are the components that contribute to make up a square wave All spectral analyses are displayed in units of decibels so that noise is shown more clearly Windowing causes the processed waveform to approach zero at

the beginning of the waveform and again at its end Low pass filtering causes high frequency harmonics to be removed from the original signal Thus, the processed wave shows the effect of a damped oscillation

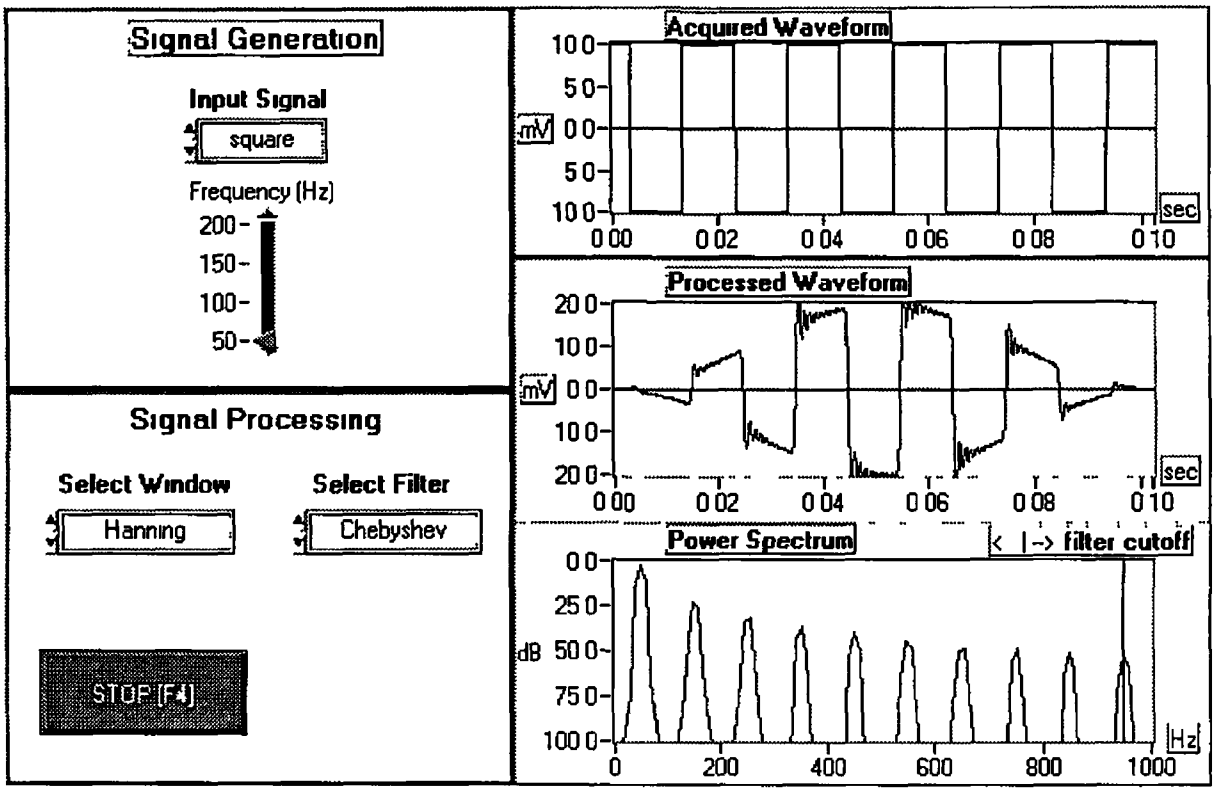

Figure 6 2 Front panel of Labview virtual instrument, shows power spectrum of ideal square wave (after windowing and filtering) at 50 Hz

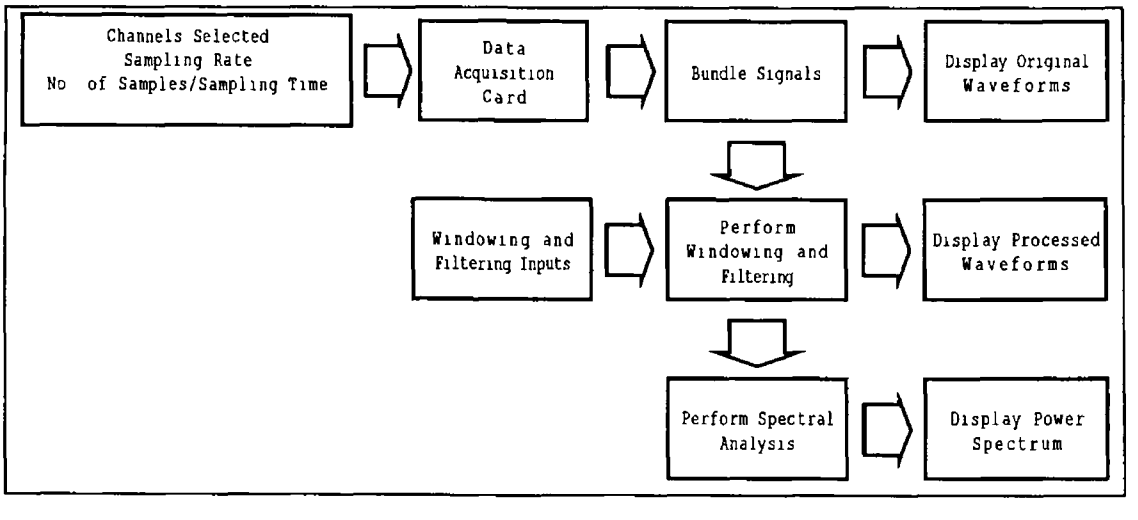

Figure 6 3 Block diagram of program for displaying power spectrum of input signal

Figure 6 3 below shows the algorithm which was used to show the spectral composition of the input signal The frequency of this input signal, a square wave, is set by the 555 timer The sensed voltage is primarily affected by low frequency noise, for this reason, we have chosen a modulation frequency of 930 Hz, well above mains noise and other low frequency noise

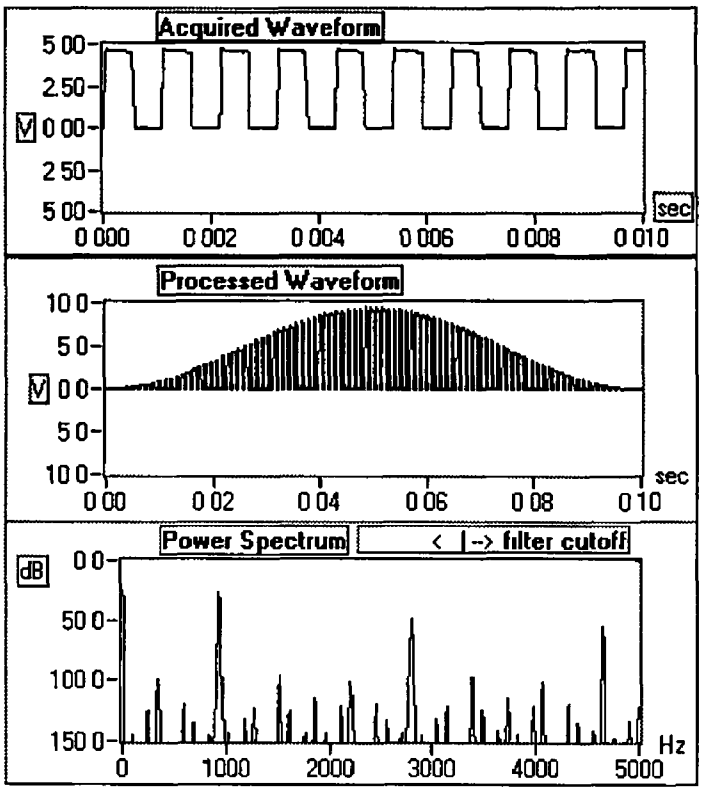

Figure 6 4 Power spectrum of sensed signal with Hanning window, unfiltered

The input signal itself, the processed signal, and a spectral analysis of this incoming signal are shown in figure 6 4 The peak at approximately 930 Hz represents the first harmonic of the square wave frequency The two other large peaks represent harmonics of the signal Figure 6 5 shows the effect of applying a bandpass filter, Chebyshev, between 700 and 1200 Hz This reduces the bandwidth over which measurement is affected by noise The power spectrum shows isolation of the first harmonic of input square wave

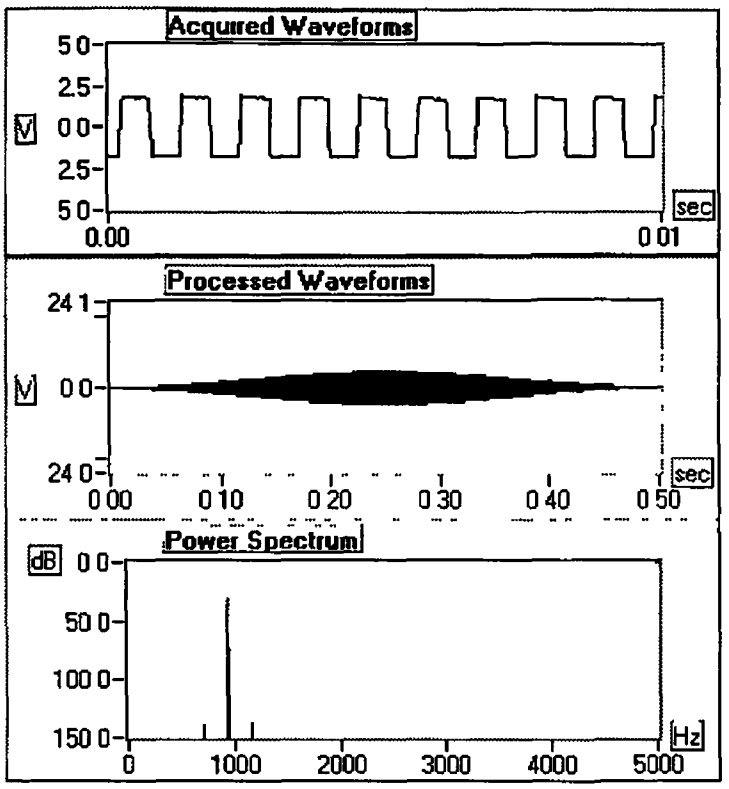

Figure 6 5 Power spectrum of bandpass filtered signal, Chebyshev filter between 700 Hz and 1200 Hz

In order to take readings it was decided to dispense with the use of the power spectral density function and to use a bandpass filter alone to reject noise This was less computationally expensive, i e data analysis could be performed much more quickly and simply An algorithm was developed that applied a bandpass filter and window to the input signal and then averages the resulting waveform It was seen that waveforms with longer sampling times rejected more noise A switch was placed on the virtual instrument that triggered the display of a point on a graph This graph displayed the displacement characteristic of the sensor from a surface A block diagram of this algorithm is shown in figure 6 6 For every movement of the Z-stage by one increment the switch was switched once In addition to adding a point to the displacement characteristic, a file recording the contents of the graph was recorded This file could then be analysed further with regard to optimising measurement of roughness

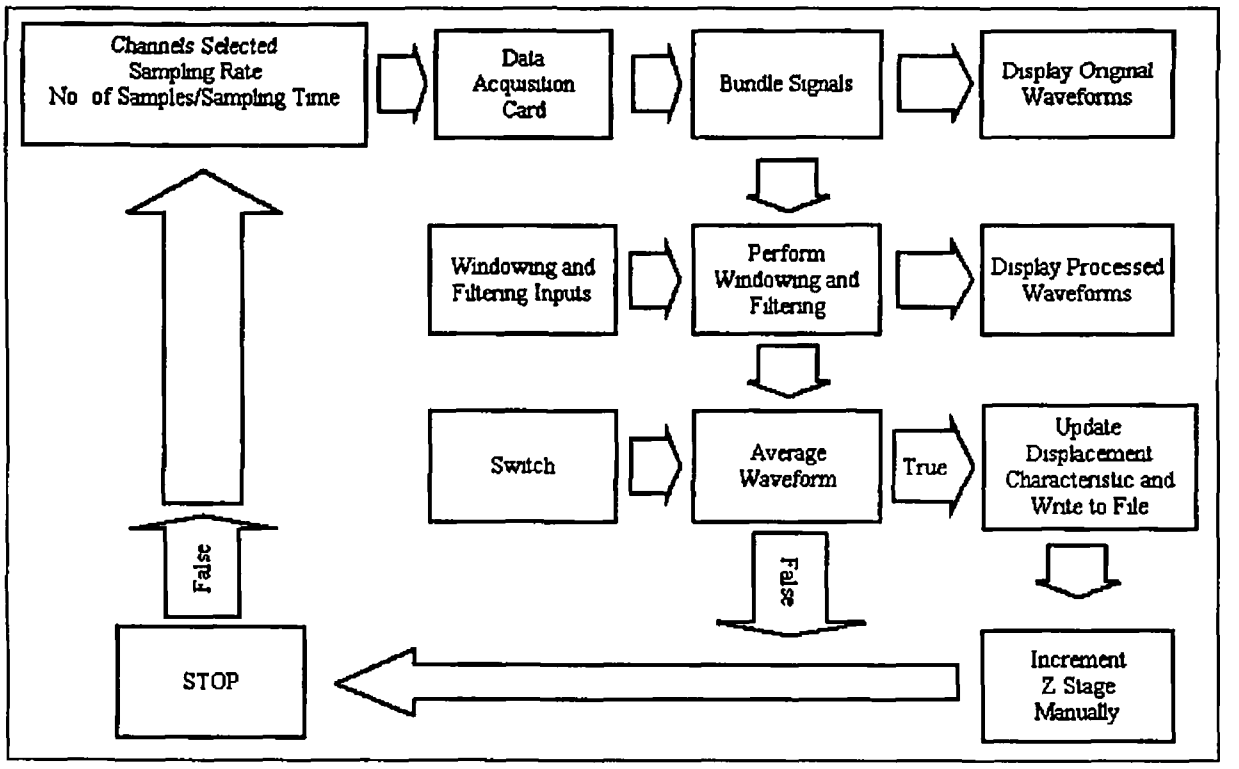

Figure 6 6 Block diagram of program to record displacement characteristic

The virtual instrument, that implemented the program shown in figure 6 6, is shown in figure 6 7 The displacement curve shows a characteristic for each of the three fibres that sensed the reflected signal The switch titled "One Reading" triggered the addition of an increment to the graph The "STOP" button caused the program to stop running, once the data flow reaches the switch The signal processing inputs could be controlled from the virtual instrument panel, but were configured as shown for all readings "Total Sampling Time" is an indicator which shows the sampling time that has been defined in the controlling program "Sampling Rate" is a control that sets the sampling rate of the device The low cut-off frequency can be controlled from the front panel For a bandpass filter, the high cut-off frequency will be 500 Hz greater than the low cut-off frequency

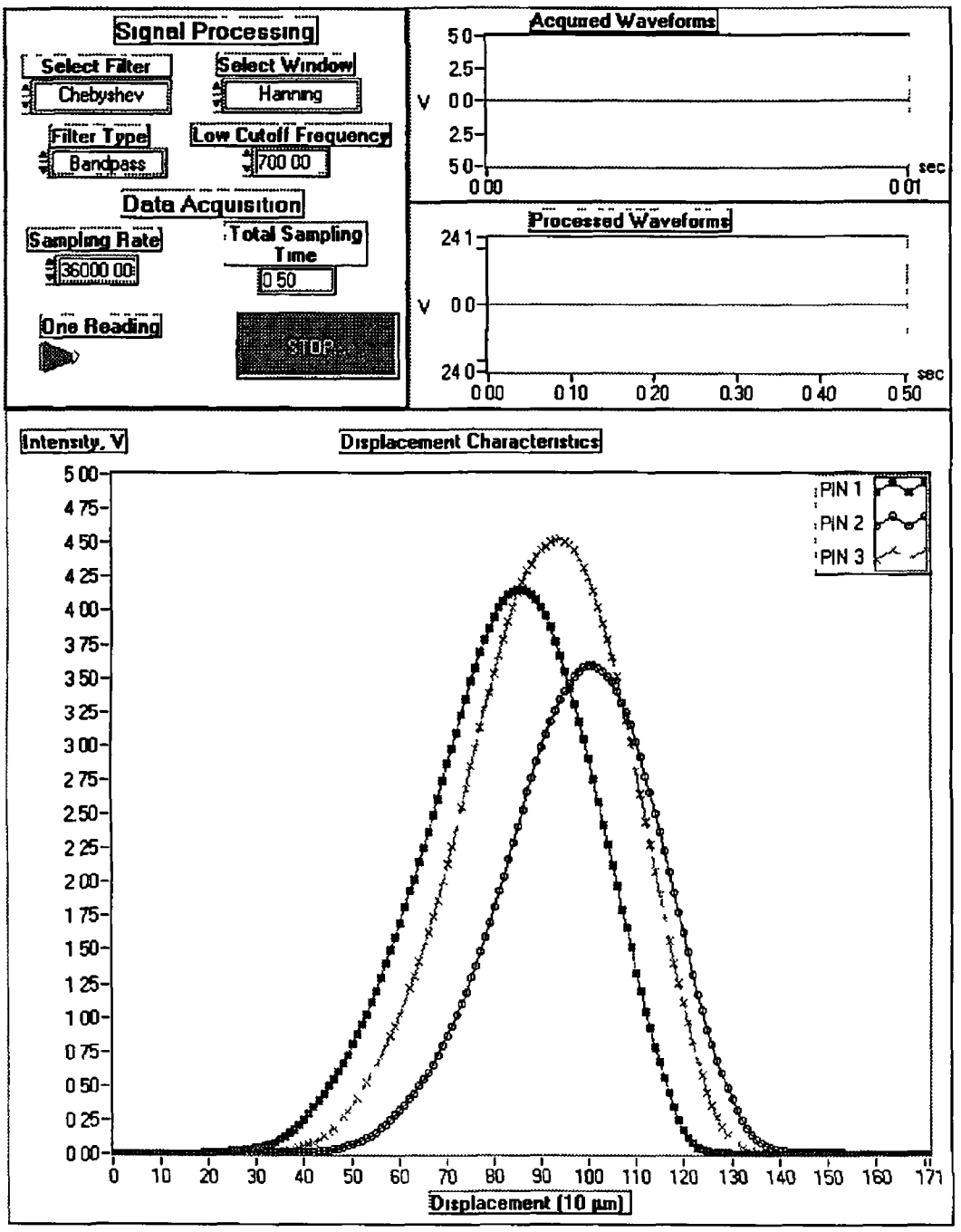

Figure 6 7 Front panel of virtual instrument described by block diagram in figure 6 6

Three displacement characteristic curves can be seen in figure 6 7 These curves correspond to three input signals from three PIN photodiodes, connected to three input fibres held in the fibre holder The orientation of these fibres is discussed in section 5 6 2 These curves show the displacement of the fibres relative to the starting position of the translation stage, rather than to the absolute displacement from the surface from the surface Each curve has a different peak value and a different position, caused by the sensitivity of the sensor to displacement

It was possible to configure the virtual instrument using different filters, Chebyshev or Butterworth, different windows, Hanning or Hamming, and different filter types, band pass, low pass, high pass, etc. The virtual instrument was configured as displayed in figure 6.7 for all measurements with the surface roughness sensor.

6.2 Surface Defect Sensor

The block diagram for data acquisition and analysis system of the surface defect sensor is shown in figure 6.8. This system could be more directly implemented if the cut-off voltage stage was applied as part of the measurement of the lateral displacement characteristics. This voltage cut-off stage was performed separately so that cut-off levels could be varied to ascertain the effect on the output graphs. The block diagram in figure 6.6 was used to measure displacement characteristics, with a low pass filter used this time to in the place of the bandpass filter. The windowing and filtering were superfluous to the operation of the system. A much shorter total sampling time was chosen, 0.01 seconds. This sampling time could be very short if speed was an important criterion in an application. Reference to Z-stage incrementation can be replaced with that of the X-stage for measurement of the lateral displacement characteristics.

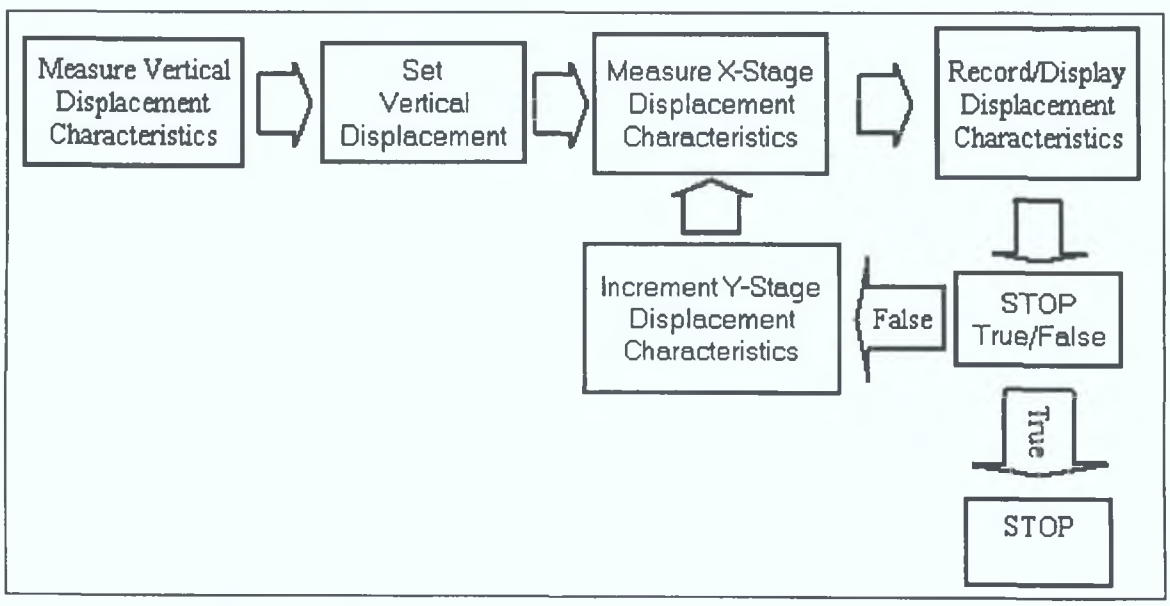

Figure 6.8 Surface defect sensor data acquisition system.

Figure 6 8 shows the flow diagram for taking surface defect readings Initially the vertical (Z-stage) displacement characteristics were measured This records the displacement characteristics and allows the vertical displacement of the sensor to be set The vertical displacement was set at close to the peak of this curve The sensor measured a region of a surface including a hole in this surface Firstly, the X-stage was displaced through a certain number of increments, with measurements being taken at each increment Secondly, the Y-stage is moved through an increment and the X-stage is traversed through the same number of increments in the opposite direction When measurement of all of the area including the hole and in its vicinity was complete, measurement was complete

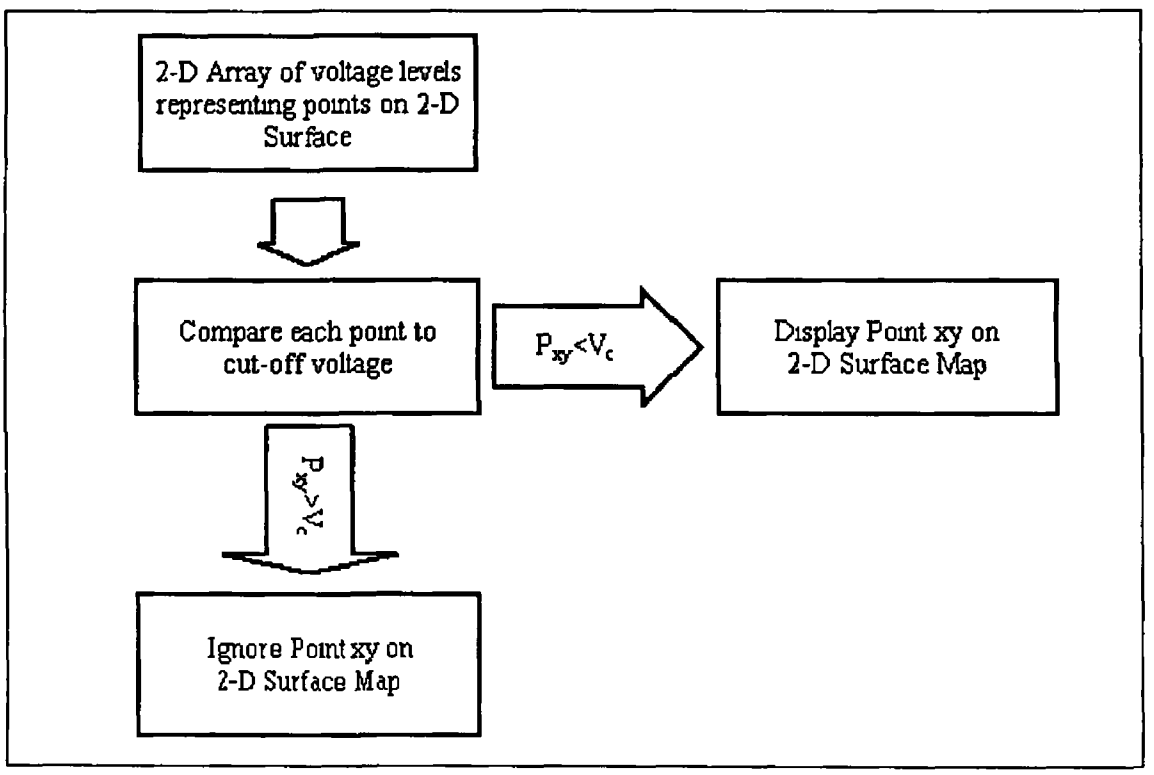

Figure 6 9 Block diagram of program to generate 2-D map of the surface

Figure 6 9 shows the program that generates a surface map, the voltage level at each point (x,y), P_{xy}, is compared to the cut-off voltage, V_c If it is less the point (x,y) is added to the surface map, if it exceeds V_c it is ignored In this way the surface map displays the areas of the surface that are below the cut-off level, points that deviate from the displacement cut-off defined by the cut-off voltage or that reflect light irregularly for some other reason

Figure 6 10 shows a surface map of a brass plate with a hole This map consists of a line on an XY graph connecting the co-ordinates that correspond to voltage measurements above the cut-off voltage The line describes the course along which the measurements were originally recorded This graph could possibly be displayed showing the points alone without showing the line

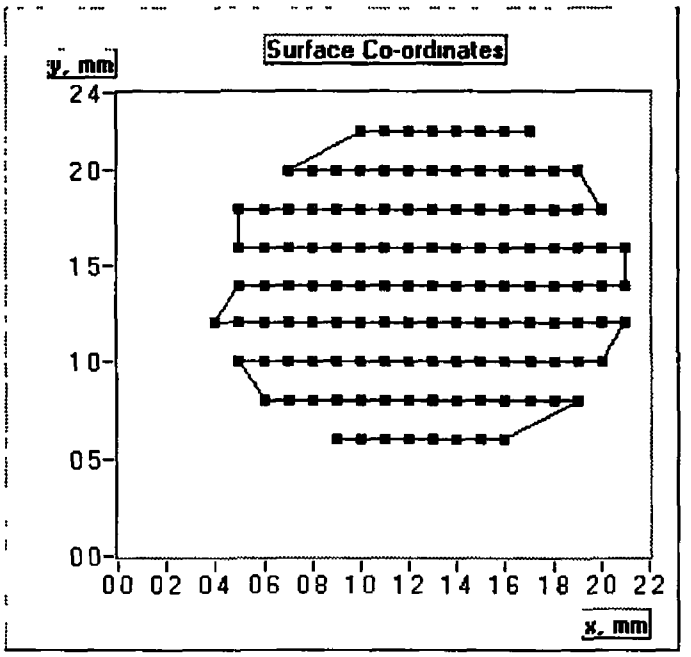

Figure 6 10 Two-dimensional surface map of a hole in a brass plate

CHAPTER SEVEN

7 Experimental Results

This chapter presents the results achieved from the two sensor systems outlined in the preceding chapters and also a preliminary fibre-optic sensor system The experimental rig is shown in figure 7 2

7 1 Preliminary System

A preliminary system was designed as a displacement sensor The mechanical design of this system was identical to the final systems A HFE4050 high power LED with an ST connector, appendix C1, served as a light source, driven by a constant current driving circuit as shown in Appendix B2 A single fibre collected reflected optical radiation and conveyed this to a Honeywell HFE3038/002BBA – a PIN photodiode with an ST connector and integral preamplifier, giving an analog output, appendix C3 This analog output was converted to digital form by a Picolog data logger This sensor used fibres with a core/cladding ratio of 65/125 μm

A displacement curve from this system is shown in figure 7 1 Note the low peak voltage, because preamplification was integral to the photodetector and the data logger possessed no amplification this was the highest output achievable This voltage output was achieved at a very low stand-off distance from the surface Also the signal to noise level of the photodetector/preamplifier was quite high – any external amplification would amplify the signal and noise without discrimination For the above reasons, it was decided to use a carrier frequency system, while also designing preamplification circuits suitable to the sensor system In addition, it was decided to use fibres with larger cores, to allow a greater stand-off distance

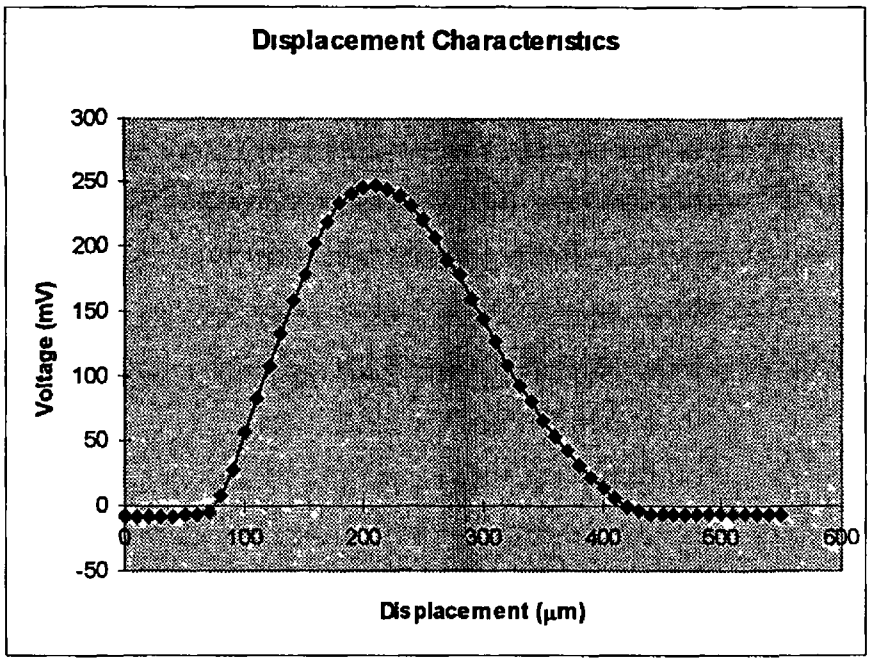

Figure 7 1 Displacement characteristics of preliminary system, for 45° angle of incidence

7 2 Surface Defect Detection System

This sensor system measures the existence of a hole in a plate, i e the size and position of a hole This estimation of the size of a hole may be to discriminate between, for example, a hole drilled with a 2mm or a 3mm drill This system is not designed for high accuracy measurement of displacement, it is designed to operate as a high-speed photoelectric defect sensor

The surface defect sensor operated using a 1300 nm multimode laser diode, Mitsubishi FU-17SLD-F1, appendix C2, driven by the circuit shown in appendix B3 The 1300 nm wavelength for this light source was chosen in order to reduce surface scattering and to maximise the proportion of optical radiation that reflects specularly, as described by equation 3 9 The signal detection circuit consisted of unbiased transimpedance amplifiers using EG&G PIN photodiodes, C30617-BST, this circuit is shown in appendix B4 These InGaAs PIN photodiodes are sensitive to infrared radiation between 900 and 1700 nm Data acquisition and analysis was performed using the algorithm illustrated by figure 6 6 Optical fibres with core to cladding ratios of 100/140 μm were used The optical fibres were oriented at an incident angle of 45°

7 2 1 Surface Samples

This set of experiments examines through and blind holes in plates of the following materials brass, stainless steel, copper, and polycarbonate The design of these plates is shown in appendices A7 and A8 Figure 7 7 shows a picture of these plates Of the holes in these plates, the area surrounding and including smallest blind and the smallest through hole was examined by the sensor Table 7 1 shows the surface roughness characteristics and surface finish of each surface sample These samples, common engineering materials, show the effect of differing surfaces, surface finish and surface roughness on the operation of the sensor

Surface Sample	R_a (μm)	R_q (μm)	R_z (μm)	Surface Finish
Stainless Steel Parallel to lay	0 32	0 48	2 0	Rolled and Polished Surface
Stainless Steel Perpendicular to lay	1 00	1 29	5 0	
Polycarbonate	0 33	0 57	1 4	Moulded Surface
Copper	1 2	1 7	3 0	Rolled Surface
Brass	0 14	0 18	1 2	Rolled Surface

Table 7 1 Surface roughness characteristics of the surface samples - obtained using Mitutoyo Surftest 402 contact stylus

The stainless steel plate had a pronounced directionality or lay, for this reason, the above table shows the effect of measuring roughness characteristics parallel and perpendicular to the lay The edges of the holes are burred The stainless steel blind hole differed from the other blind holes as a portion of the hole of around 1 mm diameter remained unmachined The polycarbonate sample was made of moulded plastic It was white in colour with some dirt discolouring the surface The copper plate had a mottled grainy surface as a result of rolling The surface colour varied It was the roughest of the samples The rolled brass plate had a tarnished surface, with fingerprints visible on the surface The surface roughness reading of the surface suggests that if it was clean that it would be quite reflective

Figure 7 2 shows the dimensions of the smallest through hole on each plate, figure 7 3 shows the dimensions of the smallest blind hole on every plate except the stainless steel plate, while figure 7 4 shows the dimensions of the end-milled blind hole on the stainless steel plate Note the island of 1 mm diameter that is left by the end-milling operation A photograph of the four samples are shown in figure 7 7 Average roughness, RMS roughness, and ten-point height were measured for each sample, using a Mitutoyo Surftest 402 contact stylus, these results are shown in table 7 1

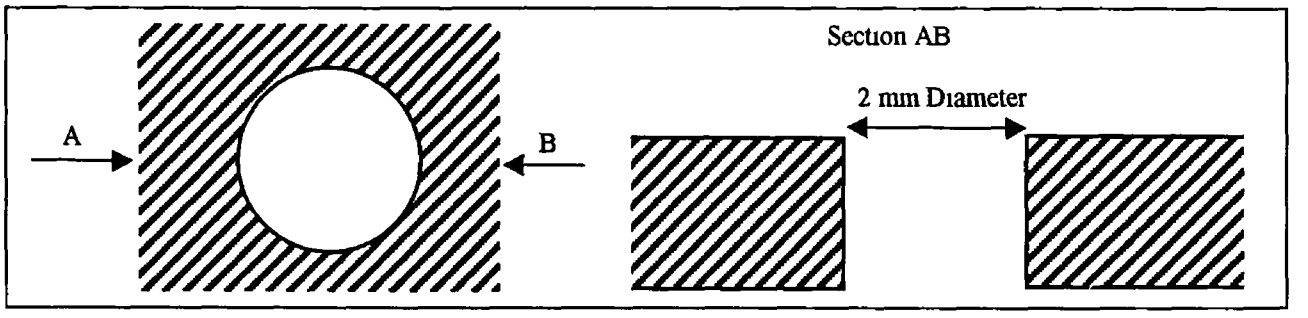

Figure 7 2 Through hole 2 mm diameter

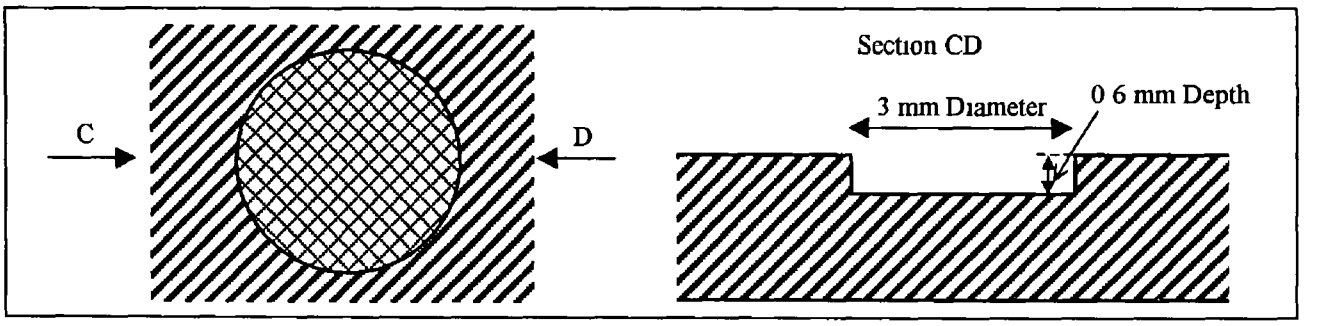

Figure 7 3 Blind Hole 3 mm diameter and 0 6 mm depth

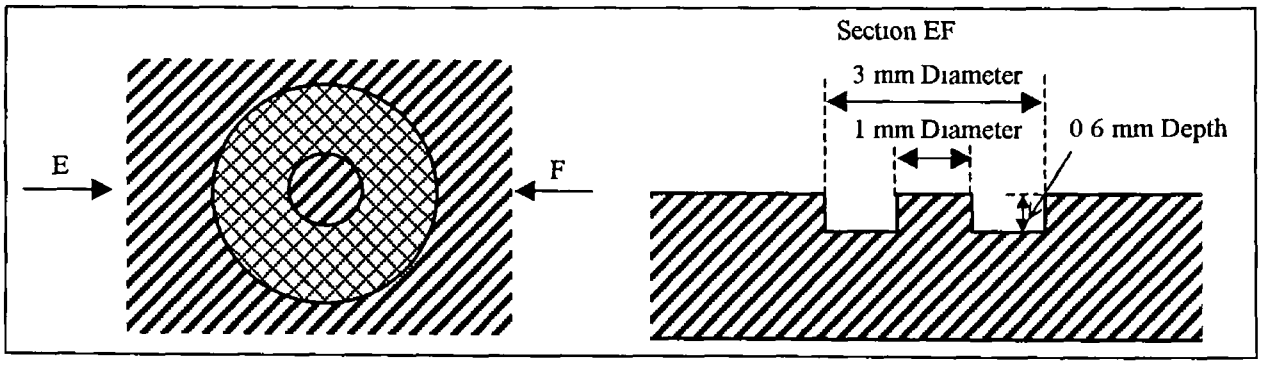

Figure 7 4 End-milled blind hole, 3 mm diameter, in stainless steel plate of 0 6 mm depth with island of 1 mm diameter

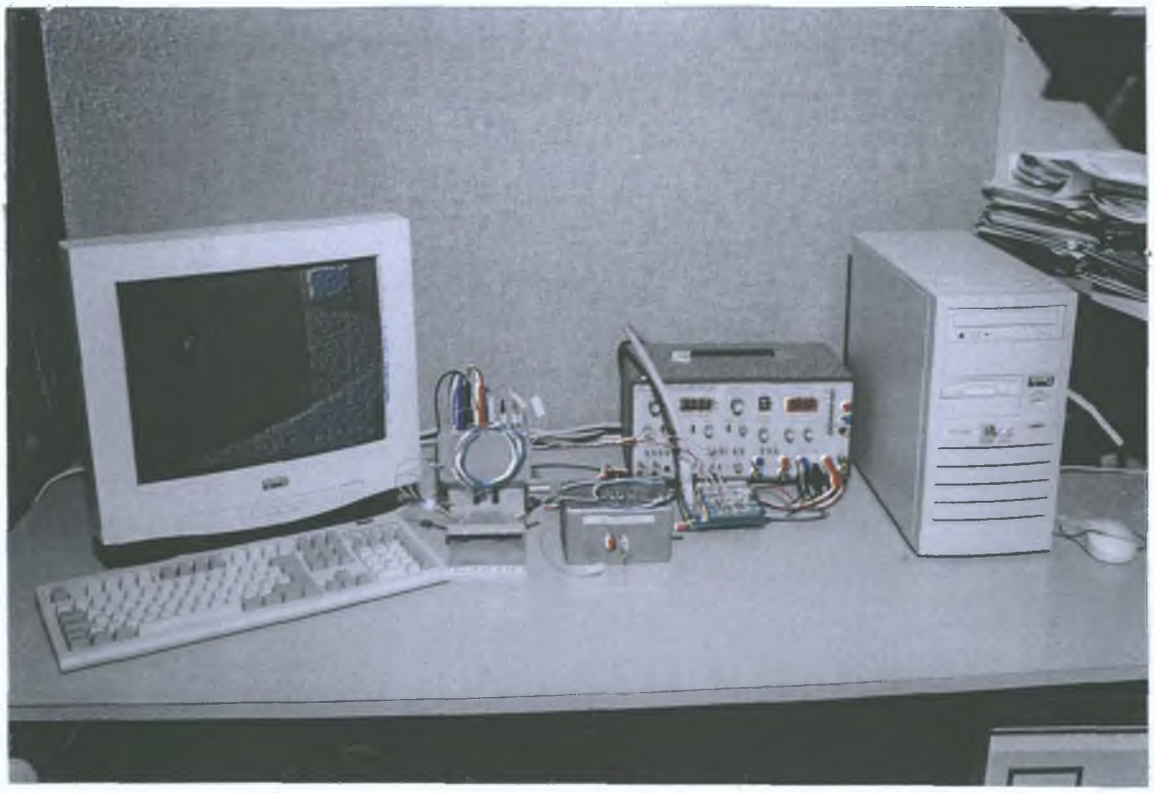

Figure 7.5 Photograph of experimental rig

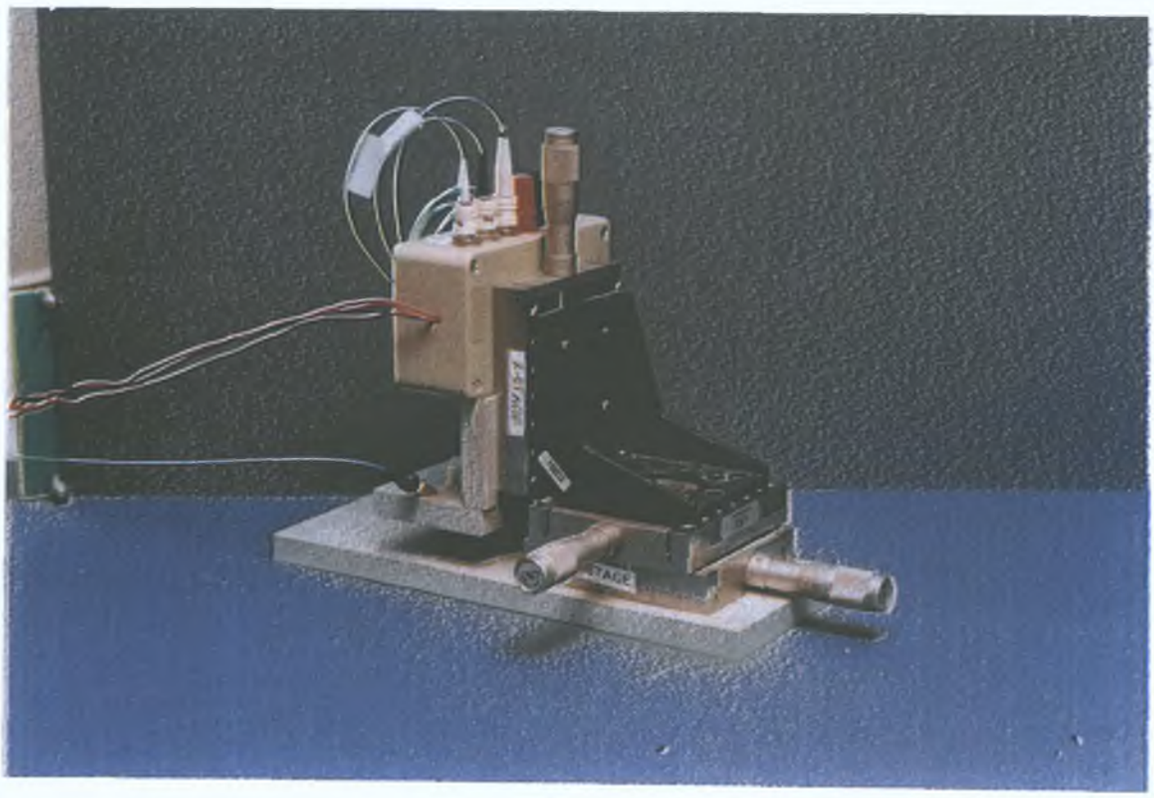

Figure 7.6 Photograph of side view of translation stage

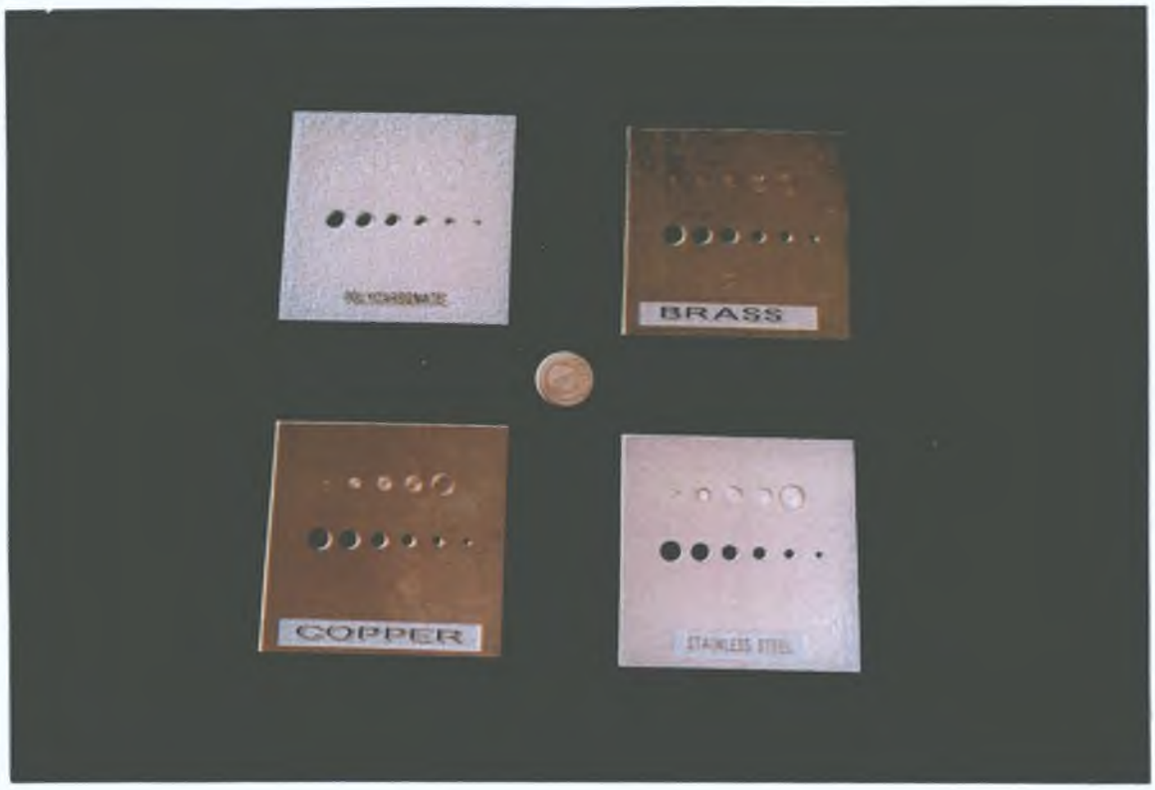

Figure 7.7 Photograph of stainless steel, brass, copper, and polycarbonate plates.

7.2.2 Measurement Procedure

Initially, the relevant sample plate was positioned using adhesive pads. For each surface the procedure noted in figure 6.8 was followed. A surface displacement characteristic was taken of the surface. The vertical displacement of the Z-stage, for the remainder of the measurement, was set close to the peak of the displacement characteristic. The translation stage was arranged so that a surface map containing all of the area of the hole and the contiguous surface area could be recorded. A first lateral displacement characteristic or scan was taken by displacing the X-stage through a certain number of 100 μm increments. After the completion of a scan, the Y-stage is translated through an increment of 200 μm and the X-stage is translated through the same number of increments in the reverse direction. This cycle continues until the area around the hole is mapped. Each reading is compared with a cut-off voltage level, as in figure 6.9, and any point with a voltage level below the cut-off voltage is displayed on the surface map.

7 2 3 Surface Measurement Details

These measurements were taken with one fibre transmitting light from the laser diode and with two fibres collecting reflected light The displacement characteristic, shown in figure 7 8, for the steel sample shows the effect of the different position of the fibres Note also that the voltage does not exceed 10 Volts, the cut-off level of the data acquisition card The preamplification level of the transimpedance amplifier doesn't rise above 12 Volts – the voltage level of the supply rail, so there is no danger of blowing the data acquisition card Taking two readings allowed one fibre to be positioned at the optimum vertical displacement The other fibre is used to gauge the effect of less than ideal positioning, if it also performs adequately, insensitivity to positioning is inferred for the particular set-up

8 sets of readings were taken, one reading for the smallest blind hole and one for the smallest through hole of each plate The block diagram in figure 6 8 shows the procedure that was used in taking a set of readings

7 2 4 Vertical Displacement Characteristics of each Sample Plate

A displacement characteristic for each hole is shown in figures 7 7-7 14 These graphs illustrate the strength of the reflected signal at each vertical displacement from the particular sample plate As can be seen these curves are quite rough, this curve is meant only as a rough estimate and is used to choose a vertical displacement for completing a set of surface scans In operation, if not in construction, this sensor differs considerably from the fibre-optic displacement sensors detailed in the literature survey The sensor is designed to withstand signal voltage variations, rather than to measure these variations accurately It is designed to measure extreme changes in light reflection, in a manner similar to photoelectric sensors

The chosen vertical displacement is illustrated on each of these figures In each case the vertical displacement was chosen so that PIN 2 switches off at a longer displacement from the surface than PIN 1 Thus PIN 1 is more likely to sense the presence of a surface incorrectly and PIN 2 is less likely to sense a blind hole PIN 1 and PIN 2 are labels used to distinguish between the two collecting fibres that are situated side to side

The vertical displacement characteristics can differ between the same plate for different sets of measurements, e g the voltage difference of the peaks of the two polycarbonate displacement characteristics differ by two volts This is because the sensor's principle of operation is based on reflectivity and ordinary engineering surfaces generally reflect irregularly The total level of reflectivity for each surface plate is dependent on the factors listed at the beginning of section 2 5 1, i e a combination of the electrical properties of the surface and the surface roughness characteristics, some of which are listed in table 7 1

A variation in the angle of the surface shifts the peak of the sensor, and seriously affects the operation of the sensor The second PIN photodiode could be used to guard against variations in the angle of the surface The differences in the position of the displacement characteristics for each PIN photodiode reflect the different inclination of each plate relative to the fibre end-faces If the surface were oriented at an angle relative to the stage this would change the stand-off distance of the fibres from the surface over a longer distance than taken in these readings

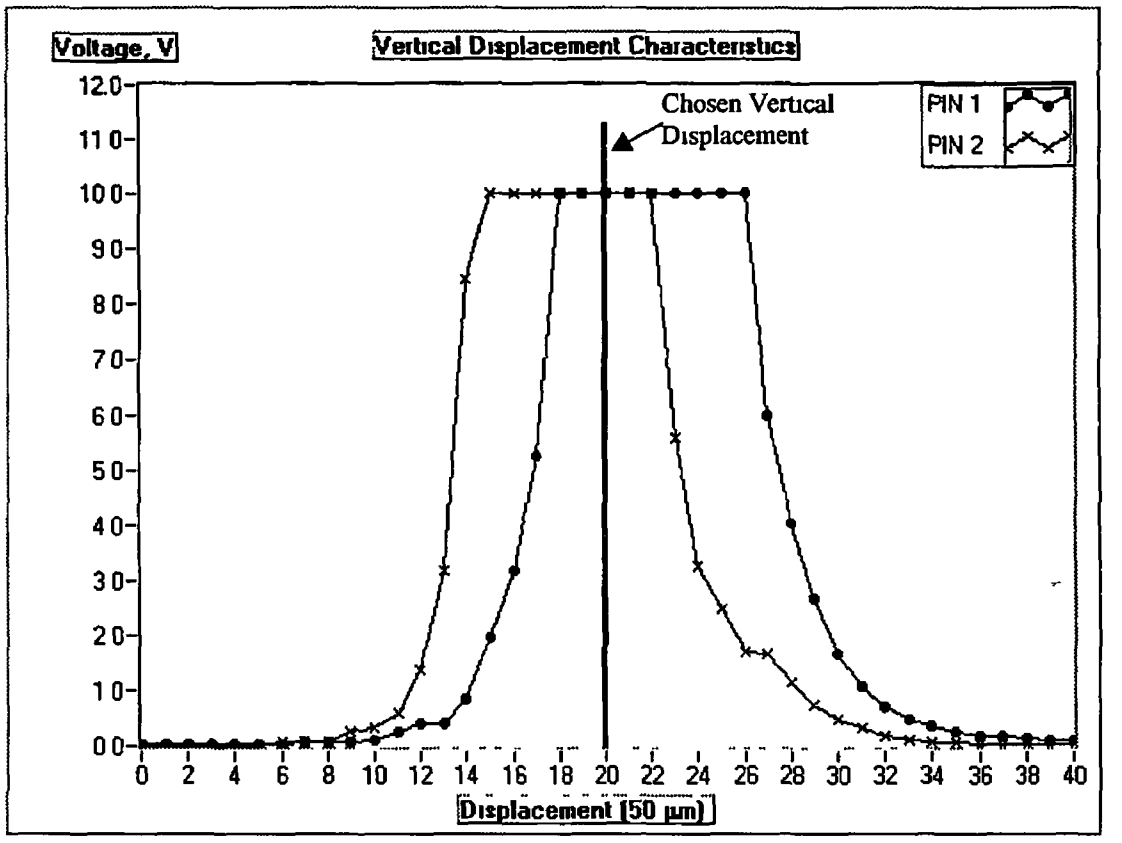

Figure 7 8 Displacement characteristic for stainless steel through hole

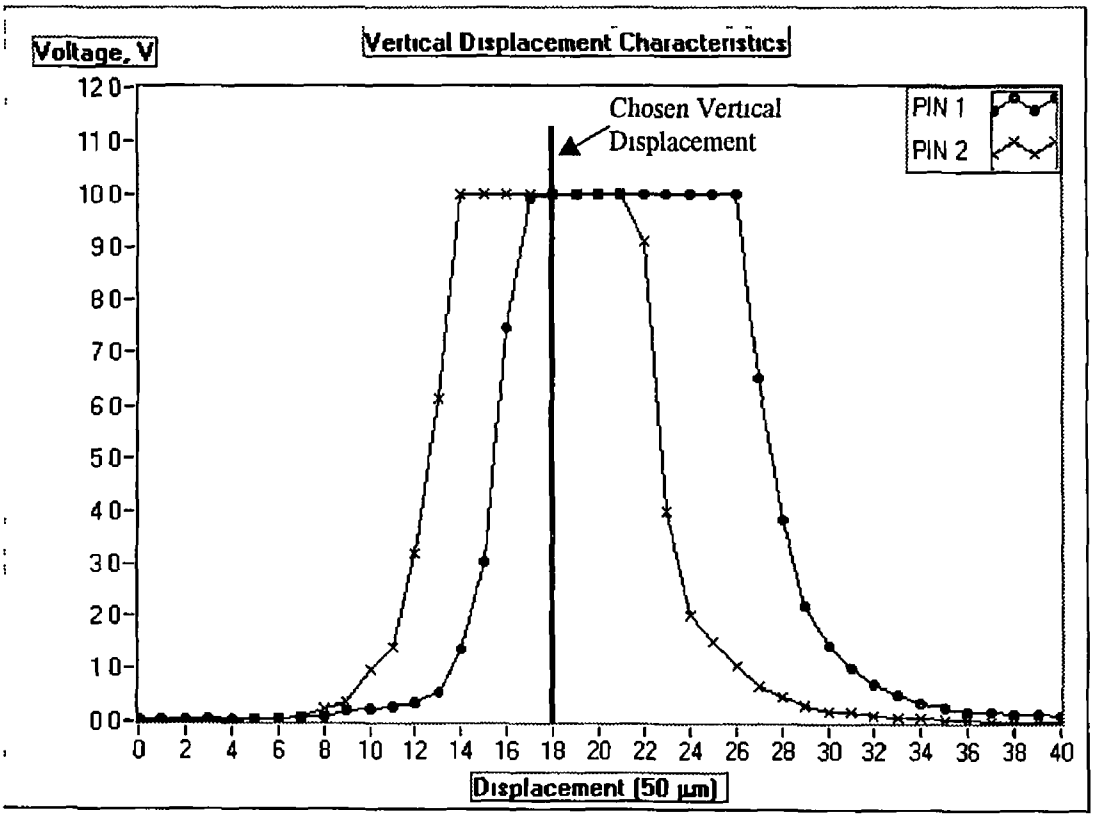

Figure 7 9 Displacement characteristic for stainless steel end-milled blind hole

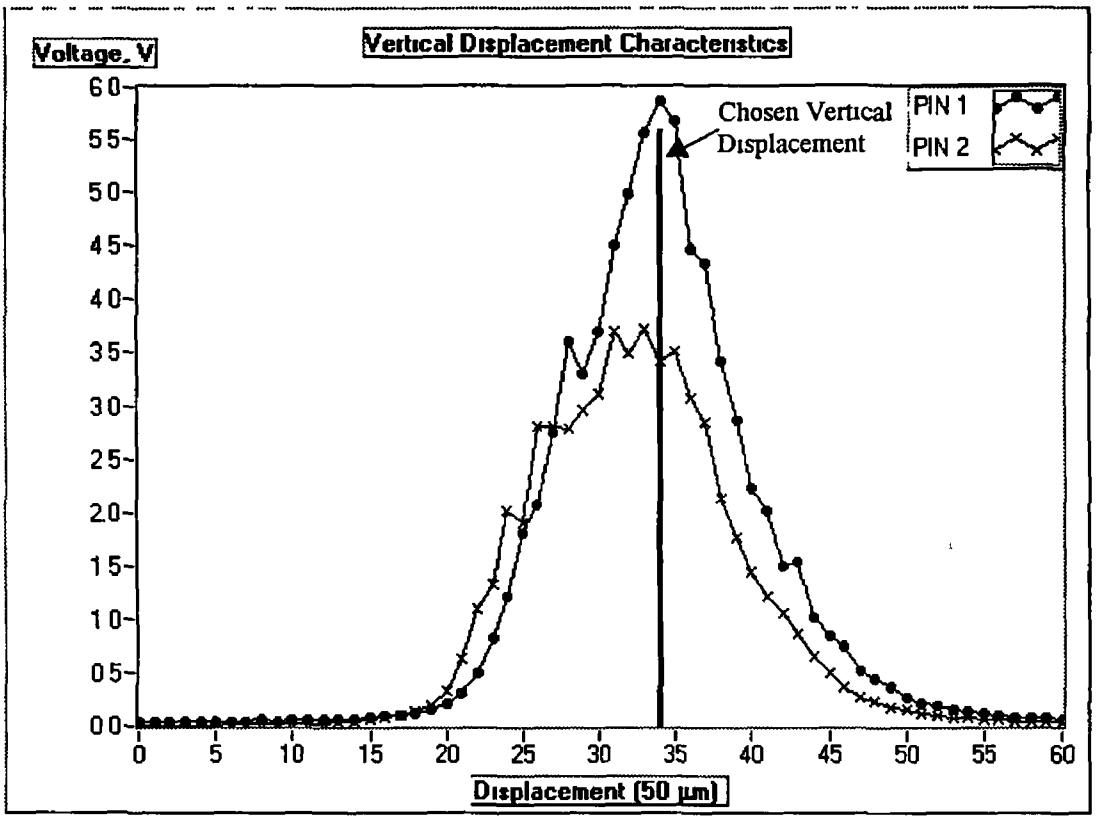

Figure 7 10 Displacement characteristic for polycarbonate through hole

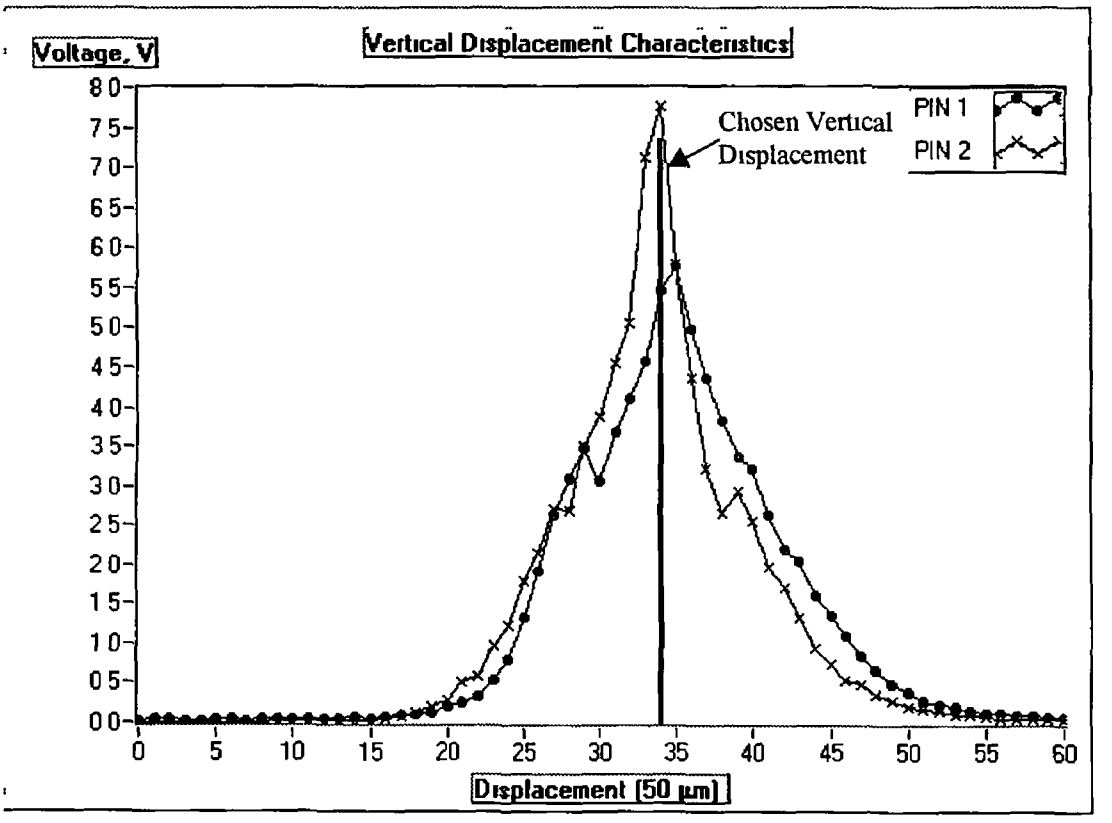

Figure 7 11 Displacement characteristic for polycarbonate blind hole

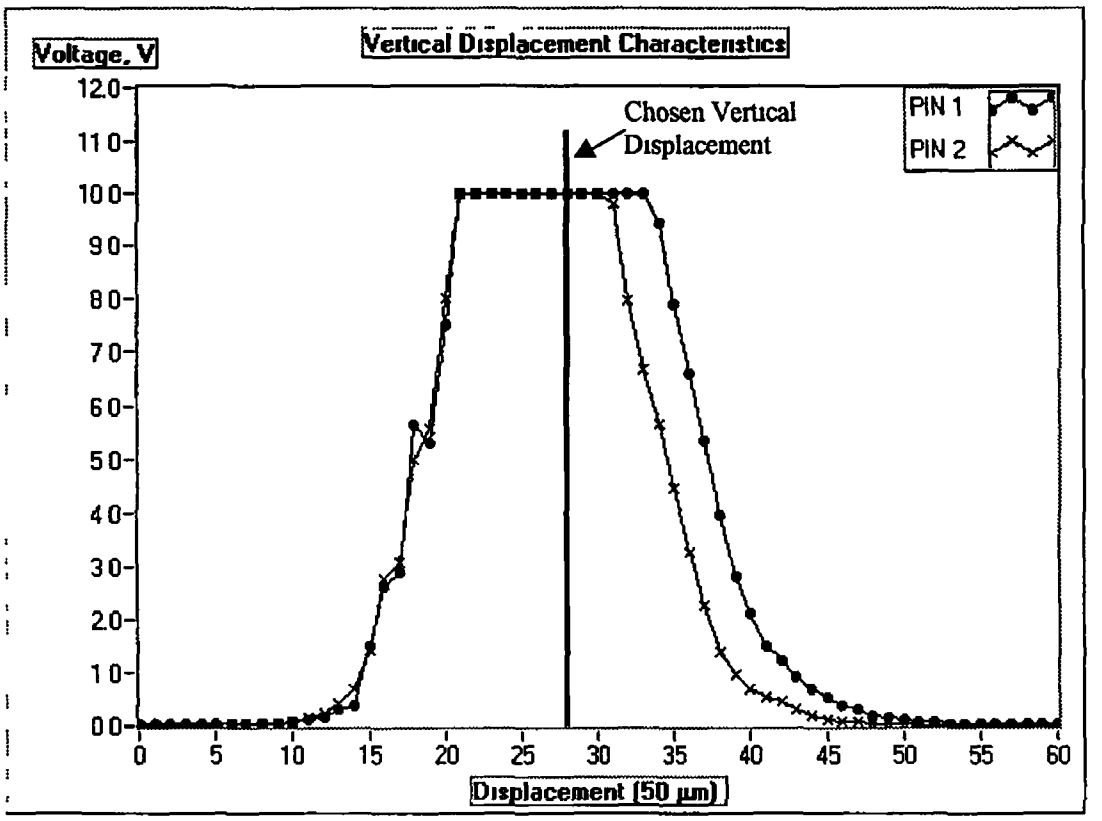

Figure 7 12 Displacement characteristic for copper through hole

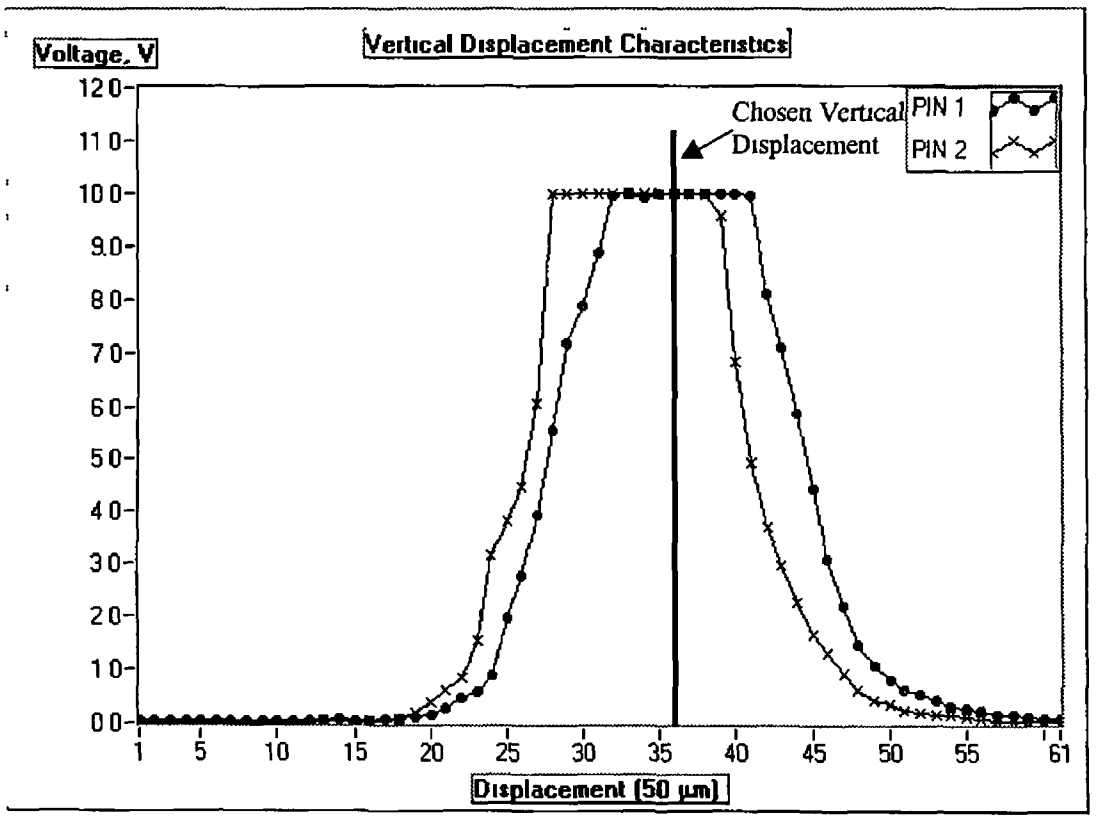

Figure 7 13 Displacement characteristic for copper blind hole

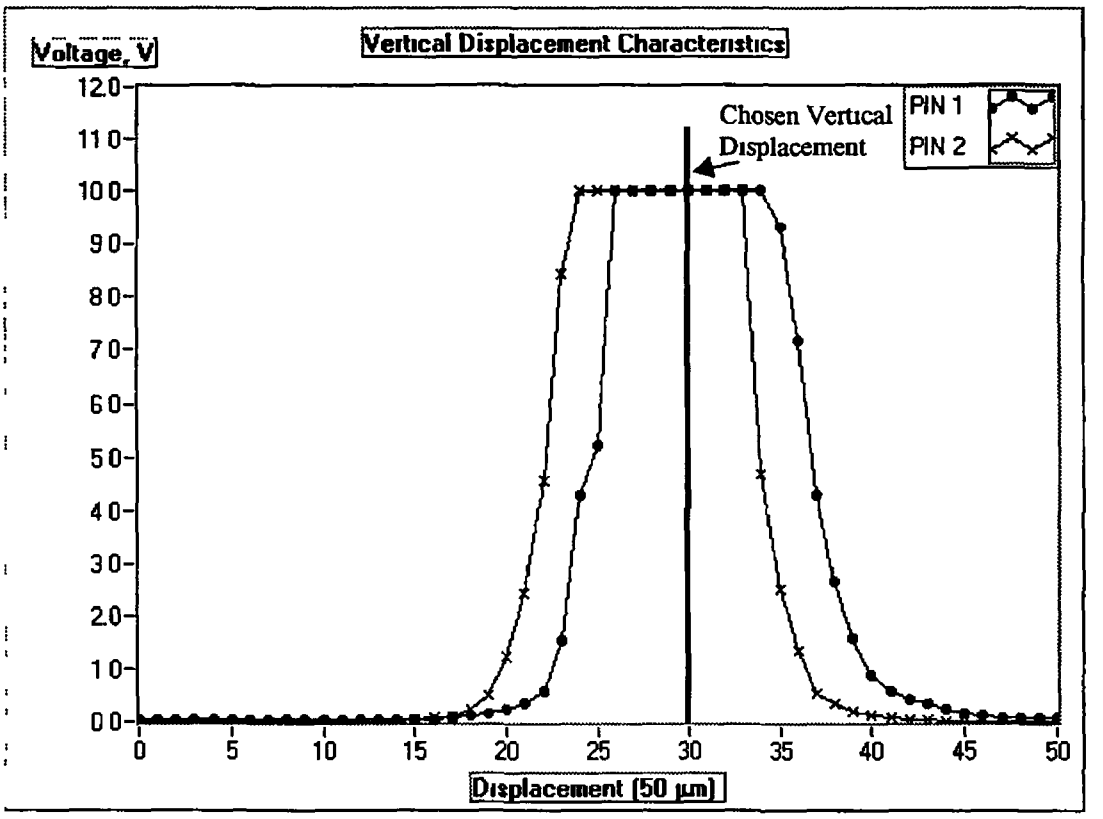

Figure 7 14 Displacement characteristic for brass through hole

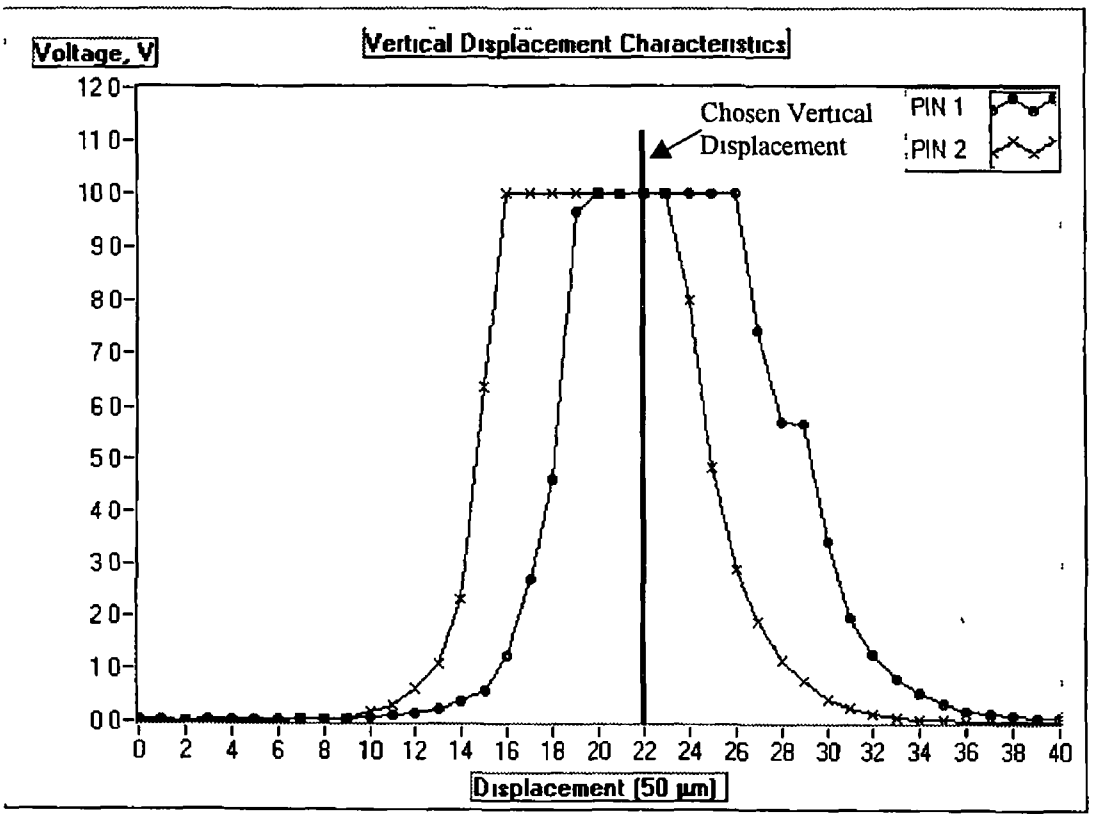

Figure 7 15 Displacement characteristic for brass blind hole

7 2 5 Lateral Displacement Characteristics of each Sample Plate

A sample lateral displacement characteristic, scan, of each set of readings is shown in figures 7 16-7 23 Many other scans were required to generate the surface maps shown in the next section, for reasons of space it is impossible to show these From scrutiny of these characteristics it can be seen which range of cut-off voltages generate surface maps adequately for each set of results For each a scan there is a line superimposed on the graph to indicate the performance of cut-off voltage of 2 Volts

Figure 7 16 shows a scan through the smallest through hole on the stainless steel plate At the edge of the hole, the system takes two measurements to switch between a reading of 10 V and below 1 V Excellent contrast is shown between the presence and the absence of a surface, thus, any cut-off voltage level chosen between 1 V and 9 V will confidently ensure correct operation

Figure 7 17 shows a scan through the smallest blind hole on the stainless steel plate The unmachined section of the hole is clearly sensed, but the hole itself isn't The unwanted spikes between the sections at 10 V hinder the sensor's operation This scan was chosen to highlight the presence of these spikes In the next section the surface map of this hole at a cut-off voltage of 2V operates successfully for PIN 1 for every scan other than this scan This hole was end-milled and an island remains in the centre of the hole, on further examination of the hole surface exhibits a slight curvature, this could possibly account for the spikes shown in this scan

Figure 7 18, a scan of the smallest polycarbonate through hole, shows the disadvantage of using a sensor of this kind with a surface that reflects light diffusely A cut-off voltage between 4 V and 1 5 V will operate adequately, but the contrast is much less than the other surfaces used The variability of the reflection from a surface is clear from this figure and more so from the next

Figure 7 19, a scan of the smallest polycarbonate blind hole, shows relatively high reflection from the blind hole surface, in comparison with the specular reflection This level is due to the diffusely reflecting nature of the polycarbonate surface The range

from which to choose a cut-off voltage is even narrower than for a through hole in a polycarbonate surface

Figure 7 20, a scan of a copper through hole, shows adequate contrast between the presence and the absence of a surface The next lateral displacement characteristic, figure 7 21, a blind hole in the same plate, shows the inconsistencies of working with a rough grainy rolled copper surface

Figure 7 21, a scan of the smallest blind hole on the copper plate, has two interesting features Firstly, the effect of the rolled copper surface is shown on the left side of the graph This surface is grainy with a pitted surface and variability in colouration, resulting in irregular surface reflection Secondly, the machined surface of the blind hole is quite different to that of the rolled surface, it is more reflective Thus it is difficult to sense blind holes machined into rolled copper of the roughness detailed in table 7 1 It was impossible to measure the roughness of the machined surface of the blind hole but it appeared to be more reflective

Figure 7 22, a scan of the smallest through hole in the brass plate, shows the high contrast achieved through this method for a smooth surface Any cut-off voltage between 10 V and 0 5 V will operate successfully

In Figure 7 23, a scan of the smallest blind hole in the brass plate, PIN photodiode 2 operates almost as well as the sensor operates for the through hole in the brass plate PIN photodiode 2 shows some noise due to closer proximity of its fibre endface to the surface, but it also operates adequately It is possible to select any cut-off voltage between 1 5 V and 9 V for this set-up for either photodiode

It can be seen that the brass and the steel blind holes have lower dark signals, i e the signal received in the absence of a reflective surface The polycarbonate and copper plates have significantly higher dark signals, even for through holes This may be because these polycarbonate and copper surfaces reflect light more diffusely than the copper and stainless steel surfaces, and thus couple optical radiation from diffuse reflections The lower specular reflectivity is confirmed from the weaker signals detected in the vertical displacement characteristics

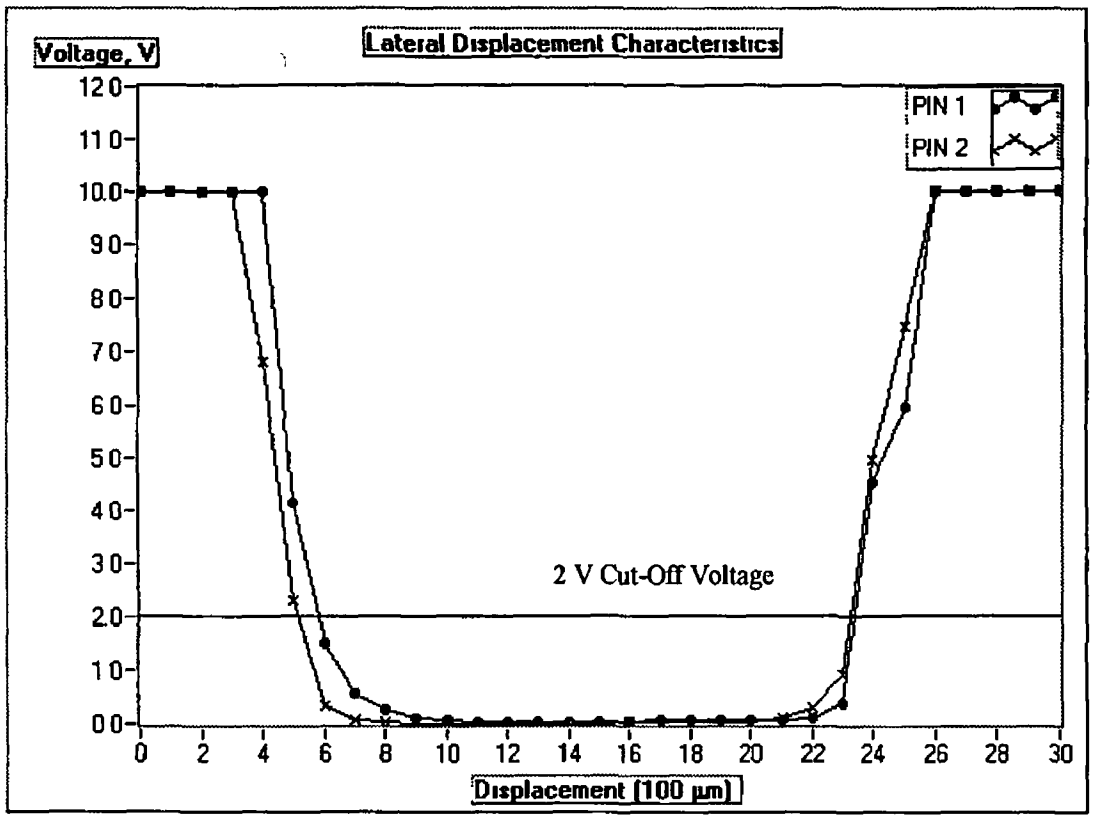

Figure 7 16 Sample scan of stainless steel through hole

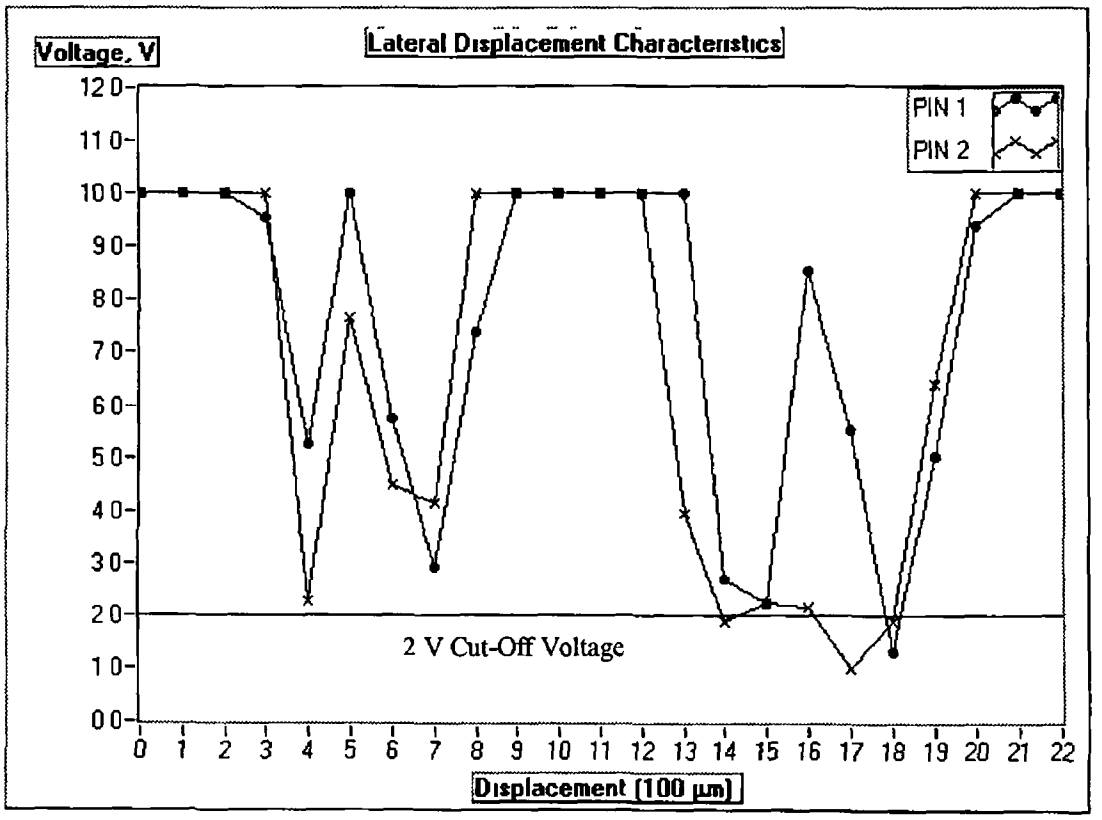

Figure 7 17 Sample scan of stainless steel end-milled blind hole with an island

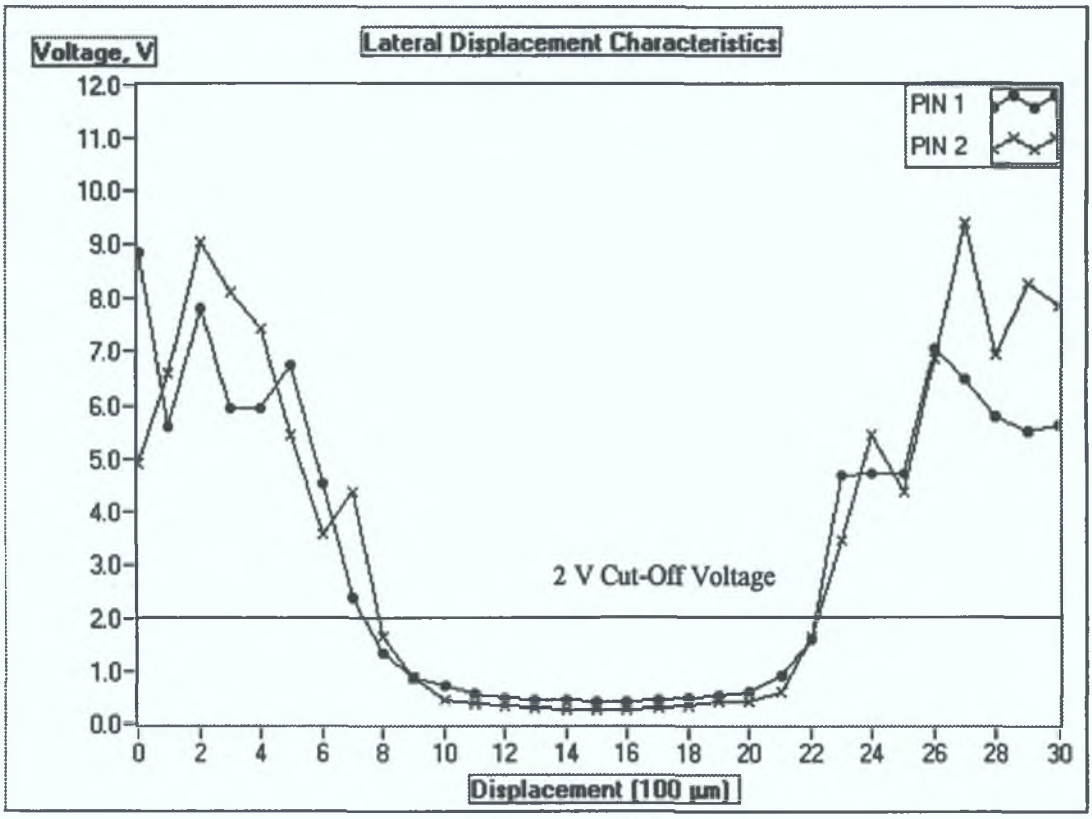

Figure 7.18 Sample scan of polycarbonate through hole.

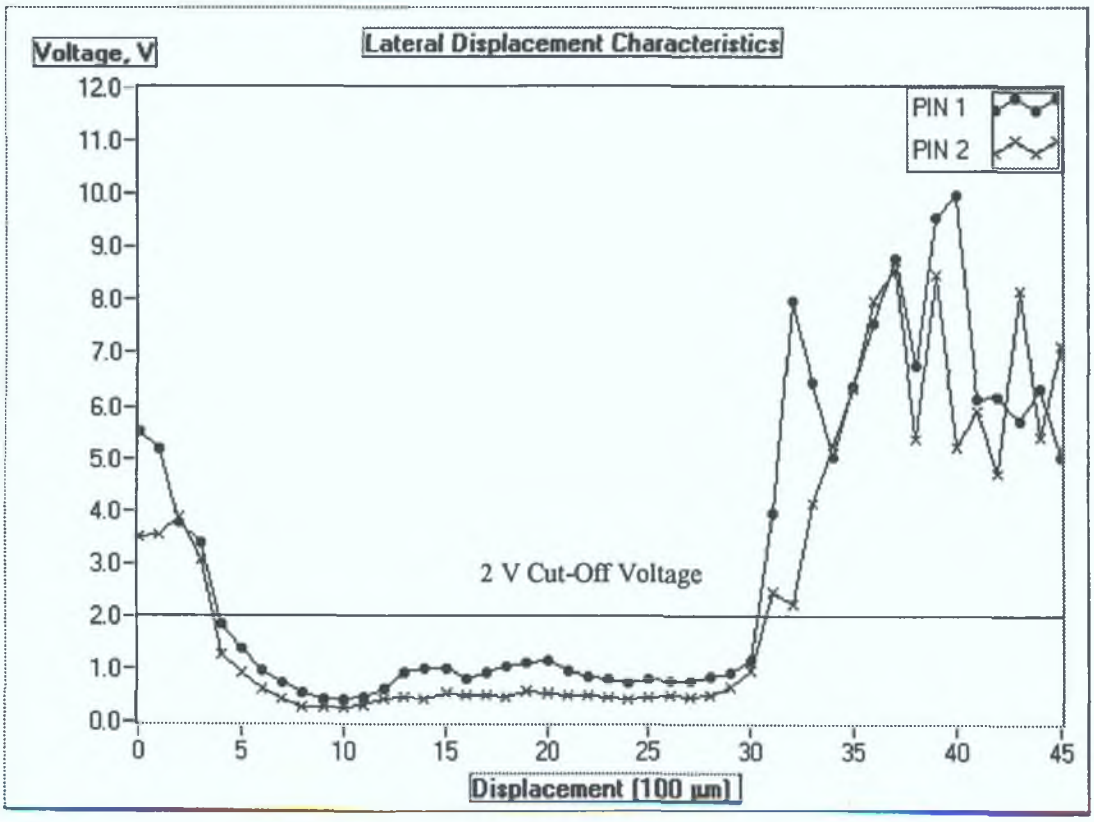

Figure 7.19 Sample scan of polycarbonate blind hole.

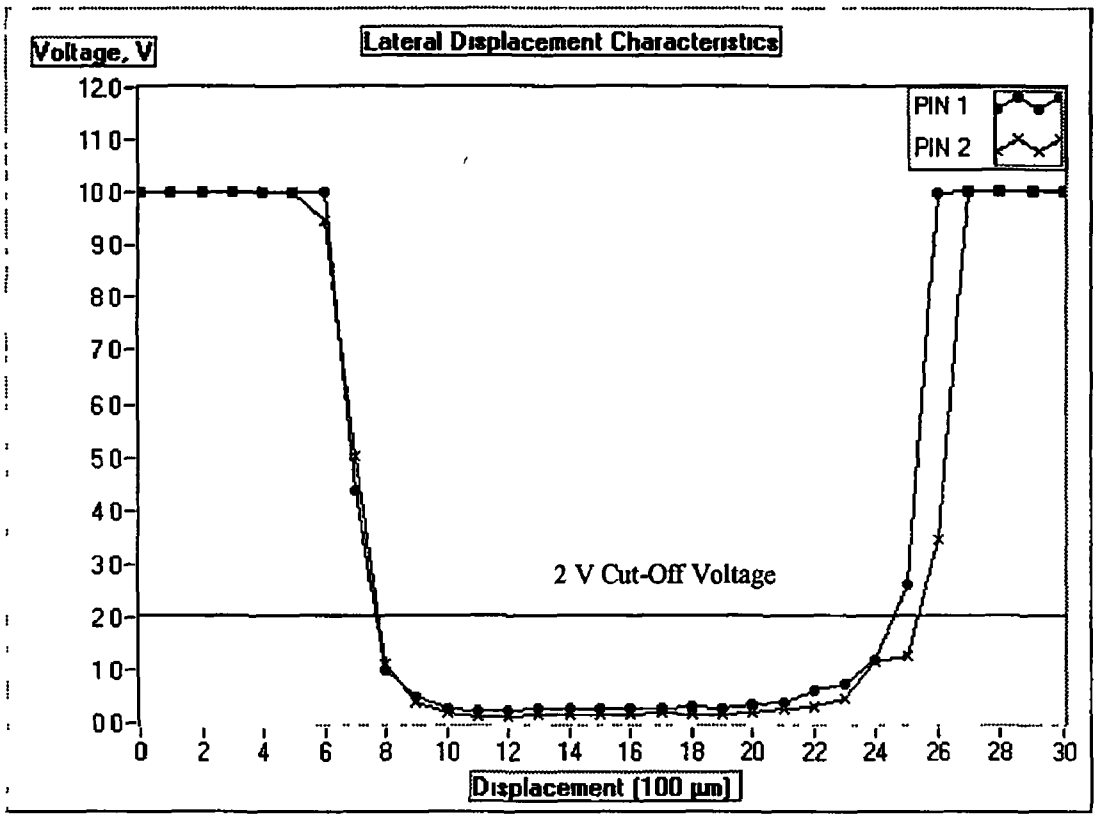

Figure 7 20 Sample scan of copper through hole

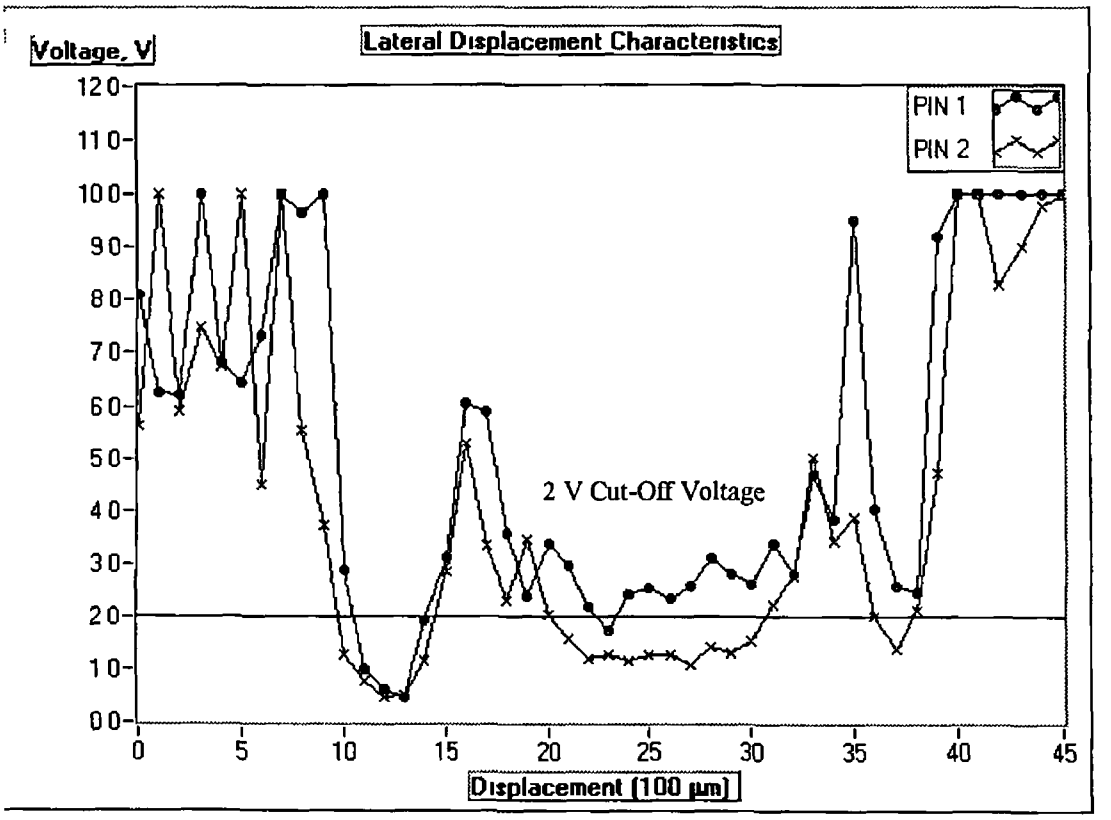

Figure 7 21 Sample scan of copper blind hole

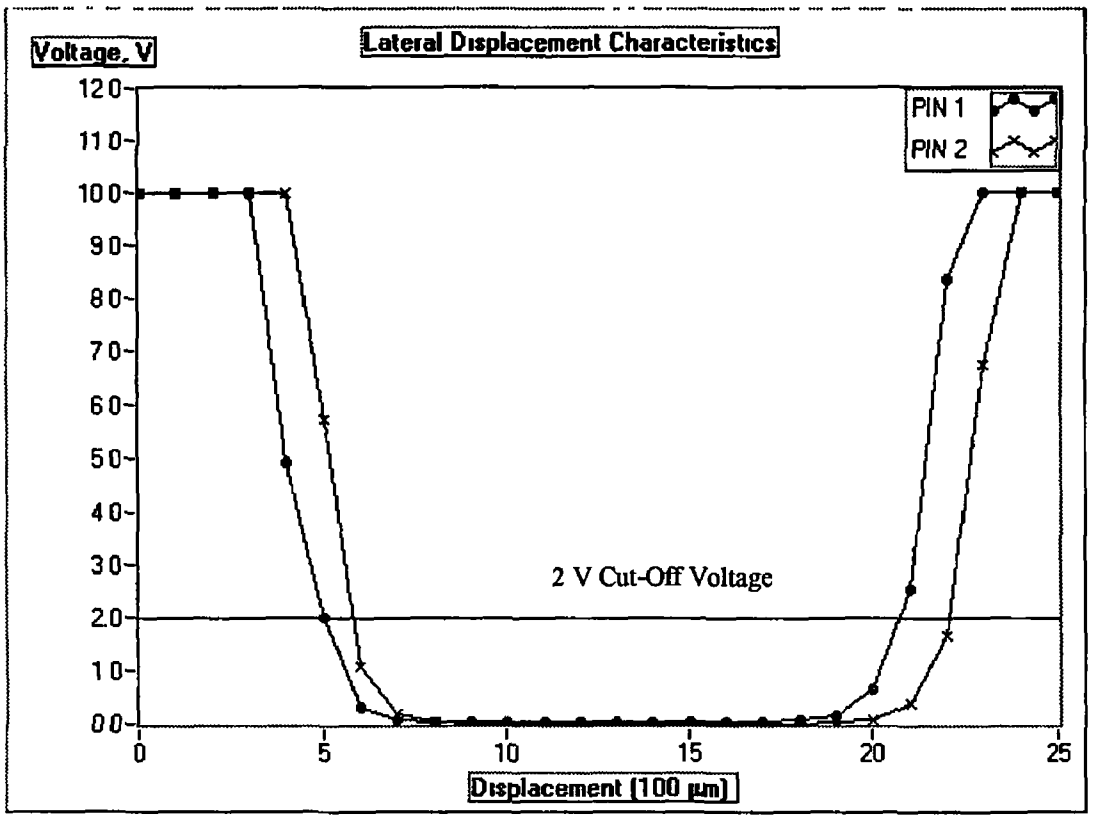

Figure 7 22 Sample scan of brass through hole

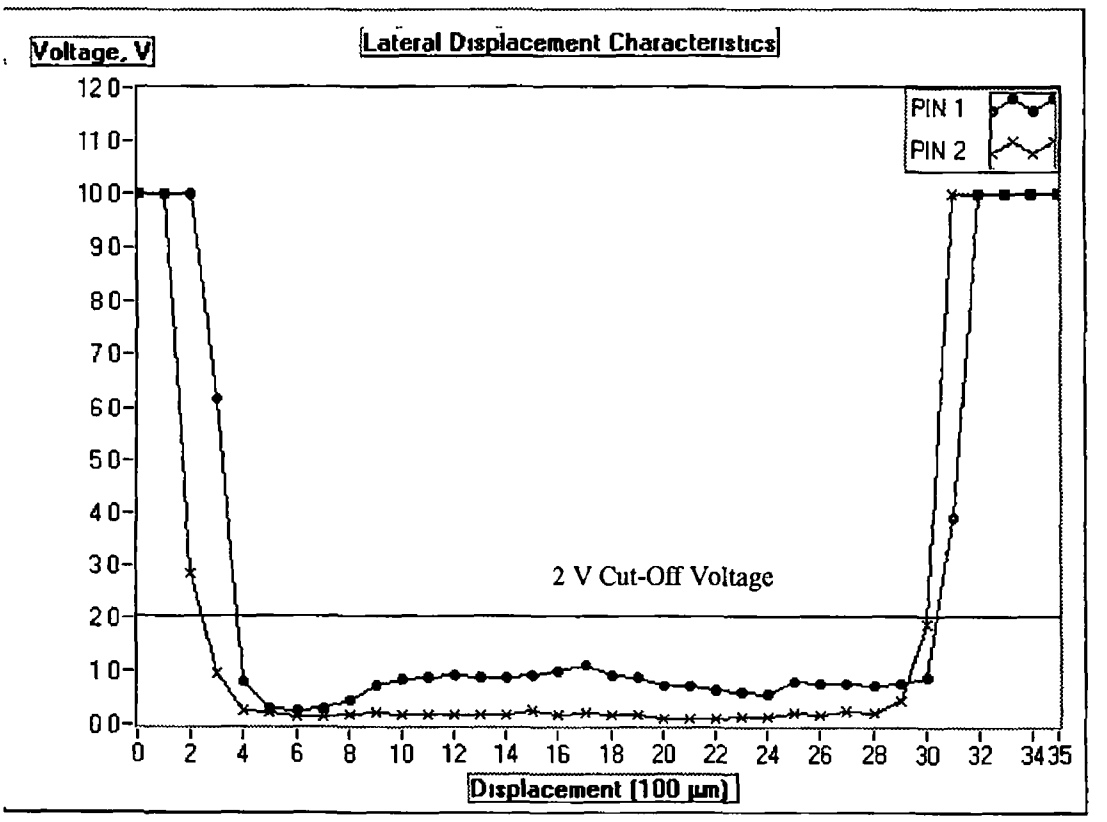

Figure 7 23 Sample scan of brass blind hole

7.2.6 Two-Dimensional Surface Map of each Sample Plate

Each of the surface maps shown in figures 7.24 to 7.31 was plotted by applying a cut-off voltage of 2 Volts, as indicated in the figures, to a set of surface lateral displacement characteristics. This cut-off voltage was suitable for all the sets of through holes, for either of the detecting PIN photodiodes. This was to be expected as detection of through holes relies solely on detecting the presence of a surface, as an absent surface reflects no optical radiation.

Detection of blind holes was more problematical as this relies on detecting a surface within certain displacement limits. This in turn relies on the vertical displacement characteristics, displayed in section 7.2.4, and the choice of vertical stand-off distance. As the blind holes had a depth of 0.6 mm, there was room for error. The depth of the shallowest blind hole that can be detected is defined by d as shown in figure 3.5. For example, in figure 7.9, the value of d for PIN 1 is around 0.6 mm and around 0.3 mm for PIN 2. Thus, in figure 7.25, apart from one scan the signal detected by PIN 1 describes the hole adequately, while the signal detected by PIN 2 fails to detect the hole, apart from at edges.

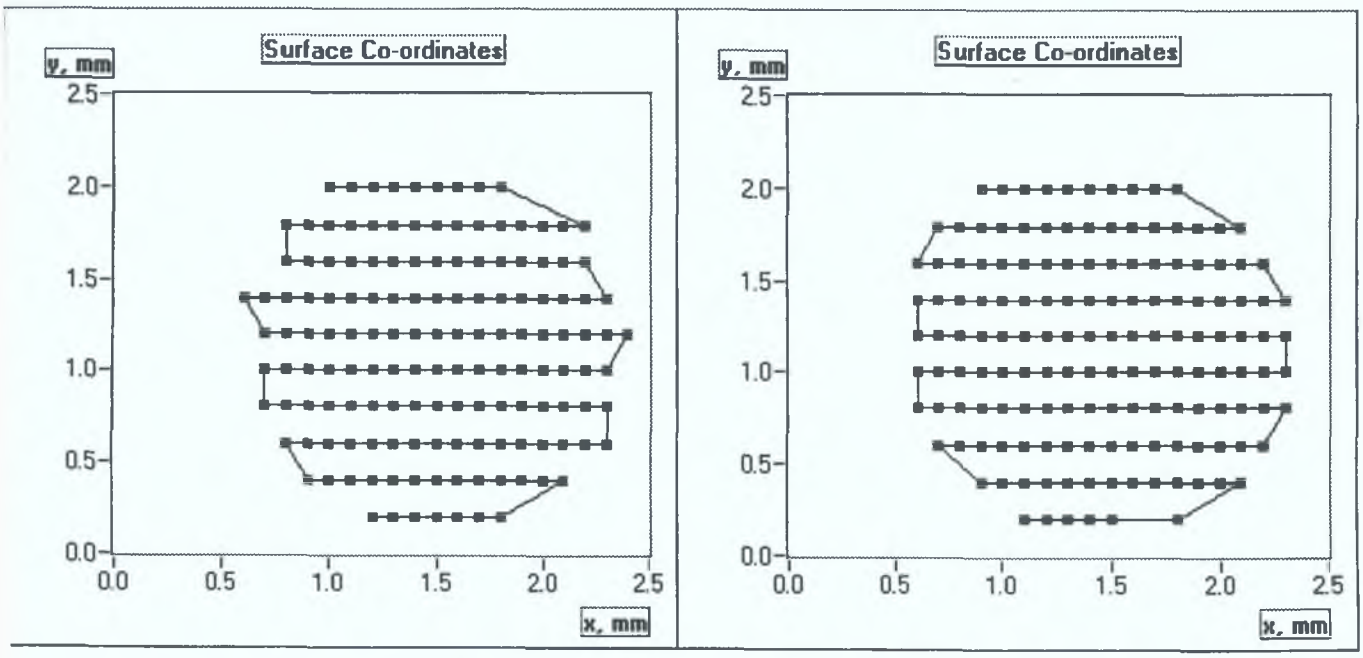

Figure 7.24 Surface map of through hole in stainless steel plate – 2V cut-off voltage, for (a) PIN 1 and (b) PIN 2.

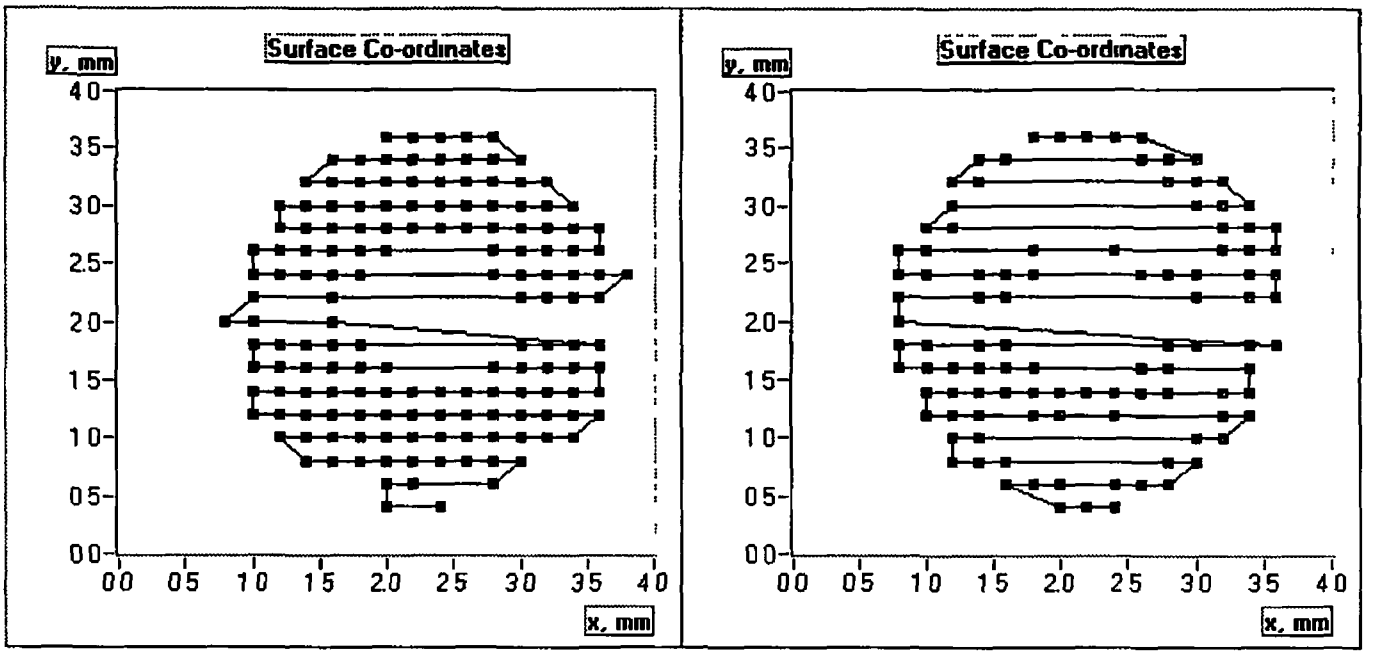

Figure 7 25 Surface map of end-milled blind hole of 0 6-mm depth with an island in the centre in stainless steel plate – 2V cut-off voltage, for (a) PIN 1 and (b) PIN 2

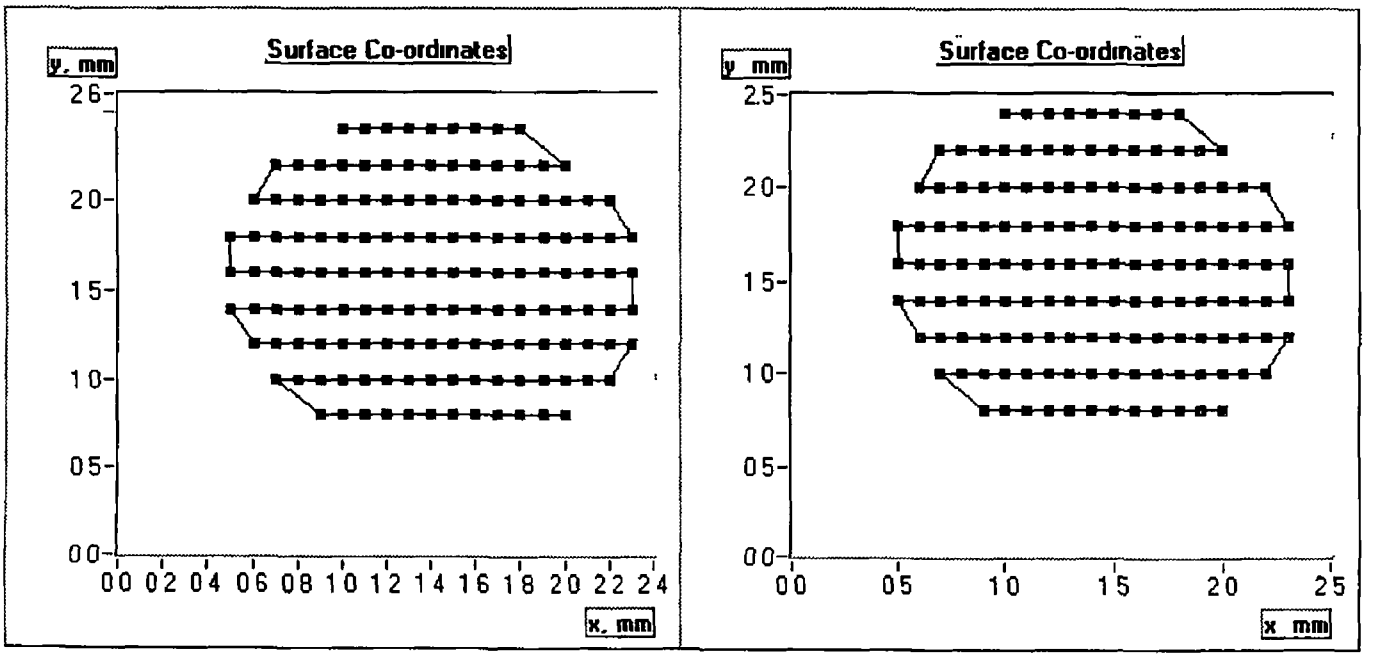

Figure 7 26 Surface map of through hole in polycarbonate plate – 2V cut-off voltage, for (a) PIN 1 and (b) PIN 2

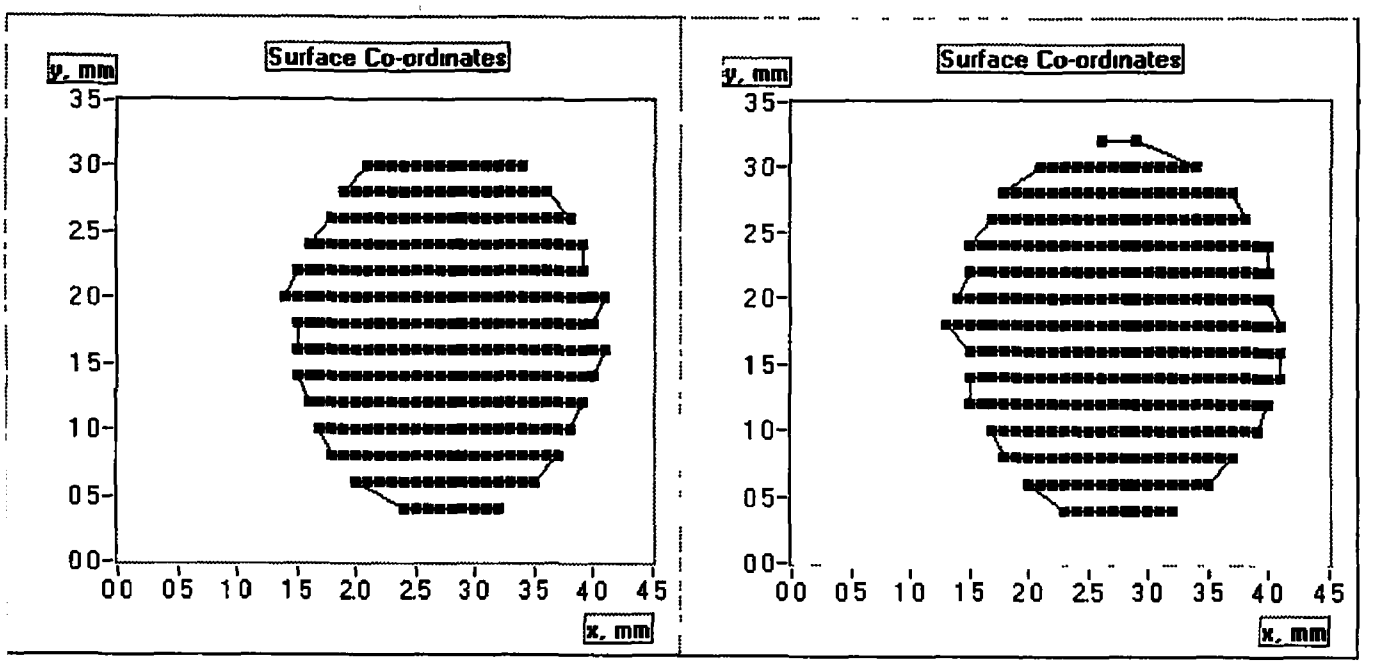

Figure 7 27 Surface map of blind hole of 0 6-mm depth in polycarbonate plate – 2V cut-off voltage, for (a) PIN 1 and (b) PIN 2

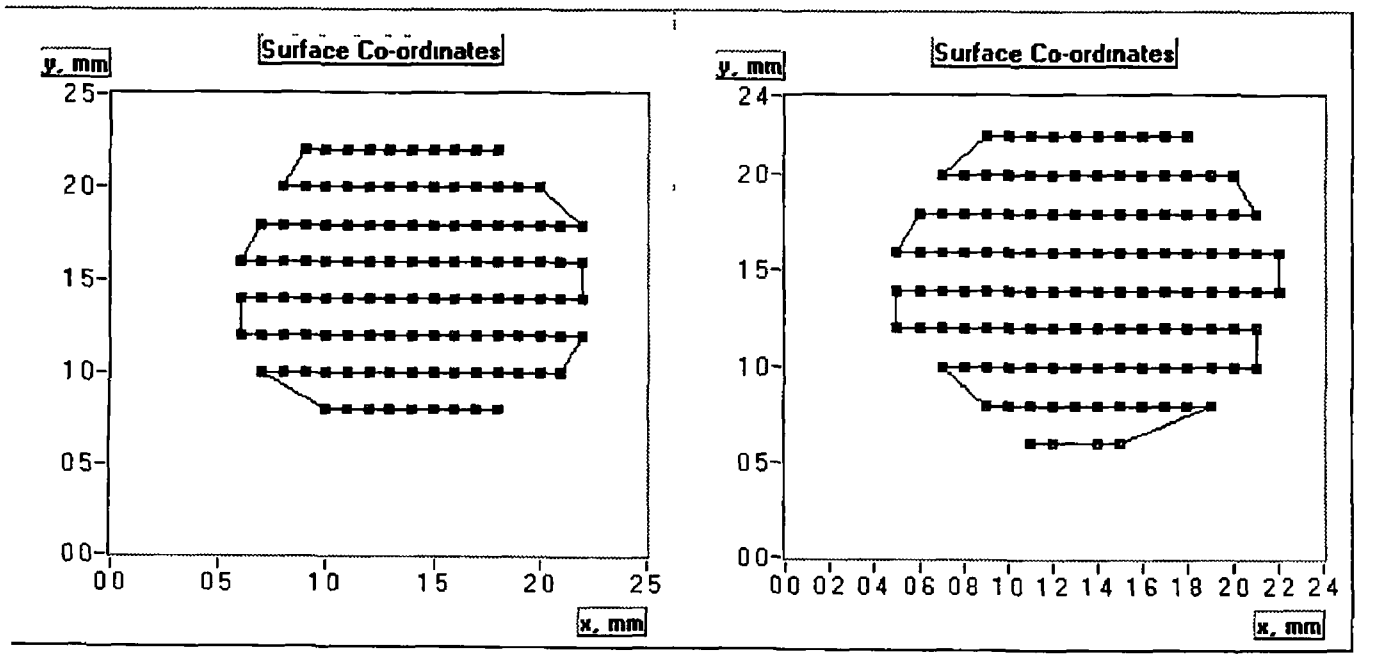

Figure 7 28 Surface map of through hole in copper plate – 2V cut-off voltage, for (a) PIN 1 and (b) PIN 2

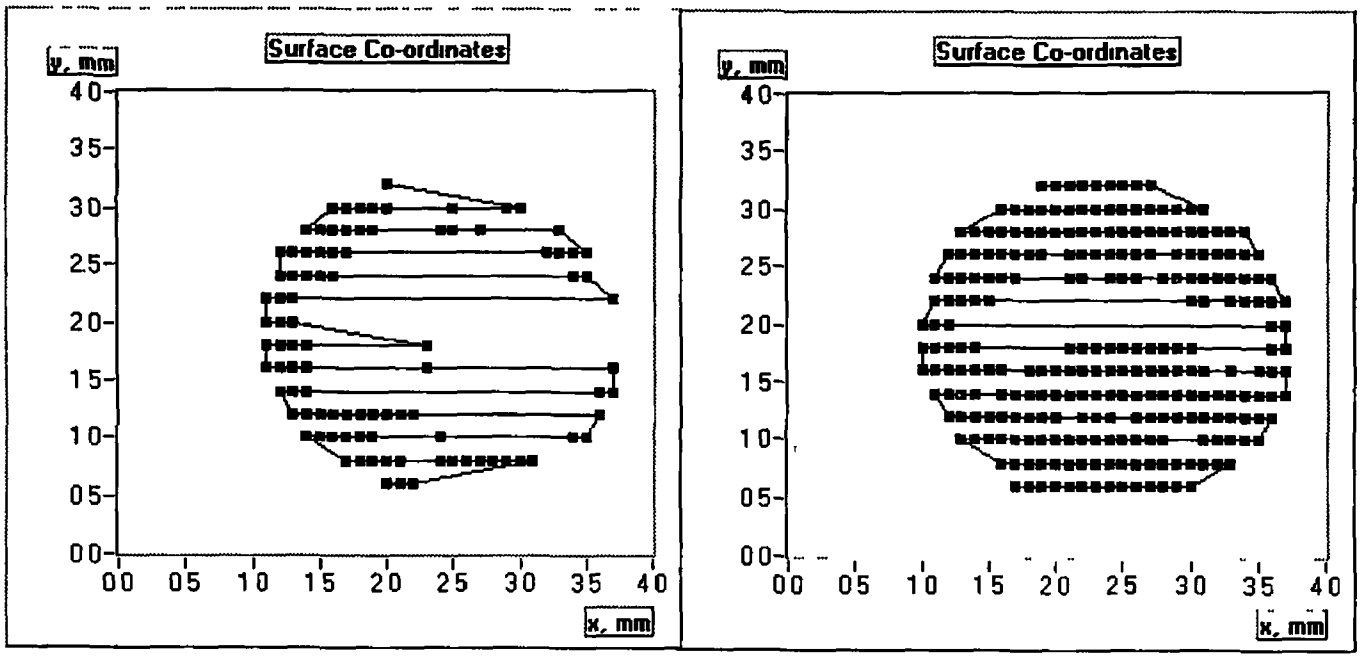

Figure 7 29 Surface map of blind hole of 0 6-mm depth in copper plate – 2V cut-off voltage, for (a) PIN 1 and (b) PIN 2

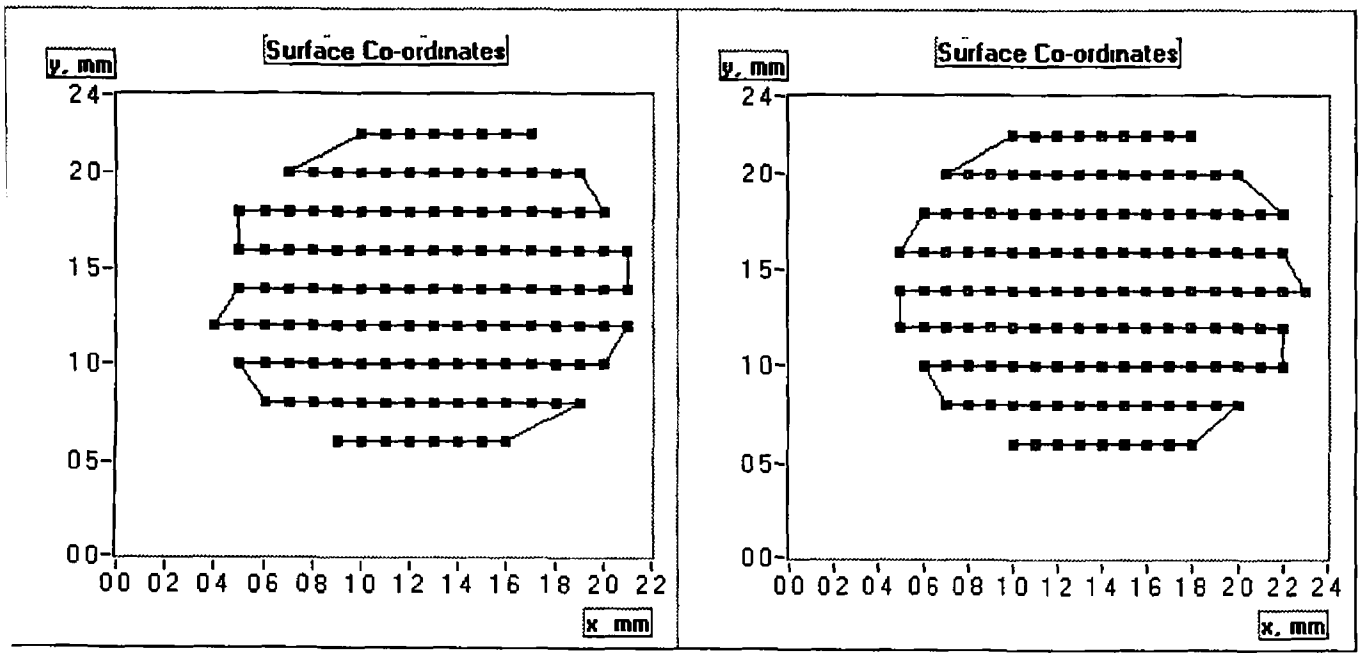

Figure 7 30 Surface map of through hole of 0 6-mm depth in brass plate – 2V cut-off voltage, for (a) PIN 1 and (b) PIN 2

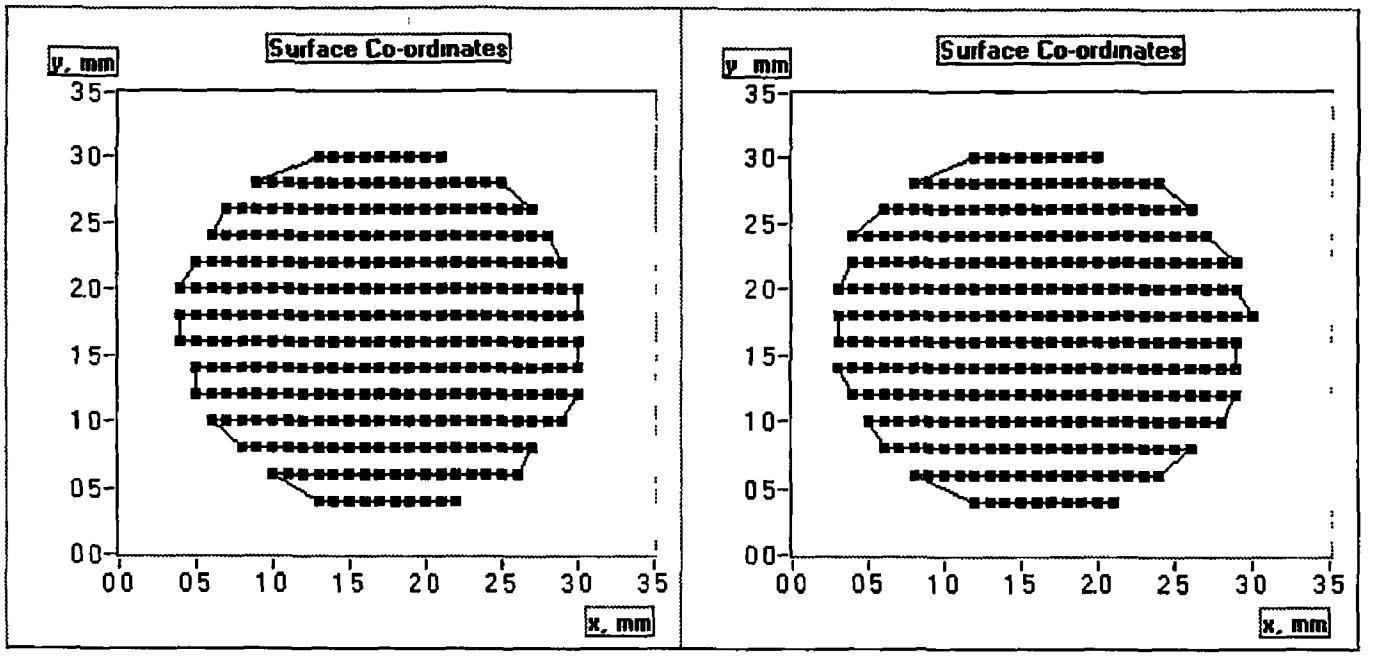

Figure 7 31 Surface map of blind hole of 0 6-mm depth in brass plate – 2V cut-off voltage, for (a) PIN 1 and (b) PIN 2

7 3 Surface Roughness Sensor System

This sensor system is designed to estimate surface roughness through the analysis of the vertical displacement characteristics of an intensity based fibre-optic sensor

The light source consisted of a HFE4050-014/BBA high power LED, appendix C1, driven by the square wave circuit, shown in appendix B1, at a frequency of 930 Hz This circuit was assembled on a prototype circuit board, PCB, and could be fixed inside a box The signal detection circuit, shown in appendix B4, consisted of unbiased transimpedance amplifiers using Honeywell PIN photodiodes, HFE3002-002/BBA, appendix C3 These silicon PIN photodiodes are sensitive to optical radiation from 400 to 1000 nm, with optimum responsivity close to 850 nm The data acquisition and analysis algorithm detailed in figure 6 6 was implemented using Labview This algorithm generates surface displacement characteristics from which surface measurements can be calculated

Three fibres collected light reflected from the surface If the position, i e displacement, and the size of the peak of the displacement curve is consistent throughout a set of readings, it suggests that the orientation of the surfaces in question is similar Any differences in these criteria may account for inconsistent results Surface orientation has affected other optical scattering systems previously

Nominal R_a value (μm)	Measured Roughness Characteristics		
	R_a (μm)	R_q (μm)	R_z (μm)
0 025	0 04	0 05	0 2
0 05	0 05	0 06	0 4
0 1	0 10	0 13	0 9
0 2	0 21	0 27	1 5
0 4	0 47	0 61	2 6
0 8	0 85	1 1	4 6

Table 7 2 Surface roughness characteristics based on measurements taken of Rubert comparator scales

The experimental samples were surface roughness comparator scales, manufactured by Rubert & Co , with the following nominal R_a values 0 025, 0 05, 0 1, 0 2, 0 4, and 0 8 The accuracy of these specimens is quoted as +12% / -17% of the nominal value [125] Equation 3 9 quotes RMS roughness values, R_q, thus, the surface roughness characteristics shown in table 7 2 were measured using the Mitutoyo Surftest 402 contact stylus, after all experiments had been concluded R_z measurements were made over a profile length of 10 μm

Equation 3 9 uses the scattering ratio to evaluate RMS surface roughness – the scattering ratio is defined in table 7 3 at incident angles of 45° and 60° for an 850 nm light source These scattering ratios will be used to plot theoretical curves in the following chapters Theoretical voltage values will be plotted in this graph using the given RMS surface roughness value of the smoothest surface roughness sample as a datum

RMS Surface Roughness	Scattering Ratio at 45° Incident Angle	Scattering Ratio at 60° Incident Angle
50 μm	0 921	0 960
60 μm	0 888	0 943
130 μm	0 574	0 774
270μm	0 091	0 302
610 μm	0 000	0 002
1100 μm	0 000	0 000

Table 7 3 Theoretical scattering ratios, based on equation 3 9, at incident angles of 45° and 60° for an 850 nm light source

This table shows how the proportions of the three peaks vary There is no link between the two calculated ratios The variation is probably caused by variation in the inclination of each surface roughness sample, this causes the spatial position of the peak intensity to shift relative to the collecting fibres

7 3 1 Vertical Displacement Characteristics of each Surface Roughness Specimen at incident angle of 45°

The vertical displacement characteristics of each surface were measured using fibres oriented at incident angles of 45°, for each of the samples shown in table 7 2 The following 6 graphs show the displacement characteristics for each sample at an incident angle of 45° This set of measurements suggests that the three fibres are oriented with the fibre supplying PIN photodiode 2 in the centre and those supplying PIN photodiodes 1 and 3 at either side These figures are used as the basis of further data analysis in section 7 3 2, which correlates properties of these curves with the surface roughness of the particular samples

Surface Roughness Sample	45° Incident Angle		
	Peak Voltage of PIN 2, V	Ratio Peak Voltage PIN 1 PIN 2	Ratio Peak Voltage PIN 3 PIN 2
0 025 μm R_a	4 62	0 59	0 31
0 05 μm R_a	4 76	0 51	0 33
0 1 μm R_a	3 77	0 53	0 29
0 2 μm R_a	1 92	0 76	0 33
0 4 μm R_a	1 87	0 67	0 61
0 8 μm R_a	1 28	0 71	0 35

Table 7 4 Peak voltage of the central PIN photodiode and the ratio with the peak voltage of the other two photodiodes for each surface roughness sample at an incident angle of 45°

Table 7 4 shows the peak value of each trace for PIN 2 for each of the displacement characteristics shown in figures 7 32 to 7 37 It also shows the ratio of the peak values of each trace for PINs 1 and 2 to that of PIN 2 The variation in the value of the ratios suggest that the receiving and emitting fibres were not always identically aligned with each different surface roughness sample This will be discussed further at a later stage

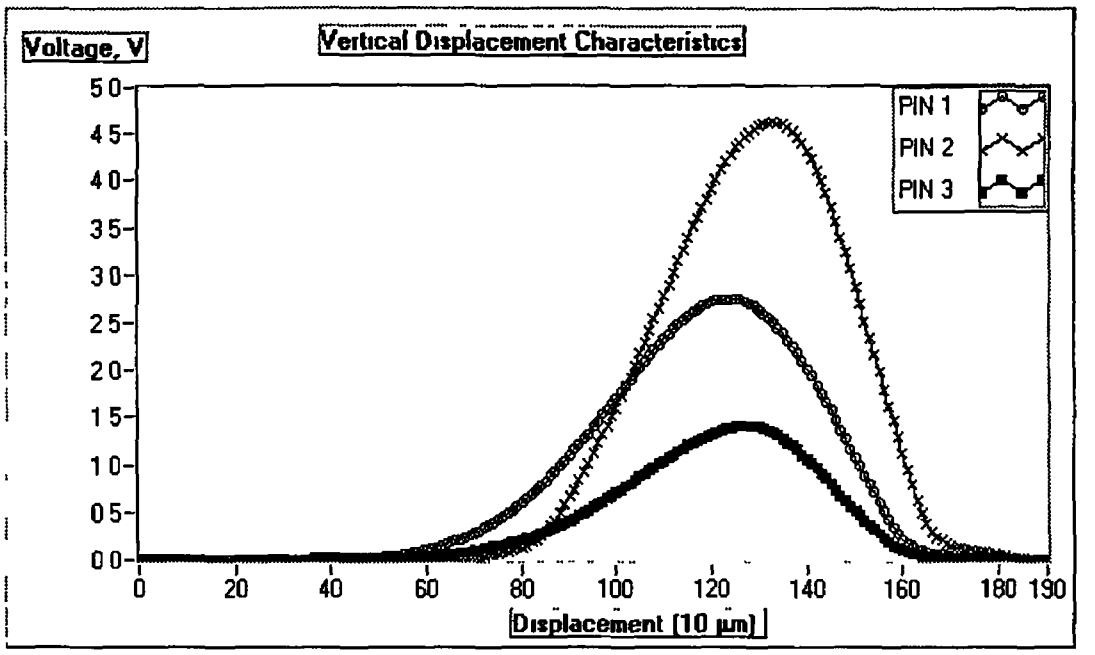

Figure 7 32 Vertical displacement characteristics of 0 025 µm R_a surface roughness sample at incident angle of 45°

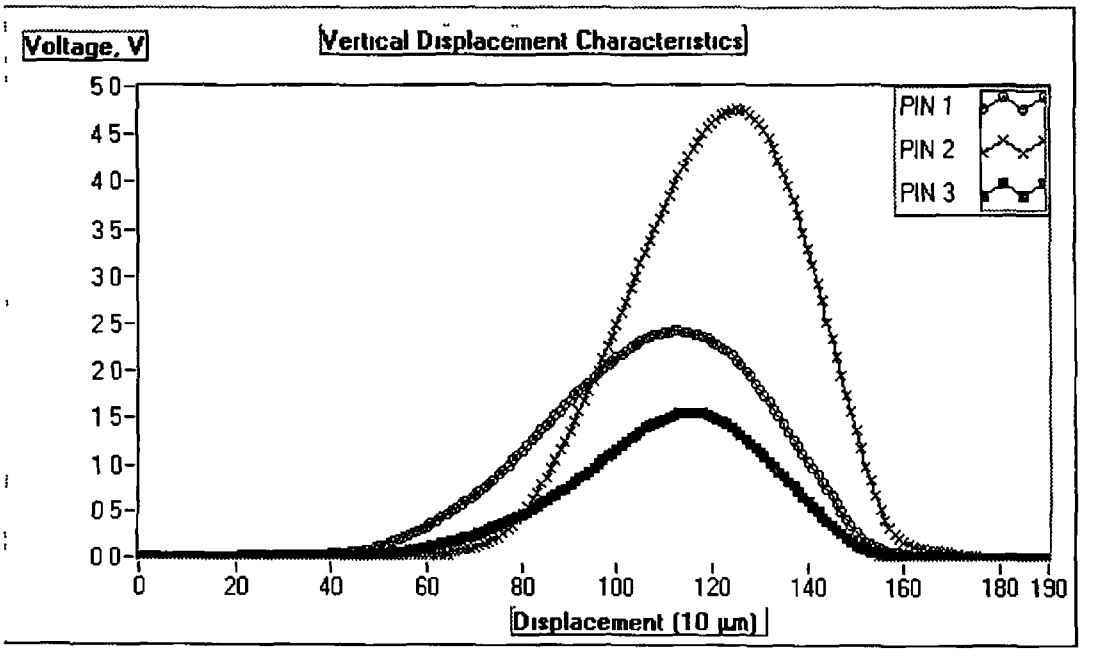

Figure 7 33 Vertical displacement characteristics of 0 05 µm R_a surface roughness sample at incident angle of 45°

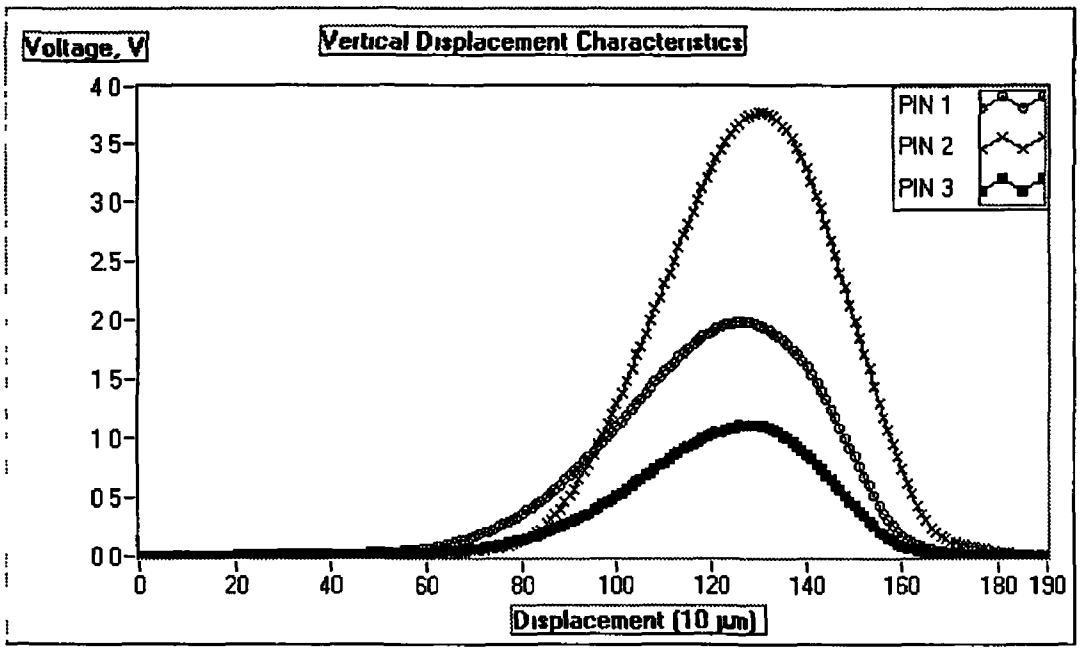

Figure 7 34 Vertical displacement characteristics of 0 1 µm R_a surface roughness sample at incident angle of 45°

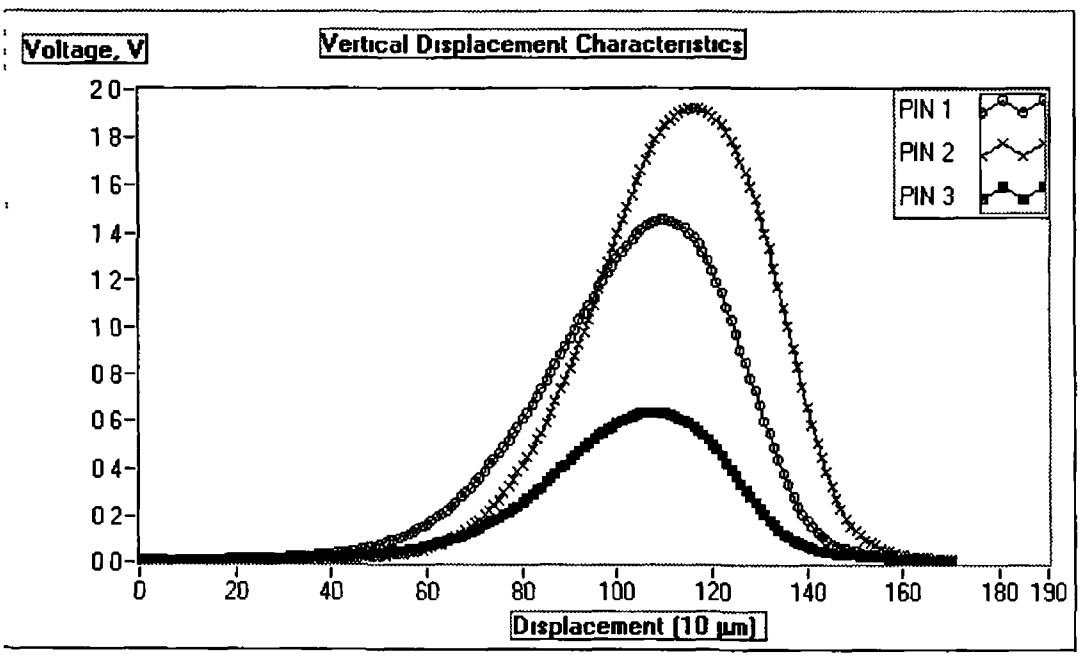

Figure 7 35 Vertical displacement characteristics of 0 2 µm R_a surface roughness sample at incident angle of 45°

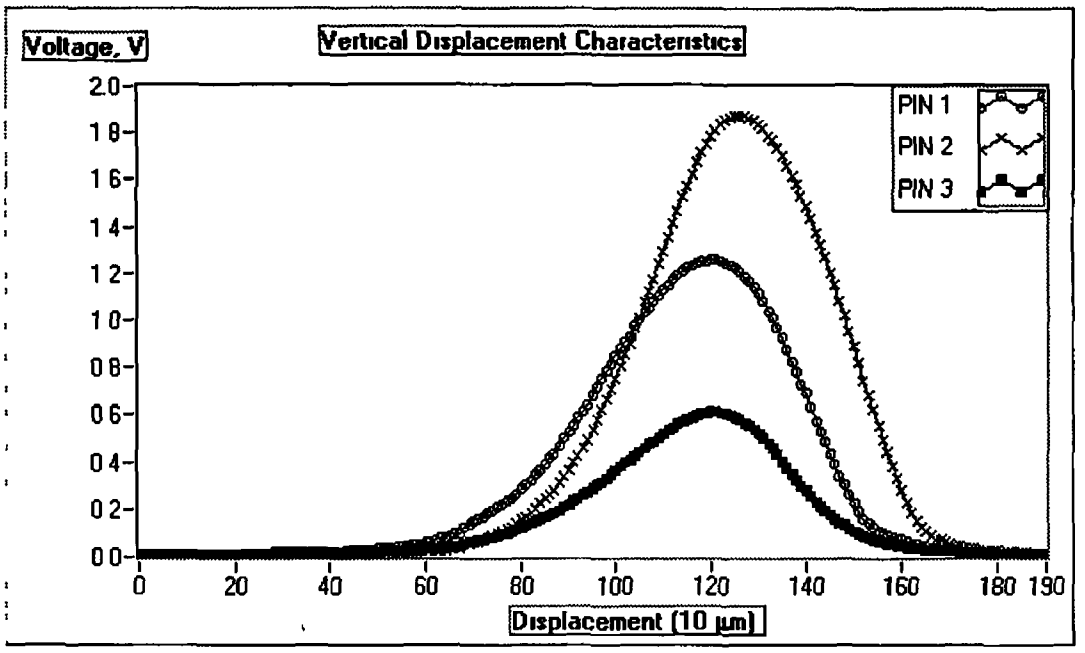

Figure 7.36 Vertical displacement characteristics of 0.4 µm R_a surface roughness sample at incident angle of 45°

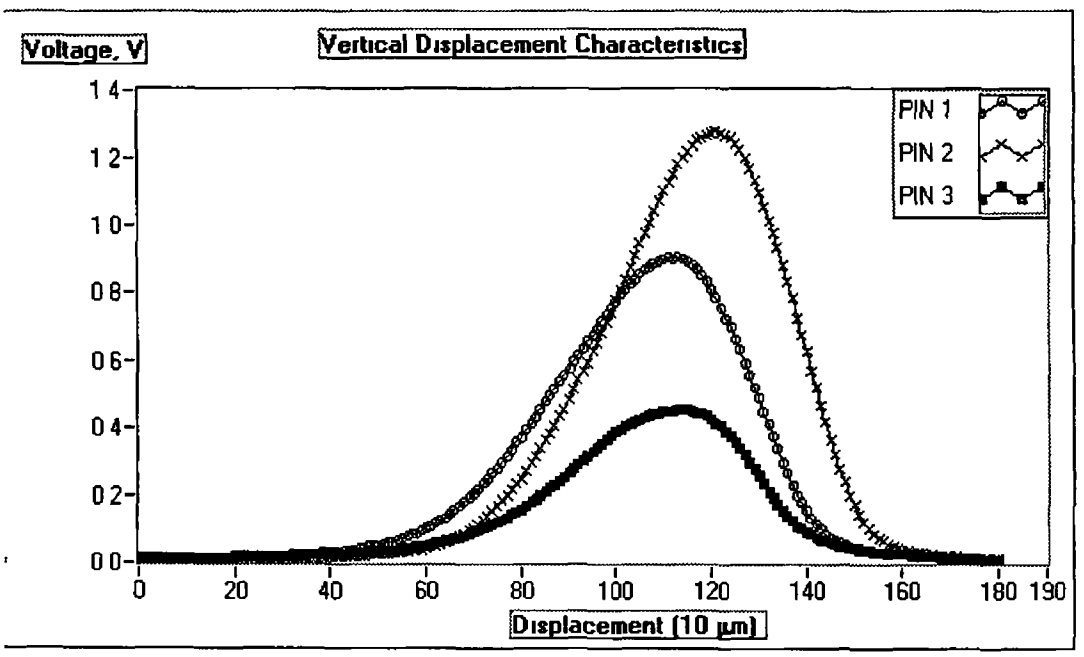

Figure 7.37 Vertical displacement characteristics of 0.8 µm R_a surface roughness sample at incident angle of 45°

7 3 2 Correlation of Displacement Characteristics at Incident Angle of 45° with Surface Roughness Properties

The effect of surface roughness is seen in the reduction of the peak of the curves, the summation of the voltage readings at over 50% and 90% of peak voltage, figures 7 38-7 40 show the variation of these quantities with R_a, as indicated by the Rubert blocks Figures 7 41-7 43 replace R_a with R_q and figures 7 44-7 47 with R_z R_a values are as indicated on the Rubert blocks, while Rq and Rz values refer to the values stated in table 7 2

The scattering ratios at the theoretical RMS roughness values have been calculated using equation 3 9 and presented in table 7 3 From these a theoretical curve is included for figures 7 41-7 43 presenting the curve of a true TIS measurement for these surfaces The theoretical voltage level for each roughness value, V_P, using the voltage level of the of the smoothest surface roughness sample, V_D, as a datum, using the equation 7 1 I_P is the theoretical scattering ratios at the particular roughness value and I_D is the theoretical scattering ratio of the surface roughness sample

$$V_P = V_D \times \frac{I_P}{I_D} \qquad 7\ 1$$

As can be seen in figures 7 41-7 43 the theoretical value is much lower than all experimental measurements Thus, equation 3 9 could not be used to calculate roughness directly using this sensor

For PIN 1 and PIN 2, figures 7 38-7 47 all show a strong linearity between surface roughness (R_a, R_q, and R_z) and reflectivity for the first four surface roughness samples, i e under 0 2 μm R_a At over 0 2 μm R_a the curve is too slight to be useful in measuring surface roughness

In figures 7 41, 7 43, and 7 46 the peak of the curve for PIN 2, the highest curve in all figures, for the second point of the curve is higher than that of the first point, a smoother surface The use of extra information from the angular profile of the vertical displacement characteristics, the sum of voltage values above 50% and 90% of peak voltage, eliminates this problem in all of the other figures in this section

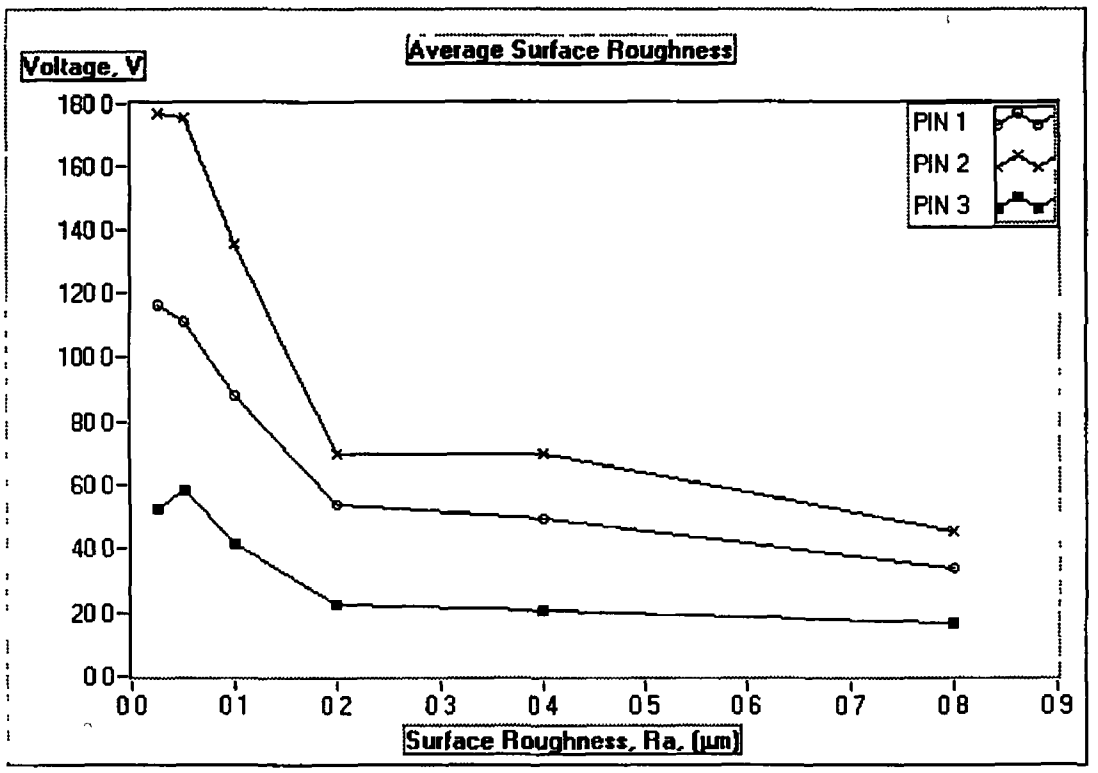

Figure 7 38 Summation of voltage values greater than 90% of peak voltage versus average roughness, R_a, for incident angle of 45°

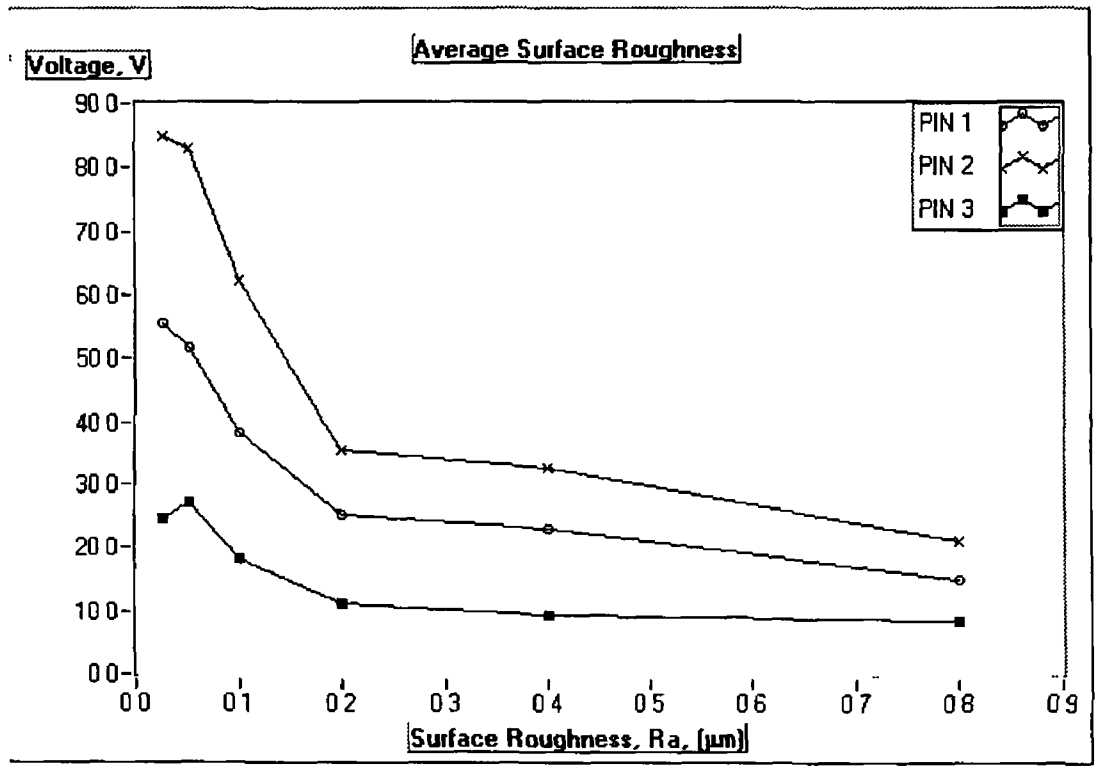

Figure 7 39 Summation of voltage values greater than 50% of peak voltage versus average roughness, R_a, for incident angle of 45°

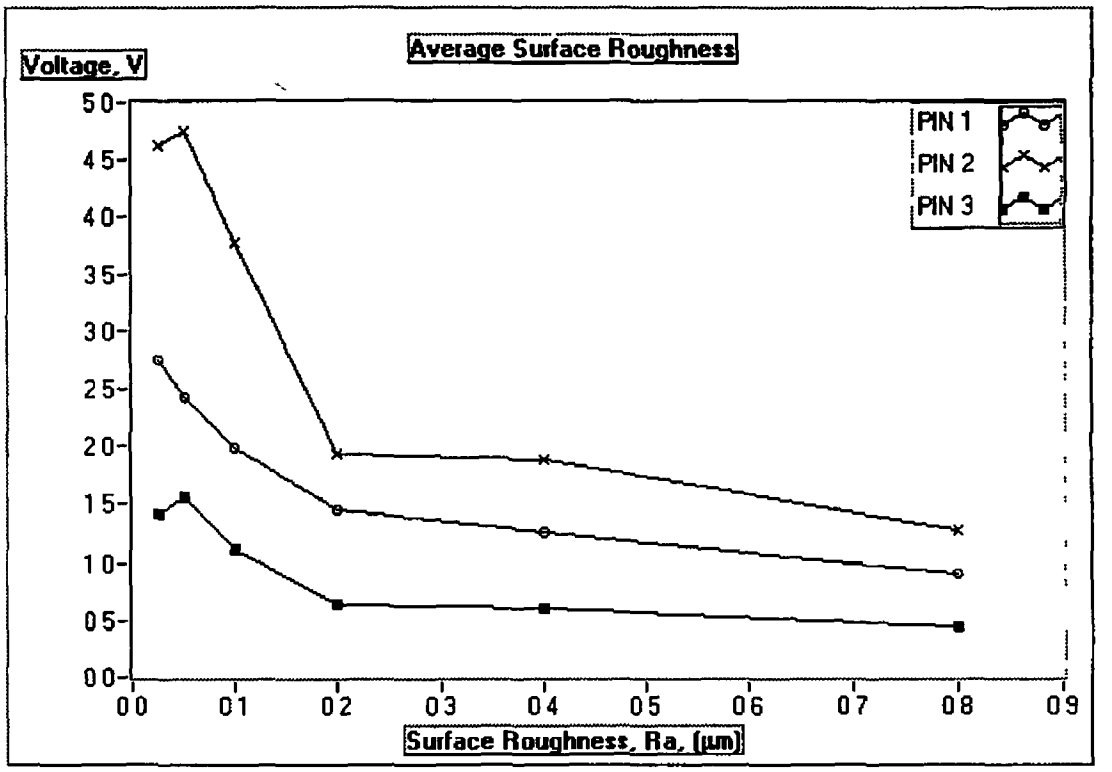

Figure 7 40 Peak voltage values versus average roughness, R_a, for incident angle of 45°

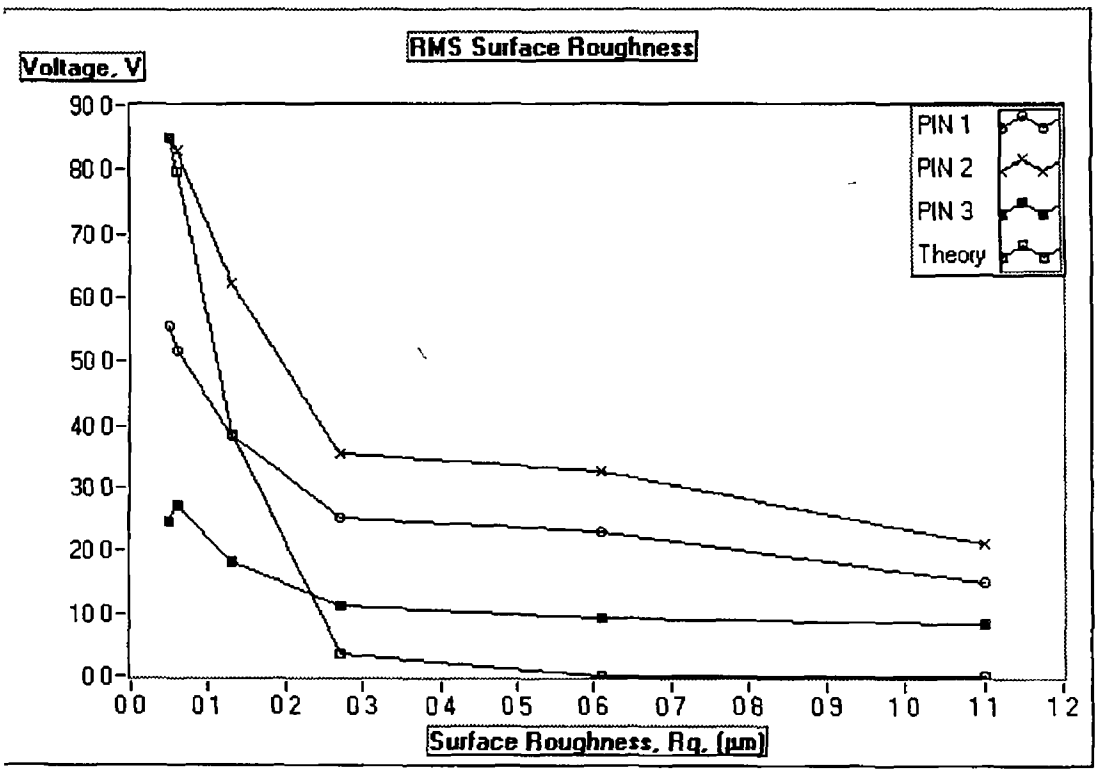

Figure 7 41 Summation of voltage values greater than 90% of peak voltage versus RMS roughness, R_q, for incident angle of 45°

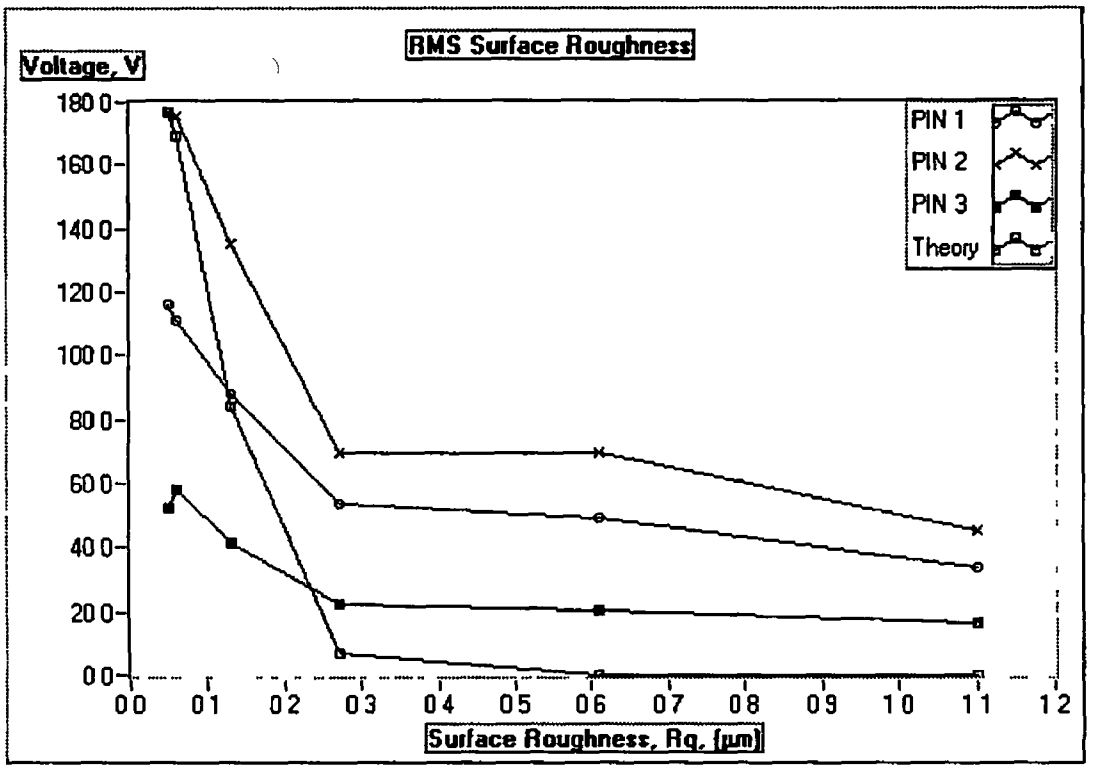

Figure 7 42 Summation of voltage values greater than 50% of peak voltage versus RMS roughness, R_q, for incident angle of 45°

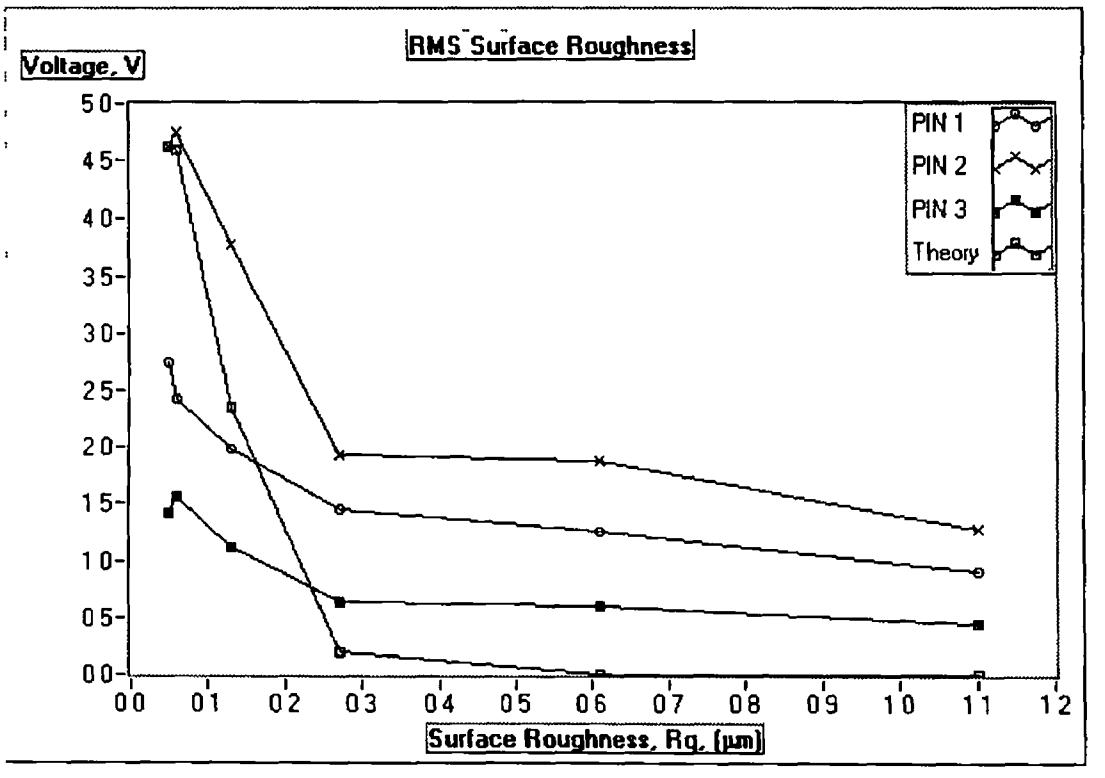

Figure 7 43 Peak voltage values versus RMS roughness, R_q, for incident angle of 45°

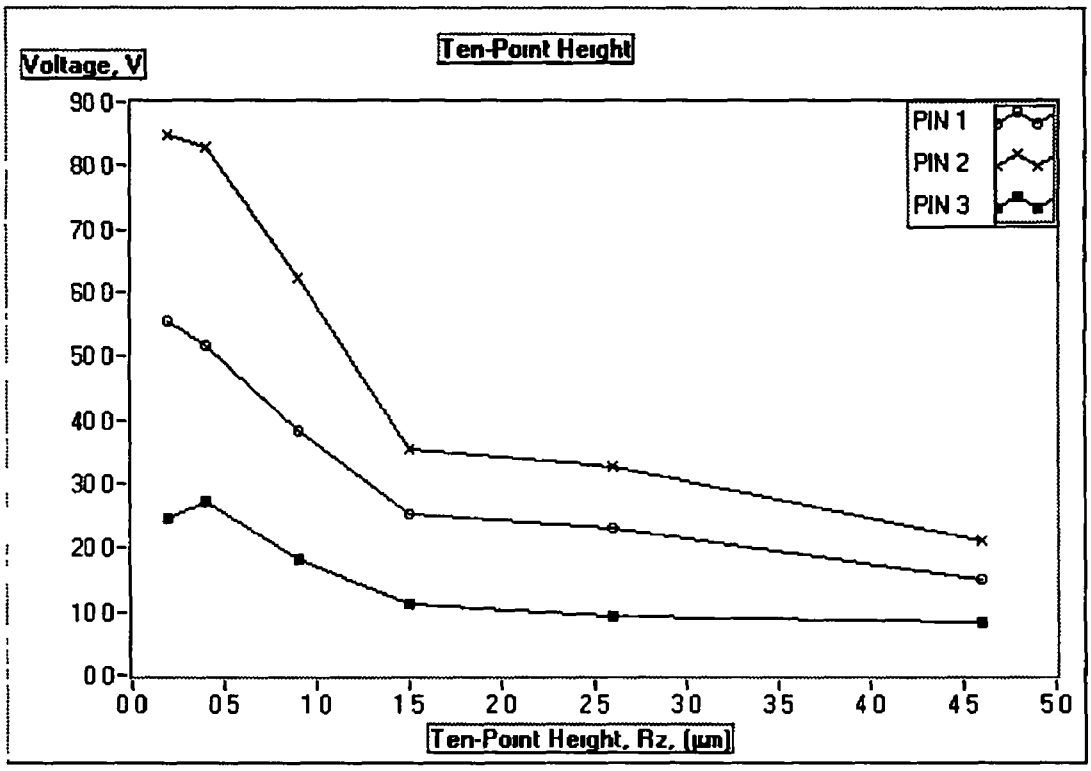

Figure 7 44 Summation of voltage values greater than 90% of peak voltage versus ten-point height, R_z, for incident angle of 45°

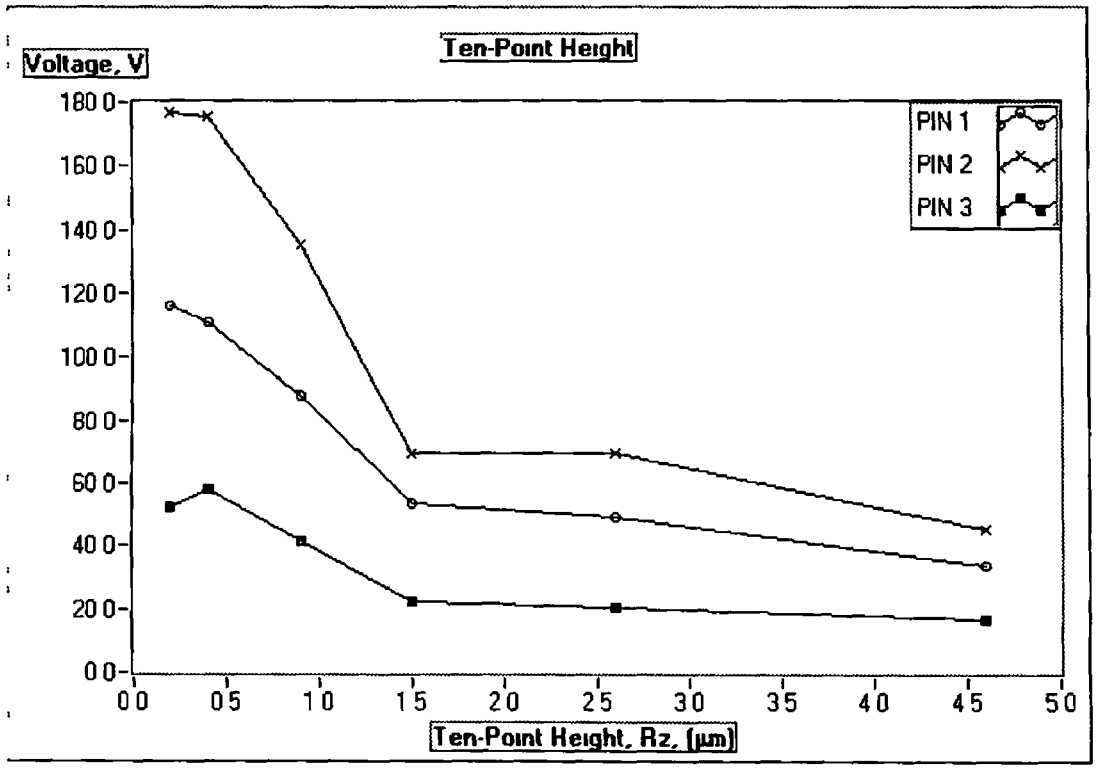

Figure 7 45 Summation of voltage values greater than 50% of peak voltage versus ten-point height, R_z, for incident angle of 45°

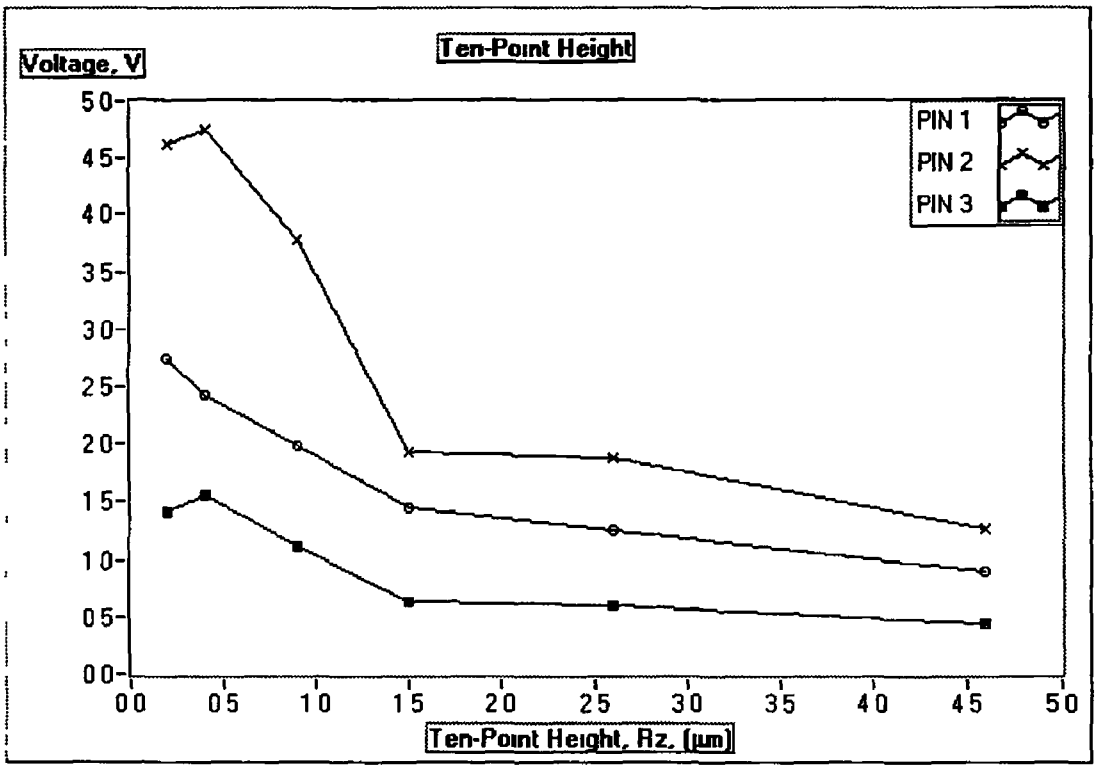

Figure 7 46 Peak voltage values versus ten-point height, R_z, for incident angle of 45°

7 3 3 Vertical Displacement Characteristics of each Surface Roughness Specimen at incident angle of 60°

This section presents the vertical displacement characteristics for each of the surface roughness samples when the experimental rig was set-up with fibres oriented at an incident angle of 60° to normal From examination of these sets of readings, it is evident that PIN 3 was connected to the central fibre with PINs 1 and 2 at either side Table 7 5 shows the peak voltage recorded from PIN 3 for each sample, and the ratios of the peak voltages recorded from PIN 1 and PIN 2 to this voltage The fluctuation of the readings for PIN 1 and PIN 2 can be seen in the figures in this section In common with table 7 4 the variation of these two ratios implies that the samples were oriented at different angles for each reading

Figures 7 47 - 7 52 are used as the basis of further data analysis in section 7 3 2, which correlates properties of these curves with the surface roughness of the particular samples

Surface Roughness Sample	60° Incident Angle		
	Peak Voltage of PIN 3, V	Ratio Peak Voltage PIN 1 PIN 3	Ratio Peak Voltage PIN 2 PIN 3
0 025 μm R_a	4 84	0 44	0 40
0 05 μm R_a	4 65	0 43	0 34
0 1 μm R_a	3 47	0 63	0 57
0 2 μm R_a	3 10	0 52	0 46
0 4 μm R_a	2 34	0 55	0 49
0 8 μm R_a	1 41	0 65	0 36

Table 7 5 Peak voltage of the central PIN photodiode and the ratio with the peak voltage of the other two photodiodes for each surface roughness sample at an incident angle of 60°

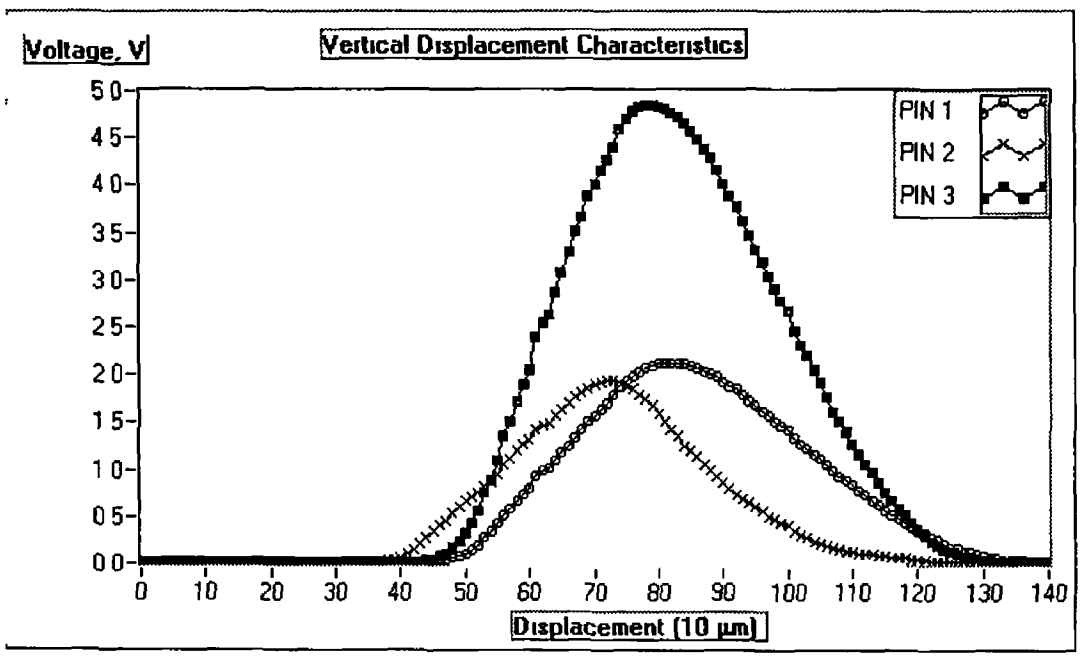

Figure 7 47 Vertical displacement characteristics of 0 025 μm R_a surface roughness sample at incident angle of 60°

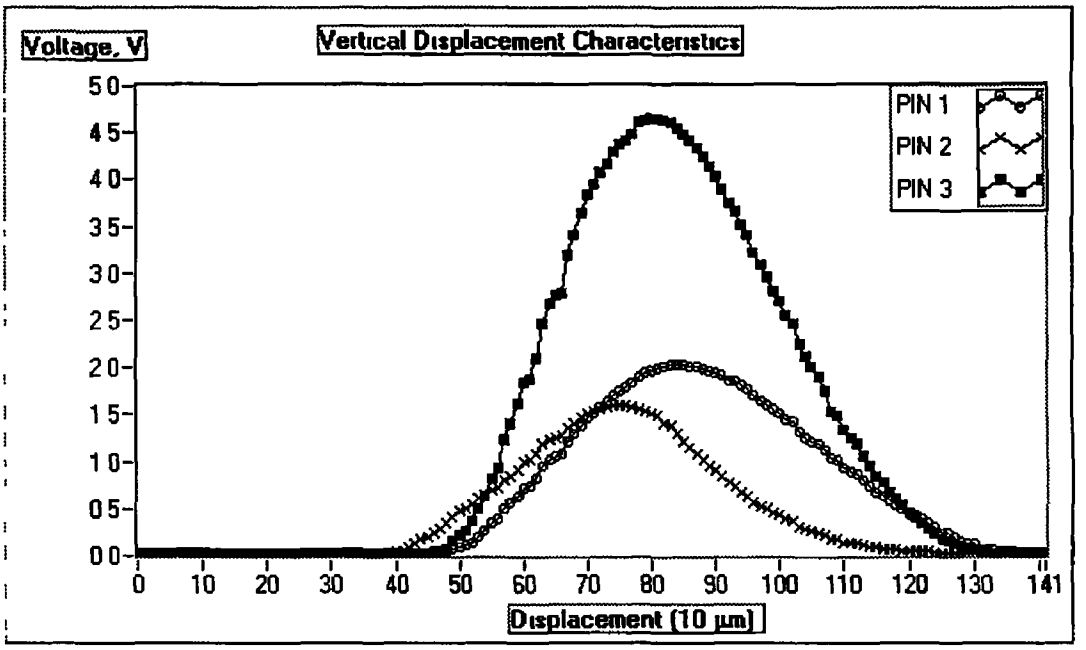

Figure 7 48 Vertical displacement characteristics of 0 05 µm R_a surface roughness sample at incident angle of 60°

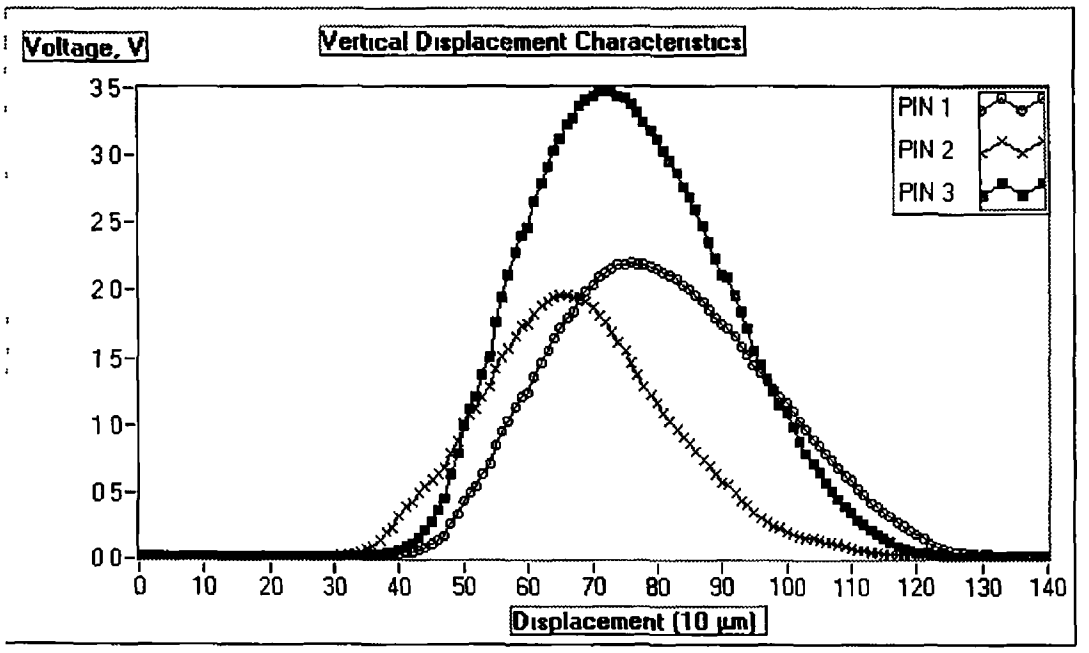

Figure 7 49 Vertical displacement characteristics of 0 1 µm R_a surface roughness sample at incident angle of 60°

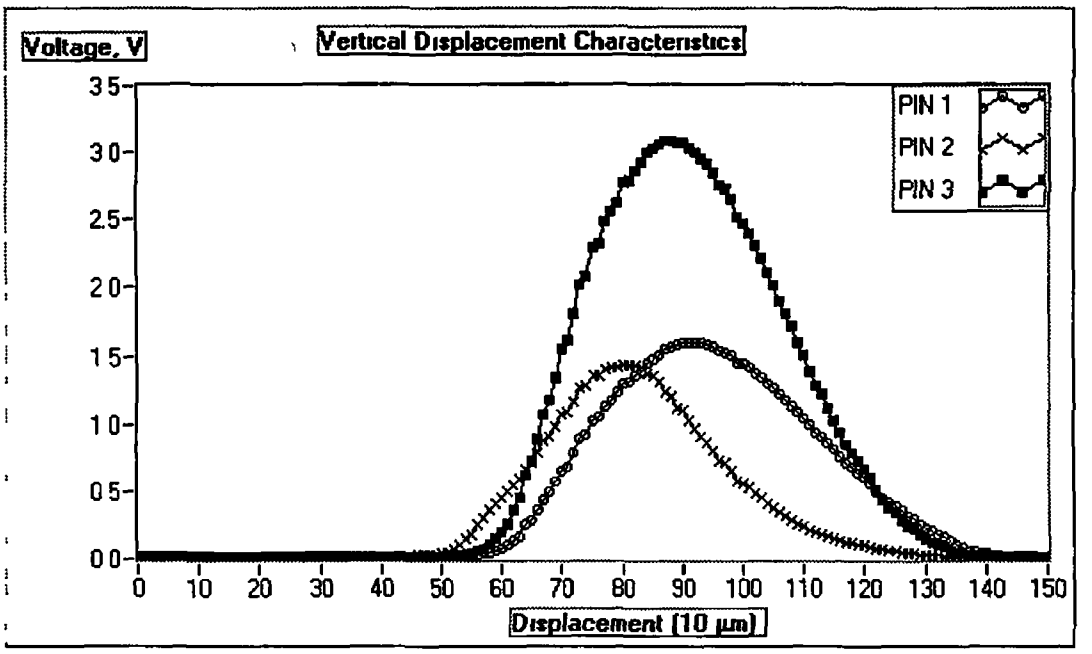

Figure 7 50 Vertical displacement characteristics of 0 2 µm R_a surface roughness sample at incident angle of 60°

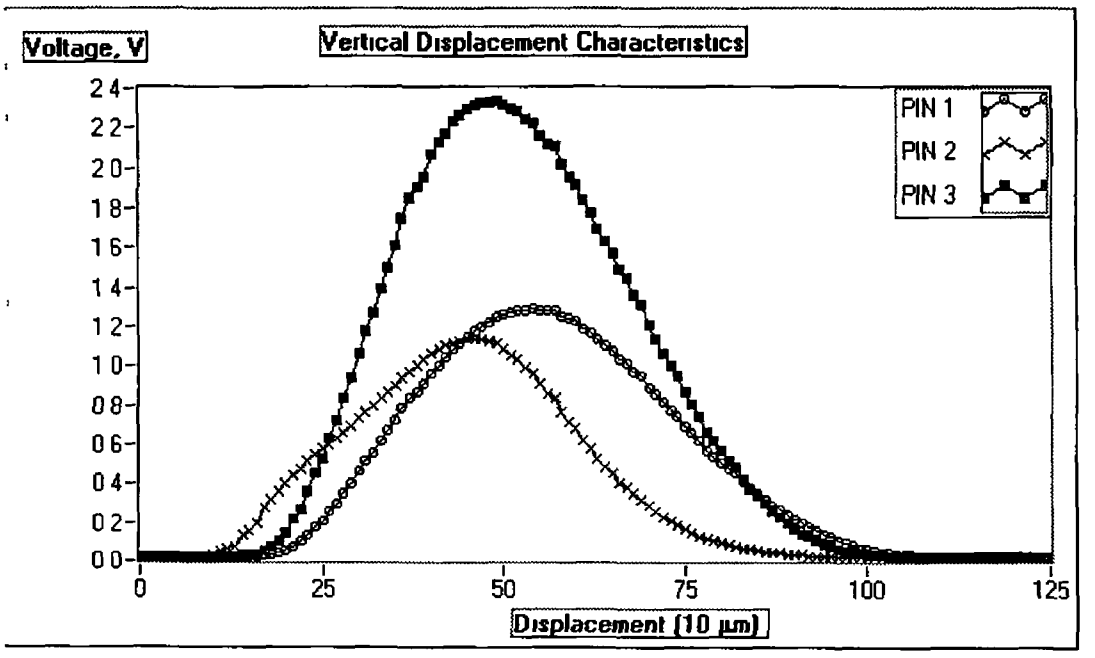

Figure 7 51 Vertical displacement characteristics of 0 4 µm R_a surface roughness sample at incident angle of 60°

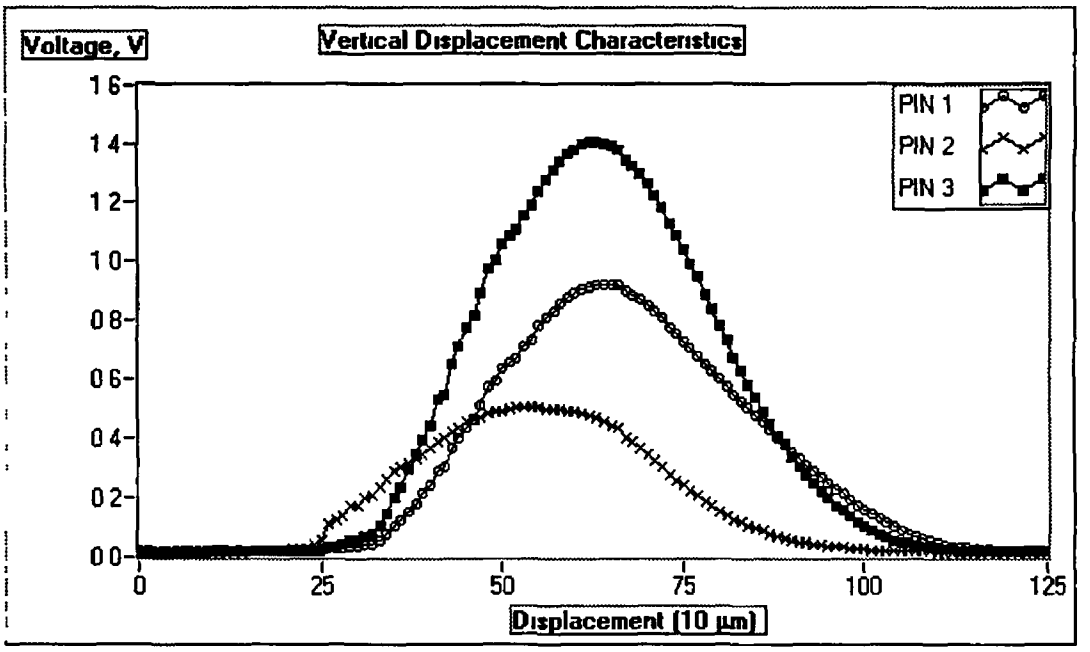

Figure 7 52 Vertical displacement characteristics of 0 8 µm R_a surface roughness sample at incident angle of 60°

7 3 4 Correlation of Displacement Characteristics at Incident Angle of 60° with Surface Roughness Properties

This section presents figures 7 53-7 61 which correlate each peak voltage, and summation of voltages above 50% and 90% of peak voltage, for the vertical displacement characteristics presented in the last section, against RMS surface roughness, average surface roughness, and ten-point height The summation of voltages above 50% of peak voltage appears to correlate most linearly with all three surface roughness parameters For this set-up there appears to be two distinct lines on these graphs, firstly at roughness up to 0 1 mm Ra and secondly above that value In all the figures PIN 3, the photodiode connected to the fibre receiving the highest intensity gives the most consistently successful readings

Equation 7 1 was used to generate the theoretical curve displayed in figures 7 56-7 58 using the data in table 7 3 and equation 3 9 using the voltage value of PIN 3 for the smoothest surface as a datum This theoretical curve is a less accurate than it was for fibres oriented at 45° to the surface, confirming the view that equation cannot be used this sensor to calculate surface roughness directly

Figures 7 53-7 61 all show that the sensor is unsuitable for measurement of surface roughness with PIN 1 and PIN 2 While for PIN 3, the photodiode connected to the fibre that collects the highest intensity, shows a strong linearity between surface roughness (R_a, R_q, and R_z) and reflectivity For PIN 3, the curves can be divided into two different regions above and below 0 1 μm R_a, or its equivalent for R_q or R_z (see table 7 2) The first area consists of the first three points of the curve and is steep, particularly between the second and third points The second area is at those points representing surface roughness values from 0 1 μm R_a to 0 8 μm R_a This area is particularly linear for curves based on the peak voltage of the curve and the sum of voltage values greater than 50% of peak voltage Those based on the sum of voltage values greater than 90% of peak voltage are only slightly less linear for this region The reasons for the difference between PIN 3 and PINs 1 and 2 are discussed later

In figures 7 41, 7 43, and 7 46 the peak of the curve for PIN 2, the highest curve in all figures, for the second point of the curve is higher than that of the first point, a smoother surface The use of extra information from the angular profile of the vertical displacement characteristics, the sum of voltage values above 50% and 90% of peak voltage, eliminates this problem in all of the other figures in this section

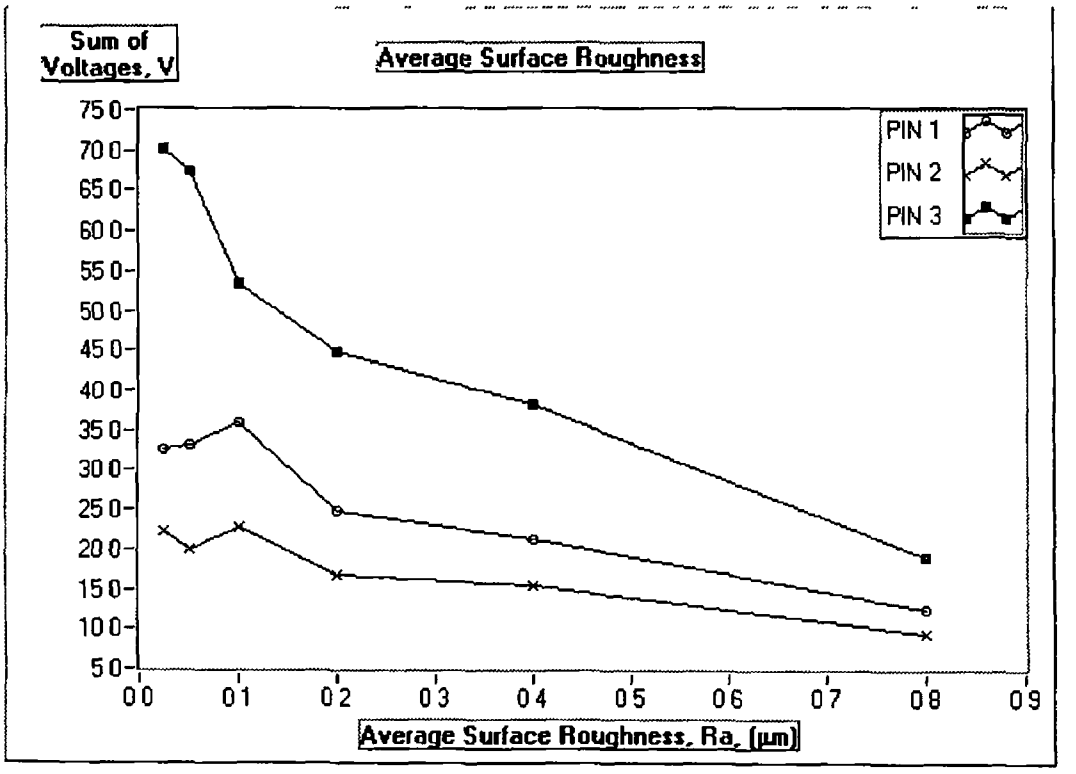

Figure 7 53 Summation of voltage values greater than 90% of peak voltage versus average roughness, R_a, for incident angle of 60°

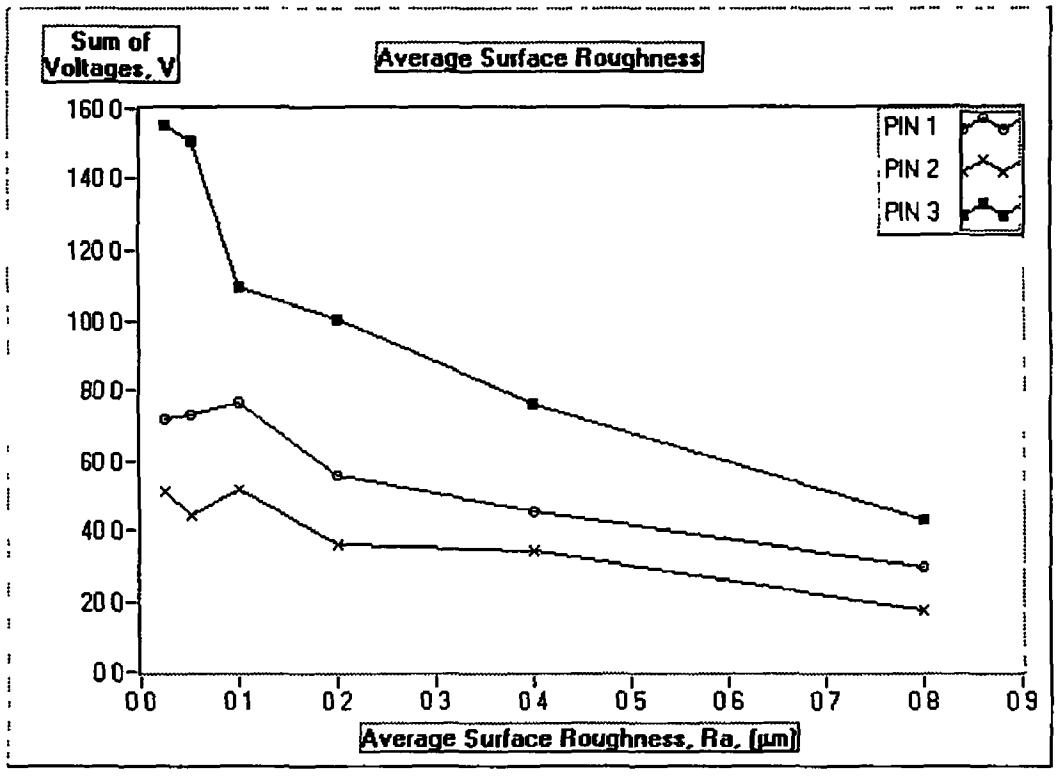

Figure 7 54 Summation of voltage values greater than 50% of peak voltage versus average roughness, R_a, for incident angle of 60°

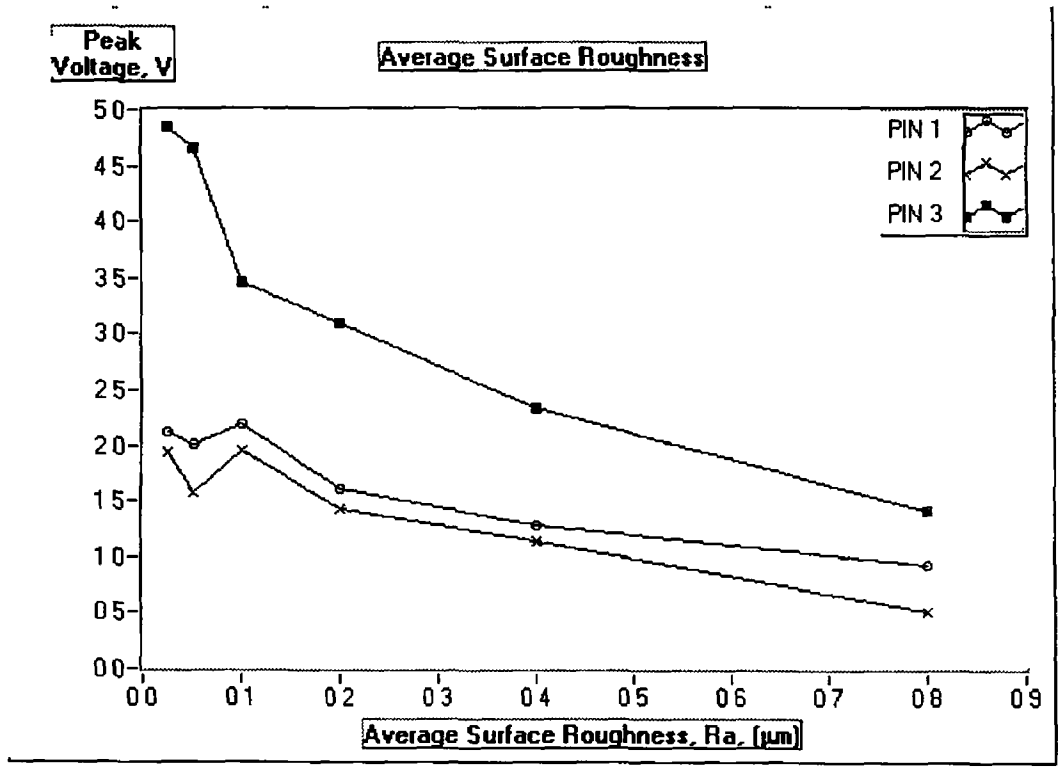

Figure 7 55 Peak voltage values versus average roughness, R_a, for incident angle of 60°

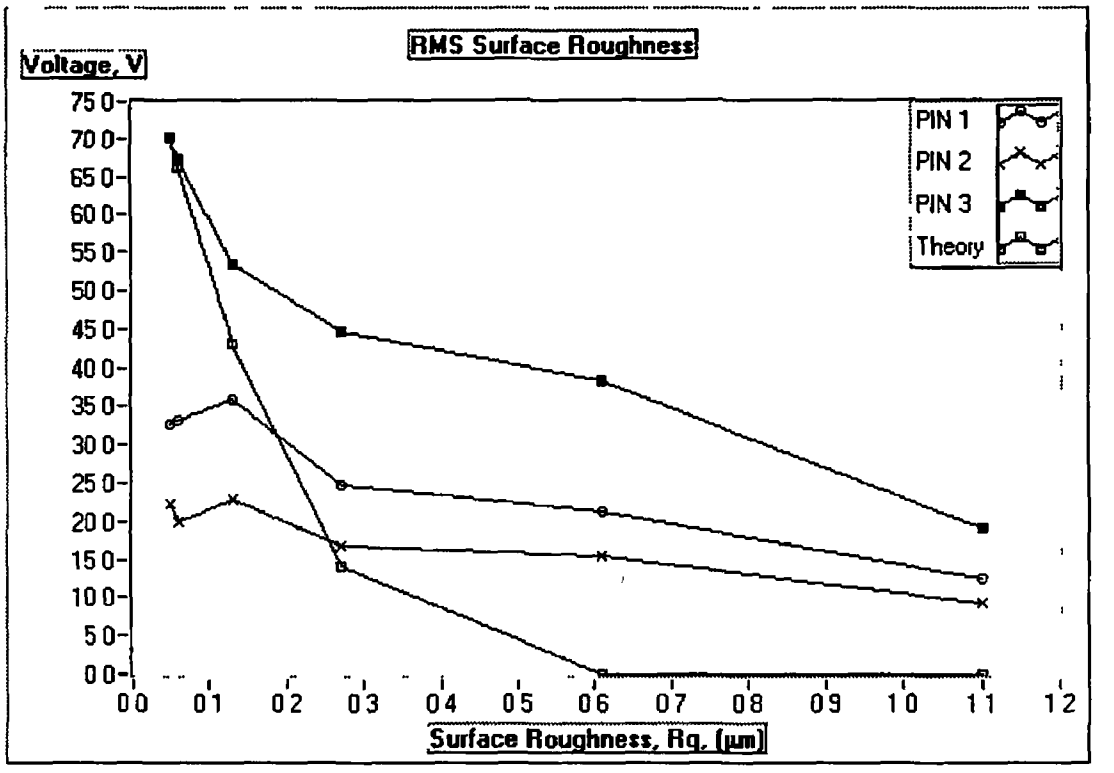

Figure 7 56 Summation of voltage values greater than 90% of peak voltage versus RMS roughness, R_q, for incident angle of 60°

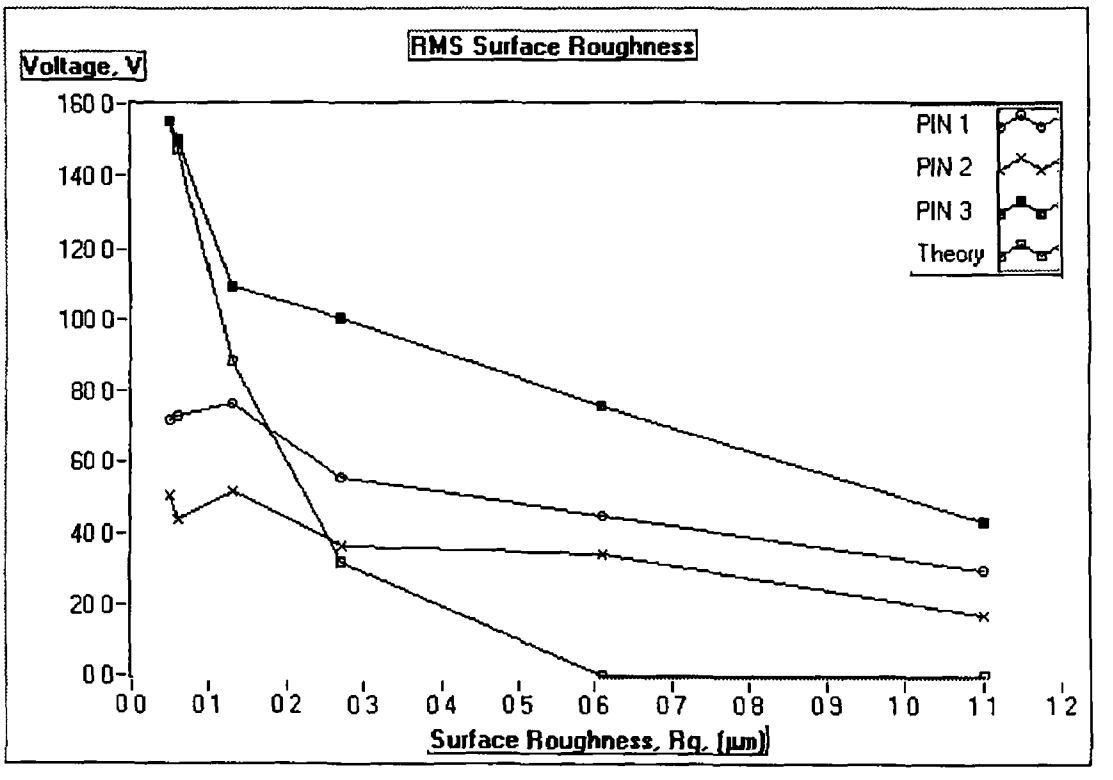

Figure 7 57 Summation of voltage values greater than 50% of peak voltage versus RMS roughness, R_q, for incident angle of 60°

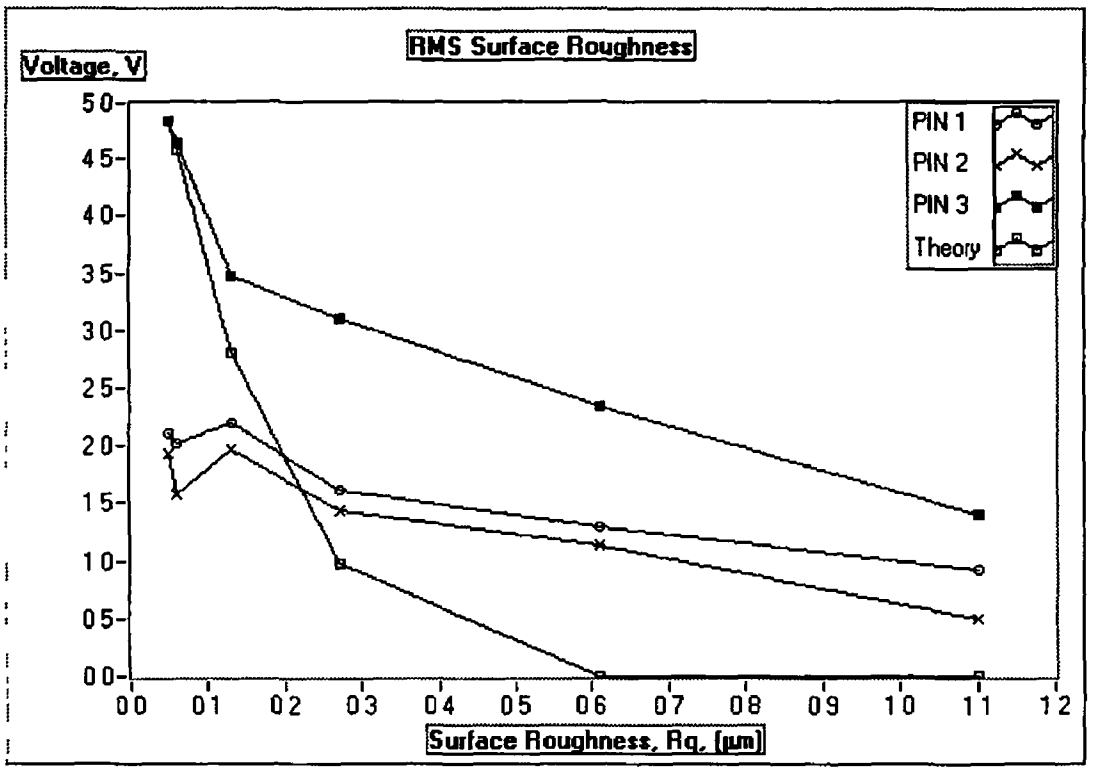

Figure 7 58 Peak voltage values versus RMS roughness, R_q, for incident angle of 60°

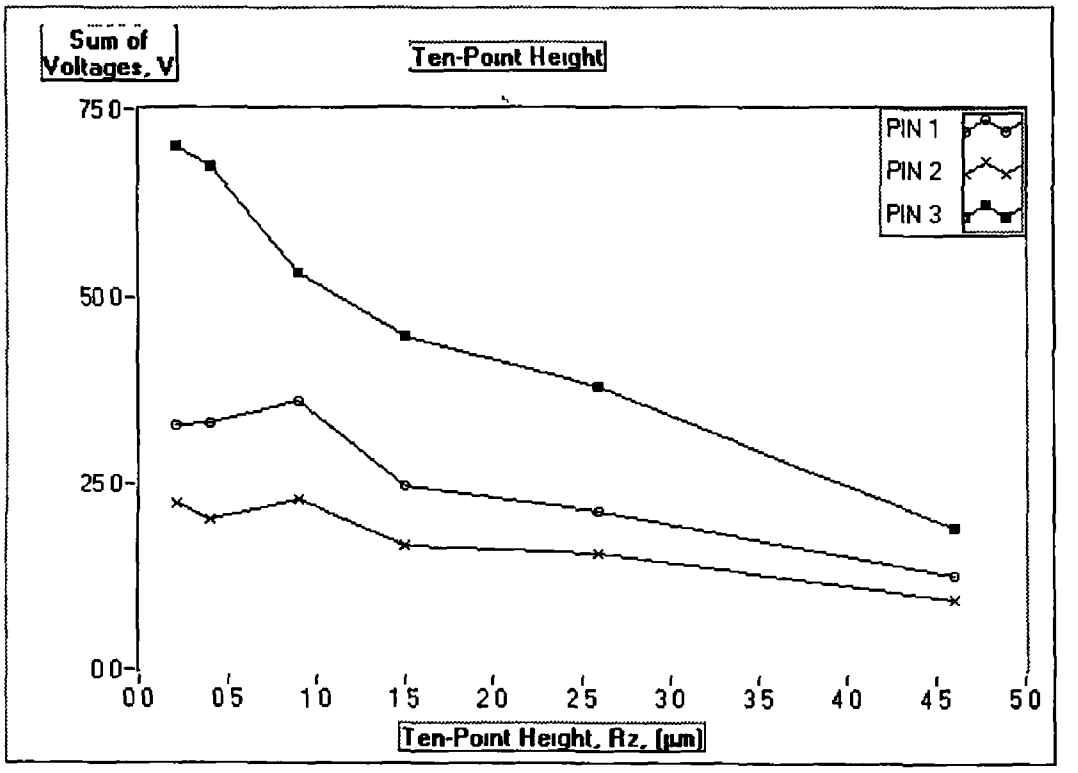

Figure 7 59 Summation of voltage values greater than 90% of peak voltage versus ten-point height, R_z, for incident angle of 60°

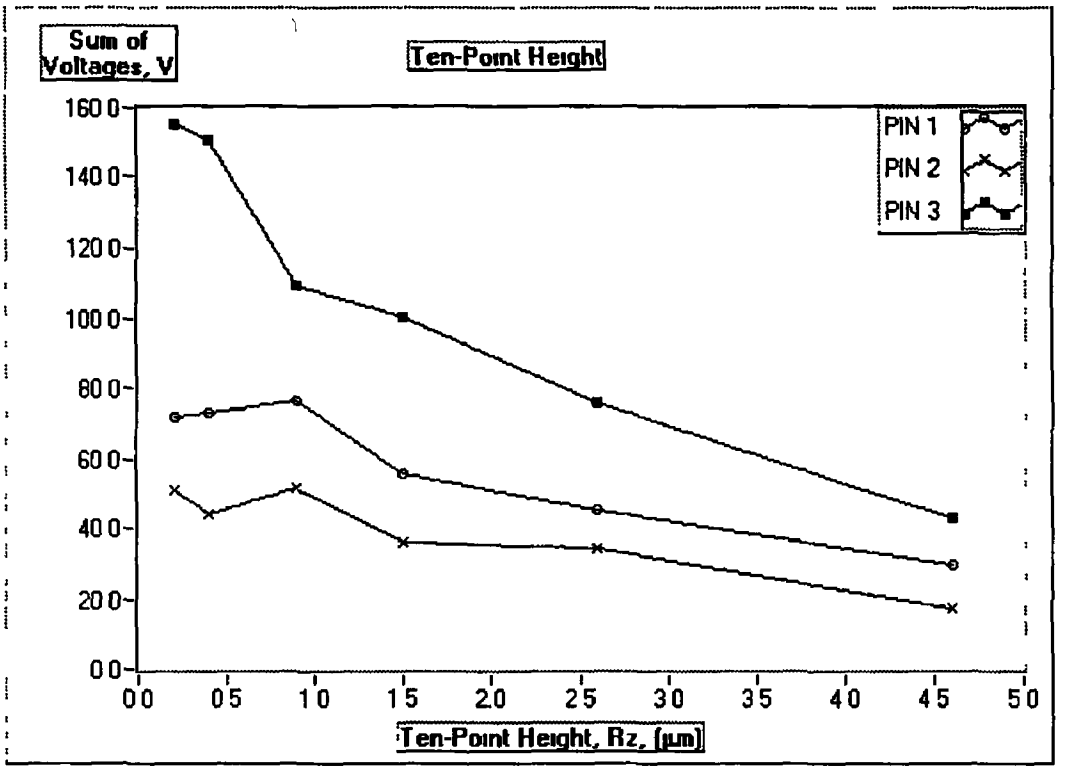

Figure 7 60 Summation of voltage values greater than 50% of peak voltage versus ten-point height, R_z, for incident angle of 60°

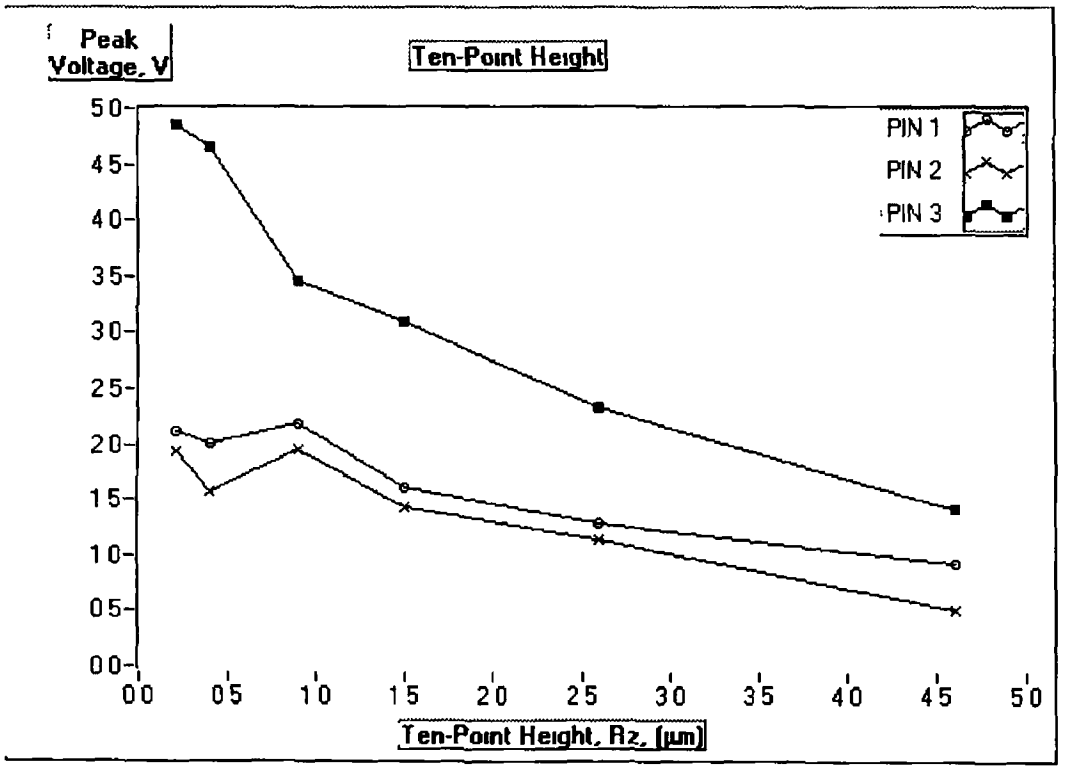

Figure 7 61 Peak voltage values versus ten-point height, R_z, for incident angle of 60°

7 3 5 Drift of Sensor System over Time

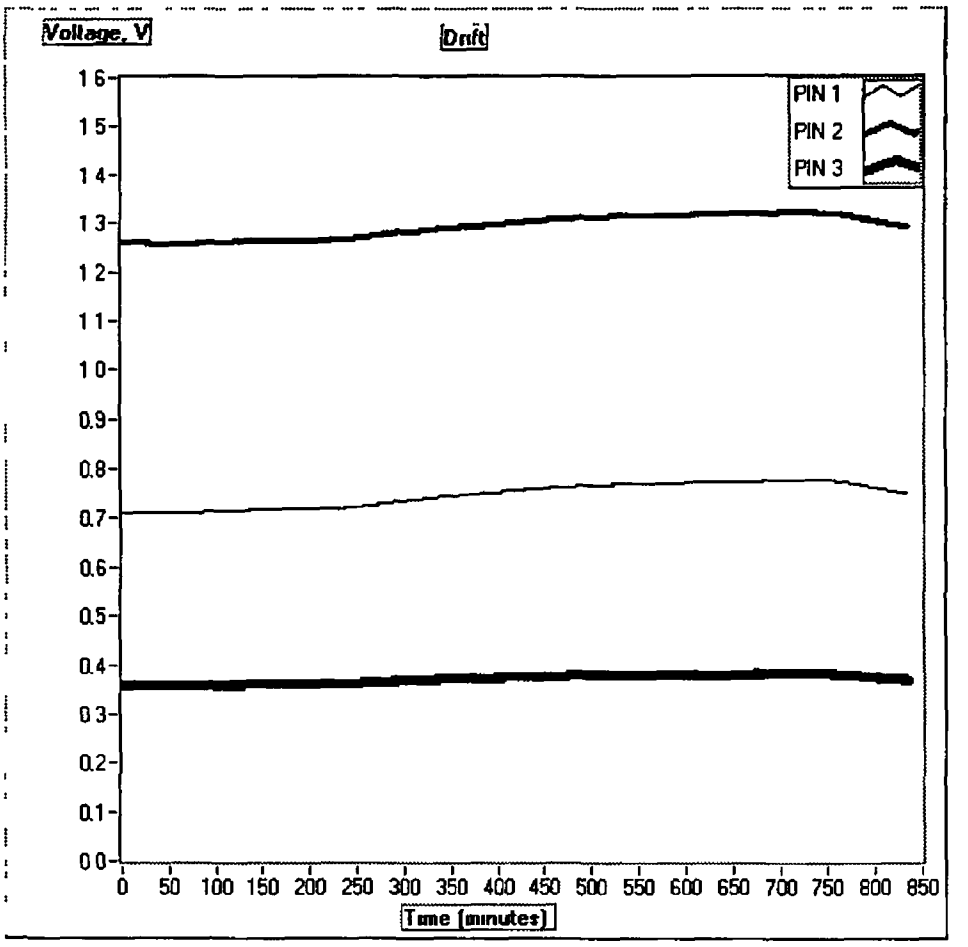

Figure 7 62 Drift of Signal System over time – Light Condition

Figure 7 62 shows the drift of the sensor system over night, from 9 PM to 11 AM This is caused by the drop in ambient temperature and its effect on the electronic components of the signal generation and signal detection circuitry, as discussed before Figure 7 62 and 7 63 were compiled by the using the algorithm presented in figure 6 6, with the addition of a timed switching mechanism, the program controlled the virtual instrument to perform a reading once a minute Both of these figures were determined using identical signal processing techniques to the other measurements of the surface roughness sensor Table 7 6 shows the maximum and minimum voltage peaks of the voltage drift data shown in figure 7 62 and the difference between these values Ultimately, the accuracy of measurement is affected by drift, primarily thermal drift The sensor's performance varies with the seasons and the time of day, a referencing scheme is required

Photodiode	Maximum Voltage	Minimum Voltage	Difference
PIN 1	0 778 V	0 711 V	68 mV
PIN 2	1 322 V	1 257 V	65 mV
PIN 3	0 356 V	0 356 V	27 mV

Table 7 6 Maximum voltage, minimum voltage, and the difference between for data presented in figure 7 62

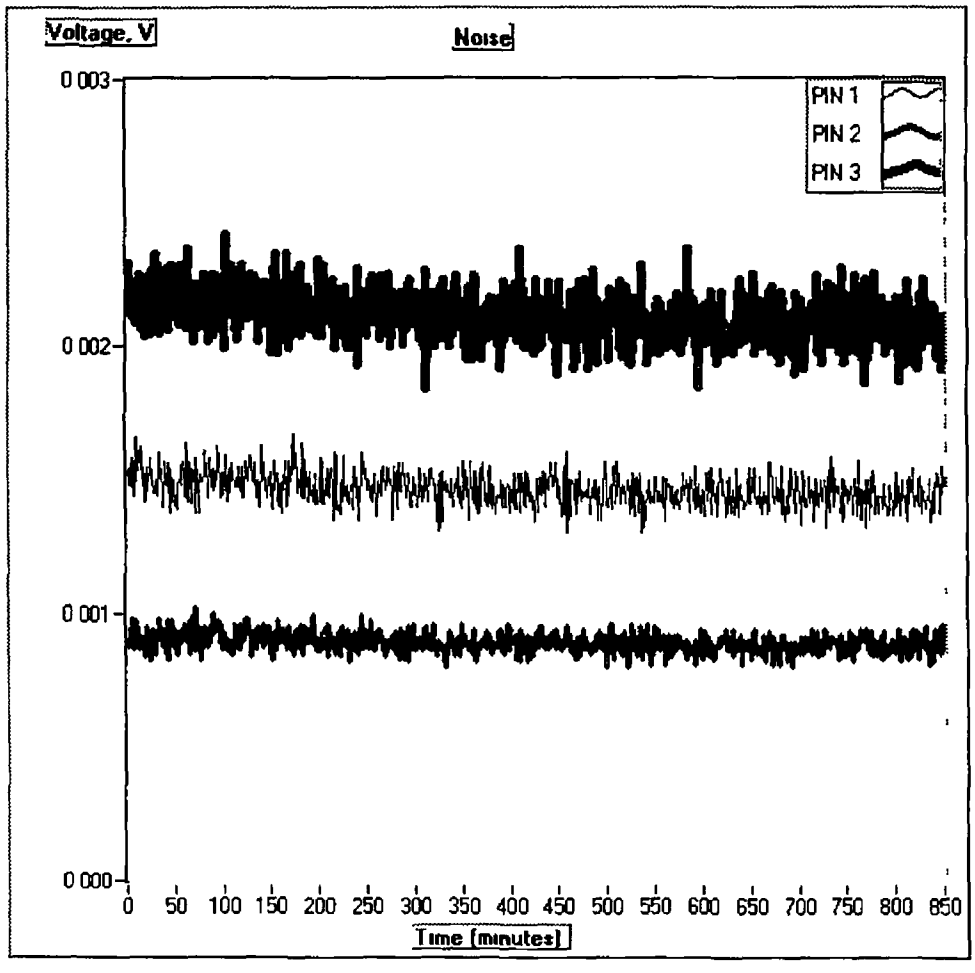

Figure 7 63 Noise characteristics of system over time – Dark Condition

Figure 7 63 shows the variation in background noise over time The PIN photodiodes were isolated from any optical radiation while these measurements were taken The total size of this dark condition signal is of the order of a couple of mV and is caused by the following photodiode dark current and the voltage offset of the op-amp This illustrates how the dark condition noise levels are well below 1 mV, for all the PIN photodiodes

CHAPTER EIGHT

8 Discussion of Experimental Results

This chapter discusses the experimental results presented for both sensors systems in the previous chapter

8 1 Surface Defect Sensor

8 1 1 Sensing of Holes

Through Holes

The surface maps presented in section 7 2 6 show that the sensor scanned all the through holes (3-mm diameter) successfully for either of the collecting fibres A high level of contrast was achieved even for rough surfaces, such as the copper plate, or diffusely reflecting surfaces such as the polycarbonate surface These results were achieved from choosing a cut-off voltage level of 2 Volts arbitrarily for all surface plates

Blind Holes

The performance of the sensor in measuring blind holes (2-mm diameter and 0 6-mm depth) was more critically affected by the surface properties of the plate In this case the surface properties of the machined surface of the hole is the critical factor The vertical displacement characteristics are measured for the surface of the plate, from these the vertical stand-off distance of the sensor is chosen When the surface of the blind hole is machined the surface does not necessarily behave in an identical manner to surface of the plate The surface of the blind hole may be slightly curved and this can result in inadequate sensing of the hole, this can be seen in the spike shown in figure 7 17, and the centre of the surface map in figure 7 25(a) Sensing of blind holes is critically affected by the choice of the vertical stand-off distance as can be seen in figure 7 25(b), where the sensing fibre is positioned In addition, edge effects such as burring may cause the edge of a hole to be sensed irregularly Even when the centre of

a blind hole is not sensed well, such as in figure 7 25(b) or figure 7 29, the edges of a surface tend to be sensed more successfully A hole is sensed even when it is sensed imperfectly

Geometry of Holes

This purpose of this section is to discuss the efficacy of this sensor in measuring the geometry of a hole The diameter, shape and position of the hole are what is meant by the geometry of a hole

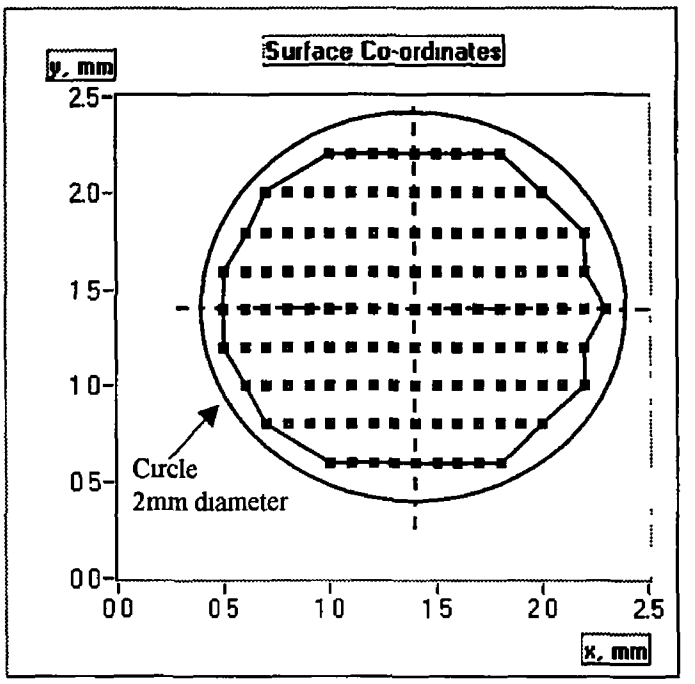

Figure 8 1 Through hole in brass plate – 2 mm-diameter

It is clear that the surface maps presented in section 7 2 6 detect the presence of a hole but they do not represent the shape of a hole perfectly Figure 8 1 shows an example of a surface map with the boundaries of the hole outlined From this figure it can be seen that the circular hole is transformed to a many sided shape by the measurement of this sensor system Figure 8 1 also shows a 2-mm-diameter circle superimposed on the surface map This shows how the sensor always represents the hole at a smaller diameter than the real value Perhaps this is caused by the low resolution of measurement – one reading for every 0 1 mm The choice of the cut-off voltage also

affects the size of the sensed hole – it takes about two readings for the sensor to switch, in this case about 200 μm

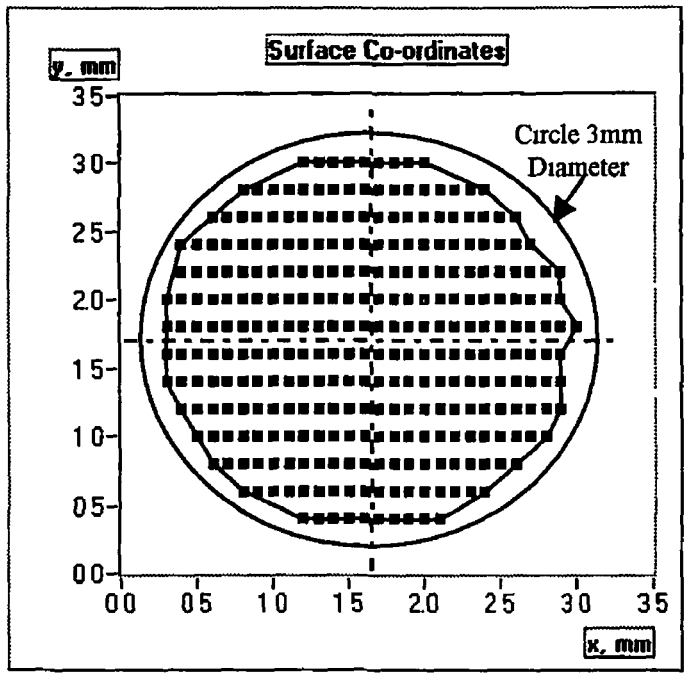

Figure 8 2 Blind hole in brass plate – 3mm-diameter

The blind holes are of 3-mm diameter, figure 8 2, and the through holes are of 2-mm diameter, it can be seen that the larger diameter holes appear to be more circular than the smaller diameter holes This suggests reproduction of the geometry of the hole will deteriorate further for holes smaller than 2 mm the, though they will probably still be sensed

A simple algorithm could consist of finding the lowest and highest x co-ordinates and subtracting one from the other, this could then be averaged against the same result performed with the y co-ordinates It is likely that the measured diameter of the hole will be about 300 μm less than the same measurement performed with Vernier calipers Finding the centre of the hole in x co-ordinates could be performed using the mid-point of a line joining the highest and lowest x co-ordinates, and similarly for the y co-ordinate of the centre This procedure was used to determine the centrelines in figure 8 1 and 8 2, their intersection determines the centre of the superimposed circles

8.1.2 Stand-off Distance

In general the stand-off distance of the end face of the optical fibres from the surface of the sample plates was between 2 and 3 mm. For online operation using present construction of the experimental rig this is unsatisfactory, as the fibres are unprotected. If protection of the fibre was satisfactorily incorporated as part of the mechanical design of the sensor this stand-off distance may be adequate.

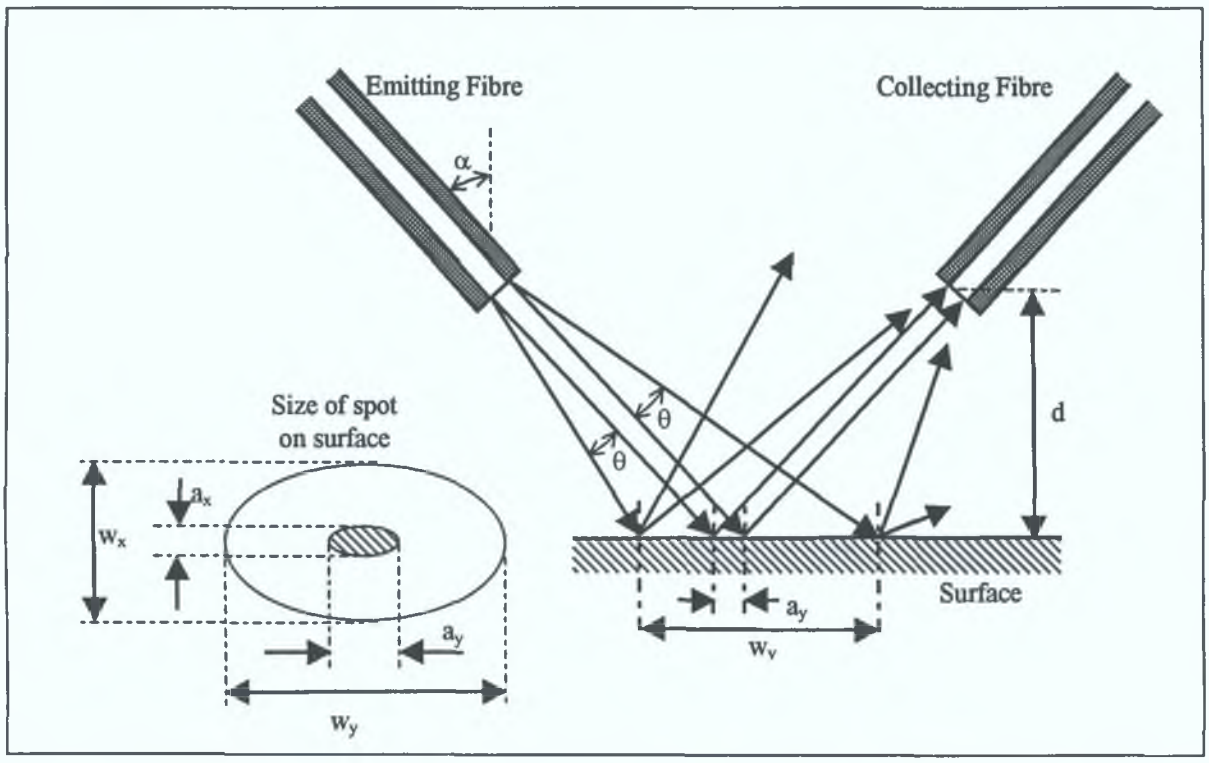

Figure 8.3 Dimensions of radiated area on surface

Increasing the stand-off distance, at least for the present design, has disadvantages. Both sensors use bare fibres to emit and collect optical radiation; the sensors are described by figure 8.3. The spatial limits of emission of optical radiation as defined by the numerical aperture are shown. θ is related to the numerical aperture as defined in equation 2.4. α is the incident angle of the fibres. Four dimensions of interest are detailed in figure 8.3: w_x, w_y, a_x, and a_y. The elliptical spot with major axes w_x and w_y defines the extents of the radiated spot on the surface. The elliptical spot with major axes a_x and a_y defines the extents of the surface area that contributes to specular reflection. Appendix D derives values for w_x and w_y, increases in d, θ, and α result in increases in both w_x and w_y. The dimensions of a_x and a_y will be considered

approximately equal to the diameter of the fibre core, a This is true for a_x but untrue for a_y which is also dependent on the angle of incidence

It is important to note that the dimensions of the radiated area are highly dependent on the stand-off distance, d, and on the numerical aperture The size of the specularly reflecting area is almost wholly dependent on the collecting fibre's core size

In addition, when the specular spot approaches the centre of the radiated area the intensity sensed by the photodetector approaches its peak value When the specular spot approaches the periphery of the radiated area the intensity drops below its peak value The cause of each receiving fibre having widely different peak voltages is because each fibre takes a different path through the radiated spot Lower peaks are caused from this path being at greater displacement from the centre line of the radiated area

For a rough surface, which doesn't reflect specularly, a proportion of the collected radiation is attributable to diffuse reflection from outside the specular spot As the specular spot becomes smaller in proportion to the radiated area, at greater stand-off distances, a lower proportion of emitted radiation is incident on this area For rough surfaces diffuse reflection becomes the predominant factor, while for smooth surfaces the intensity of reflection decreases very significantly If the proportion of light that reflects specularly is predominant the spatial resolution of measurement can be considered comparable to the core size of the receiving fibre This enables the sensor to detect edges effectively When diffuse reflection is considerable the sensor is less sensitive to the edge of a hole This is significant in determining the size of the smallest hole that can be sensed

To increase the stand-off distance the optical design of the system needs to change, an emitting fibre with lower numerical aperture could be chosen The defect sensor used 62 5/125-μm fibre with numerical aperture of 0 275, $\theta = 16°$, while standard 50/125-μm fibre has numerical aperture of 0 2, $\theta = 11\ 5°$, that would allow a slightly higher stand-off distance The incident angle also affects stand-off distance, higher incident angles having lower stand-off distances, for the same lateral separation of the fibres

The choice of incident angle also affects the ability of the sensor to sense blind holes A higher intensity light source could be chosen This would introduce further consideration of laser safety, in particular for online use

8 1 3 Effect of Misalignment

This sensor assumes that the surface is aligned so that the emitting and receiving fibres are at equal angles to the normal, in practice this is not always true Misalignment is one of the factors including vibration, light source fluctuation etc that this sensor is designed to tolerate Misalignment is particularly critical to this sensor's operation when the vertical range, D, as defined in figure 4 5, is small In this case the vertical displacement characteristics will shift From analysis of the results it can be seen that in no case did the sensor sense a hole when the plate surface was present The effect of misalignment was most often seen when the surface of a blind hole was incorrectly sensed such as in figure 7 29, i e due to machining of the blind hole surface

8 1 4 Effect of Surface Characteristics

Table 7 1 shows the surface roughness characteristics of each of the surfaces This does not fully describe each plate as regards reflection – the material properties of each surface contribute to an absolute level of reflectivity Where polycarbonate is not exceptionally rough it has by far the lowest reflectivity In another case the reflectivity of the copper plate can be quite high though it is very inconsistent due to the rough, grainy nature of the plate's surface In this way the sensor operates more comfortably in sensing holes in polycarbonate plate than it does for copper plate

It is important to note that this is not an all-purpose sensor, it is very dependent on the surface or surfaces to be sensed Generally the sensor will work best with smooth reflective surfaces and with through or deep blind holes As the sensor reaches its limits it will become more unreliable This thesis discusses the design and development of a sensor to measure holes in a surface based on the premise that these holes are defects In fact this sensor will work best for detecting the presence of holes

or edges which have been machined or punched in material An array of such sensors could inspect the position and size of holes in industrial use at high speed

8 2 Performance of Surface Roughness Sensor

This sensor is ultimately intended for use as an online sensor though in this incarnation the sensor operates by assessing the displacement characteristics of the surface and then analysing this data – this is not wholly suitable for online use and requires some changes to develop into an online sensor This section discusses the results of section 7 3 with regard to improving this sensor

With single fibres collecting reflected radiation the sensor was too sensitive to variation in position to function successfully as an online sensor It is planned to construct a sensor that collects a larger proportion of reflected light through use of a lens or of a fibre bundle For this reason section 6 3 presents graphs that sum the voltage levels of the displacement characteristic that were above a certain percentage of peak voltage Collecting a larger proportion of reflected light would enable a larger stand-off distance

8 2 1 Stand-off Distance

The performance of this sensor is affected by the factors mentioned above in section 8 1 2 The reflected signal comprises of the specular reflection and the diffuse reflection that is collected by the receiving fibre For this reason the sensor is not a true measure of Total Integrated Scattering The proportion of the signal that is contributed by specular reflection decreases as the stand-off distance increases The area of specular reflection does not affect the performance of this sensor, so a lensed or bundled sensor could only improve the performance of the sensor, particularly by extending the stand-off distance and by gathering the reflected optical radiation more efficiently

8 2 2 Effect of Misalignment

Tables 7 4 and 7 5 show through the variation of the peaks of the two less intense traces how misalignment affects the operation of this sensor While these curves are affected by the surface roughness properties of the particular specimen it is clear that measurement is also sensitive to other factors, these two curves are a less confident indicator of the surface roughness characteristics Figure 8 4 describes the pitch and roll angles for a surface sample Pitch is rotation around a lateral axis of the surface sample and roll is rotation through a lateral axis of the surface sample perpendicular to the pitch axis In this way misalignment is defined by these angles For the purposes of this project no attempt was made to control pitch and roll

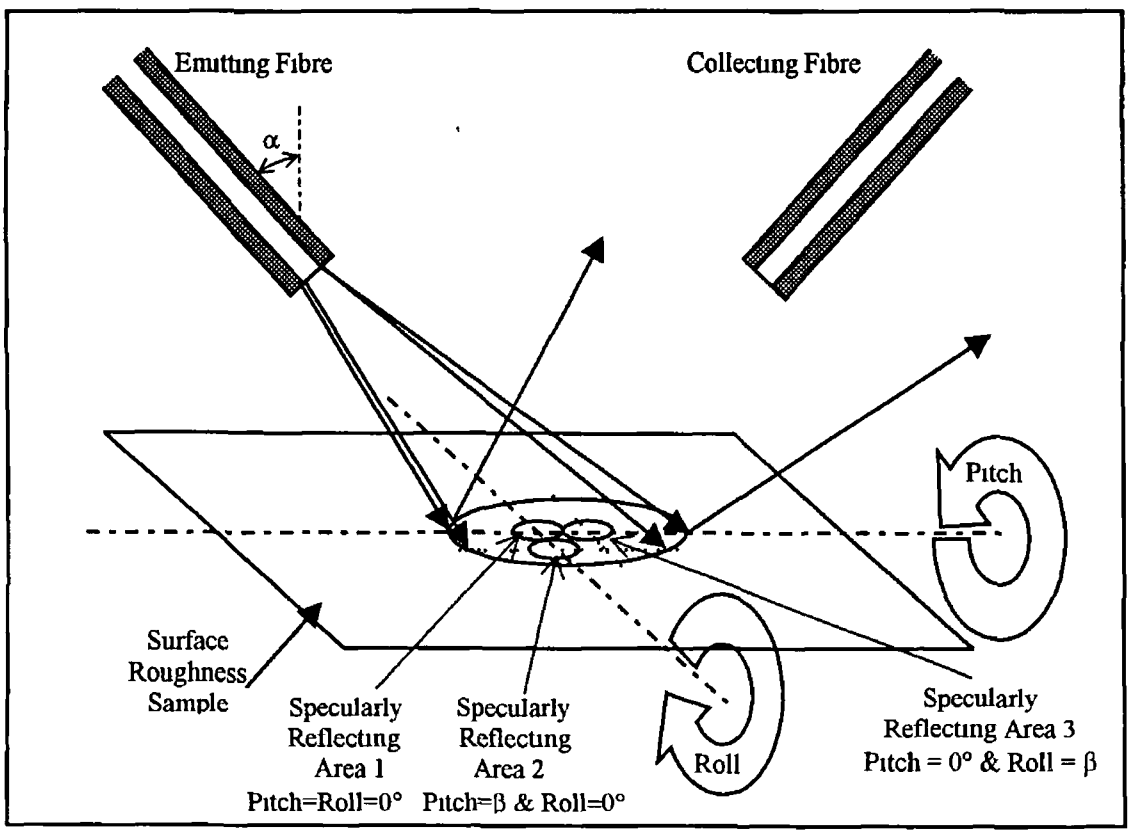

Figure 8 4 Surface Misalignment – Pitch and Roll angles

Figure 8 4 shows the sensitivity of this sensor to pitch and roll angle Specularly reflecting area 1 describes the optimum set-up of this sensor, the position where the receiving fibre, emitting fibre and surface roughness sample are all perfectly aligned, this is the position that the sensor records peak intensity Emphasis is placed here on

the orientation of the surface roughness sample as the fibre positioning is assumed to be imperfect but fixed, while that of the surface roughness sample changes for sample considered Specularly reflecting area 2 describes the effect of varying the pitch angle through an angle b while roll angle is still 0° The collected intensity drops relative to specularly reflecting area 1, this is the peak intensity for a vertical displacement characteristic taken at these pitch and roll angles Similarly for specularly reflecting area 3 if roll angle is varied while pitch is preserved at 0° its position shifts away from peak intensity Changing these angles also changes the shape of the specularly reflecting area and displacement further affecting the reflected signal

It may be argued that a fibre that is more centrally positioned, i e positioned so that it collects a higher intensity of optical radiation, is less affected by misalignment of the surface than a more peripherally positioned fibre This is explained by the fact that at peak intensity there is less sensitivity to displacement, while less peripherally positioned fibres experience the high sensitivity to displacement that permits their use in the precision measurement of displacement For this reason the fibre that collects the highest peak intensity will be discussed in the next section and other traces will be ignored

8 2 3 Correlation with Surface Roughness Properties

It was decided to correlate roughness against sum of values above a percentage of peak intensity as well as against peak intensity because of the effect that misalignment of the surface roughness sample has on performance of the sensor Correlation against the sum of values above a certain percentage of peak intensity makes fuller use of the information gathered through the vertical displacement characteristics and gives an indication of the performance of a lensed or bundled sensor that collects reflection from a larger area Figure 7 40 shows the peak intensity of each displacement characteristic plotted in section 7 3 1 plotted against the average roughness of the samples It can be seen that the smoothest sample, 0 025 R_a, has a lower peak intensity than that of a rougher sample, 0 05 R_a This result is erroneous as the 0 025 R_a sample is visibly more mirror-like than the 0 05 R_a sample The stylus measurement of roughness properties, table 7 2, measured values for R_a and R_q that were quite close for these two samples Though this may be because these

measurements were close to the limits of the stylus Figures 7 38 and 7 39 use the percentage method and use the gathered results to reduce the effect of misalignment

Theoretical Curve versus Measured Curve

A curve based on the theoretical equation derived by Beckmann and Spizzichino [72], equation 3 9, was included with the curves correlated against RMS surface roughness The results achieved with this system do not agree with this equation There are a number of reasons for this As mentioned previously the reflected signal was not isolated from diffuse reflection This accounts for the fact that for all of the graphs the measured value exceeds the theoretical value The stylus measurement of RMS surface roughness may be inaccurate or unrepresentative

Equation 3 9 is limited to scattering ratios above 0 6 Thus, smoother surfaces, less than 150 nm R_q, are likelier to conform to equation 3 9, more rigorous experiment with smooth surfaces would be necessary to investigate this This equation is limited to application with smooth surfaces It is not important that the sensor does not obey equation 3 9 if the sensor is consistent and reliable

Incident Angle: 45° versus 60°

Equation 3 9 includes the incident angle of the sensor Figures 4 8 and 4 9, using equation 3 9, contrast the effect of these two incident angles Higher incident angles should have a more gradual decrease in scattering ratio, and correspondingly in specular reflectivity

The results plotted in section 7 3 2 for experiments at incident angles of 45° include a steep incline from first two smooth specimens, 0 025 and 0 05 R_a, to the fourth specimen, 0 2 R_a Thereafter the points for rougher surfaces, greater than 0 2 R_a, show a gradual decrease that is less useful for roughness measurement 0 2 R_a is assigned as the endpoint of the steep incline but further experiment with specimens of roughness of between 0 1 R_a and 0 2 R_a would clarify the situation The design of this sensor depends on application, e g in an industrial application the critical surface roughness level determines the incident angle chosen

The results plotted in section 7 3 4 for experiments at incident angles of 60° include a steep incline from first specimen, 0 025 R_a, to the third specimen, 0 1 R_a, similar to the results plotted in section 7 3 2 Roughness specimens from 0 1 R_a to 0 8 R_a then show a gradual decrease, which may be useful for roughness measurement in contrast to results at 45° incident angle The influence of incident angle included in equation 2 18 is borne out by the results of this project – the sensor operating at an incident angle of 60° functions over a larger range of surface roughness

Roughness Characteristics

Equation 3 9 uses RMS surface roughness, results are presented using average surface roughness, RMS surface roughness and ten-point height and it is difficult to quantify which property correlates most closely with surface reflectivity The curves for each different roughness property differ very little As the sensor doesn't measure any roughness property absolutely it may be most properly termed a surface finish sensor

This project did not investigate a number of surface roughness properties that have influence over reflection from a surface, such as surface spatial frequency, surface slope, and wavmess Surface spatial frequency is particularly important as it can vary considerably for surfaces with equal average or RMS surface roughness The effect of differing surface spatial frequency on light scattering measurement of surface roughness is noted in the literature survey [55,57,99]

CHAPTER NINE

9 Conclusions and Recommendations for Further Work

These conclusions examine the results that were achieved by the systems Recommendations for further work examines the performance of the design of the systems with regard to possible improvements

9 1 Conclusions

The objective of this project was the development of a fibre-optic sensor system that would form a unit element of a hnescanmng sensor for sensing the surface properties of metal plate

Surface Defect Sensor

- Holes of 2 mm diameter can be sensed on the surface of plates of the following materials stainless steel, brass, polycarbonate, and copper The roughness and reflectivity of these plates affects the performance of the sensor All 2-mm diameter through holes were sensed successfully Blind holes of 3-mm diameter and 0 6-mm depth were sensed in plates of all materials except the copper plate

- An adequate representation of the diameter, shape and position of the holes is given for 2-mm and 3-mm diameter holes As the diameter of the hole increases the representation of the shape improves

- The spatial resolution of measurement is around 100 to 150 μm Surface roughness and stand-off distance can affect the spatial resolution as a higher proportion of collected radiation contributed by diffuse scatter will increase the spatial resolution

- Choice of the stand-off distance and cut-off voltage determines the depth of the shallowest blind hole that can be sensed

- There is less contrast between the absence and presence of a surface when sensing blind holes than when sensing through holes – the surface finish of the surface of the blind hole affects detection of these holes When the surface finish of a shallow blind hole and the plate itself differ the contrast achieved may be limited For this reason the blind hole in the copper plate was not sensed successfully The edges of a blind hole are particularly sensitive to scanning even when the interior of the hole is not sensed

- The operation of the sensor was relatively unaffected by misalignment, light source fluctuation, vibration, ambient light, and surface roughness These factors never caused a point on a plate's surface to be sensed as a hole (for a cut-off voltage of 2 Volts)

- This sensor has the potential for high-speed operation In practice the limiting factor measurement is the speed of the data acquisition card – 100,000 cycles per second or 50,000 cycles per second for two channels The above disregards the limitation introduced by taking manual measurements

Surface Roughness Sensor

- The results indicate that for an incident angle of 60° the range of measurement extends from 0 025 μm R_a to 0 8 μm R_a This range consists of two sections, firstly a steep section between 0 025 μm R_a and 0 1 μm R_a and a less steep section between 0 1 μm R_a and 0 8 μm R_a For an incident angle of 45° the range of measurement was shorter from 0 025 μm R_a to 0 2 μm R_a – this range consists of one steep section This shows the effect of incident angle on the performance of the sensor

- The sensitivity of the curves of correlation of peak intensities against surface properties are less consistent than the corresponding curves based on the correlation sum of voltages above a certain percentage of peak voltage against surface properties This suggests that a sensor which collects optical radiation from a larger area would have superior performance

- The experimental results do not conform to the theoretical equation proposed by Beckmann and Spizzichino [72] The most likely reason for this is that the design of the sensor doesn't isolate specular scatter from diffuse scatter This lack of isolation is probably responsible for the extended range of the sensor for operation at an incident angle of 60° It is not necessary for this sensor to conform to equation 3 9 if it operates consistently and reliably

- The sensitivity of this sensor to misalignment was clearly seen in the poor performance of the signal collected by the peripherally positioned fibres The centrally positioned fibre was less sensitive to misalignment

- Correlation against average surface roughness, RMS surface roughness or ten-point height performed equally well This suggests that all of these are related to surface reflectivity Further work needs to be performed in assessing the performance of the sensor with surface specimens of similar surface roughness but differing surface spatial frequencies and surface specimens prepared through differing machining processes

- The principle of operation of this sensor, recording the displacement characteristics for a specimen and performing data analysis, caused the operating speed to be very slow It is necessary that the design of the sensor be improved so that a single measurement is correlated against surface finish Collecting optical radiation from a larger area may allow this Recommendations for further work contains some suggestions to achieve this through design improvement

- Figure 7 61 shows the drift that occurs with temperature with the use of a unreferenced fibre-optic sensor There is a need for a referencing scheme – details of referencing for fibre-optic sensors can be found in section 2 2 2

9 2 Recommendations for Further Work

This section provides recommendations for further work through analysing the performance of the design of the sensor and pinpointing components of the design of the sensors that need improvement The possibility of the wider application of optical technology is indicated

9 2 1 Optical Design

Optical Fibres

The use of optical fibres in these sensors contributes to the performance of the sensors In both sensors the specularly reflective area of the surface is comparable to the core size of the optical fibre In the case of the surface defect sensor this is the factor that allows the spatial resolution of measurements to be around 0 1 mm In the case of the surface roughness sensor the core size of the fibre contributes to the sensitivity of the sensor to angular misalignment and limits the sensor with regard to online use Both sensors suffer through low stand-off distances particularly the surface roughness sensor

Three potential solutions to these problems are (i) a higher intensity light source could be used, (ii) the emitted optical radiation could be emitted over a narrower beam angle, through use of lenses or an emitting fibre with lower numerical aperture, and (iii) the reflected optical radiation could be collected more efficiently through the use of lenses, receiving fibre with larger core size, e g 0 5 – 1 mm diameter, or a fibre bundle The first two points apply most readily to the surface defect sensor while the last two points apply to the surface roughness sensor Perhaps certain applications of this surface defect sensor would not require such high spatial resolution and use of lenses would significantly improve ease of use A focussing rather than collimating lens might improve the spatial resolution of the measurement

Optical Wavelength

The surface defect sensor operated at an optical wavelength of 1300 nm, this was chosen to limit the effect of diffuse scatter on the sensor. As the sensor was not tested at lower wavelength it is impossible to determine whether this had a positive effect on the operation of the sensor, yet it will be assumed that it did.

The surface roughness sensor operated at a wavelength of 850 nm. Reflectivity is dependent on wavelength, equation 3.9, and longer wavelengths should extend the range of roughness [87]. High performance telecommunications-style LEDs are available at wavelengths of 1300 nm and 1550 nm, but are relatively expensive. A system could be implemented using modulated LEDs of differing wavelengths, perhaps 850 nm and 950 nm. It would be possible for digital or analog filtering to separate signals from the two LEDs using a single photodiode.

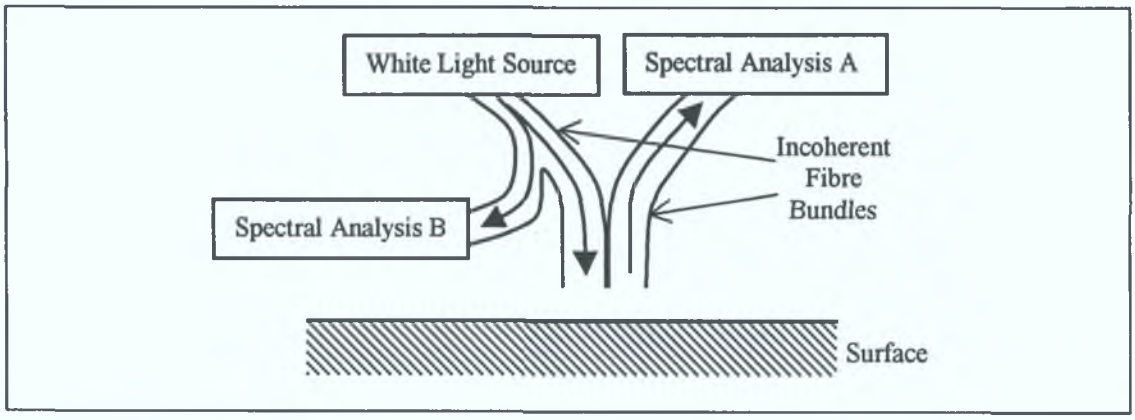

Figure 9.1 System based on spectral analysis of sensor using white light source

A white light system, figure 9.1, could apply spectral analysis to the reflected light, while applying spectral analysis against the input light source for reference. A white light source, for example a quartz tungsten halogen lamp, emits light over wide range of wavelengths, figure 9.2. Spectral analysis analyses the intensity at particular wavelengths [3]. Rudimentary spectral analysis could be implemented by using two or three photodiodes with responsivity at differing wavelengths, figure 9.2, this differential responsivity could either be a property of the particular photodiode or could be caused by the use of optical filters. Incoherent fibre bundles [23-25,52]

would be the most efficient way to couple light from a white light source and would allow multiple measurements to be taken without need for expensive fibre couplers Referencing is necessary in this system because of the fluctuation of the light source This method would be sensitive to interference from ambient light In effect such a white light system is identical to a system using two or more LEDs of differing wavelengths

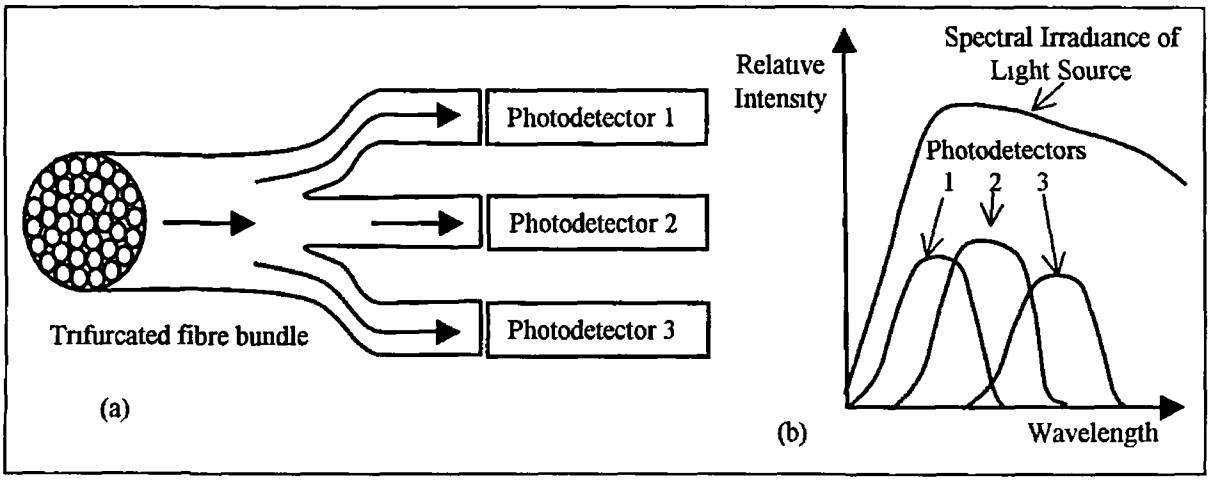

Figure 9 2 (a) Trifurcated fibre bundle for simple spectral analysis (b) Spectral response of photodiodes and spectral irradiance of white light source

9 2 2 Optoelectronic Design

Absolute accuracy of measurement isn't critical for the surface defect sensor – because of this the design of the photodetection system could be simplified by using phototransistors – phototransistors are cheaper If an array of defect sensors is fabricated another alternative would be to couple an array of fibres to a linear photodiode array - Geary [105] describes such an arrangement

Misalignment and thermal drift, section 6 3 5, were the critical factors affecting measurement with the surface roughness sensor The optoelectronic design of the surface roughness sensor implemented a carrier frequency system based on a square wave The digital filtering of the acquired data isolated the first harmonic of the square wave, filtering out all other harmonics If the LED was driven using a sine wave input the digital filtering would be more efficient On the other hand a lock-in

amplifier [121-123] could be constructed to reject noise using the square wave driving circuit A carrier frequency system diminishes interference due to ambient light which will become more pronounced if a system using a lens or fibre bundle is used

Use of a laser diode light source with an integral photodiode, and an appropriate referencing system, may result in a sensor system that could perform both surface roughness and defect sensing online

9 2 3 Mechanical Design

Though the mechanical design sufficed for use as an experimental rig, there are a number of improvements that are necessary to improve the performance of the sensors particularly for use online

Firstly, the use of manual translation stages meant that the speed of measurement was very slow, the focus of the optoelectronic design sensors was high-speed online use To take a full set of readings with the defect sensor of one hole on a sample plate took about 45 minutes This included positioning fibres, fixing the surface sample, assessing vertical displacement characteristics, setting vertical stand-off distance, finding a starting point, and finally performing surface scans An array of sensors to perform linescanning along with motorised scanning would improve the speed of measurement considerably

Secondly, bare fibres are very delicate The fibres protruded beyond the end of the fibre holder and could be easily damaged It is necessary that protection be developed for industrial use A fibre connected to a collimating lens would have protection Incoherent fibre bundles are robust and have the advantage that one broken fibre does not result in catastrophic failure of the sensor

In some industrial processes it is necessary distinguish between blind and through holes, e g in detecting punched holes Use of opposed-mode sensing [52] alone or in conjunction with the reflective-mode sensing used in this project could achieve this Orienting fibres at normal incidence to the surface would reduce sensitivity to blind holes significantly

9 2 4 Wider Applications

This project explored engineering applications of optical technology in the areas of fibre-optics, fibre-optic sensing, optoelectronics, surface properties and photoelectric sensing The thesis contains basic information that may be useful as a starting point for further work that is unrelated to determination of surface properties or even industrial inspection, i e much of the literature survey directly relates to fibre-optic displacement sensing and its application Optical technology is a vibrant area that is becoming a significant part of Irish industry and research [126] Applications in the automotive industry [127,128], medical devices [44,45,129], vibration [36,37], and semiconductor industry [92,93] are growing A possible inspection project is the use of low coherency interferometry to measure the width of perspex or glass sheets online [20]

Holographic structured light projectors [130] in conjunction with CCD cameras and the laser triangulation principle [131] have superseded the use of mechanical laser scanning in many industrial applications for inspection of defects Gaynor et al [130] provide a comprehensive review of these systems Such laser line generators are commercially available and can gather three-dimensional data of a surface for use with CAD systems By projecting a line of laser radiation on a surface there is no need for any moving parts The main advantage of this system over the proposed array of defect sensors designed in this project is that structured light projectors allow the three-dimensional data to be gathered rather than two-dimensional data For detection of holes it may not be a necessity to generate three-dimensional data and lower cost and a simpler operating principle may be the critical criteria

REFERENCES

[1] Yeh, C , 1990, Handbook of Fiber Optics – Theory and Applications, Academic Press, Inc , San Diego, California

[2] Chaimowicz, J C A., 1989, Optoelectronics – An Introduction, Butterworth-Heinemann Ltd , Oxford

[3] Grattan, K T V , Meggitt, 1995, B T , Optical Fiber Sensor Technology, Chapman & Hall, London

[4] Uiga, E, 1995, Optoelectronics, Prentice Hall, Inc , New Jersey

[5] Marcuse, D , 1981, Principles of Optical Fiber Measurements, Academic Press, Inc , New York

[6] Briley, B E , 1988, An Introduction to Fiber Optics System Design, Elsevier Science publishers B V , Amsterdam

[7] Ungar S , 1990, Fibre Optics – Theory and Applications, John Wiley, Chichester, West Sussex

[8] Davis, C M , Carome, E F , Weik, M H , Ezekiel, S , Einzig, R E , 1986, Fiberoptic Sensor Technology Handbook, Optical Technologies, Inc , Virginia

[9] Udd, E , 1996, Fiber Optic Smart Structures, Proceedings of the IEEE, 84, 6, pp 884-894

[10] During, C , Komeda, T , Matsuto, M , Funakubo H , 1997, An inexpensive light source and detector module for fibre-optic measurements, Measurement Science and Technology, 8, pp 209-212

[11] Bouwhuis, G , 1985, Principles of optical disc systems, Hilger, Bristol

[12] Hill, P , 1997, White-light diodes are set to tumble in price, Opto & Laser Europe, Issue 44, October, pp17-20

[13] Nakamura, S , Fasol, G , 1997, The Blue Laser Diode - Gallium-Nitride Light Emitters and Laser, Springer-Verlag

[14] Jackson, D A , 1985, Monomode optical fibre interferometers for precision measurement, Journal of Physics E Scientific Instruments, 18, pp 981-1001

[15] Rao, Y J , Jackson, 1996, D A , Recent progress in fibre optic low-coherence interferometry, Measurement Science and Technology, 7, pp 981-999

[16] Weir K , Palmer, A W , Grattan, K T V , 1994, Accurate measurement of small displacement using optical techniques, International Journal of Optoelectronics, 9, 6, pp 449-455

[17] Ning, Y , Grattan, K T V , Meggitt, B T , Palmer, A W , 1989, Characteristics of laser diodes for interferometric use, Applied Optics, 28, 17, pp 3657-3661

[18] Chen, S , Palmer, A W , Grattan, K T V , Meggitt, B T , 1992, Extrinsic optical-fiber mterferometric sensor that uses multimode optical fibers system and sensing-head design for low noise operation, Optics Letters, 17, 10, pp 701-703

[19] Weir K , Boyle, W J O Meggitt, B T , Palmer, A W , Grattan, K T V , 1992, A Novel Adaption of the Michelson Interferometer for the Measurement of Vibration, Journal of Lightwave Technology, 10, 5, pp 700-703

[20] Lawson, C M , Michael, R R , 1994, Fiber optic low-coherence interferometry for non-invasive silicon wafer characterization, Journal of Crystal Growth, 137, pp37-40

[21] Lee, C E , Taylor, H F , 1991, Fiber-Optic Fabry-Perot Temperature Sensor Using a Low-Coherence Light Source, Journal of Lightwave Technology, 9, 1, pp 129-134

[22] B Cahill & M A El Baradie, 1997, Industrial Applications of Optical Fibre Sensors, Proceedings of the 14th conference of the Irish Manufacturing Committee, pp 577-586

[23] Shimamoto, A , Tanaka, K , 1996, Geometrical analysis of an optical fiber bundle displacement sensor, Applied Optics, 35, 34, pp 6767-6774

[24] Shimamoto, A , Tanaka, K , 1995, Optical fibre bundle displacement sensor using an ac-modulated light source with subnanometer resolution and low thermal drift, Applied Optics, 34, 25, pp 5854-5860

[25] Hoogenboom, L , Hull-Allen, G , Wang, S , 1984, Theoretical and experimental analysis of a fiber optic proximity probe, Proc SPIE, 478, pp 46-57

[26] Hok, B , Tenerz, L , Gustafsson, K , 1989, Fibre-optic sensors a micro-mechanical approach, Sensors and Actuators, 17, pp 157-166

[27] Powell, J A , 1974, A simple two-fiber optical displacement sensor, Revue of Scientific Instruments, 45, 2, pp 302-303

[28] Cook, R O , Hamm, C W , 1979, Fiber optic lever displacement transducer, Applied Optics, 18, 19, pp 3230-3241

[29] Murtaza, G , Senior, J M , 1994, Referenced intensity-based optical fibre sensors, International Journal of Optoelectronics, 9, 4, pp 339-348

[30] Cockshott, C P, Pacaud, S J, 1989, Compensation of an optical fibre reflective sensor, Sensors and Actuators, 17, pp 167-171

[31] Libo, Y, Anping, Q, 1991, Fiber-optic diaphragm pressure sensor with automatic intensity compensation, Sensors and Actuators A, 28, pp 29-33

[32] Simpson, J A, 1971, The use of a microscope as a noncontacting microdisplacement measuring device, Revue of Scientific Instruments, 42, 9, pp 1378-1380

[33] Senior, J M, Cusworth, S D, 1989, Wavelength division multiplexing in optical fibre sensor systems and networks a review, Optics and Laser Technology, 22, pp 113-126

[34] Senior, J M, Murtaza, G, Stirling, A I, Wainwright, G H, 1992, Single LED based dual wavelength referenced optical fibre sensor system using intensity modulation, Optics and Laser Technology, 24 ,4 , pp 187

[35] Wang, A, Miller, M S, Plante, A J, Gunther, M F, Murphy, K A, Claus, R O, 1996, Split-spectrum intensity based optical fiber sensors for measurement of microdisplacement, strain, and pressure, Applied Optics, 35, 15, pp 2595-2601

[36] Remo, J L, 1996, Solid state vibration/displacement sensors, Optical Engineering, 35, 10, pp 2798-2803

[37] Gerges, A S, Newson, T P, Jones, J D C, Jackson, D A, 1989, High Sensitivity fiber-optic accelerometer, Optics Letters, 14, 4, pp 251-253

[38] Marty, J, Malki, A, Renouf, C, Lecoy, P, Baillieu, F, 1995, Fibre-optic accelerometer using silicon micromachining techniques, Sensors and Actuators A, vol 46-47, pp 470-473

[39] Wang, H, Valdivia-Hernandez, R, 1995, Shaft Runout Inspection by a Fibre Optic Displacement Sensor, Fiber and Integrated Optics, 14, pp 159-169

[40] Haslam, J A, Summers, G R, Williams, D, 1981, Engineering instrumentation and control, Arnold, London

[41] Libo, Y, Anping, Q, 1991, Fiber-optic diaphragm pressure sensor with automatic intensity compensation, Sensors and Actuators A, 28, pp 29-33

[42] Libo, Y, Shunling, R, Jian, P, 1993, Automatic compensation of a fiber-optic differential pressure sensor, Sensors and Actuators A, 36, pp 183-185

[43] Iwamoto, K, Kamata, I, 1990, Pressure sensor using optical fibers, Applied Optics, 29, 3, pp 375-378

[44] Tohyama, O , Kohashi, M , Yamamoto, K , Itoh, H , 1996, Sensors and Actuators A, 54, pp 622-625

[45] Strandman, C , Smith, L, Tenerz, L , Hok, B , 1997, A production process of silicon sensor elements for a fibre optic pressure sensor, Sensors and Actuators A, 63, pp 69-74

[46] Wood, D , 1997, Microengineering and the small business, IEE Review, January 1997, pp 21-24

[47] Dorey, A P , Bradley, D A , 1994, Measurement science and technology – essential fundamentals of mechatronics, Measurement Science and Technology, 5, pp 1415-1428

[48] Pottenger, M , Eyre, B , Kruglick, E , Lin, G , 1997, MEMS The maturing of a new technology, Solid State Technology, 40, 9, pp 89-96

[49] Jones, B E , 1985, Optical fibre sensors and systems for industry, Journal of Physics E Scientific Instruments, pp 770

[50] Garwood, R , 1995, Principles of Photoelectric Sensing - Part I, Sensors, 12, July, pp 14-21 & pp 60-63

[51] Garwood, R , 1995, Principles of Photoelectric Sensing - Part II, Sensors, 13, August, pp 38-42 & p 59

[52] Banner Engineering Corp , 1994, Handbook of Photoelectric Sensing, Banner Engineering Corp , Minneapolis, USA

[53] Streckenbach, J , 1990, A short course in Photoelectric Sensors Part I, Sensors, 7,9, pp 10-16

[54] Streckenbach, J , 1990, A short course in Photoelectric Sensors Part II, Sensors, 7,10, pp 48-53

[55] Bennett, J M , Mattson, L , 1989, Introduction to surface roughness and scattering, Optical Society of America, Washington D C

[56] Nicholls, M O , The measurement of surface finish, De Beers Technical Service Centre, Charters, UK

[57] Stover, J C , 1990, Optical Scattering measurement and analysis, McGraw-Hill, Inc , New York

[58] Whitehouse, D J , Surface Metrology, 1997, Surface Metrology, Measurement Science and Technology, 8, pp 955-972

[59] McGillem, C D , Cooper, G R , 1991, Continuous and discrete signal and system analysis, Saunders College Pub , Philadelphia

[60] Sherrington, I, Smith, E, 1988, Modern Measurement Techniques in Surface Metrology Part I, Stylus Instruments, Electron Microscopy and Non-optical Comparators, Wear, 125, pp 271-288

[61] Peterson, R W, Robinson, G M, Carlsen, R A, Englund, C D, Moran, P J, Wirth, W M, 1984, Interferometric measurements of the surface profile of moving samples, Applied Optics, 23, 10, pp 1464- 1466

[62] Dobosz, M, 1983, Optical profilometer a practical approximate method of analysis, Applied Optics, 22, 24, pp 3983-3987

[63] Hand, D P, Carolan, T A, Barton, J S, Jones, J D C, 1993, Profile measurement of optically rough surfaces by interferometry, Optics Letters, 18, 16, pp 1361-1363

[64] Kidd, S R, Hand, D P, Carolan, T A, Barton, J S, Jones, J D C, 1996, Measurements of aspects of surface form using an optical differential height measurement technique, Measurement Science and Technology, 7, pp 1579-1582

[65] Bohlmann, J, 1995, Fibre Optic Sensor for Surface Roughness Measurement, Master of Applied Science Thesis, University of Victoria, Canada

[66] Brodmann, R, Allgauer, M, 1988, Comparison of light scattering from rough surfaces with optical and mechanical profilometry, Proc SPIE, 1009, pp 111-118

[67] Stedman, M, Lindsey, K, 1988, Limits of surface measurement by stylus instruments, Proc SPIE, 1009, pp 56-61

[68] Stedman, M, 1988, Limits of surface measurement by optical probes, Proc SPIE, 1009, pp 62-67

[69] Stout, K J, 1984, Optical assessment of surface roughness, Precision Engineering, 6, 1, pp 35-39

[70] Stout, K J, Davis, E J, Sullivan, P J, Atlas of machined surfaces, Chapman and Hall, London

[71] Dresel, T, Hausler, G, Venzke, H, 1992, Three dimensional sensing of rough surfaces by coherence radar, Applied Optics, 31, pp 919-925

[72] Beckmann, P, Spizzichino, A, 1963, The Scattering of Electromagnetic Waves from Rough Surfaces, Pergamon Press, Oxford

[73] Hensler, D H, 1972, Light scattering from fused polycrystalline aluminium oxide surfaces, Applied Optics, 11, 11, pp 2522-2528

[74] Depew, C A, Weir, R D, 1971, Surface Roughness Determination by the Measurement of Reflectance, Applied Optics, 10, 4, pp 969-970

[75] Bennett, J M, 1992, Recent developments in surface roughness characterization, Measurement Science and Technology, 3, pp 1119-1127

[76] Marx, E, Vorburger, T V, 1989, Direct and inverse problems for light scattered by rough surfaces, Applied Optics, 29,25, pp 3613-3626

[77] Howland, R S, Wells, K B, Trafas, B M, 1995, High-speed detection of pattern defects using laser scattering, Solid State Technology, November, pp 123-126

[78] Warner, T L, Bawolek, E J, 1993, Reviewing angle resolved methods for improved surface particle detection, Microcontamination, September/October, pp 35-39 & 109

[79] Liu, B Y H, Chae, S K, Bae, G N, 1993, Sizing accuracy, counting efficiency, lower detection limit and repeatability of a wafer surface scanner for ideal and real-world particles, Journal of the Electrochemical Society, 140, 5, pp 1403-1409

[80] Chae, S K, Liu, B Y H, Bae, G N, Myong, H K, Lee, C S, 1993, Performance characteristics of the PMS SAS-3600 wafer surface scanner, Proc Institute of Environmental Sciences, pp 336-344

[81] Miller, M, Lakes, R S, Conner, S, 1996, Optical testing of hard disks, Optics & Laser Technology, 28, 3, pp 151-156

[82] Cielo, P, 1990, Optical Techniques for Industrial Inspection, Academic Press, Boston

[83] Griffiths, B J, Middleton, R H, Wilkie, B A, 1994, Light Scattering for the measurement of surface finish a review, International Journal of Production Research, 32, 11, pp 2683-2694

[84] Mitsui, K, 1986, In-process sensors for surface roughness and their applications, Precision Engineering, 8, 4, pp 212-220

[85] Domanski, A W, Karpierz, M A, Rzysko, T J, 1986, The method of surface roughness measurement with application of optical fibers, Proc SPIE, 670, pp 119-122

[86] Domanski, A W, Ejchart, W, Jedrewski, J, Siegoczynski, R M, Tlaczala, W, 1986, The fiber-optic instrument for extremely small roughness measurement, Proc SPIE, 670, pp 116-118

[87] Domanski, A W, Wolinski, T R, Rzysko, T J, 1988, Optimal distribution of optical fibers in surface roughness sensor, Proc SPIE, 1009, pp 134-139

[88] Domanski, A W, Karpierz, M A, Malinowski, D, Wolinski, T R, Bock, W J, 1989, Fiber-optic surface roughness sensor based on polarization measurements, Proc SPIE, 1169, pp 558-566

[89] Domanski, A W, Wolinski, 1992, Surface roughness measurement with optical fibers, IEEE Transactions on Instrumentation and measurement, 41, 6, pp 1057-1061

[90] Dowden, S, Patterson, J R, Wild, N, 1997, Reflectometer for fast measurements of mirror reflectivity, Measurement Science & Technology, 8, pp 1258-1261

[91] Collins, M, 1996, Using Photoelectric Fiber Optic Sensors to Detect Changes in Surface Reflectivity, Sensors, 13, 9, pp 27-28

[92] Moslehi, M M, Mar 8, 1994, Sensor for semiconductor device manufacturing process control, U S Patent No 5,293,216

[93] Moslehi, M M, Dec 12, 1995, Method for real-time semiconductor wafer temperature measurement based on the surface roughness characteristic of the wafer, U S Patent No 5,474,381

[94] Fawcett, C F, Keltie, R F, 1990, Use of a fiber optic displacement probe as a surface finish sensor, Sensors and Actuators A, 24, pp 5-14

[95] Gardner, C S, Streight, W E, Dec 21, 1982, Surface roughness gauge and method, U S Patent No 4,364,663

[96] Dapeng, F, Honghai, Z, Jihong, C, Riyao, C, 1991, Measurement of surface roughness using optical-fibre sensor and microcomputer, Proc SPIE, 1572, pp 11-14

[97] Dandliker, R, Mottier, F M, Nov 25, 1975, Device for measuring the roughness of a surface, U S Patent No 3,922,093

[98] Thurn, G, Gast, T, Aug 22, 1989, Optoelectrical measuring system and apparatus, U S Patent No 4,859,062

[99] Brodmann, R, Gerstorfer, O, Thurn, G, 1985, Optical roughness for fine machined surfaces, Optical Engineering, 24, 3, pp 408-413

[100] Brodmann, R, 1986, Roughness form and waviness measurement by means of light-scattering, Precision Engineering, 8, 4, pp 221-226

[101] Brodmann, R , Thurn, G , 1986, Roughness measurement of ground, turned and shot-peened surfaces by the light scattering method, Wear, 109, pp 1-13

[102] Valliant, J G , Goebel, D G , Mar 4, 1997, Apparatus and method for dynamic measurement of surface roughness, U S Patent No 5,608,527

[103] Luk, F , Huynh, V , North, W , 1989, Measurement of surface roughness by a machine vision system, J Phys E Sci Instrum , 22, pp 977-980

[104] Yanagi, K , Tetsuji, M , Tsukad, T , 1985, A practical method of optical measurement for the minute surface roughness of cylindrical machined parts, Wear, 109, pp 57-67

[105] Geary, J M , Hull-Allen, C G , Feb 12, 1991, Fiber optic scatterometer, for measuring optical surface roughness, U S Patent No 4,991,971

[106] Savant, C J , Roden, M S , Carpenter, G , 1991, Electronic Design, The Benjamin/Cummings Publishing Company, Inc , Redwood City, California

[107] Honeywell Europe S A , date unknown, Application Note - Long-Term Power Output Reliability of Cap Rock (SEC589) LED Chip, Honeywell Europe S A

[108] Godfrey, L , date unknown, Choosing the Detector for your Unique Light Sensing Application, EG&G Optoelectronics Canada

[109] Bertone, N , Webb, P , date unknown, Noise and Stability in PIN Detectors, EG&G Optoelectronics Canada

[110] Sell, D D , Feb 22, 1977, Laser Control Circuit, U S Patent No 4,009,385

[111] Melles Griot, 1995, Melles Griot catalog 1995/1996, Melles Griot, USA

[112] Tompkins, W J , Webster, J G , 1988, Interfacing sensors to the IBM® PC, Prentice Hall, Inc , New Jersey

[113] Newport, 1994, The Newport Catalog 94/95, Newport Corporation, USA

[114] Fujikura Ltd , date unknown, Instruction Manual for the Optical Fiber Cleaver, Fujikura Ltd, Tokyo, Japan

[115] Ikeda, M , Murakami, Y , Kitayama, K , 1977, Mode scrambler for optical fibers, Applied Optics, 16, 4, pp 1045-1049

[116] Mikoshiba, K , Kajioka, H , 1978, Transmission characteristics of multimode W-type optical fiber experimental study of the effect of the intermediate layer, Applied Optics, 17, 17, pp 2836-2841

[117] Ichimura, K , Okada, H , Takahashi, S , Komiya, M , June 19, 1990, Mode Scrambler, U S Patent No 4,934,787

[118] Tokuda, M, Seikei, S, Yoshida, K, Uchida, N, 1977, Measurement of baseband frequency response of multimode fiber by using a new type of mode scrambler, Electronics Letters, 13, 5, pp 146-147

[119] National Instruments Corporation, 1996, AT-MIO/AI E Series User Manual, National Instruments Corporation, Austin, Texas

[120] National Instruments Corporation, 1996, LabVIEW User Manual, National Instruments Corporation, Austin, Texas

[121] Meade, M L, 1983, Lock-in amplifiers principles and applications, P Peregrinus on behalf of the IEE, London

[122] Wolfson, R, 1991, The lock-in amplifier A student experiment, American Journal of Physics, 59, 6, pp 569-572

[123] Sconza, A, Torzo, G, 1994, Spectroscopic measurement of the semiconductor energy gap, American Journal of Physics, 62, 8, pp 732-737

[124] National Instruments Corporation, 1996, LabVIEW Analysis VI Reference Manual, National Instruments Corporation, Austin, Texas

[125] Rubert & Co, date unknown, Product Literature and Technical Information, Rubert & Co, Cheadle, England

[126] McMillan, N, Diskin, M, June 1997, Optical Engineering in Ireland the wider vision, New Engineering, A supplement to the Engineers Journal (Institution of Engineers in Ireland), pp 6-14

[127] Lewotsky, K, 1996, Smart cars take the high-tech road, Laser Focus World, 32, 6, pp117-123

[128] Kaplan, H, 1997, Auto Manufacturing Solutions Wanted, Inquire Within, Photonics Spectra, 31, 8, pp 98-101

[129] Wheeler, M D, 1997, Medical Sensing Photonics gets under your skin, Photonics Spectra, 31, 8, pp 125-127

[130] Gaynor, E S, Massimi, M S, Blase, W P, Aug 20, 1996, Holographic Structured Light Generator, U S Patent No 5,548,418

[131] Beary, S, 1997, Development of a laser scanning system for the inspection of surface defects, M Eng Thesis, Dublin City University, Ireland

APPENDIX - A1

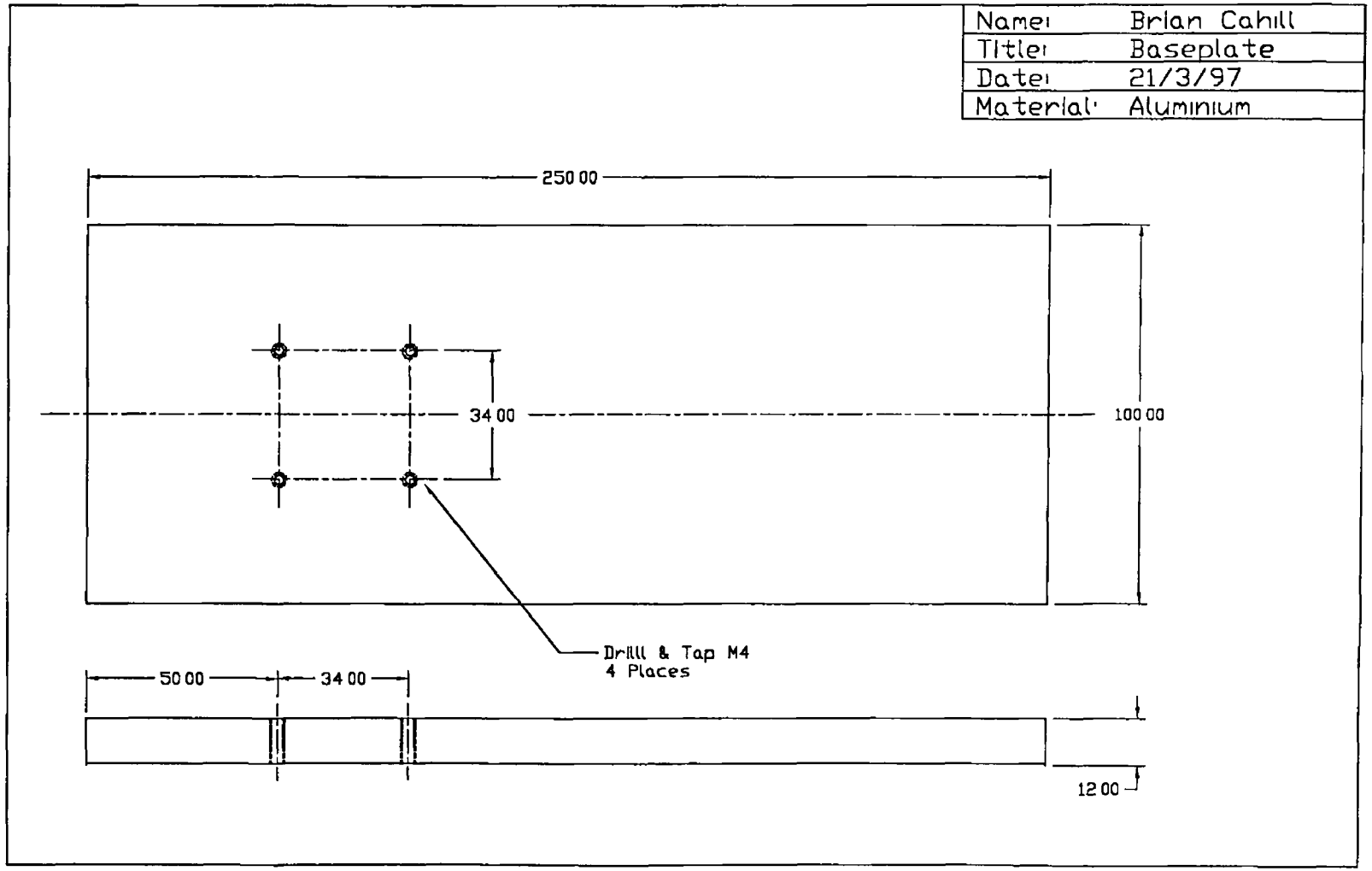
Name: Brian Cahill
Title: Baseplate
Date: 21/3/97
Material: Aluminium
250 00
34 00
100 00
Drill & Tap M4
4 Places
50 00
34 00
12 00

APPENDIX – A2

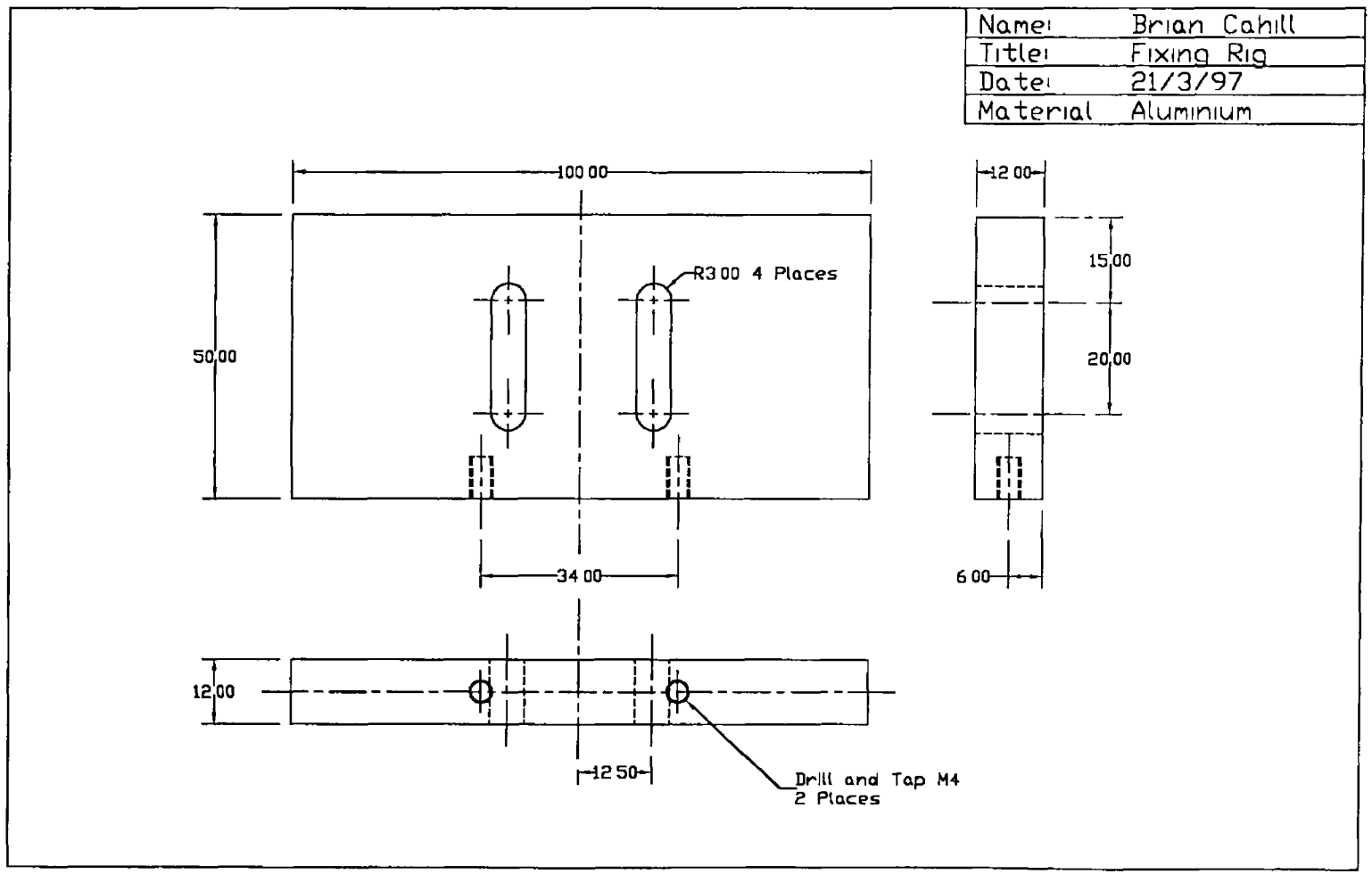
Name: Brian Cahill
Title: Fixing Rig
Date: 21/3/97
Material Aluminium
100.00
12.00
15.00
20.00
R3.00 4 Places
50.00
34.00
6.00
12.00
12.50
Drill and Tap M4
2 Places

APPENDIX – A3

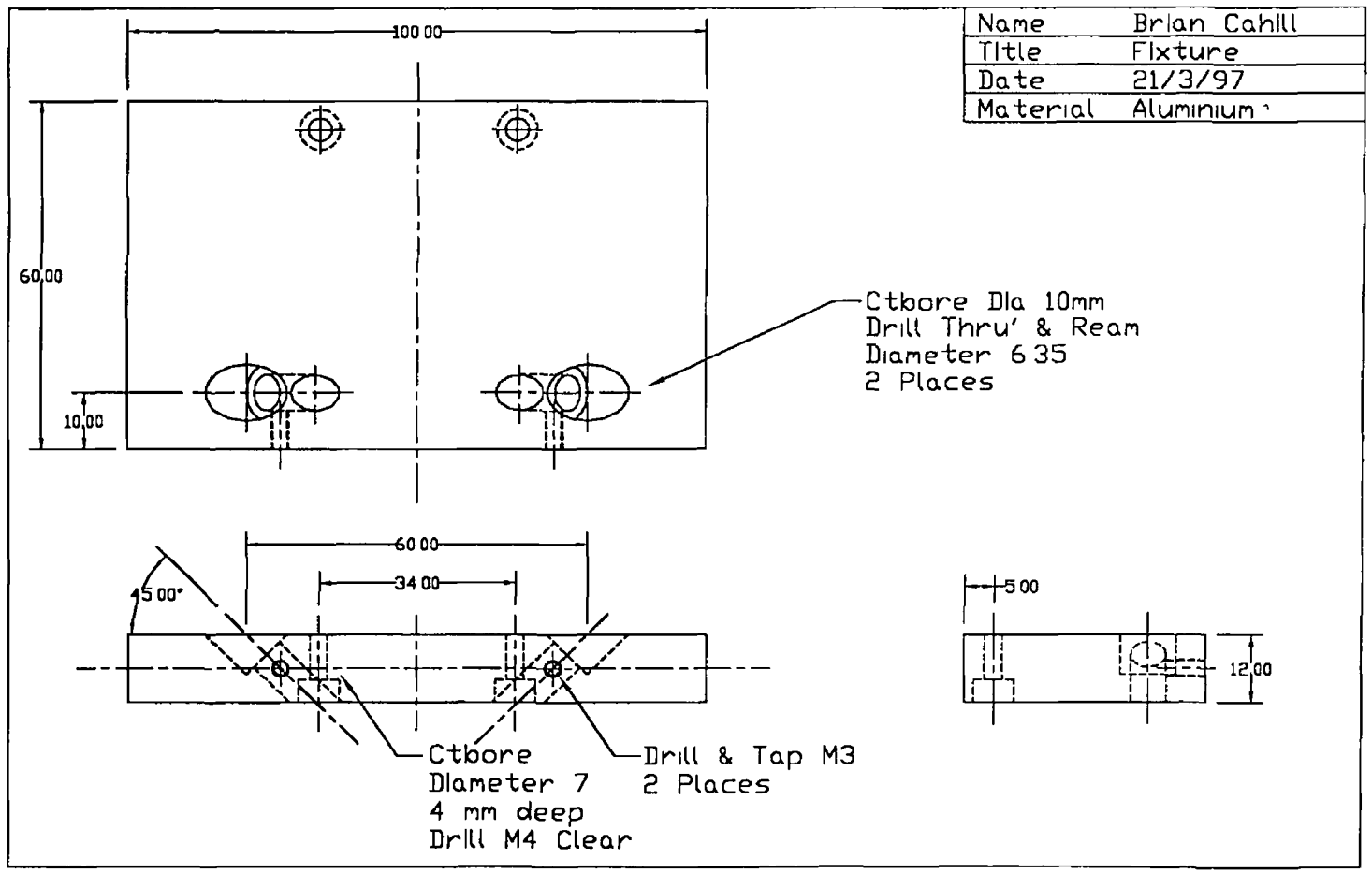
Name Brian Cahill
Title Fixture
Date 21/3/97
Material Aluminium
100 00
60.00
10.00
Ctbore Dia 10mm
Drill Thru' & Ream
Diameter 6 35
2 Places
60 00
34 00
5 00°
5 00
12.00
Ctbore
Diameter 7
4 mm deep
Drill M4 Clear
Drill & Tap M3
2 Places

APPENDIX – A4

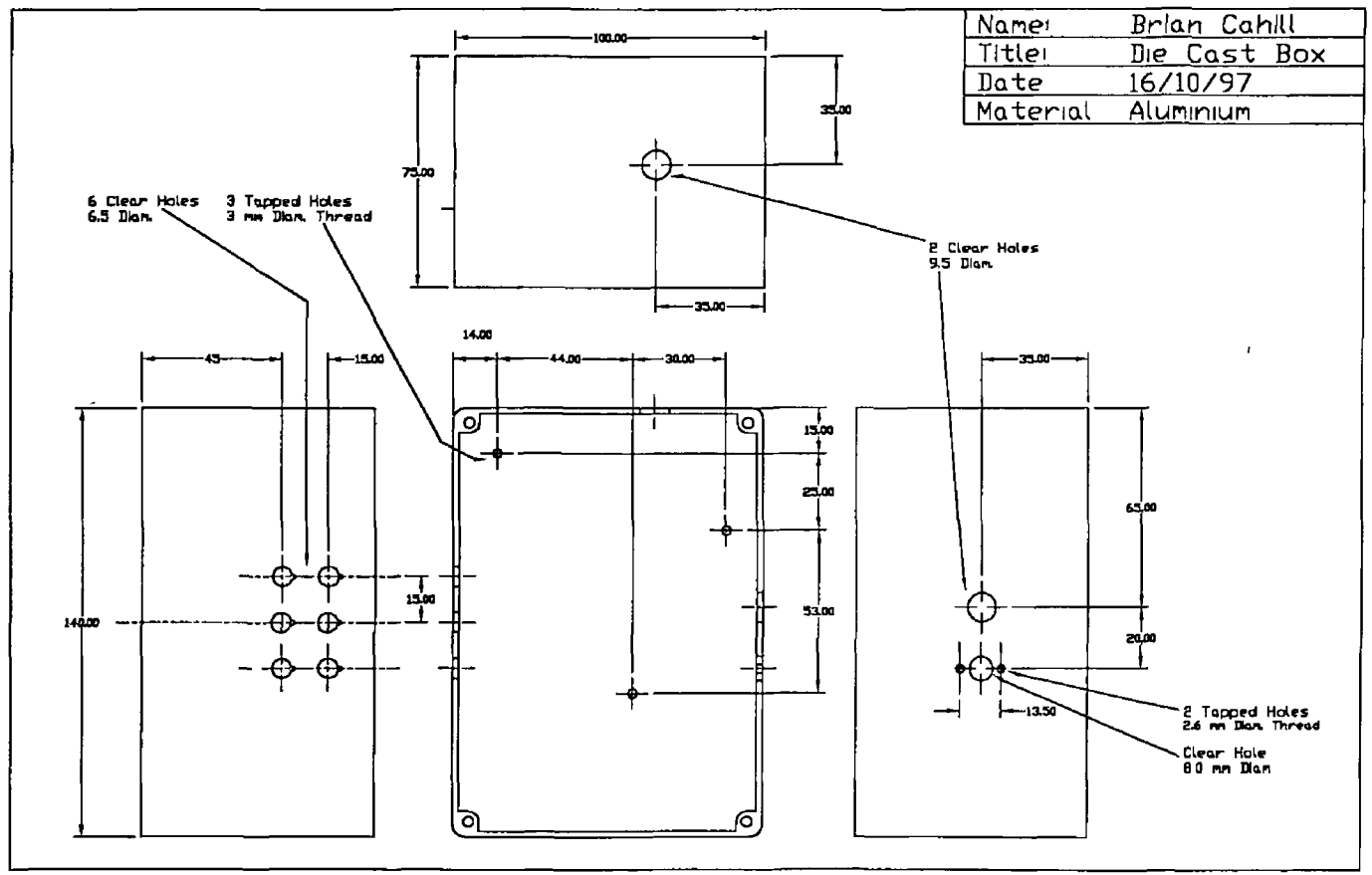
Name: Brian Cahill
Title: Die Cast Box
Date 16/10/97
Material Aluminium
100.00
35.00
75.00
35.00
6 Clear Holes
6.5 Diam.
3 Tapped Holes
3 mm Diam. Thread
2 Clear Holes
9.5 Diam.
14.00
45
15.00
44.00
30.00
35.00
15.00
25.00
65.00
140.00
15.00
53.00
20.00
13.50
2 Tapped Holes
2.6 mm Diam Thread
Clear Hole
8.0 mm Diam

APPENDIX – A5

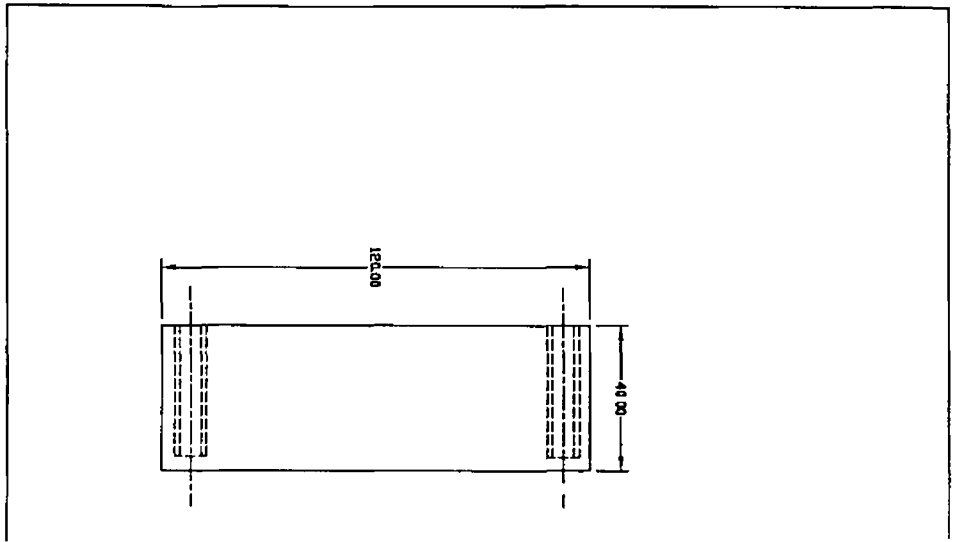

Name	Brian Cahill
Title	ABS Box
Date:	16/10/97
Material	ABS Plastic

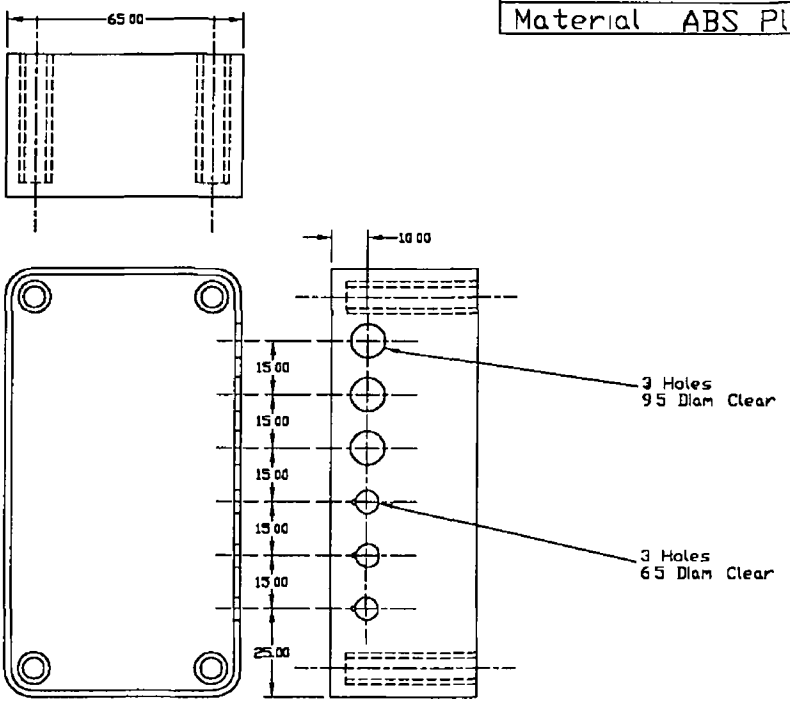

APPENDIX – A6

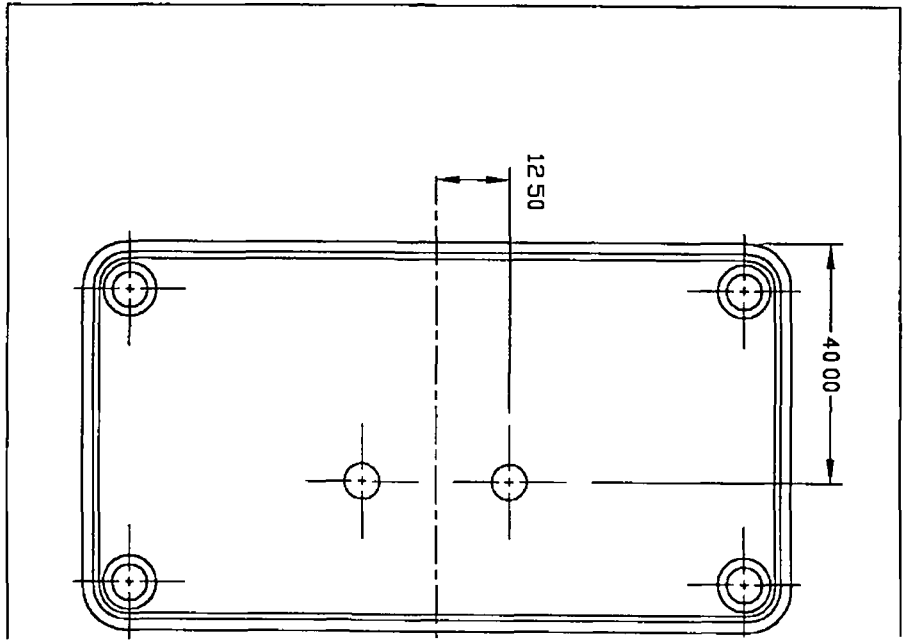

Name	Brian Cahill
Title	Lid
Date:	16/10/97
Material:	ABS Plastic

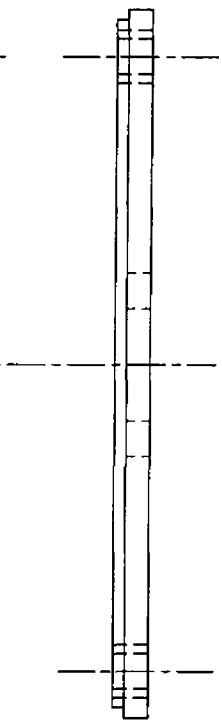

APPENDIX – A7

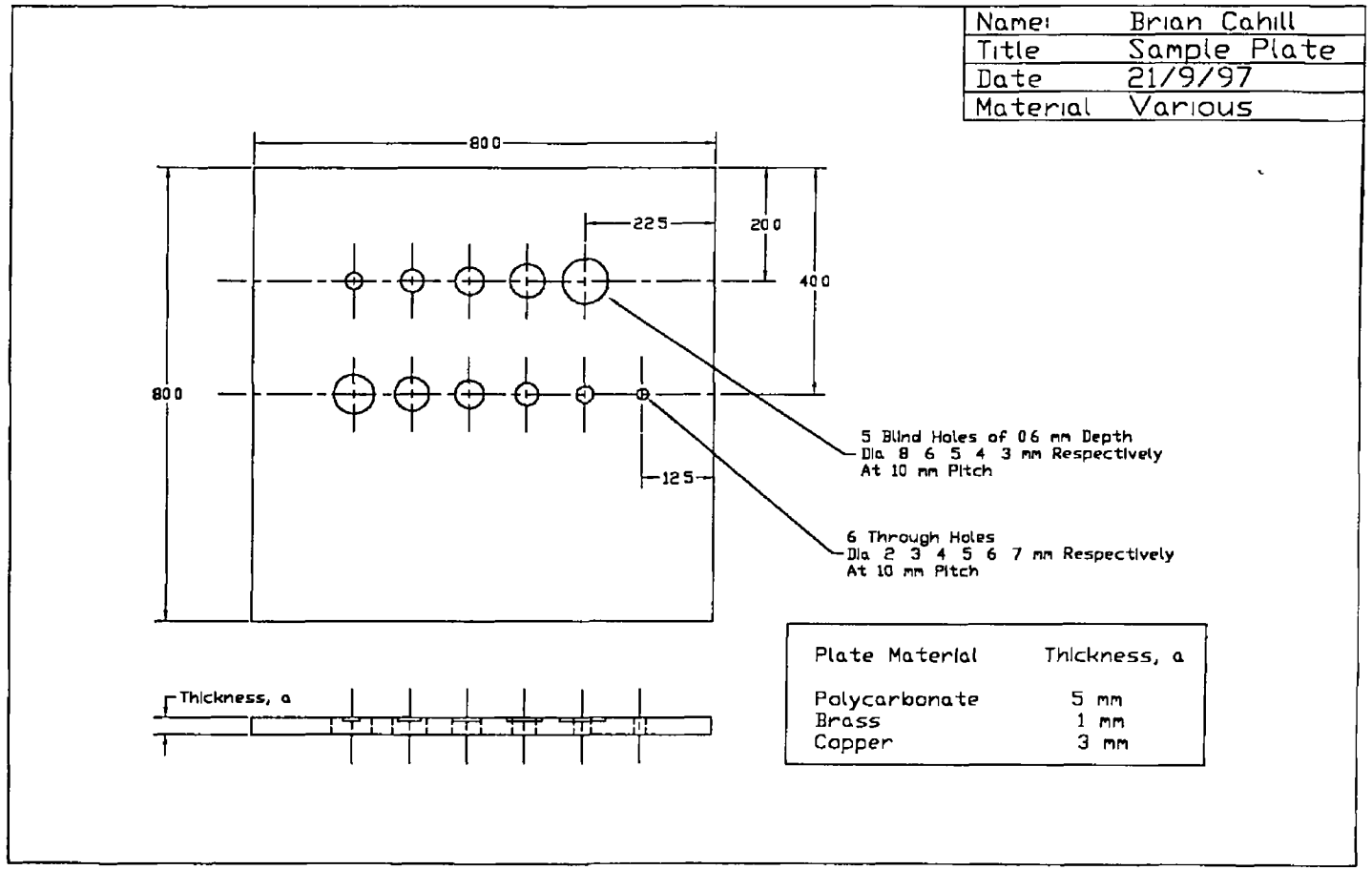
Name: Brian Cahill
Title Sample Plate
Date 21/9/97
Material Various
800
225
200
400
800
125
5 Blind Holes of 0.6 mm Depth
Dia 8 6 5 4 3 mm Respectively
At 10 mm Pitch
6 Through Holes
Dia 2 3 4 5 6 7 mm Respectively
At 10 mm Pitch
Thickness, a
Plate Material Thickness, a
Polycarbonate 5 mm
Brass 1 mm
Copper 3 mm

APPENDIX – A8

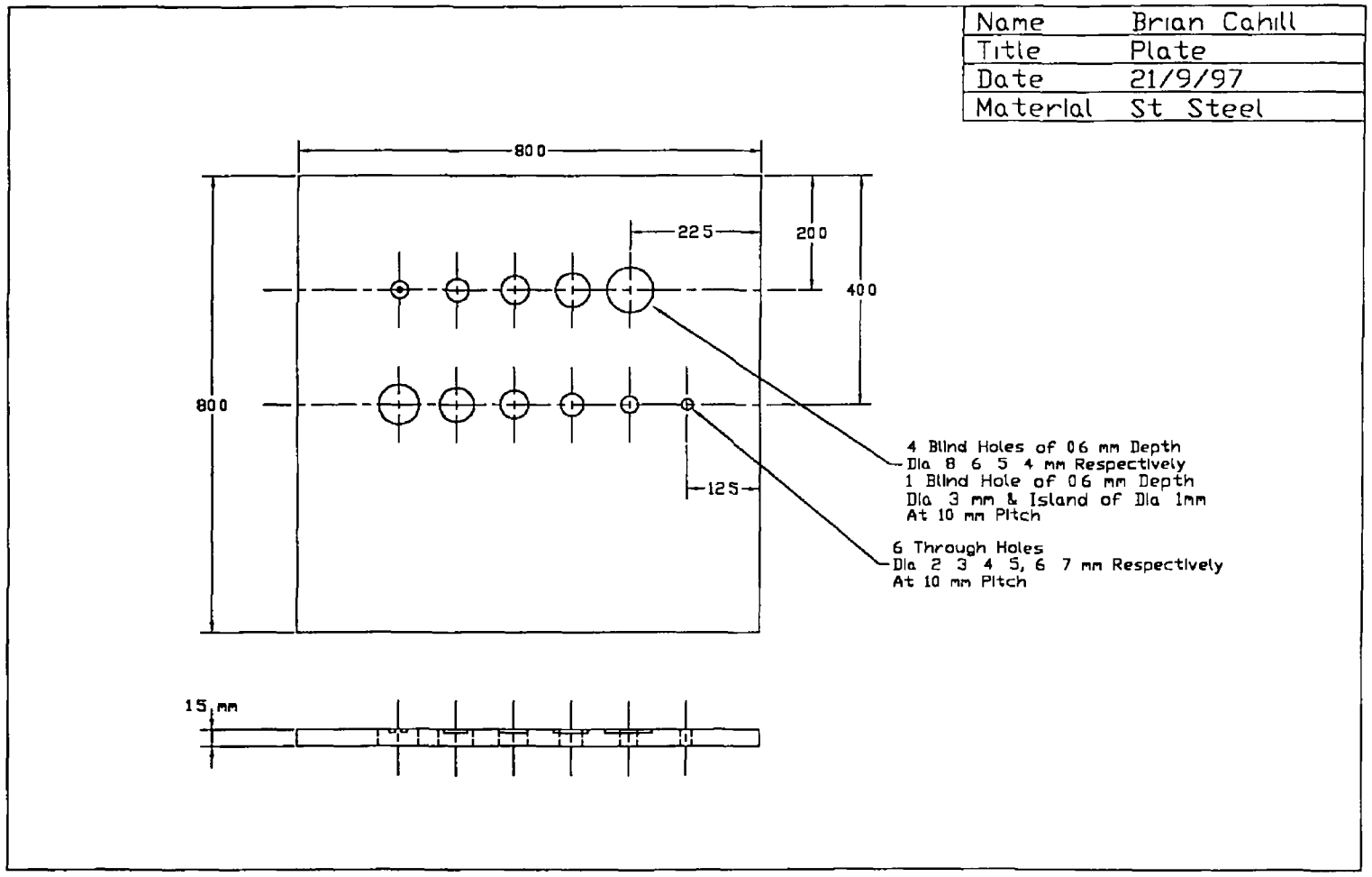
Name Brian Cahill
Title Plate
Date 21/9/97
Material St Steel
800
225
200
400
800
125
4 Blind Holes of 06 mm Depth
Dia 8 6 5 4 mm Respectively
1 Blind Hole of 06 mm Depth
Dia 3 mm & Island of Dia 1mm
At 10 mm Pitch
6 Through Holes
Dia 2 3 4 5, 6 7 mm Respectively
At 10 mm Pitch
15 mm

APPENDIX – A9

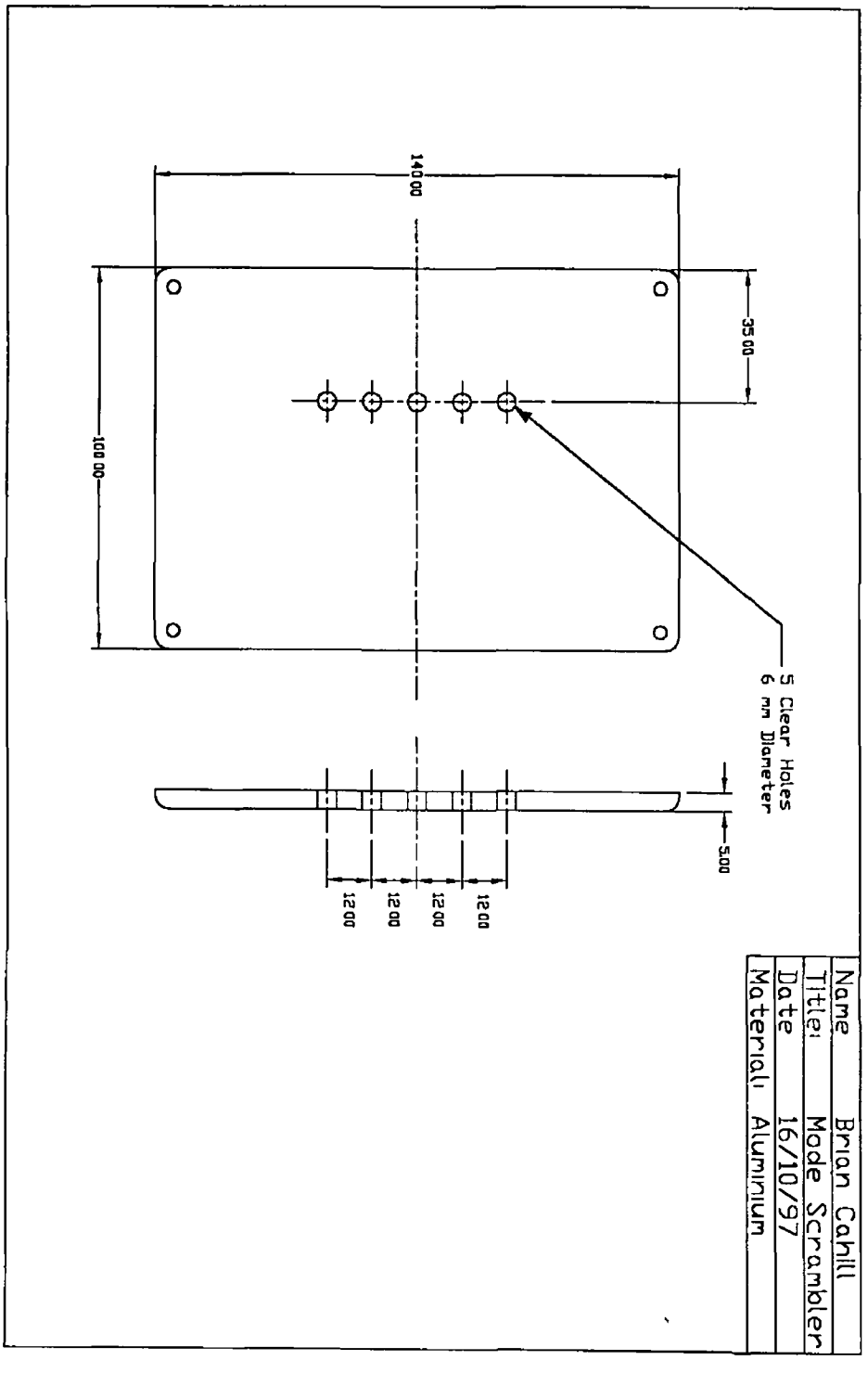
140.00
100.00
35.00
5 Clear Holes
6 mm Diameter
5.00
12.00
12.00
12.00
12.00
Name Brian Cahill
Title: Mode Scrambler
Date 16/10/97
Material Aluminium

APPENDIX A10

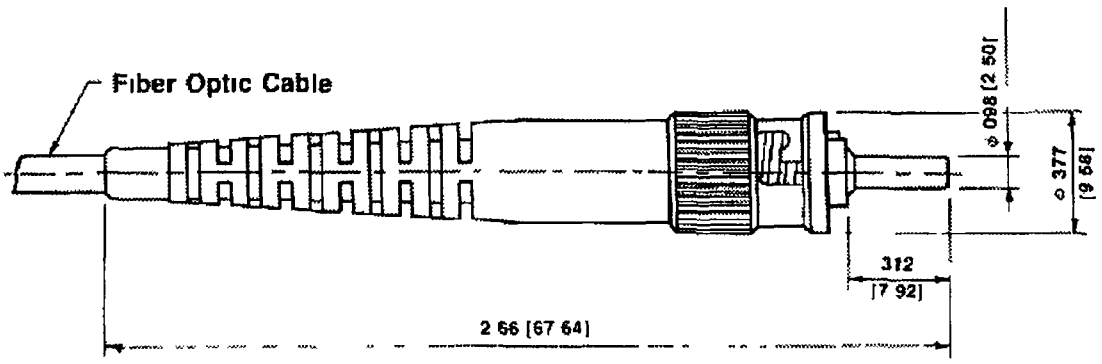

APPENDIX A11

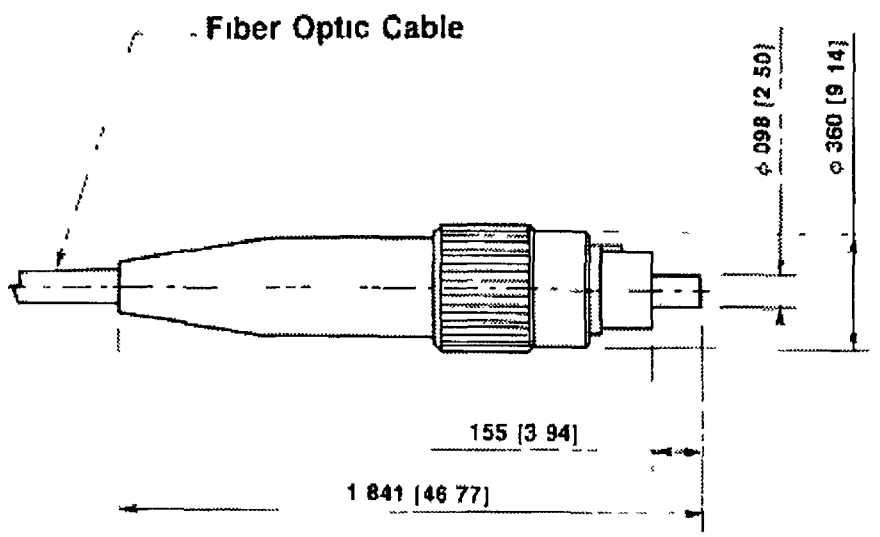

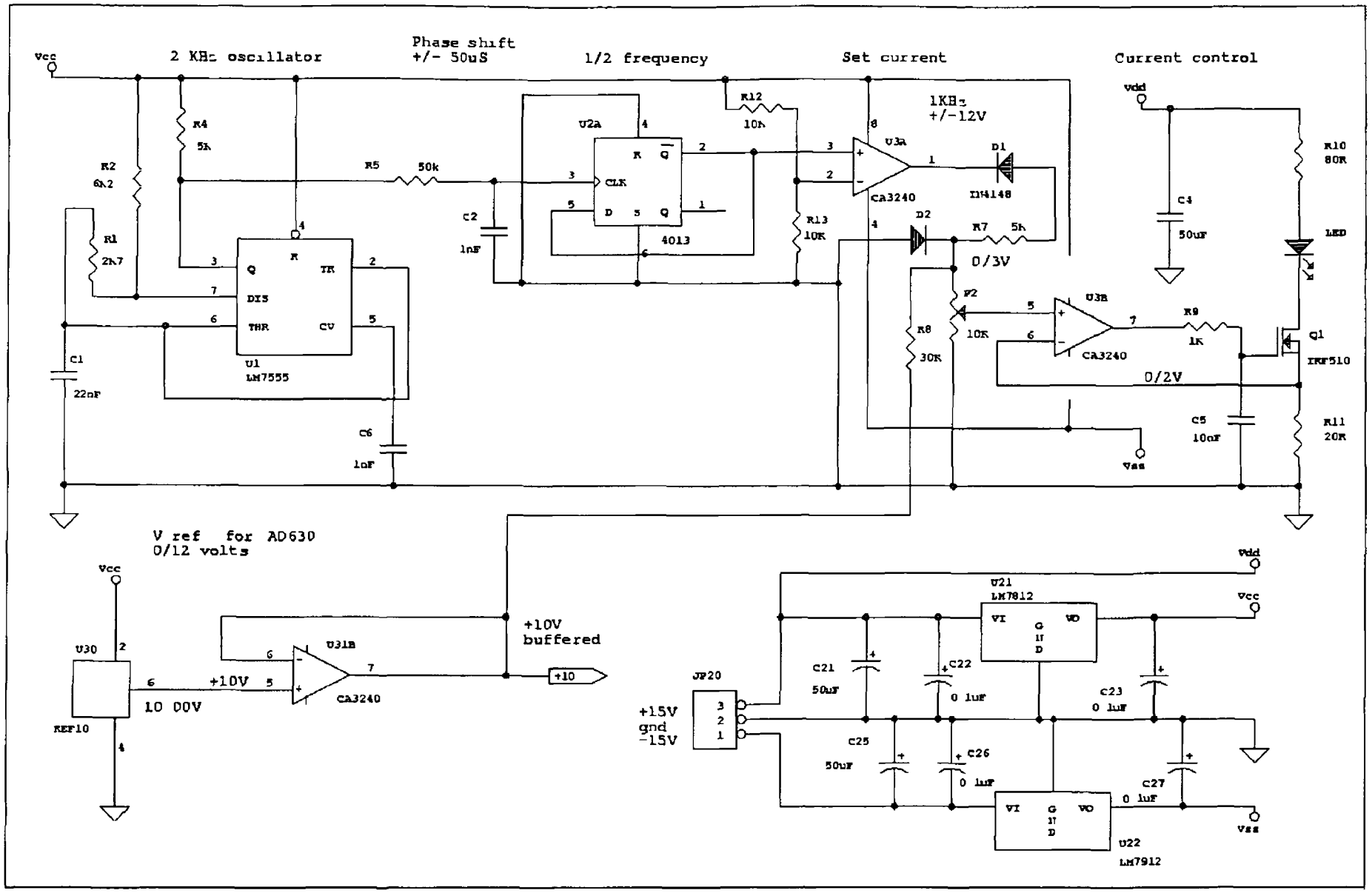
Vcc
2 KHz oscillator
Phase shift
+/- 50uS
1/2 frequency
Set current
Current control
R4
5k
R2
6k2
R1
2k7
C1
22nF
U1
LM7555
R5
50k
C2
1nF
U2a
4013
R12
10k
R13
10K
1KHz
+/-12V
U3A
CA3240
D1
IN4148
D2
R7
5k
0/3V
RV2
10K
R8
30K
U3B
CA3240
R9
1K
0/2V
Q1
IRF510
Vdd
R10
80R
C4
50uF
LED
C5
10nF
R11
20R
Vss
C6
1nF
V ref for AD630
0/12 volts
U30
REF10
10 00V
+10V
U31B
CA3240
+10V
buffered
+10
JP20
+15V
gnd
-15V
U21
LM7812
C21
50uF
C22
0 1uF
C23
0 1uF
C25
50uF
C26
0 1uF
C27
0 1uF
U22
LM7912

APPENDIX – B1

APPENDIX - B2

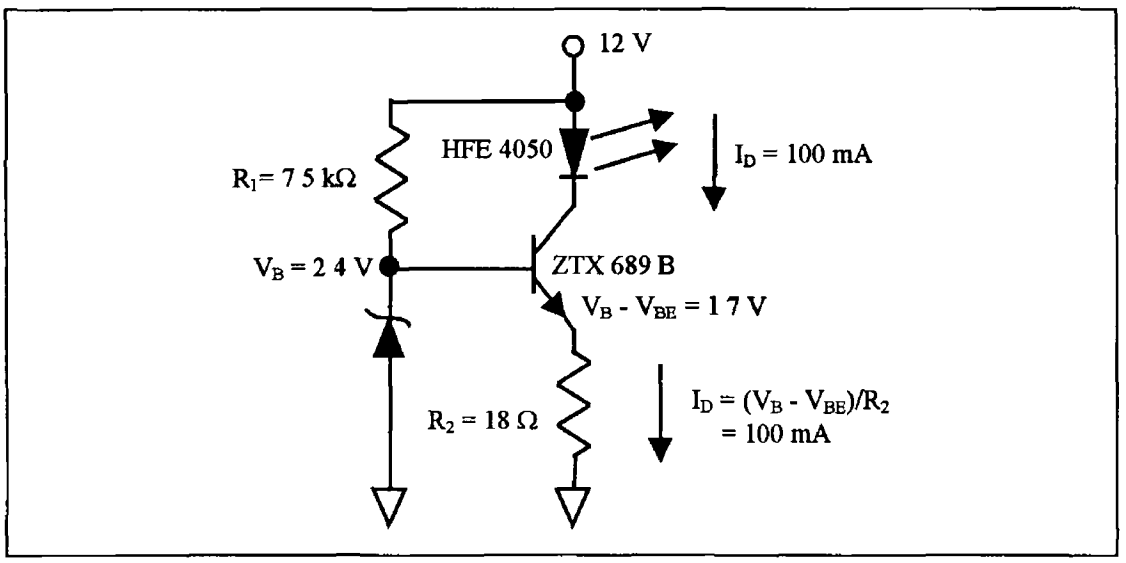

APPENDIX - B3

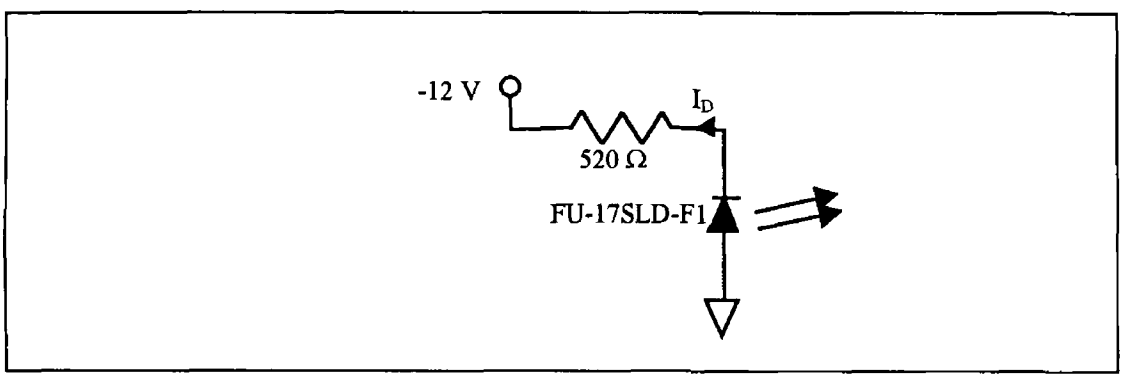

APPENDIX – B4

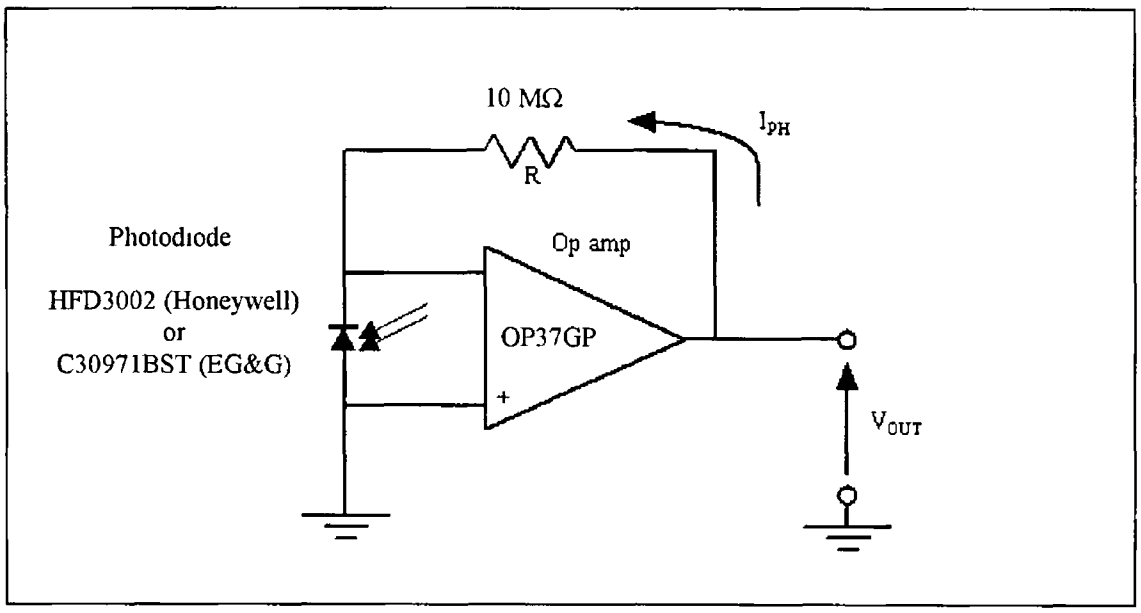

This circuit uses the same voltage regulation as appendix B1 to provide ±12V to the supply rails of the operational amplifier

APPENDIX – C1

18 September 1997

HFE4050-01X/BBA

High Power Fiber Optic LED

FEATURES

- High power LED sends 410 µW into 100/140 micron fiber
- High speed 85 MHz
- Rated to 100 mA forward current operation
- Wave solderable
- Designed to operate with Honeywell fiber optic receivers
- Industry standard ST® LP fiber connector
- Popular straight lead low profile package

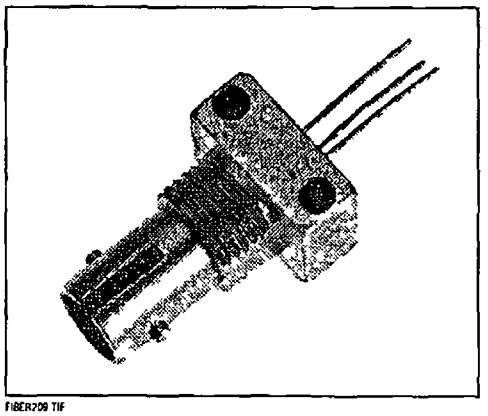

FIBER208.TIF

OUTLINE DIMENSIONS In Inches

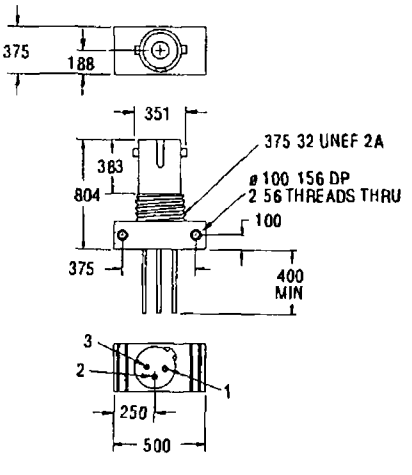

FBER101.DIM

DESCRIPTION

The HFE4050 01X/BBA is a high radiance GaAlAs 850 nanometer LED optimized for coupling into small fiber core diameters at a forward current of up to 100 mA The patented "Caprock ™ LED chip combines high power coupling with wide bandwidth The peak wavelength is matched for use with Honeywell silicon fiber optic detectors and receivers The mechanical construction uses a highly reliable ST® LP fiber optic connector / housing designed for easy mounting on printed circuit boards

APPLICATION

The HFE4050 01X/BBA is a high radiance LED packaged in a ST® LP metal housing Data rates can vary from DC to above 85 MHz depending upon component application The LED is designed to convert electrical current into optical power that can be used in fiber optic communications As the current varies (typically from 10 to 100 mA) the light intensity increases proportionally

The HFE4050 01X/BBA LED provides the maximum amount of radiance for the amount of forward current in the industry A 0 25 mm diameter glass microlens over the Caprock ™ junction collimates the light increasing the intensity Thus greater power is directed toward standard fiber optic cables

Pinout

1 Anode
2 Cathode
3 Not connected

Pin 1 identified by red sleeve

ST is a registered trademark of AT & T

Honeywell

Honeywell reserves the right to make changes in order to improve design and supply the best products possible

18 September 1997

HFE4050-01X/BBA

High Power Fiber Optic LED

ELECTRO-OPTICAL CHARACTERISTICS (T_C = 25°C unless otherwise stated)

PARAMETER	SYMBOL	MIN	TYP	MAX	UNITS	TEST CONDITIONS
Fiber Coupled Power [1]	P_{OC}					I_F = 50 mA 50/125 micron 0.20 NA fiber [2]
HFE4050-013/BBA		20	25		µW	
		17.0	16.0		dBm	
HFE4050-014/BBA		30	33		µW	
		15.2	14.8		dBm	
Forward Voltage	V_F		1.85	2.20	V	I_F = 100 mA
Reverse Voltage	B_{VR}	1.0	5.0		V	I_R = 10 µA
Peak Wavelength	λ_P		850		nm	I_F = 100 mA DC
Spectral Bandwidth	$\Delta\lambda$		60		nm	I_F = 100 mA DC
Response Time						
T = 25 C 10 90%	t_R		4	8	ns	1 V Prebias 100 mA peak
T = 25 C, 90 10%	t_F		6	10	ns	1 V Prebias 100 mA peak
Analog Bandwidth	BWE		85		MHz	I_F = 100 mA DC small signal sinusoidal modulation
P_O Temperature Coefficient	$\Delta P_O/\Delta T$		0.03		dB/°C	I_F = 100 mA
Series Resistance	r_S		4.0		Ω	DC
Capacitance	C		70		pF	V_R = 0 V f = 1 MHz
Thermal Resistance			150		°C/W	Heat sinked

Notes

1 Dash numbers indicate power output See ORDER GUIDE

2 HFE4050 01X/BBA is tested using a 50/125 micron fiber cable Actual coupled power values may vary due to mechanical alignment procedures and/or receptacle and fiber tolerances

ABSOLUTE MAXIMUM RATINGS

(25 C Free Air Temperature unless otherwise noted)

Storage temperature	65 to + 150°C
Case operating temperature	55 to + 125 C
Lead solder temperature	260 C 10 s
Continuous forward current (heat sinked)	100 mA
Reverse voltage	1 V @ 10 µA

Stresses greater than those listed under Absolute Maximum Ratings may cause permanent damage to the device This is a stress rating only and functional operation of the device at these or any other conditions above those indicated in the operational section of this specification is not implied Exposure to absolute maximum rating conditions for extended periods of time may affect reliability

FIBER INTERFACE

Honeywell LEDs are designed to interface with multimode fiber with sizes ranging from 50/125 to 200/230 microns Honeywell performs final tests using 50/125 micron core fiber All multimode fiber optic cables between 50/125 and 200/230 should operate with similar excellent performance See table for typical powers

TYPICAL COUPLED POWER (µW/dBm) @ I_F=50 mA

Dia	Index	N.A	013	014
8/125	Step	—	6/ 32.0	8/ 30.8
50/125	Graded	0.20	25/ 16.0	33/ 14.8
62.5/125	Graded	0.28	55/ 12.6	72/ 11.4
100/140	Graded	0.29	145/ 8.4	191/ 7.2

18 September 1997

HFE4050-01X/BBA

High Power Fiber Optic LED

ORDER GUIDE

Description	Catalog Listing
Standard screening, typical power out 25 µW	HFE4050-013/BBA
Standard screening, typical power out 33 µW	HFE4050-014/BBA

WARNING

Under certain application conditions the infrared optical output of this device may exceed Class 1 eye safety limits as defined by IEC 825-1 (1993 11) Do not use magnification (such as a microscope or other focusing equipment) when viewing the device s output

CAUTION

The inherent design of this component causes it to be sensitive to electrostatic discharge (ESD) To prevent ESD induced damage and/or degradation to equipment take normal ESD precautions when handling this product

Fig 1 Typical Optical Power Output vs Forward Current

FIBER021.GRA

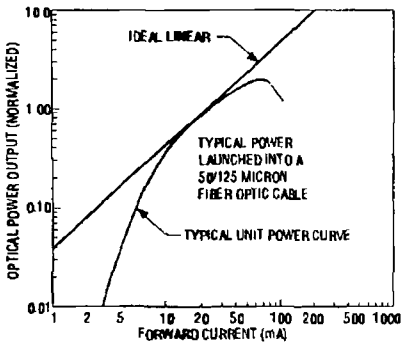

Fig 2 Typical Spectral Output vs Wavelength

FIBER105.GRA

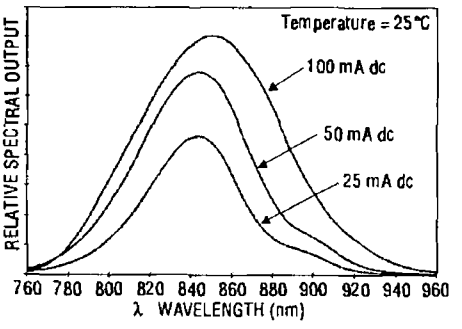

Fig 3 Typical Optical Power Output vs Case Temperature

FIBER023.GRA

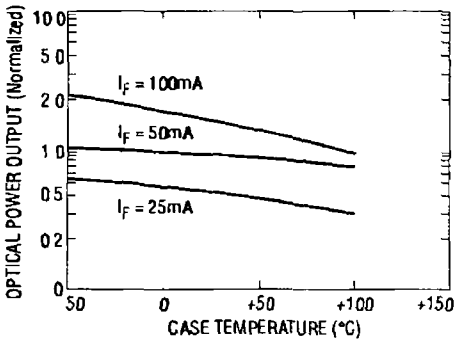

All Performance Curves Show Typical Values

Honeywell

Honeywell reserves the right to make changes in order to improve design and supply the best products possible

MITSUBISHI (OPTICAL DEVICES)

FU-17SLD-F1

FC-CONNECTORIZED MODULE

DESCRIPTION

FU-17SLD-F1 is FC-connectorized devices designed to be used with singlemode optical fiber
This module is the optimum light source for medium haul digital optical communication systems.

FEATURES

- FC connectorized package
- High optical output
- Low threshold current
- Built-in photodiode for output monitoring
- Wide operating temperature range (– 40 °C to + 85 °C)
- MQW* active layer
- FSBH** structure fabricated by all MOCVD process

* Multiple quantum well

** Facet selective-growth buried heterostructure

APPLICATION

FttL, LAN

ABSOLUTE MAXIMUM RATINGS (Tc = 25 °C)

Parameter		Symbol	Conditions	Rating	Unit
Laser diode	Optical output power from fiber end (Note1)	P_F	CW	2.5	mW
	Reverse voltage	V_{RL}	–	2	V
Photodiode for monitoring	Reverse voltage	V_{RD}	–	15	V
	Forward current	I_{FD}	–	2	mA
Operating case temperature		Tc	–	– 40 ~ + 85	°C
Storage temperature		Tstg	–	– 40 ~ + 85	°C

Note 1 Singlemode fiber master plug with mode field diameter 10 μm

OUTLINE DIAGRAM

(Unit mm)

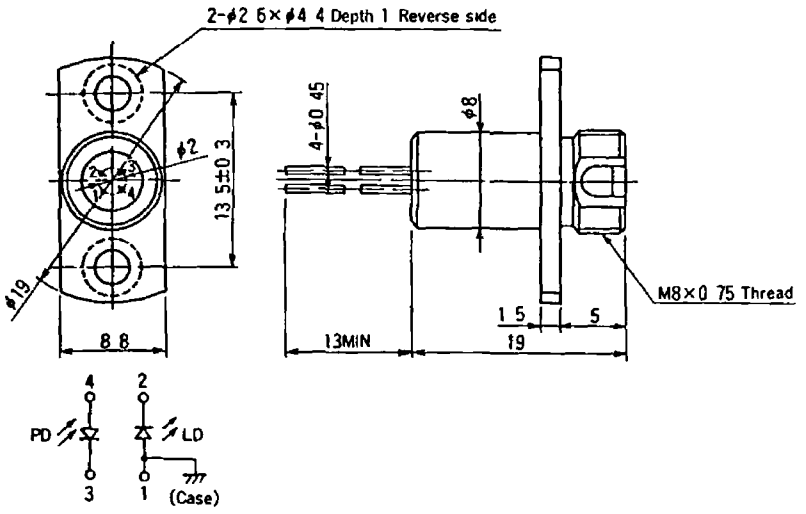

FU-17SLD-F1

ELECTRICAL/OPTICAL CHARACTERISTICS (Tc = 25°C unless otherwise noted)

Parameter	Symbol	Test conditions	Limits			Unit
			Min.	Typ	Max.	
Threshold current	I_{th}	CW	3	7	15	mA
Modulation current	I_{mod}	CW	8	–	28	mA
Operating voltage	V_{OP}	CW, $I_F = I_{th} + I_{mod}$ (Note 2)	–	1.2	1.6	V
Optical output power from fiber end (Note 3)	P_F	CW $I_F = I_{th} + I_{mod}$	1	–	–	mW
Central wavelength	λc	CW, $I_F = I_{th} + I_{mod}$	1285	1300	1330	nm
Rise and fall time (LD)	t_r, t_f	$I_B = I_{th}$, 10~90% (Note 4)	–	0.3	0.5	ns
Tracking error (Note 5)	E_r	Tc = – 40~+ 85°C, CW, APC	–	0.5	–	dB
Differential efficiency (Note 3)	η	–	–	0.07	–	mW/mA
Monitor current	I_{mon}	CW, $I_F = I_{th} + I_{mod}$, $V_{RD} = 5V$	0.2	0.9	1.5	mA
Dark current (Photodiode)	I_D	$V_{RD} = 5V$	–	0.1	0.5	μA
Capacitance (Photodiode)	Ct	$V_{RD} = 5V$, f = 1MHz	–	–	20	pF

Note2. I_F Forward current (LD)

3 Singlemode fiber master plug with mode field diameter 10μm

4 I_B Bias current (LD)

5

$$E_r = MAX \left| 10 \log \frac{P_F}{P_F(25°C)} \right| \quad [dB]$$

TYPICAL CHARACTERISTICS

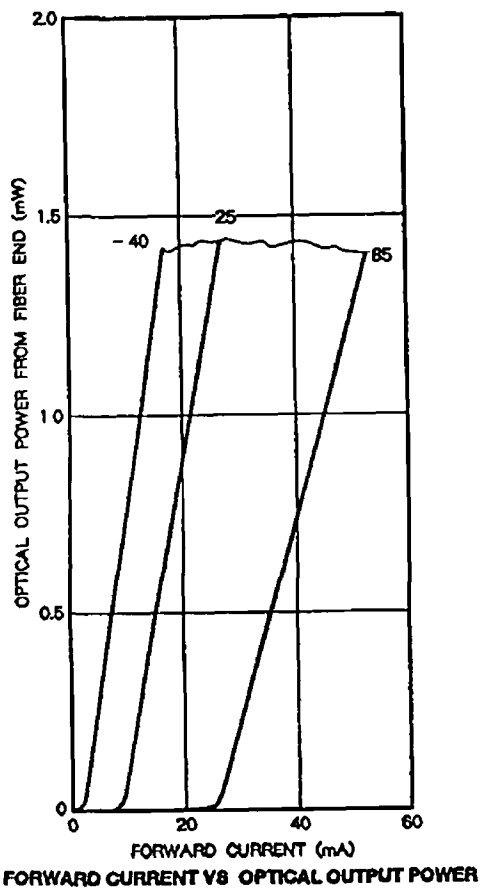

FORWARD CURRENT VS OPTICAL OUTPUT POWER

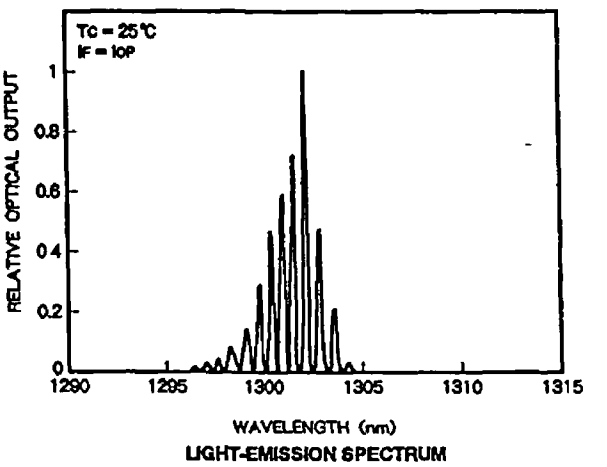

LIGHT-EMISSION SPECTRUM

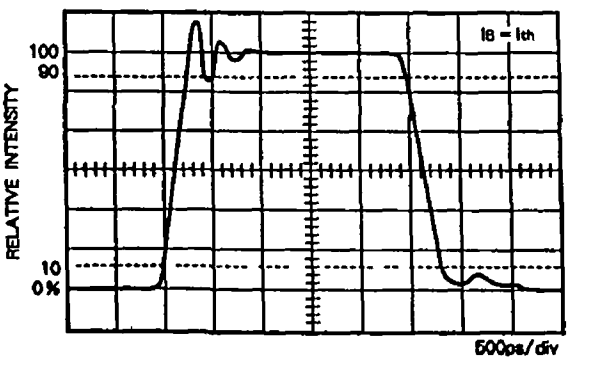

PULSE RESPONSE

APPENDIX – C3

HFD3002-002/BBA

Silicon PIN Photodiode

FEATURES

- Low capacitance
- High speed t_r = 30 ns max at V_R = 5 V 10 ns max at V_R = 15 V
- High responsivity
- Industry standard ST® LP fiber connector
- Housing electrically isolated
- Wave solderable

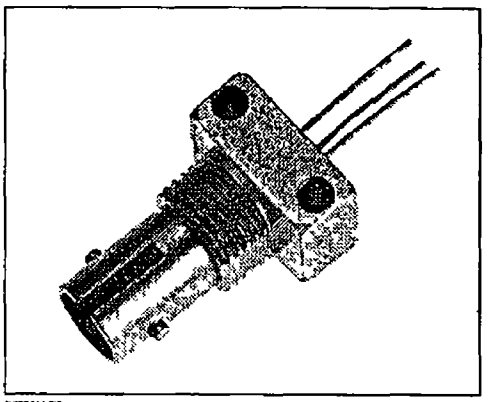

FIBER00A.TIF

DESCRIPTION

The HFD3002 002/BBA PIN Photodiode is designed for high speed use in fiber optic receivers It has a large area detector providing efficient response to 50 1000 mm diameter fibers at wavelengths of
650 to 950 nanometers The HFD3002 002/BBA is comprised of an HFD3002 PIN photodiode which is mounted in a low profile ST® fiber optic connector The ST® connector housing aligns the component s optical axis with the axis of the optical fiber

The HFD3002 002/BBAs case is electrically isolated from the anode and cathode terminals to enhance the EMI/RFI shielding which increases the sensitivity and speed The metal ST® housing acts as a shield for the PIN photodiode component

OUTLINE DIMENSIONS in inches (mm)

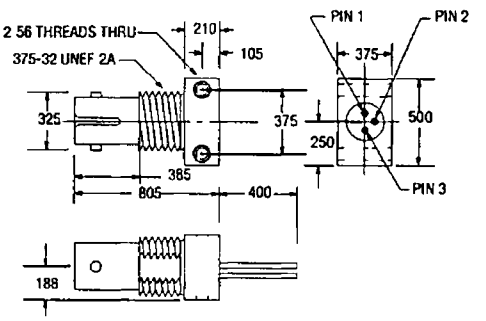

FIBER103.DIM

Pinout

1 Anode (P type)
2 Cathode (N type)
3 Ground

ST is a registered trademark of AT & T

Honeywell

Honeywell reserves the right to make changes in order to improve design and supply the best products possible

HFD3002-002/BBA

Silicon PIN Photodiode

ELECTRO OPTICAL CHARACTERISTICS (T_C = 25 C unless otherwise stated)

PARAMETER	SYMBOL	MIN	TYP	MAX	UNITS	TEST CONDITIONS
Peak Response Wavelength	λ_P		850		nm	
Flux Responsivity [1]	R				A/W	λ = 850 nm
			0 6			50 µm core fiber 0 20 µA
		0 45	0 6			100 µm core fiber 0 28 µA
			0 55			200 µm core fiber 0 40 µA
			0 30			1000 µm core fiber 0 53 µA
Dark Leakage Current	I_D		0 05	2	nA	V_R = 5 V
Reverse Breakdown Voltage	B_{VR}	110	250		V	I_R = 10 mA
Package Capacitance	C		1 4		pF	V_R = 5 V f = 1 MHz
Rise Time	t_r				ns	
10 90%			17	30		V_R = 5 V
			5	10		V_R = 15 V
			1			V_R = 90 V
Field of View	FoV		85		Degrees	

Notes

1 Responsivity is measured with a fiber optic cable centered on the mechanical axis using an 850 nm LED as the optical source to the fiber

ABSOLUTE MAXIMUM RATINGS

(Tcase = 25°C unless otherwise noted)

Storage temperature	65 to +15 C
Operating temperature	55 to +125 C
Lead solder temperature	260 C for 10 s
Case/cathode (anode) voltage	110 V
Power dissipation	200 mW
Reverse voltage	110 V

Stresses greater than those listed under Absolute Maximum Ratings may cause permanent damage to the device This is a stress rating only and functional operation of the device at these or any other conditions above those indicated in the operational section of this specification is not implied Exposure to absolute maximum rating conditions for extended periods of time may affect reliability

Honeywell

HFD3002-002/BBA

Silicon PIN Photodiode

ORDER GUIDE

Description	Catalog Listing
Standard silicon PIN photodiode	HFD3002 002/BBA

CAUTION

The inherent design of this component causes it to be sensitive to electrostatic discharge (ESD) To prevent ESD induced damage and/or degradation to equipment take normal ESD precautions when handling this product

FIBER INTERFACE

Honeywell detectors are designed to interface with multimode fibers with sizes (core/cladding diameters) ranging from 50/125 to 200/230 microns Honeywell performs final tests using 100/140 micron core fiber The fiber chosen by the end user will depend upon a number of application issues (distance link budget cable attenuation splice attenuation and safety margin) The 50/125 and 62 5/125 micron fibers have the advantages of high bandwidth and low cost making them ideal for higher bandwidth installations The use of 100/140 and 200/230 micron core fibers results in greater power being coupled by the transmitter making it easier to splice or connect in bulkhead areas Optical cables can be purchased from a number of sources

Fig 1 Rise/Fall Time vs Reverse Bias Voltage

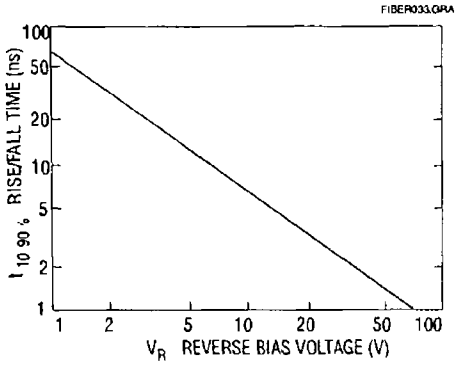

Fig 2 Package Capacitance vs Reverse Bias Voltage

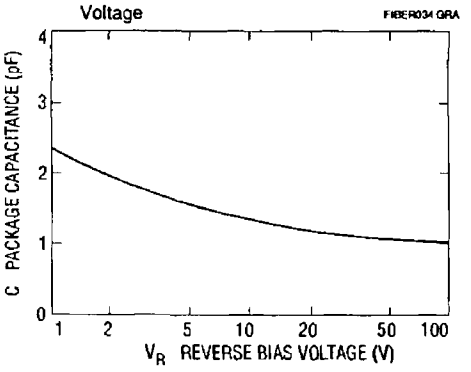

Fig 3 Spectral Responsivity

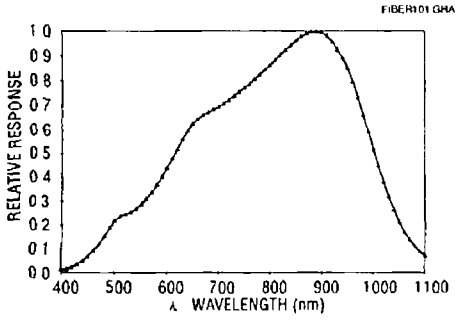

Fig 4 Dark Leakage Current vs Temperature

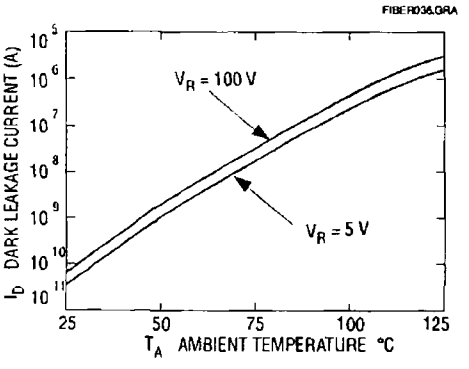

Honeywell

HFD3002-002/BBA

Silicon PIN Photodiode

Fig 5 Angular Response

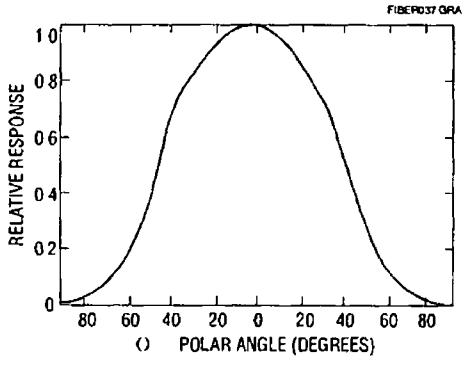

All Performance Curves Show Typical Values

APPENDIX D

This appendix contains the derivations necessary to represent the extent of a radiated spot on a surface due to incident radiation from an optical fibre The maximum extent in the x and y directions are derived In figure the lines AD and AC represent on the cartesian plane the extent of fibre emission, as defined by numerical aperture of said fibre, in x direction Point A represents the endface of the fibre The plane z=0 represents a reflecting surface d is the stand-off distance from this surface The line AB represents a continuation of the centre axis of the emitting fibre, the line along which peak intensity occurs α is the angle of incidence θ is derived from the numerical aperture of the fibre, equation 2 4

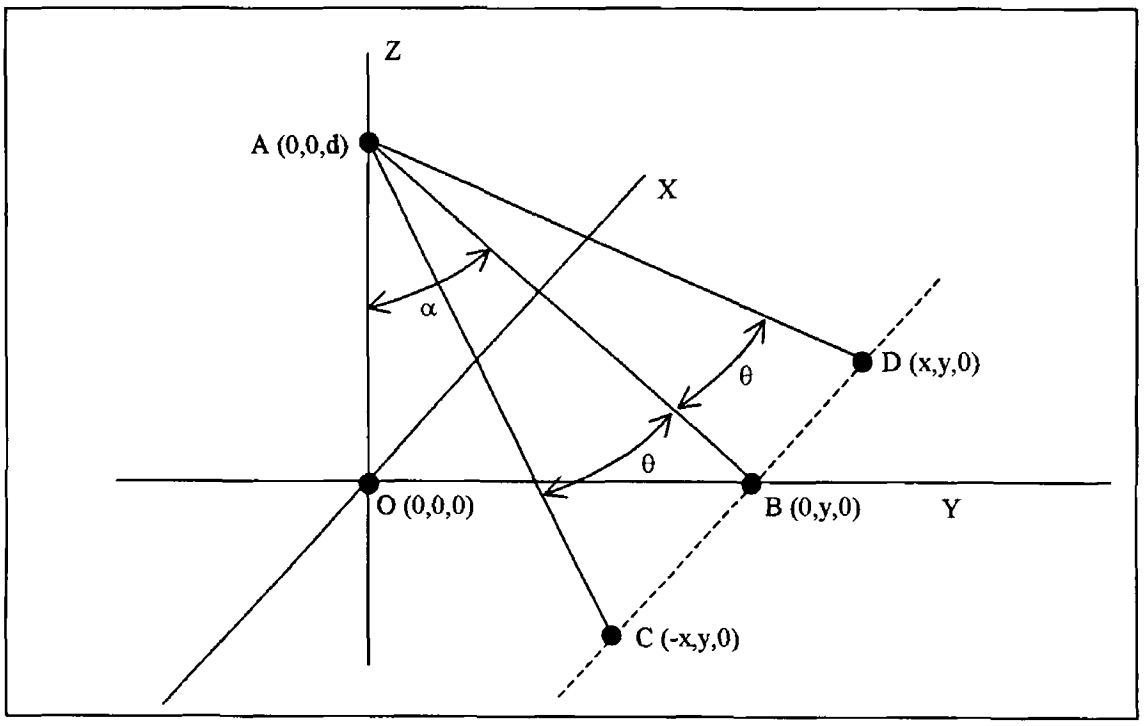

Figure D1 The extent of fibre emission, as defined by numerical aperture of said fibre, in x direction

From triangle ABO

$$\text{Tan } \alpha = y / d$$

Thus

$$y = d \, Tan \, \alpha$$

From triangle ABC

$$Tan \, \theta = x / \|AB\|$$

Where

$$\|AB\| = \sqrt{d^2 + y^2} = d\sqrt{1 + Tan^2 \alpha} = dSec\alpha$$

Thus

$$x = d \, Tan \, \theta \, Sec \, \alpha$$

Thus, the width of the spot in the X direction, w_x, is equal to the following

$$w_x = 2d \, Tan \, \theta \, Sec \, \alpha$$

In figure D2, lines AE and AF show the extents of the emitted radiation in the zy plane

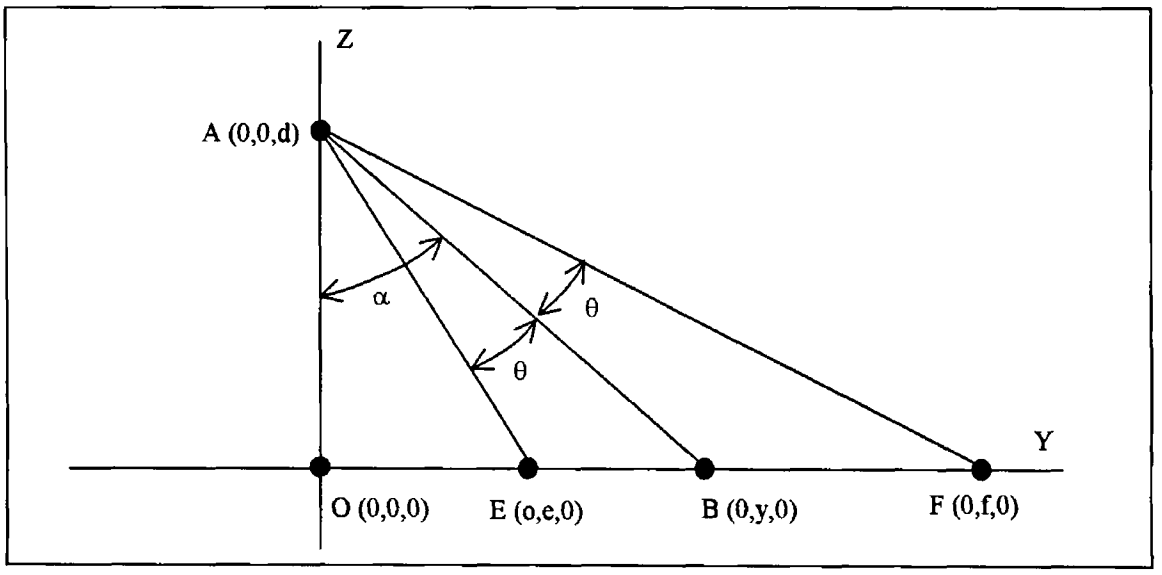

Figure D2 The extent of fibre emission, as defined by numerical aperture of said fibre, in y direction

From triangle AFO

$$Tan \, (\alpha + \theta) = f / d$$

Thus

$$f = d \, Tan \, (\alpha + \theta)$$

Similarly for triangle AEO

$$e = d \, \mathrm{Tan}(\alpha - \theta)$$

Thus the width of the spot in the Y direction, w_y is equal to the following

$$w_y = e + f = d \, (\mathrm{Tan}(\alpha - \theta) + \mathrm{Tan}(\alpha + \theta))$$

The width of the spot in both x and y directions depends on the stand-off distance, d, the numerical aperture, and the angle of incidence These derivations considered the core of the optical fibre to be negligible, which is true when the stand-off distance is large in comparison to core size